UNIVERSITÄT
BAYREUTH

Lehrstuhl für Kristallographie

Temperature dependent magnetic order in FeOCl type compounds

Von der Universität Bayreuth
zur Erlangung des akademischen Grades eines
Doktors der Naturwissenschaften (Dr. rer. nat)
genehmigte Abhandlung

vorgelegt von
Jian Zhang
aus Changle, China

1. Gutachter: Prof. Dr. Sander van Smaalen
2. Gutachter: Prof. Dr. Christine Kuntscher

Tag der Einreichung: 09. Juli 2014
Tag des Kolloquiums: 22. Oktober 2014

Dedicated to...

My beloved Family

Contents

1 Introduction **1**

2 Theoretical background **5**

2.1 Magnetism in materials 5

2.2 Interactions between electrons 7

2.3 Spin-Peierls transition 10

2.4 Nuclear and magnetic structure 12

3 X-ray experimental techniques **13**

3.1 Sample preparation 13

3.1.1 Criterion for determining the size of crystal 13

3.1.2 Technique of crystal holder 14

3.2 X-ray diffraction experiments 15

3.2.1 Experiments by the radiation of sealed tube 16

3.2.2 Experiments by synchrotron radiation 21

3.2.3 Control of the temperature of the crystal 23

3.3 Integration of reflections 25

4 Transition-metal oxyhalides MOX **27**

4.1 Crystal structure 27

4.2 Spin Peierls phase transition 28

4.3 Behavior of doped TiOCl 32

4.4 Magnetic structure of VOCl and CrOCl 33

4.5 Incommensurate magnetic structure of FeOCl 35

5 Magnetoelastic coupling in the incommensurate antiferromagnetic phase of FeOCl **37**
5.1 Abstract . . . 37
5.2 Introduction . . . 38
5.3 Experimental . . . 39
5.3.1 Crystal growth . . . 39
5.3.2 Magnetic and thermal measurements . . . 40
5.3.3 Single-crystal x-ray diffraction . . . 42
5.4 Discussion . . . 46
5.5 Conclusions . . . 48

6 Transformation between spin-Peierls and incommensurate fluctuating phases of Sc-doped TiOCl **51**
6.1 Abstract . . . 51
6.2 Introduction . . . 52
6.3 Experimental and results . . . 54
6.3.1 Crystal growth . . . 54
6.3.2 Specific heat . . . 55
6.3.3 Temperature-dependent x-ray diffraction . . . 55
6.4 Discussion . . . 63
6.5 Conclusions . . . 66

7 Enlargement of incommensurate phase in TiOCl by intercalating Na **69**
7.1 Introduction . . . 69
7.2 Experimental and results . . . 72
7.3 Discussion . . . 78
7.4 Conlusion . . . 80

8 Nuclear and magnetic superstructure of CrOCl at 8 K **83**
8.1 Introduction . . . 83
8.2 Experimental . . . 85
8.2.1 Preparation of CrOCl . . . 85

8.2.2 X-ray diffraction experiments 85
8.3 Structure refinement and discussion 87
8.4 Conclusion 94

9 Summary **97**

10 Zusammenfassung **101**

A Supplementary materials: FeOCl **105**
A.1 Profiles of 2θ-dependent ω-scans 106
A.2 Profiles fitting for determination of the peak position of FeOCl 112
A.3 Structural distortion with modulation wave vector 116

B Supplementary materials: $\mathbf{Sc}_x\mathbf{Ti}_{1-x}\mathbf{OCl}$ **117**
B.1 Profiles of main reflections at selected temperatures 118
B.2 Dependence of the scattered intensity on diffraction angle 2θ 122
B.3 Reflection positions by q scans 127
B.4 ω Scans at the positions of main reflections and commensurate and incommensurate satellite reflections 136

C Supplementary materials: $\mathbf{Na}_x\mathbf{TiOCl}$ **149**
C.1 Dependence of the scattered intensity on diffraction angle 2θ 150
C.2 Dependence of intensity on ω 151
C.3 Reflection positions by q scans 153
C.4 ω Scans at the positions of commensurate and incommensurate satellite reflections 158

D Supplementary materials: CrOCl **161**

Publications **173**

Acknowledgements **175**

Erklärung **177**

Chapter 1

Introduction

Low-dimensional systems exhibit a wide range of physical behaviors, among which magnetic properties have attracted huge interest (Hone and Richards, 1974; Kimura and Tokura, 2000; Landee and Turnbull, 2013). This thesis reports on the structural and magnetic properties of the low-dimensional transition-metal oxychlorides MOCl (M = Ti, Cr, Fe), the doped compound $Sc_xTi_{1-x}OCl$ ($x = 0.005$) and the intercalated compound Na_xTiOCl ($x = 0.01$). The transition-metal atoms are responsible for the magnetic properties. Single-crystal x-ray diffraction experiments, which were performed with synchrotron radiation at DESY (Hamburg), have been used to study these compounds.

The magnetic order in substances can be investigated by many techniques, such as Mössbauer spectroscopy (for compounds that contain Fe atoms) (Maddock, 1997), neutron diffraction (Chatterji, 2006), magnetic susceptibility (Gregson, 1974) and so on. In the transition-metal oxychlorides, the change of the magnetic state (magnetic transition) is often accompanied by a structural distortion (Shaz et al., 2005; Angelkort et al., 2009), which is typically small. However, x-ray diffraction is a very sensitive technique to reveal these weak lattice distortions (Lovesey and Collins, 1996). Furthermore, the structure refinement against single-crystal synchrotron x-ray radiation data can disclose the atomic coordinates and the site occupancies of atoms, as well as the displacive modulation of the atoms. All of these information can be used to develop an understanding of the interactions responsible for the magnetic behavior.

Layered isostructural compounds MOCl reveal different magnetic behaviors, resulting from orbital order of the different numbers of $3d$ electrons of the M^{3+} ions. Ti^{3+} possesses a single $3d$ electron, that is responsible for the quasi-one-dimensional magnetic character of TiOCl. Upon cooling, TiOCl develops an incommensurate state at $T_{c2} = 90$ K, and then transforms into a spin-Peierls state at $T_{c1} = 67$ K (Seidel et al., 2003). Both phases have been found to be monoclinic (Shaz et al., 2005; Schönleber et al., 2006). The other metal ions possess more than one $3d$ electron, forming two-dimensional magnetic systems and revealing antiferromagnetic behavior at low temperatures. VOCl is in a two-fold magnetic superstructure at low temperatures (Wiedenmann et al., 1983), exhibiting monoclinic symmetry with a monoclinic angle of γ (Schönleber et al., 2009). CrOCl possesses a four-fold magnetic superstructure with **a**–unique monoclinic symmetry at low temperatures (Angelkort et al., 2009). FeOCl develops into an antiferromagnetic phase at 82.0(2) K, accompanied by a temperature-dependent **c**–unique monoclinic lattice distortion (Chapter 5 of the present thesis).

Additional electrons or holes play an important role in the superconductors with low-dimensional structures (Hong and Hirsch, 1992; Yamanaka et al., 1996). TiOCl, a layered Mott insulator at room temperature, is a suitable candidate for the study of insulator-metal transitions by the doping of electrons or holes. The quasi-one-dimensional structure of TiOCl favors the transport of electrons or holes. Experimentally, the doping of electrons could be achieved by intercalating alkali metal atoms (Kuntscher et al., 2010); and the doping of holes have been carried out by replacing Ti by Sc (Beynon and Wilson, 1993).

A description of the origin of magnetism in materials is given in Chapter 2, followed by a discussion of $3d$ orbitals in an octahedral crystal field. At the end a definition of the spin-Peierls transition and the relation between nuclear structure and magnetic structure are presented.

Chapter 3 focuses on x-ray diffraction experimental techniques, which have been employed in this thesis. The criterion for determining the size of the crystal and the technique of crystal holder are discussed. The properties of conventional and synchrotron radiation as well as the setup of the used diffractometers and equipments for cooling the crystals are described. The method for integrating the intensities of

synchrotron x-ray radiation reflections is explained.

Chapter 4 is dedicated to the crystal-chemical description of structural properties of the transition-metal oxyhalides MOX (M = Ti, V, Cr and Fe; X = Br, Cl). The spin-Peierls state and phase transitions of TiOCl are reviewed. Furthermore, an overview is given of the literatures on doped TiOCl compounds. The commensurate magnetic structures of VOCl and CrOCl and the incommensurate magnetic structure of FeOCl are described.

FeOCl was the first compound synthesized among MOCl compounds. Chapter 5 reports the magnetoelastic coupling in the incommensurate antiferromagnetic phase of FeOCl. Temperature-dependent x-ray diffraction experiments reveal the antiferromagnetic phase transition is accompanied by a monoclinic lattice distortion. The temperature-dependent behavior of superlattice reflections indicates an incommensurate character of the magnetic order.

Chapter 6 reports the behavior of $Sc_xTi_{1-x}OCl$ ($x = 0.005$). Different from the absence of spin-Peierls phase in the other $Sc_xTi_{1-x}OCl$ ($x \geq 0.01$), a spin-Peierls-like phase is revealed by the presence of commensurate superlattice reflections. However, both the low temperature phases in $Sc_xTi_{1-x}OCl$ ($x = 0.005$) lack long-range order.

Chapter 7 reports the influence to the spin-Peierls state in TiOCl caused by intercalating Na. Temperature-dependent synchrotron x-ray diffraction experiments reveal that the phase transition temperatures of Na_xTiOCl ($x = 0.01$) are changed comparing to pure TiOCl, resulting in a larger temperature range of incommensurate phase.

In chapter 8 the structural refinement of CrOCl at 8 K against the integrated intensities of synchrotron x-ray radiation reflections is reported. Furthermore, the magnetic structure of CrOCl at 8 K is refined with introducing the atomic modulation parameters those are derived from nuclear modulated structure.

Chapter 2

Theoretical background

2.1 Magnetism in materials

Magnetism is a character of materials in which there is a force of repulsion or attraction between like or unlike poles. An electronic current loop can generate a magnetic dipole with the direction perpendicular to the plane of the current loop. The right-hand-rule provides the direction of the north pole; the other direction is the south pole. Within this model, atomic electrons in circular orbits around the nuclei will produce magnetic moments, which are called orbital magnetic moments. In the year 1925, G. E. Uhlenbeck and S. Goudsmit proposed that the electron is not a simple point charge, but rotating around itself. It can not only produce orbital magnetic moment but also contribute a spin magnetic moment to the magnetic system. Both of these kinds of magnetic moments contribute to the magnetism in materials. So far we know from many experiments that electrons carry spin $S = 1/2$, which is important to help us to understand the magnetic behavior of materials. Substances can be classified according to their distribution of magnetic moment, $\mathbf{m(r)}$. If $\mathbf{m(r)} \equiv 0$ at every point $\vec{\mathbf{r}}$, the substance can be either diamagnet or paramagnet. If $\mathbf{m(r)} \neq 0$, the substance possesses a magnetic structure. These magnetic materials can be divided in two categories, ferromagnets and antiferromagnets (Borovik-Romanov and Grimmer, 2006). Here we shall give a short review of disordered magnetics and ordered magnetics.

Paramagnet and diamagnet can be distinguished by the sign of the magnetic susceptibility χ_m. The concept of magnetic susceptibility comes from the following equation:

$$M = \chi_m H \tag{2.1}$$

In this equation M is the magnetization of the material, and H is the strength of the applied magnetic field. Both of them are measured in amperes per meter (SI units).

Diamagnetism is an intrinsic property of all materials, which is the tendency of a material to oppose an applied magnetic field. The diamagnetic susceptibility is negative. For most materials it is very small, around -10^{-6}, and isotropic (Borovik-Romanov and Grimmer, 2006). Diamagnetism can only be observed in a purely diamagnetic material. If any other magnetism is present, the diamagnetism is too weak to be observed directly. There are no electrons with unpaired spins in diamagnetic materials.

Most paramagnetic materials include ions or atoms with a partly filled inner electronic shell, such as the $3d$ shell of transition metals, the $4f$ shell of rare earths, and the $5f$ shell of actinides. In $3d$ ions the orbital magnetic moments are quenched, therefore only the spin-magnetic moments should be considered. There are unpaired electrons in a paramagnetic material. The paired electrons must point their spin magnetic moments in opposite directions, resulting in counteracting each other's moments. The unpaired electrons produce a spin magnetic moment pointing in any direction. Under an external magnetic field, the magnetic moment originated in unpaired electrons will tend to align with the external magnetic field.

Ordered magnetic materials can be either ferromagnets or antiferromagnets. In ferromagnetic materials, magnetic moments of different atoms line up parallel with each other in a region called a magnetic domain. The magnetic field is intense within the domain, but the material will show a non-magnetized state due to different orientations of the magnetization of different domains. When a ferromagnetic material is put into an external magnetic field, the magnetic domains will tend to align parallel to the field. After the external magnetic field being removed, these magnetic domains still maintain a parallel orientation. All ferromagnetic materials

will lose the ferromagnetic property above the Curie temperature T_c. Above this temperature, the materials are paramagnetic.

In antiferromagnetic materials, the magnetic moment, which is generated by the spins of electrons of one atom, align with neighboring atoms, with magnetic moments pointing in opposite directions. Therefore, antiferromagnets have zero magnetization. Most of antiferromagnetic order may exist at low temperatures and disappear above the Néel temperature T_N. The material is paramagnetic above the Néel temperature. Most transitions from a paramagnetic into an ordered magnetic state are second-order phase transitions (Borovik-Romanov and Grimmer, 2006).

Another special magnetic state is ferrimagnetism. In ferrimagnets, as antiferromagnets, neighboring magnetic moments from different sublattices align in opposite directions. But the magnitudes of opposing magnetic moments in different sublattices are not equal to each other and hence a spontaneous magnetization remains (Spaldin, 2010). Their macroscopic behavior is similar to that of ferromagnets.

2.2 Interactions between electrons

Strongly correlated electronic materials are a wide category of electronic materials, which show unusual electronic and magnetic properties. In simple solid state theory, the electrostatic interactions between electrons are ignored. There each electron is regarded as an individual electron, without interacting with other electrons. But in many materials, the interactions between electrons cannot be neglected. In strongly correlated electronic systems, many novel physical phenomena appear due to the strong interactions between electrons. Examples are high-temperature superconductors, charge-density waves in one-dimensional conductors. In transition-metal materials MOX (M = Ti, V, Cr and Fe; X = Br, Cl), the magnetic moments arise from the spins of the d electrons of the transition-metal atoms M. The d electrons interact with each other through orbital coupling.

In an octahedral crystal fields, the XYZ coordinate system is defined by the six anion ligands that surround the cation. There are five $3d$ orbtials, which are labeled $3d_{xy}$, $3d_{xz}$, $3d_{yz}$, $3d_{x^2-y^2}$, and $3d_{z^2}$ (Fig. 2.1 a). $3d_{xy}$, $3d_{xz}$ and $3d_{yz}$ belong to t_{2g} group, $3d_{x^2-y^2}$ and $3d_{z^2}$ belong to e_g group. Owing to the repulsions between the d

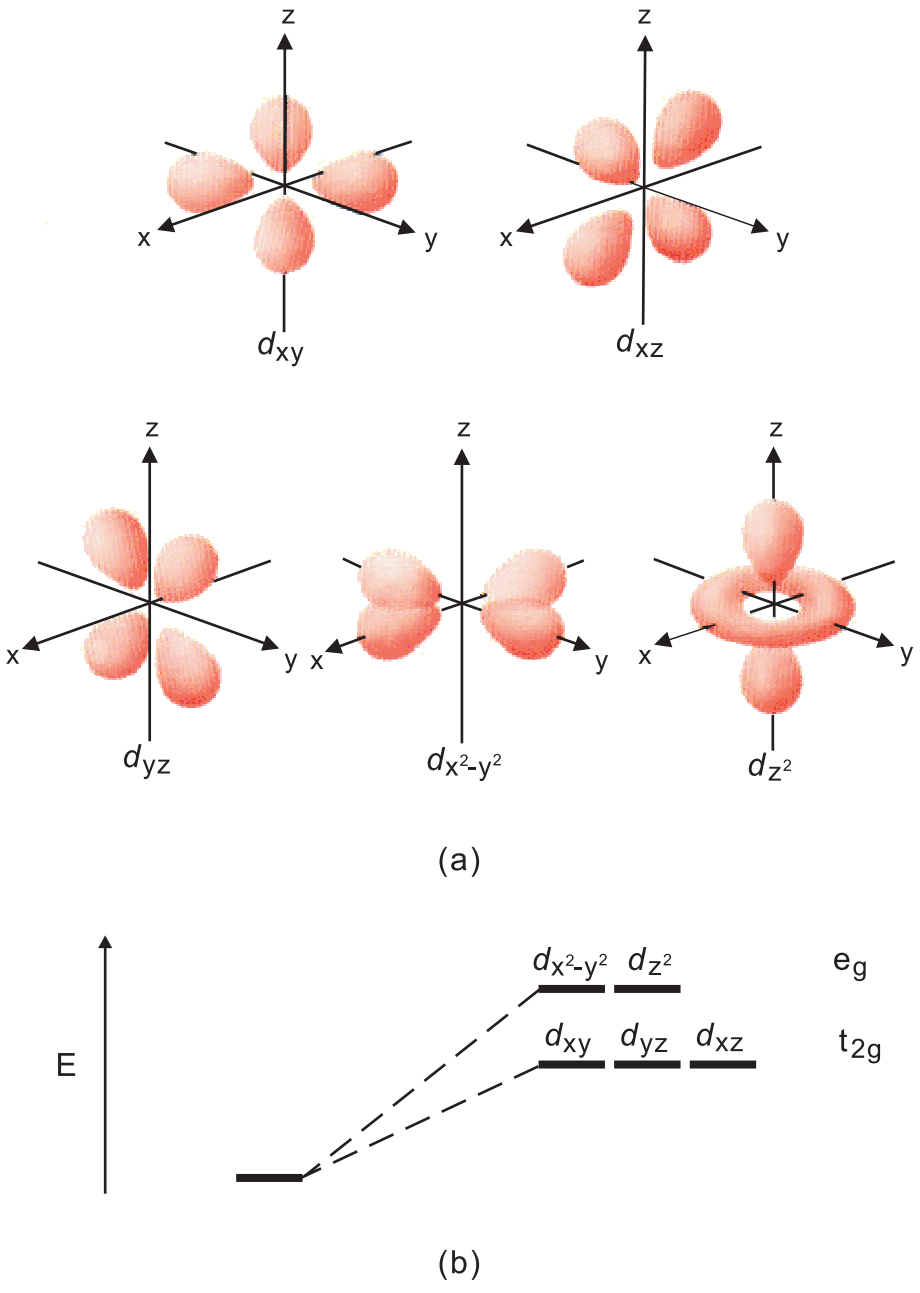

Figure 2.1: (a) The shapes and orientations of the d orbitals. Graphic was taken from *http://chem.wisc.edu/deptfiles/genchem/sstutorial/Text5/Tx53/tx53.html*. (b) The energy of the five $3d$ orbitals in an octahedral crystal fields.

orbital electrons and the surrounding negative charge, the energies of the d orbitals will be influenced depending on the geometry of the surrounding anions. The energy

of t_{2g} is lower than that of e_g (Fig. 2.1 b). In this thesis, a different XYZ coordinate system has been employed, which relates to the site symmetry of M and the lattice symmetry of MOCl. Here, x is along **b**, y is along **c**, and z is along **a** (Fig. 2.2 a). Thus the energy of $3d_{xz}$, $3d_{yz}$, and $3d_{x^2-y^2}$ is lower than that of the other two orbitals in this setting (Fig. 2.2 b).

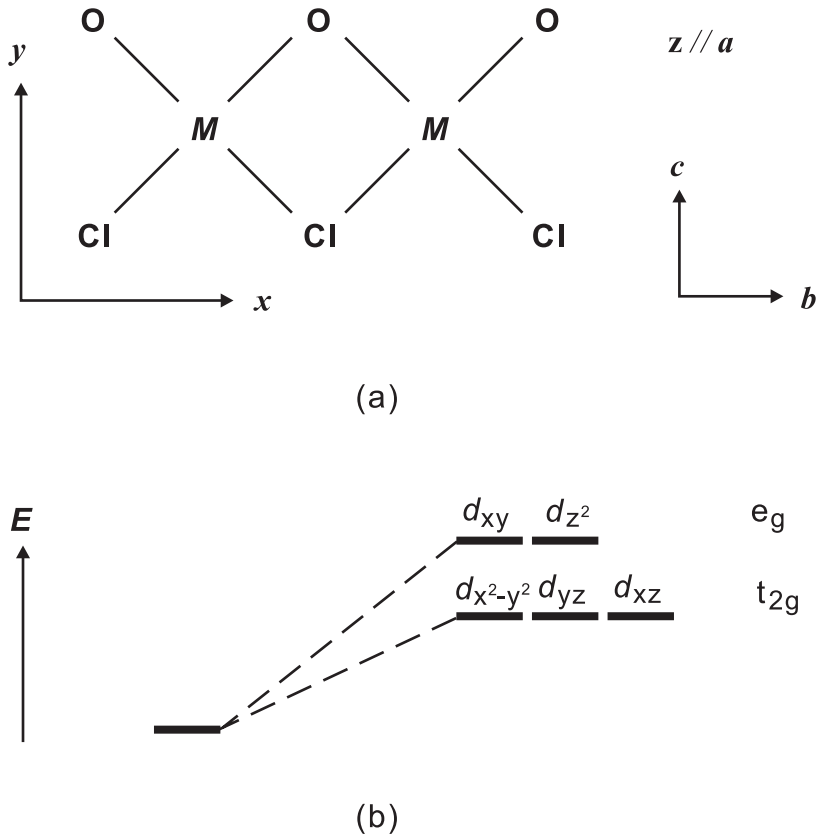

Figure 2.2: (a) The setting of XYZ coordinate system in MOCl (M = Ti, V, Cr and Fe) crystal. (b) The energies of the five $3d$ orbitals in an octahedral crystal field in the setting of (a). $3d_{xz}$, $3d_{yz}$, and $3d_{x^2-y^2}$ possess lower energy.

The behavior of transition-metal oxyhalides MOCl depends on the numbers of d electrons of the transition-metal atom, and the $3d$ orbitals they occupy. The trivalent cations of the transition-metal atoms Ti, V, Cr and Fe possess 1, 2, 3 and 5 d electrons, respectively. Detailed discussion will be given in the Chapter 4.

2.3 Spin-Peierls transition

The name "spin-Peierls transition" originates from the fact that this transition is the magnetic analogue of the Peierls transition, which is a metal-insulator transition occurring in quasi-one-dimensional metals. The Peierls transition is accompanied by static displacements of ions according to a wave with wave vector $Q = 2k_F$, where k_F is the Fermi wave vector in a 1-D crystal. The transition gives rise to a splitting of the conduction band at $k = k_F$, and a reduction in the energy of electrons (Buzdin and Bulaevskiĭ, 1980).

The spin-Peierls transition was predicted by Chesnut (1966) in the general context of physical chemistry and the properties of certain organic free radicals in particular (Miller, 1983). The initial experimental studies of this transition were limited to a few organic compounds, TTF-$MS_4C_4(CF_3)_4$ (M=Cu,Au; TTF is tetrathiafulvalene) (Bray et al., 1975; Jacobs et al., 1976), MEM$(TCNQ)_2$ (MEM is N-methyl-N-ethyl-morpholinium, TCNQ is ditetracyanoquinodimethanide) (Huizinga et al., 1979), M-TCNQ (M=Li,K) (Holz et al., 1977; Lépine et al., 1978; Takaoka and Motizuki, 1979). $CuGeO_3$ was the first inorganic spin-Peierls transition compound, attracting widespread attention due to its high magnetic moment densities (Hase et al., 1993). Transition-metal oxyhalides TiOCl and TiOBr were found to be spin-Peierls compounds in spite of some unconventional features, for instance the existence of two phase transitions (Seidel et al., 2003; van Smaalen et al., 2005).

The spin-Peierls transition occurs in a crystal that possesses quasi-one-dimensional antiferromagnetic spin chains of spin 1/2 and a finite magneto-elastic coupling. A material with $S > 1/2$ is not favorable for a spin-Peierls transition, since the quantum fluctuations decrease rapidly with increasing magnetic moment (Hoinkis, 2006). The spin-Peierls transition is a kind of magneto-elastic transition, which can be described as follows: a substance contains a series of quantum spin chains which can be described by a spin 1/2 Heisenberg Hamiltonian with nearest neighbor exchange coupling of antiferromagnetic type (Miller, 1983). The interchain magnetic coupling is small and can be neglected in first approximation. The exchange energy of the spin chains (J) is a function of distance (a) between neighboring spins. Above a phase transition temperature T_{sp} the magnitude of J is constant (Fig. 2.3 b). Below

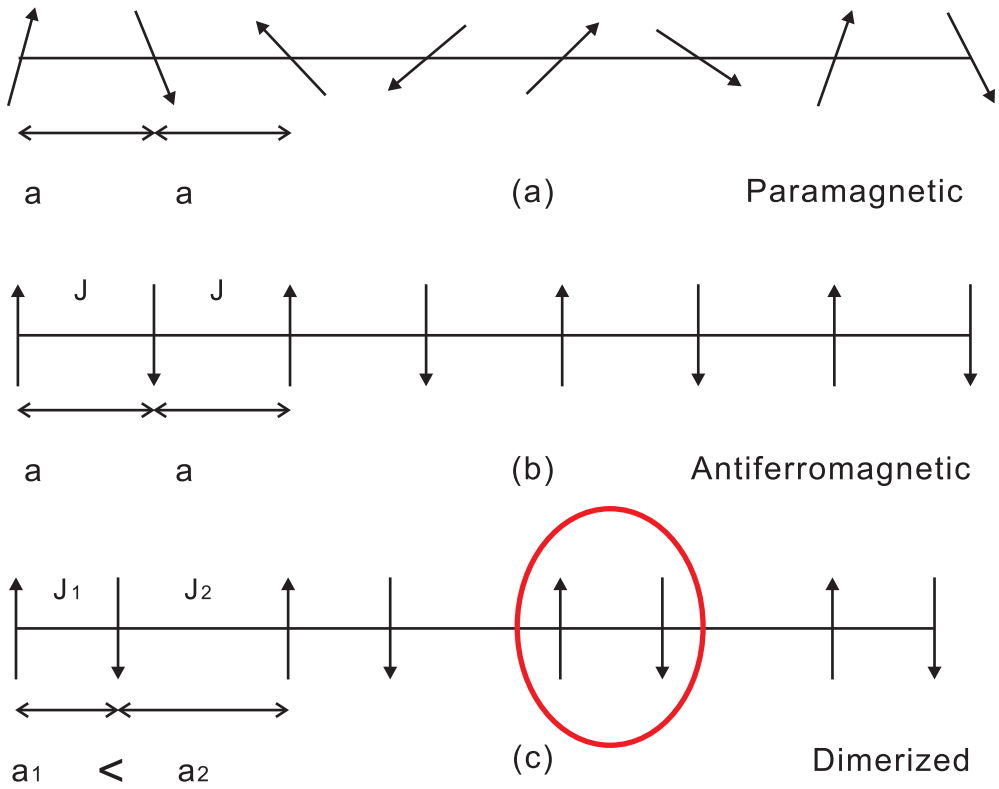

Figure 2.3: Schematic representation of (a) paramagnetic, (b) Antiferromagnetic states, and (c) spin singlet pairs in spin-Peierls compounds. The exchange coupling constants $J_1 > J_2$.

T_{sp}, these distances are not uniform anymore, resulting in a spin-Peierls dimerized ground state. The cations move alternately closer and further apart. Hence, the exchange energy of the spins J_1 and J_2 are not equal to each other (Fig. 2.3 c). In the meanwhile, the lattice (unit cell) is doubled, resulting in the existence of a two-fold superstructure. Unlike the long-range magnetic order of the antiferromagnetic state, there is no long-range magnetic order in spin-Peierls state. The superlattice magnetic reflection is absent in the neutron diffraction. Another characteristic property of spin-Peierls materials is a drop of the magnetic susceptibility below the phase-transition temperature due to the formation of spin singlets. The magnetic free energy decreases due to the formation of singlet spin pairs outweighs the increase in lattice free energy occurring as a result of the dimerization of the regular array. The role of the electron-phonon coupling is taken over by the spin-phonon

coupling (Hoinkis, 2006).

2.4 Relations between nuclear structure and magnetic structure

Although x-ray diffraction experiments cannot measure the magnetic moments directly, the magnetic induced displacement modulation can be linked to the magnetic modulation (spin wave). A long-period magnetic modulation wave vector $\mathbf{q}_m$ will often induce a lattice modulation of $\mathbf{q} = 2\mathbf{q}_m$. This period halving arises because the atomic displacements are sensitive mainly to the magnitude of the orientational changes from ion to ion (Lovesey and Collins, 1996). The magnetic modulation and the induced displacement in a simple lattice are shown in Fig. 2.4.

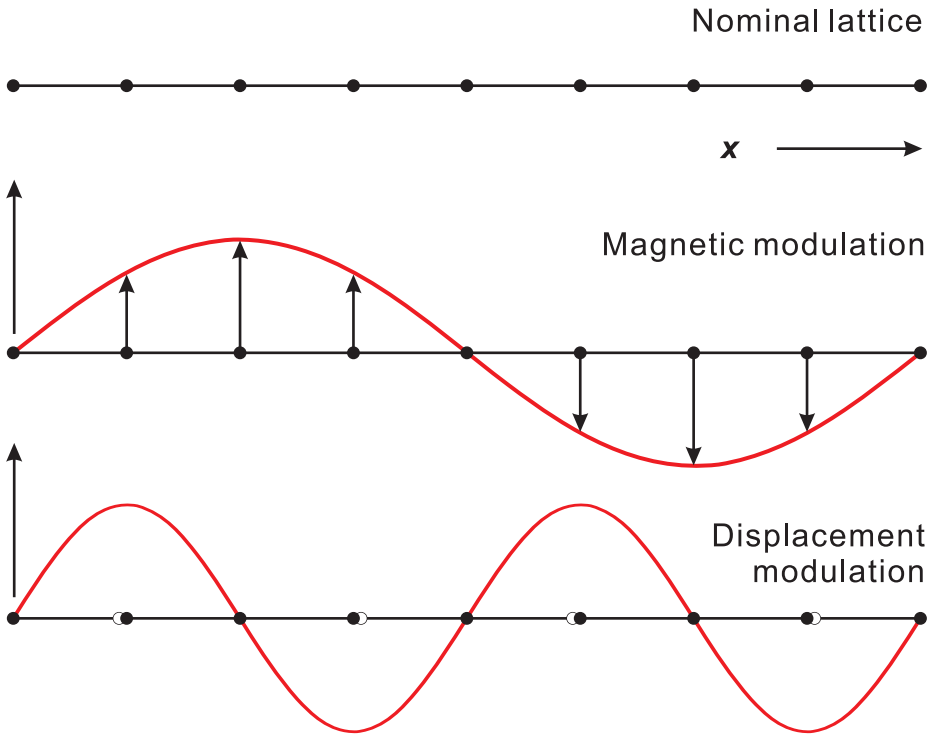

Figure 2.4: The magnetic modulation and induced displacement modulation in a simple lattice. Graphic was replotted from *Non-resonant magnetic diffraction from antiferromagnetis* (Lovesey and Collins, 1996).

Chapter 3

X-ray experimental techniques

3.1 Sample preparation

3.1.1 Criterion for determining the size of crystal

All oxyhalide crystals, which are investigated in the course of this thesis have been grown in the Lab of Crystallography, University of Bayreuth by Alfred Suttner. The chemical vapor transport method was employed for the synthesis of the compounds (Schäfer et al., 1956; Schäfer et al., 1958; Schäfer and Wartenpfuhl, 1961; Binnewies et al., 2012). Considering the beam sizes of 0.5 × 0.5 mm^2 at the synchrotron, the longest length of a crystal should be less than 0.5 mm, otherwise during the experiment parts of the crystal will be out of the beam, which results in the wrong intensities of the reflections. Another criterion is a practical rule about the linear absorption coefficient,

$$\tau_{opt} = \frac{1}{\mu}. \tag{3.1}$$

where τ_{opt} stands for the optimum thickness of crystal and μ is the linear absorption coefficient. In the synchrotron experiments, x-rays with a wavelength of 0.5600 Å was employed, which is involved in the determination of the linear absorption coefficients. According to the linear absorption coefficient in Table 3.1, the optimum size of crystal should be smaller than 0.4 mm.

Furthermore, larger crystals increase the possibilities of large mosaic spreads and

Table 3.1: The linear absorption coefficient of transition-metal oxychlorides. Values were calculated by the computer program JANA2006.

	Linear absorption coefficient (mm^{-1})	
Compound	Mo K_α radiation	0.56 Å
TiOCl	5.084	2.549
VOCl	5.900	2.905
CrOCl	7.002	3.483
FeOCl	8.503	4.186

defects. This makes the reflection peaks broader, which is unfavorable for diffraction studies. But the rule for selecting the crystal is not the smaller the better, because a too small crystal cannot provide enough scattering power. Some reflections will be too weak to be recognized from background, especially for the weak satellite reflections. Optimal dimensions of a crystal are $0.1 \times 0.1 \times 0.1$ mm^3. The layered character of the structure of MOCl is responsible for a highly anisotropic morphology of the crystals. The longest length of the sample can be extended to 0.3 mm, from which the intensity of reflections can benefit.

3.1.2 Technique of crystal holder

Crystals are carefully chosen under an optical microscope by a very thin metal pin. There are two kinds of materials for mounting crystals: glass fibers and carbon fibers, with the properties of low and high thermal conductivity, respectively. At room temperature both of these fibers can be used. But at low temperature, the most suitable candidate of fibers is based on the cooling technique. Glass fibers should be employed with open-flow cryostats, while carbon fiber is utilized with closed-cycle cryostats, which is the choice of our experiments. Carbon fiber is glued together as a piece of hair by two-component glue, and then stuck to a copper holder with the help of thermal conducting silver lacquer.

The sample is glued to the end of carbon fiber, where a sharp corner should be made by cutting the fiber. The optimal length of the fiber is about 2.5 mm above the copper pin (Fig. 3.1).

FeOCl and CrOCl crystals are stable in an atmospheric environment, therefore

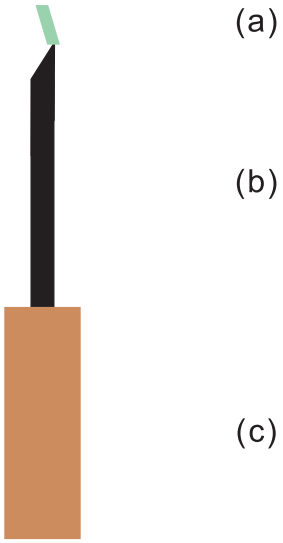

Figure 3.1: Schematic diagram of how to mount crystal. (a) crystal, (b) carbon fiber, (c) copper holder.

it is not difficult to attach the samples to the carbon fiber. TiOCl and its doped samples by Sc or Na are moderately air-sensitive, for the reason of that we should finish preparing our sample in about 5 minutes and put it back into glove box.

3.2 X-ray diffraction experiments

X-rays were discovered by Wilhelm Conrad Röntgen in 1895. X-rays are electromagnetic wave with the wavelength in the range from 0.1 to 100 Å, between gamma ray and ultraviolet, corresponding to energies in the range 100 eV to 100 keV. Generally, x-rays can be generated by two methods. The first method is employing high-energy electrons to hit an anode metal target in vacuum, which can be tungsten, molybdenum, copper, and others. The generated radiation includes bremsstrahlung with a continuous spectrum. The wavelength of the much more intense characteristic radiation depends on the anode metal. Another method of generating x-ray radiation is synchrotron radiation that is provided by particle accelerators. It is emitted from fast electrons, which are accelerated in magnetic fields, with the velocity almost equal to light velocity.

The single-crystal diffractometer is an instrument used to measure Bragg reflec-

tions of crystals. In this thesis a Mar345 dtb diffractometer and a Nonius Mach3 diffractometer were employed for testing the crystal quality at the University of Bayreuth. The diffractometers contain x-ray sources, goniometers and detectors as the three main components. The difference between them is that the Mar345 dtb diffractometer was equipped with an area detector but the Mach3 diffractometer was equipped with a point detector. Further experiments were performed at the synchrotron radiation station Hasylab beamline D3, where a 4-circle difffractometer with a point detector was used.

3.2.1 Experiments by the radiation of sealed tube

Experiments on the Mar345 dtb diffractometer

It is difficult to prepare excellent crystals of MOX, because of the fragile property, especially for sodium- and scandium-doped TiOCl. So we need to test hundreds of crystals, which is a time consuming work. Compared to a point detector, a diffractometer equipped with an area detector has several advantages, for instance, collecting data without determining the orientation of the crystal. According to this benefit, a diffractometer with an area detector is an efficient instrument for a preliminary test of crystal quality.

The experiments were performed with a Mar345 dtb desktop diffractometer in the Laboratory of Crystallography, University of Bayreuth (Fig. 3.2). The mounted crystals ware placed on a goniometer head, with the help of which the crystals can be centered easily. The sample can be rotated around the ϕ-axis, perpendicular to the incident beam. The Mar345 dtb software was used to control the diffractometer and collect data automatically (Klein, 2010).

The quality of crystal is judged by the shapes of the scattering points that are collected on the area detector. Without considering the different wavelengths of the Kα_1 and Kα_2 radiation, the reflections from a good crystal should show single dots, while those from not good ones have other shapes. Actually, double peaks appear very often. The Mar345 dtb diffractometer was equipped with molybdenum as the anode, and the incident beam is composed of two wavelengths due to the radiations of Kα_1 and Kα_2. If double peaks resulting from the effect of Kα_1 and Kα_2 are

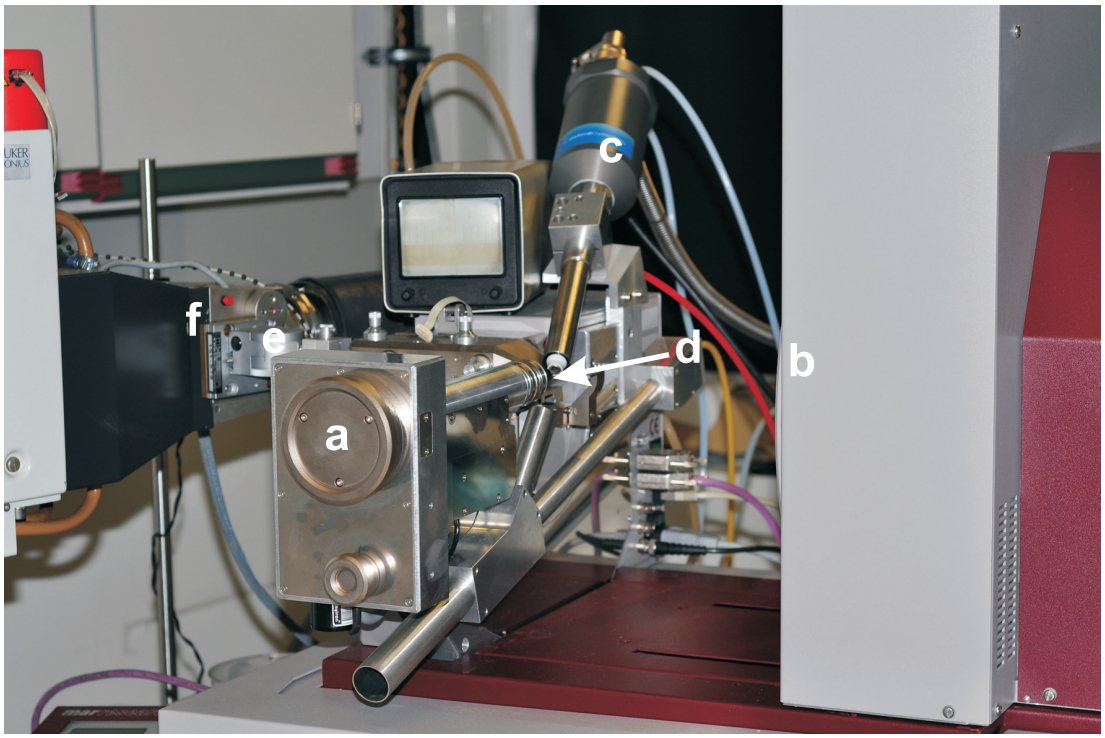

Figure 3.2: Setup of a mar345 dtb imageplate diffractometer (installed at the Laboratory of Crystallography, University of Bayreuth). (a) ϕ-axis, (b) 2-dimensional detector, (c) cooling system, (d) crystal, (e) monochromator, (f) rotating anode x-ray source.

arranged in the radial direction, the crystal quality is good. Otherwise, it means bad crystal quality (Fig. 3.3).

Experiments on Nonius Mach3 diffractometer

Further experiments for testing the quality of crystals were performed on a Nonius Mach3 diffractometer, which is equipped with a scintillation counter (point detector) and a rotating anode generator of molybdenum target (Fig. 3.4). The acceleration voltage and electric current of this diffractometer were set to be 55 kV and 75 mA respectively, corresponding to a generating power of 4.125 kV. It is installed at the Laboratory of Crystallography, University of Bayreuth. The Mach3 diffractometer is a four-circle diffractometer in κ-geometry, controlled by a software CAD4.

The quality of crystals can be examined by the following two stages. First of all, The orientation of the crystals should be determined. In principle, the orientation

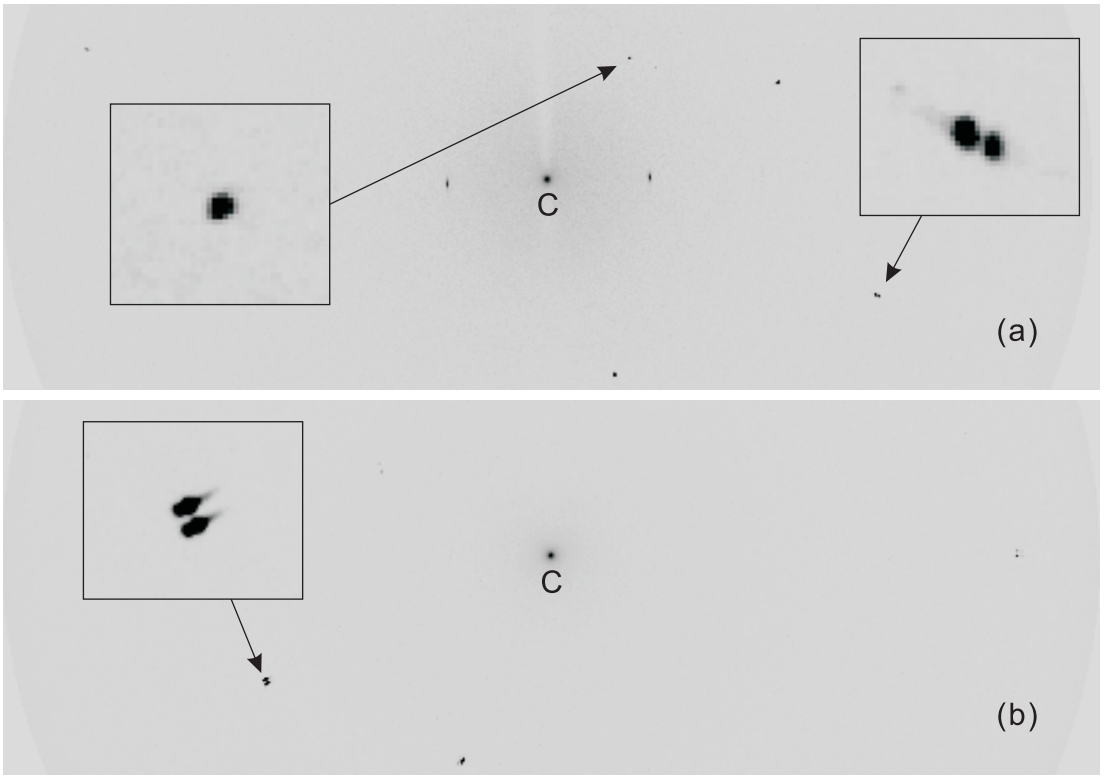

Figure 3.3: Sections of Mar345-image plate frames exposed over a ϕ-range of 1 deg. (a) The frame is obtained from FeOCl (code: foc031), the reflections spots in the left rectangular box indicate the good quality of this crystal, the two reflections in the right rectangular box arranged in the radial direction is the result of the two wavelengths of incident beam. (b) The frame is obtained from FeOCl (code: foc044), the reflections spots in the rectangular box shows the bad quality of this crystal. C marks the position of the primary beam.

matrix can be calculated from the setting angles of about 10 reflections (at least 3 reflections). The speed for searching reflections should not be too fast, otherwise some reflections can be missed. Considering the inorganic nature of our sample, a maximum speed of (12 $\times$ 16.48) deg/min was used in the reflections searching stage. Discrimination factor of 2.5 was chosen to reduce the time spent in trying to center weak peaks or noise. However, the preliminary orientation matrix was not so accurate, a further procedure was necessary to obtain more precise orientation matrix. Thus, a list of 25 reflections having considerable intensities and scattering angle 20° $\leq 2\theta \leq$ 25° was prepared for refining the orientation matrix. After centering these 25 reflections, the final orientation matrix can be determined.

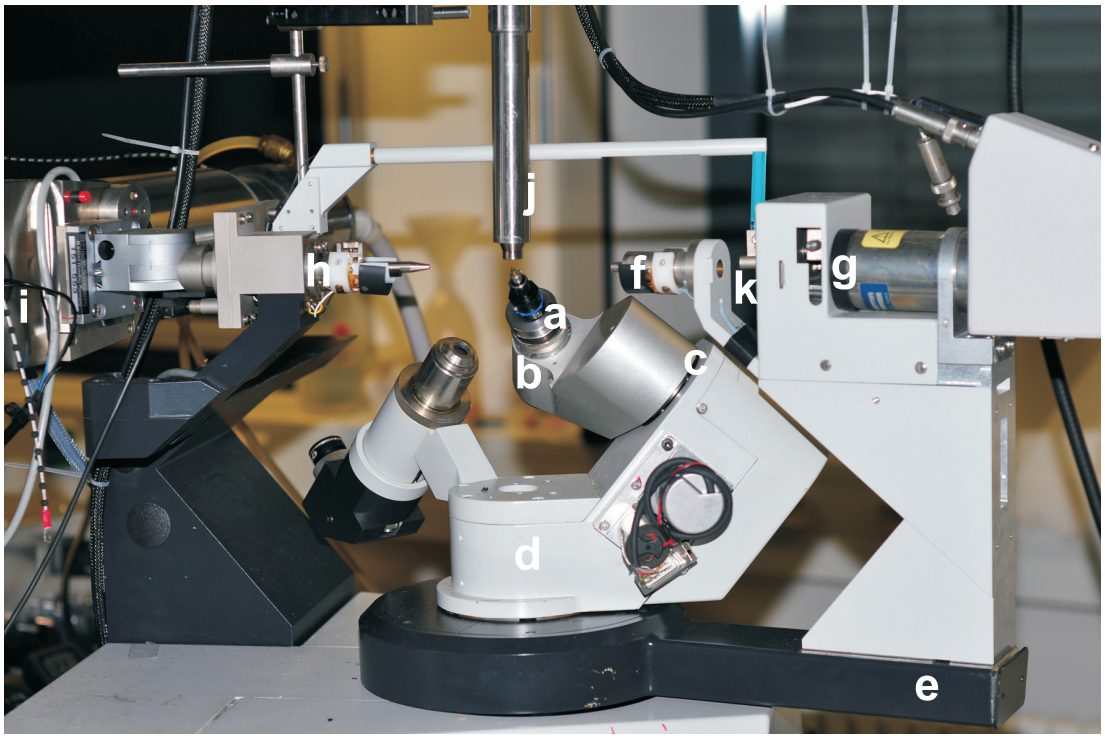

Figure 3.4: Setup of a Mach3 four-circle diffractometer with κ-geometry (installed at the Laboratory of Crystallography, University of Bayreuth). (a) goniometer head with crystal, (b) ϕ-axis, (c) κ-axis, (d) ω-axis, (e) 2θ arm, (f) detector collimator, (g) scintillation counter, (h) incident beam collimator, (i) rotating anode, (j) open-flow cooling system, (k) beam stop.

In order to examine the quality of crystal, ω scans were performed on strong reflections that are distributed over the three reciprocal lattice directions of the crystal. The quality of the crystal can be determined by inspecting the shape and FWHM of the profiles of the reflection peaks. An ideal shape should only contain a single sharp peak, and the FWHM should not exceed the lowest experimentally reachable value of about 0.1°. Thus the profiles with peak splitting or with large FWHM are not suitable for synchrotron experiments. In the experiments the rotation angles of ω scans are 1°. Gaussian or pseudo-Voigt functions were employed to fit the profile of peaks, from which the FWHM are determined. Here several profiles of ω scans on different FeOCl crystals are presented (Fig. 3.5).

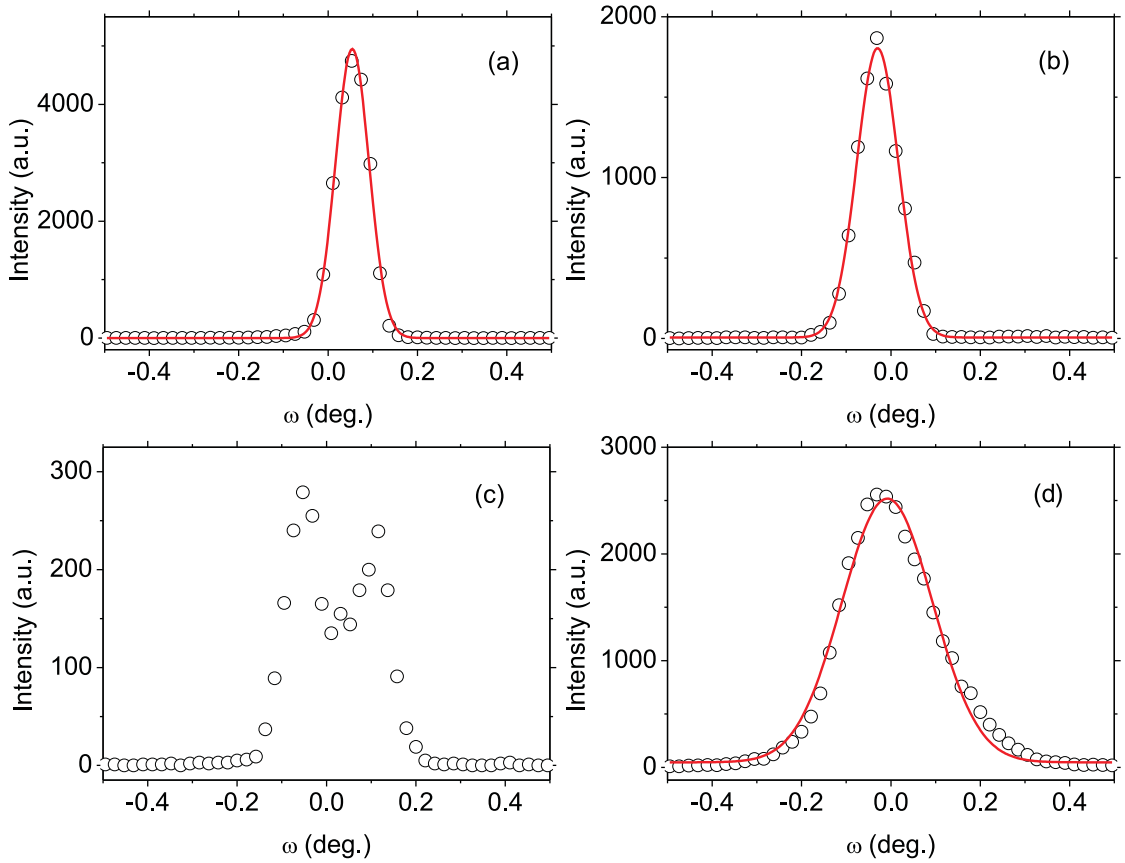

Figure 3.5: (a) ω scan of (0 2 0) on crystal FOC013; the FWHM is 0.088(1) deg. The single peak indicates the good quality of this crystal. (b) and (c) ω scans of (0 2 0) and (0 0 4) on crystal FOC015; the FWHM is 0.109(1) deg. The split on peak (0 0 4) indicates the insufficient quality of this crystal. (d) ω scan of (0 2 0) on crystal FOC041; the FWHM is 0.239(5). Large FWHM indicates the insufficient quality of this crystal. All FWHM were derived from the fitting of Gauss functions.

Technique to protect the air sensitive crystal

The quality of TiOCl, and TiOCl doped by sodium or scandium, will become worse upon prolonged exposure to air. For this reason, we can apply the nitrogen open-flow cryostat during the measurements both on Mar345 dtb diffractometer and on Nonius Mach3 diffractometer. In contrast to low-temperature experiments, we set the temperature of the cryostat to room temperature. This operation avoids the crystal to come in contact with air. In the experiment with synchrotron radiation the crystals were in vacuum in a beryllium cylinder, therefore no additional action

was necessary to protect the samples from air.

3.2.2 Experiments by synchrotron radiation

Generation of synchrotron radiation

The name of synchrotron radiation arise from a specific type of particle accelerator. Synchrotron radiation is widely used in many fields, such as materials science, medicine, condensed matter physics and biology. Among these fields, structure analysis is an important application. Synchrotron radiation is produced in particle accelerator storage rings, in which bending magnets redirect the propagation direction of the particles and keep them in a closed orbit. The frequencies of radiation, which is generated in this way, can cover the entire electromagnetic spectrum. The typical range of spectrum lies between infrared and hard x-ray radiation (Jens Als-Nielsen, 2011). Many x-ray optical devices are equipped in a beamline, for example attenuators, slits, crystal monochromators, and mirrors. They are responsible for adjusting the bandwidth, focus, photon flux, beam dimensions, collimation of the rays and so on. Most of the experiments in this thesis were performed at beamline D3 of the Hamburger Synchrotronstrahlunglabor (HASYLAB) at the Deutsches Electronen-Synchrotron (DESY) in Hamburg, Germany. The beamline was equiped with a Huber four-circle diffractometer.

Advantages of synchrotron radiation

Compared to the conventional x-ray radiation generated by rotating anode, synchrotron radiation has many advantages in single-crystal x-ray diffraction experiments. First of all, the wavelength of synchrotron x-ray radiation is adjustable. In an analysis of structure by x-ray diffraction, the x-ray absorption by a crystal is an unavoidable effect. It can reduce the intensity of outgoing radiation, resulting in an inaccurate structure solution. Both the crystal size and the absorption coefficient can affect the magnitude of the x-ray absorption. The linear absorption coefficient is related both to the compound forming the crystal and to the energy of the radiation. Generally, employing x-ray with shorter wavelength can reduce the absorption.

However, shorter wavelength corresponds to lower 2θ angle of Bragg's Law. Then too many reflections are located in the low 2θ shell, which is not conducive to accurate structure refinement. All the synchrotron experiments in this thesis employed a wavelength of 0.5600 Å, corresponding to the linear absorption coefficient in Table 3.1.

The effective intensity of the x-ray synchrotron radiation beam is determined by the number of photons produced per second, the angular divergence of the photons, the cross-sectional area of the beam, and the a relative energy bandwidth (BW) of the monochromator crystal. These aspects can be combined into a single quantity, called the brilliance. Then, one defines the figure-of-merit for the source as:

$$Brilliance = \frac{Photons/second}{(mrad)^2(mm^2\ source\ area)(0.1\%\ BW)}. \tag{3.2}$$

The intensity in photons per second after the monochromator crystal is the product of the brilliance, angular divergences set by the horizontal and vertical apertures (in milli-radian), the source area (in mm^2), and the relative bandwidth of the monochromator crystal relative to 0.1% of the central wavelength or frequency (Jens Als-Nielsen, 2011).

The maximum brilliance of the third generation synchrotrons is about 10 orders of magnitude higher than that of a conventional rotating anode at the K_α line (Jens Als-Nielsen, 2011). The higher magnitude of brilliance, the more photons that can be concentrated on a spot. It gives support to observe very weak satellite reflections of the modulated crystal structure, which is hard to find by conventional x-ray radiation sources. For this reason, the experiments presented in this thesis were performed with synchrotron x-ray radiation. An important aspect of determining the full width of half maximum (FWHM) of Bragg reflections is the divergence of synchrotron radiation beam. The lower beam divergence respects to narrower FWHM. On account of the excellent properties of beam divergence, the FWHM of the reflections by synchrotron x-ray diffraction is mainly determined by the crystal mosaic, which can reach as low as 0.01°. On the other hand, the minimal FWHM of the reflection measured on Nonius Mach3 diffractometer is about 0.1°, dominated by the properties of the x-ray beam (Fig. 3.6). Therefore a crystal that was tested

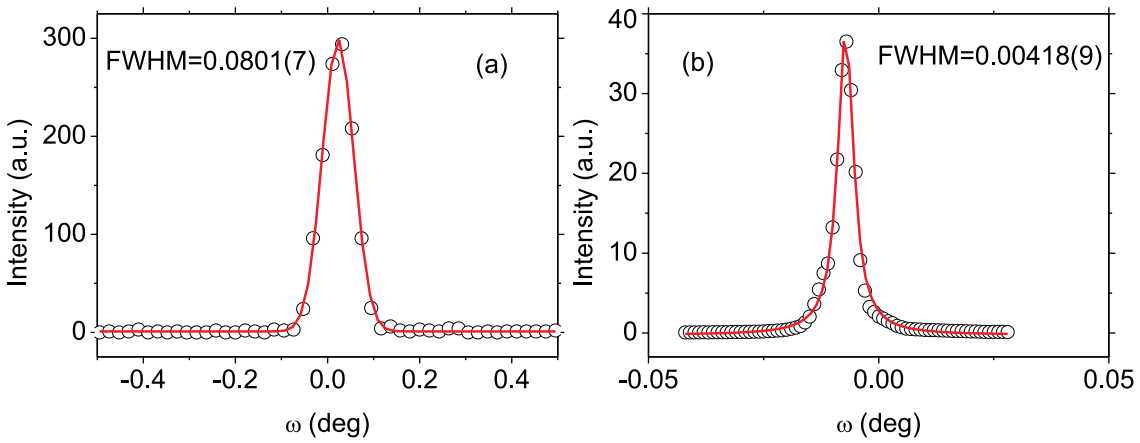

Figure 3.6: Diffracted instensity as a function of the scattering angle ω for the reflections (2 0 0) of CrOCl (Code:CROC17). (a) data was collected by diffractometer Nonius Mach3 in University of Bayeruth, FWHM was derived from the fitting of Gauss function. (b) data was collected at Hasylab beamline D3, FWHM was derived from the fitting of Lorentz function.

to be a good crystal on Mach3 diffractoemeter may show split peaks by the ω scans at synchrotron station.

3.2.3 Control of the temperature of the crystal

All the phase transitions and lattice distortions of transition-metal oxyhalides MOCl occur at low temperatures, hence a cooling system is required that can provide precise and stable temperatures of the crystal. Considering both the temperature range of the experiments from room temperature down to 8 K and the boiling point of nitrogen of 77.35 K at the ambient pressure, helium was selected as cooling transport medium. Two different cryostats, open-flow and closed-cycle cryostat, were employed in the experiments of this thesis.

On Nonius Mach3 and Mar345 dtb diffractometer, open-flow cryostats is an optional components. The experiments of preliminary test of crystals at University Bayreuth were performed at room temperature, therefore low temperature circumstance is not needed. But during the experiments on TiOCl and TiOCl doped by sodium & scandium, open-flow cryostat was applied to generate nitrogen stream to protect crystals from air. Both open-flow cryostat and closed-cycle cryostat can be

used on Huber four-circle diffractometer, as well as on beamline D3 at Hasylab. The model of closed-cycle cryostat is DE-202G, specially designed to fit into the Huber 512, 4 circle goniometer by APD Cryogenics Inc.. The temperature can be adjusted between room temperature and 6.5 K.

The closed-cycle cryostat operates on a pneumatically driven Gifford-McMahon refrigeration cycle (GM Cycle). First of all, helium gas compressed by a compressor is transported into an evacuated chamber, and then the pressure differential drives the displacer to open a path allowing the gas at the bottom of chamber to expand and cool. Second, the rotation of the valve disk opens the low pressure path to the compressor allowing the gas to flow back, and then the pressure differential returns the displacer to its original position. The whole procedure can run continuously for an indefinite period, without refilling the helium gas but consuming large amounts of electrical power.

The crystal is mounted at the end of the cold finger of the cryostat, connected to an oxygen-free copper cylinder that is cooled by compressed helium vapour. An electrical heater is attached to the copper cylinder to regulate the crystal temperature up to 325 K. As discussed in section 3.1.2, carbon fibers are used to connect crystal to the copper holder. The end of cryostat including crystal is covered by two beryllium caps, enclosing an evacuated volume. This part can produce a thermal isolation and prevent icing of the cooled crystal.

The beryllium caps also generate three unfavorable effects. With the temperature decreasing, not only the copper cylinder but also the other parts of cryostat will shrink, resulting in the change of crystal position. The beryllium caps prevent recentering the crystal optically, which is the first disadvantage. The height of crystal was adjusted by the knowledge from previous experiments (Angelkort, 2009), and examined by intensity measurements of reflections and the help of the primary beam. The second disadvantage is the powder diffraction rings generated by beryllium caps. The intensity of reflections of the samples, that are located on these rings cannot be correctly determined. To reduce this effect, a detector collimator was employed. The last and the most serious effect is the limitation of the movement of the diffractometer axes, which is caused by the cryostat and compressor hoses. Due to the restrictions in 2θ, ω, χ, and ω, not all octants of reflections (h k l)

can be reached. This makes many reflections unreachable, which may include those required for observing the monoclinic distortion by ω-2θ maps.

3.3 Integration of synchrotron x-ray radiation reflections

In contrast with that of the conventional laboratory diffractometer, the intensity of the primary beam of the synchrotron is gradually decreasing in time, because of the energy loss in the particle storage ring. The initial beam current at DORIS III is about 120 mA at the beginning of each run cycle, then it gradually reduced to about 90 mA. For this reason, the diffracted intensities measured by the detector not only depend on the orientation of the crystal but also on the intensity of incident beam. Hence, it is important to scale the measured intensities according to the intensity of incident beam. The data collection at beamline D3, Hasylab, Desy, was performed in a step-scan-measured way. The integrated intensities of reflections were obtained by processing the raw data with the computer program REDUCE (Eichhorn, 1991). REDUCE includes routines that perform a profile analysis, combined with automatic search algorithms to separate peak from background; routines for background subtraction and calculation of the integrated intensity and its standard deviation; segments for treatment of 'bad' profiles, of weak reflections, and of counts from beam-monitors; plot and analysis standard reflections (Eichhorn, 1991).

During the data collection, the vertical monitor counts CNT1 and horizontal monitor counts CNT2 were measured at the same time and stored in data files. A monitor count rate for scaling CMON was used in REDUCE. Data were multiplied by the factor $CMON/(< CNT1 > + < CNT2 >)$, $< CNT1 >$ and $< CNT2 >$ being the countrates of the two beam-monitors (Eichhorn, 1991). Generally, it is recommended to set CMON equal to the average monitor count rates. The quality of integrated and scaled intensities can be inspected via checking the intensities of standard reflections, which were measured periodically. Fig 3.7 shows the intensities of standard reflection (0 -1 -3), during the data collection of scandium-doped TiOCl, before and after being scaled by program REDUCE. It is obvious that the intensities

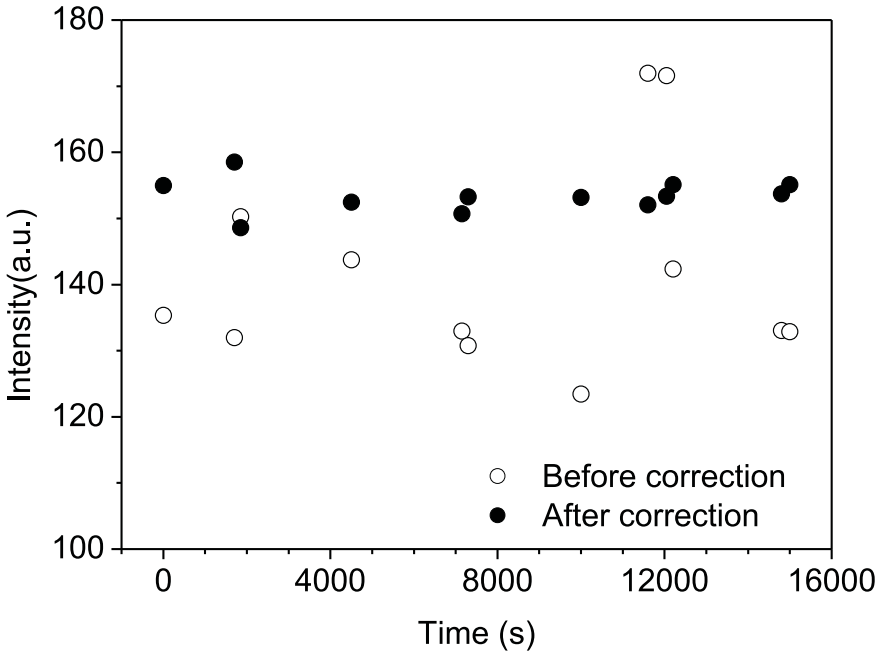

Figure 3.7: Diffracted intensity as a function of time for the standard reflection (0 -1 -3) during the data collection of Sc-doped TiOCl. Open circles indicate the intensity before correction; and closed circles indicate those after correction for variation of the primary-beam intensity..

of (0 -1 -3) tend to be constant after scaling, indicating all the reflections measured between these standard reflections were also scaled properly.

Chapter 4

Transition-metal oxyhalides MOX

4.1 Crystal structure of the transition-metal oxyhalides

FeOCl was the first compound, which was synthesized among the transition-metal oxyhalides MOX (M = Ti, V, Cr and Fe; X = Br, Cl). These compounds have been widely studied because of their quasi-two-dimensional crystal structures, which provide strongly anisotropic properties, for instance electrical and magnetic properties. Compounds MOX crystallize in layered FeOCl-type structure at room temperature (Goldstaub, 1935). The symmetry is orthorhombic with spacegroup $Pmmn$ (No. 59) and Z = 2 formula units per unit cell. Metal atoms and oxygen atoms form a double layer, which is sandwiched between layers of halogen atoms. These slabs stack along the lattice direction **c**, metal-oxygen double layer is separated by two halogen layers. The halogen layers between adjacent bilayers along **c** were connected to each other by a weak van der Waals force. In the lattice direction **b**, every kind of atoms forms a chain (Fig. 4.1). The ionic bonding inside the metal-oxygen double layers is expected to possess a partial covalent character, while the halogens are expected to have pure ionic characters (Macovez et al., 2007). The metal ion is surrounded by a distorted octahedron defined by two halogen and four oxygen atoms, with mm2 point group symmetry. These octahedral groups share edges along the **b** axis and corners along the **a** axis. The lattice parameters of MOX (M = Ti, V, Cr

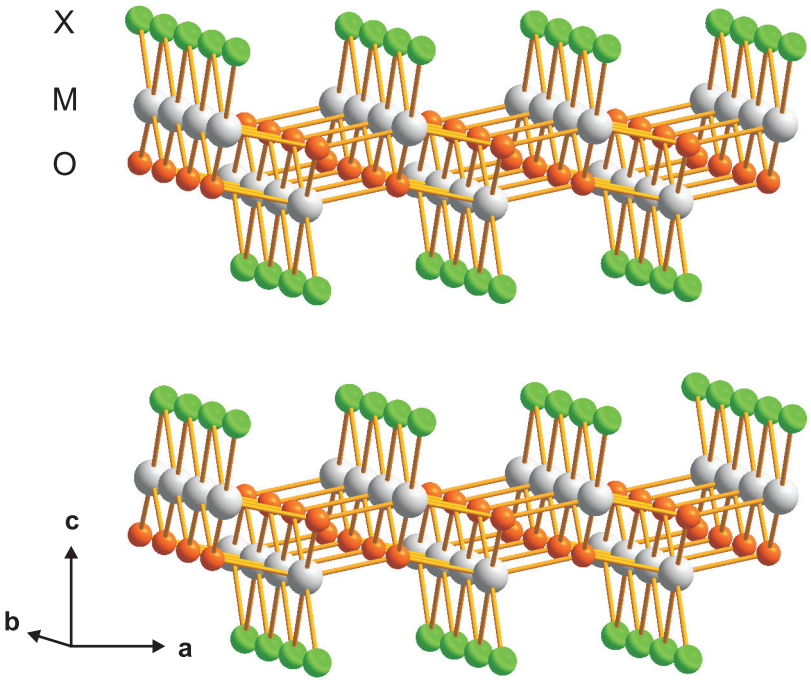

Figure 4.1: MOX crystal structure at room temperature. The labels M , O and X are referring to metal, oxygen and halogen atoms, respectively.

and Fe; X = Cl and Br) are listed in Table 4.1.

4.2 Spin Peierls phase transition of TiOCl and TiOBr

TiOCl has been confirmed to possess the spin-Peierls ground state below 67 K (Seidel et al., 2003; Shaz et al., 2005). It is the third inorganic spin-Peierls compound after $GuGeO_3$ and NaV_2O_5 (Hase et al., 1993; Fujii et al., 1997). Recently another compound $TiPO_4$ was proposed to be a spin-Peierls compound (Law et al., 2011; Bykov et al., 2013). In contrast to a single phase transition occurring in canonical spin-Peierls compounds, TiOCl and TiOBr undergo two phase transitions on cooling, which were evidenced by temperature dependencies of the magnetic susceptibilities, heat capacities, ESR data, NMR spectra and synchrotron x-ray diffraction experiments (Seidel et al., 2003; Kataev et al., 2003; Imai and Chou, 2003; Hemberger

Table 4.1: Lattice parameters of MOX (M = Ti, V, Cr and Fe; X = Br and Ti.) at room temperature.

	a (Å)	b (Å)	c (Å)	V (Å)^3
TiOCl[a]	3.7826(1)	3.3662(1)	8.0519(1)	102.41
VOCl[b]	3.7691(12)	3.3004(10)	7.9219(30)	98.54
CrOCl[c]	3.8525(7)	3.1714(5)	7.6932(19)	93.99
FeOCl[c]	3.7773(6)	3.3046(7)	7.9156(16)	98.80
$Sc_xTi_{1-x}OCl$[c]	3.7794(11)	3.3385(7)	8.0440(15)	102.11
Na_yTiOCl[c]	3.8115(48)	3.3875(40)	8.1070(104)	104.67
TiOBr[d]	3.78458(2)	3.48528(2)	8.52520(5)	112.45

[a]Powder diffraction on Spodi by A. Schöenleber.
[b]Schönleber et al. (2009).
[c]Present work; $x = 0.005$ and $y = 0.01$.
[d]Sasaki et al. (2005).

et al., 2005; Shaz et al., 2005; van Smaalen et al., 2005; Schönleber et al., 2006). As the temperature is lowered, the room temperature phase transforms into a so called incommensurately modulated intermediate phase at T_{c2} (91 K for TiOCl; 48 K for TiOBr). A following phase transition appears at T_{c1} (67 K for TiOCl; 28 K for TiOBr), transforming the incommensurate modulated structure into a commensurate modulated structure which is a twofold superstructure of the room temperature structure.

In TiOCl, the phase transition at about 67 K was confirmed by magnetic susceptibility experiments as a first-order phase transition, which was also in clear contrast with canonical spin-Peierls transition of second order (Hoinkis et al., 2005). The character of the phase transition at about 91 K was considered of second-order. However, this character was questioned by Schönleber et al. (2008), and a first-order character was proposed. The magnetic susceptibility above T_{c2} can be explained by a Bonner-Fisher model of a one-dimensional Heisenberg spin chain (Seidel et al., 2003).

The nature of the intermediate phase between T_{c2} and T_{c1} is very difficult to establish. The formation of incommensurate order in this phase was first realized from NMR experiments (Imai and Chou, 2003). The incommensurate modulated structure was first proved by x-ray experiments on TiOBr (van Smaalen et al.,

2005), and then confirmed also by x-ray diffraction on TiOCl (Krimmel et al., 2006). Detailed structure refinements of the intermediate phase of TiOCl was carried out by Schönleber et al. (2006). Compared to the high temperature orthorhombic phase, the space group symmetry was lowered to a monoclinic **c**-unique ($\gamma = 90.023°$) superspace group $P2/n(\sigma_1, \sigma_2, 0)00$ (Schönleber et al., 2008). Fig. 4.2 shows the temperature dependence of the modulation wave vector $\mathbf{q}$=(q_1, $\frac{1}{2}$+δ, 0).

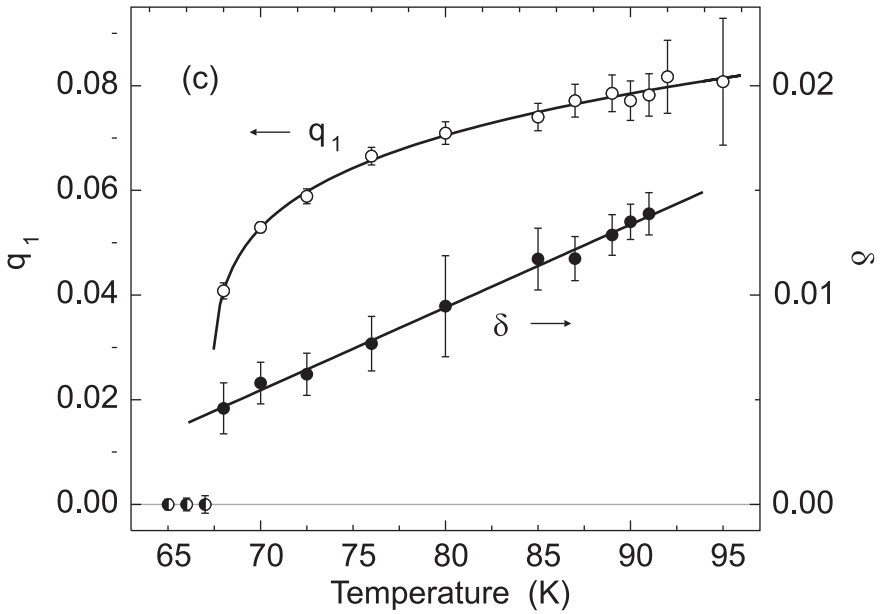

Figure 4.2: Temperature dependence of the modulation wave vector $\mathbf{q} = (q_1, \frac{1}{2}+\delta, 0)$. Lines represent fits to the data: $q_1 = q_1^0(T - T_{c1})^\gamma$ with $q_1^0 = 0.044(1)$, $\gamma = 0.18(1)$, and $T_{c1} = 67.4(2)$ K; δ = -0.0222(8) + 0.00040(1)T. Error bars are indicated. Reproduced from Schönleber et al. (2006).

In spite of differences to canonical spin-Peierls systems, the anomaly at T_{c1} was interpreted as a spin-Peierls transition according to x-ray diffraction studies (Shaz et al., 2005). Below the spin-Peierls phase transition temperature, the appearance of a superlattice reflection indicates a doubling of the unit cell along **b** (Fig. 4.3), which is also the evidence of an accompanying dimerization of Ti chains along **b** in a spin-Peierls scenario. Respecting to orthorhombic symmetry at room temperature, structure refinements of the low-temperature phase of TiOCl showed a lower symmetry with superspace group $Pmmn(0\beta0)000$, corresponding to supercell space group $P2_1/m$ (**a** unique) when t_0=1/8. According to the structure analysis two symmetry

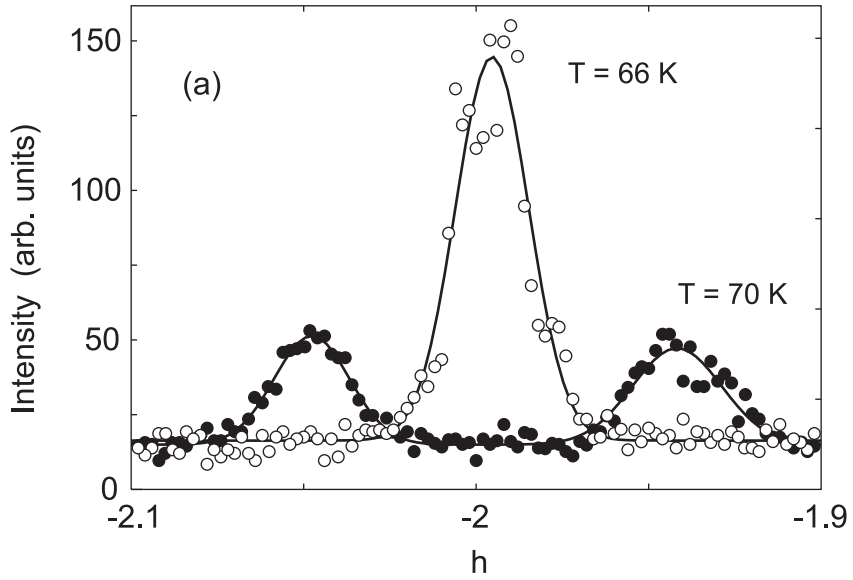

Figure 4.3: q Scans along $\mathbf{a}^*$ centered on (-2, -1.5, -1), below and above the lock-in transition at 67 K. Lines represent Gauss functions fitted to the data. Reproduced from Schönleber et al. (2006).

independent Ti and O sites were concluded, consistent with NMR experiments by (Imai and Chou, 2003).

As mentioned in section 2.2, only one d electron exists in a $3d$ orbital in TiOCl. A conventional complete active space self-consistent field (CASSCF) calculation concluded to a ground state with one electron in a Ti $3d_{x^2-y^2}$ orbital with some O $2p$ character mixed in (for x along **b**, y along **c**, and z along **a**. Section 2.2) (Macovez et al., 2007), confirming previous results (Fausti et al., 2007). The occupied orbital is oriented in the **b** and **c** directions that favor the direct exchange interaction between Ti atoms along the **b** direction, resulting in a spin-Peierls pairing of the magnetic moments at low temperatures. In addition to the spin-Peierls interaction, a superexchange interaction generated by a hybridization of the $d_{x^2-y^2}$ orbitals with the $2p$ orbitals of oxygen was concluded (Macovez et al., 2007).

4.3 Behavior of doped TiOCl

In order to understand the ordering mechanism in spin-Peierls compounds, both theoretical and experimental investigations of doped spin-Peierls compound have been performed. In $CuGeO_3$, nonmagnetic Zn^{2+} (Hase et al., 1993; Oseroff et al., 1995; Kojima et al., 1997; Manabe et al., 1998), Mg^{2+} (Grenier et al., 1999), Cd^{2+} (Haravifard et al., 2007; Lumsden et al., 1998) and magnetic Ni^{2+}, Mn^{2+} (Oseroff et al., 1995), Co^{2+} (Anderson et al., 1997) can be doped into the Cu^{2+} sites . With $Cu_{1-x}Zn_xGeO_3$ as an example, the dimerized order of the spin-Peierls state was maintained for low doping concentrations. Once the doping concentration reaches a critical value of $x_c = 0.02$, the spin-Peierls order was lost and a uniform antiferromagnetic ground state occurred (Uchinokura, 2002). The spin-Peierls transition temperature T_{SP} was depressed under the influence of doping.

Similar studies were performed on TiOCl with substituting nonmagnetic Sc^{3+} ($3d^0$) for Ti^{3+} ($3d^1$), a analogue of Zn^{2+} doping in $CuGeO_3$. One expects that the lack of d electrons of Sc^{3+} ($3d^0$) results in the destruction of some dimers and release free 1/2 spins. The first study on $Sc_xTi_{1-x}OCl$ was focused on magnetic susceptibility of compounds with relatively high level of doping ($x = 0.06$ and 0.15) (Seidel et al., 2003). It was concluded that the doped compound did not undergo a spin-Peierls transition. Detailed x-ray scattering measurements were performed on single crystals of the doped compound $Sc_xTi_{1-x}OCl$ ($x = 0$, 0.01, 0.03) by Clancy et al. (2008). The Sc doping prevents the formation of a long-range spin-Peierls state down to 7K at both doping concentrations. Instead, an incommensurate short-range ordered state is present from T_{c2} down to 7 K. The temperature dependence of integrated scattering intensity of $Sc_xTi_{1-x}OCl$ ($x = 0.01$) at the ($2\pm\delta_H$, 1.5, 1) superlattice peak positions can be fitted by a power-law function consistent with mean-field-like behavior, while the pure TiOCl data can be well described by a straight power-law fit which is consistent with conventional 3D universality class. This fundamental change might originate in the presence of local lattice strains which result from the larger ionic radius of Sc^{3+} ions (Clancy et al., 2010). Zero-field (ZF) and longitudinal-field (LF) μSR study did not provide any evidence for magnetic order down to 1.7 K in compound $Sc_xTi_{1-x}OCl$ ($x = 0.01$, 0.03), in contrast to

doped $CuGeO_3$ (Aczel et al., 2011). Very recently, we studied $Sc_xTi_{1-x}OCl$ ($x = 0.005$) by synchrotron x-ray radiation. Novel behavior has been observed, which is presented in Chapter 6.

Apart from doping electron holes, doping electrons into titanium oxyhalides was also studied by various groups (Craco et al., 2006; Kuntscher et al., 2010; Zhang et al., 2010). In section 4.1, we pointed out that the X sandwiched M-O bilayers of MOX (M = Ti, V, Cr and Fe; X = Br, Cl) are only coupled via van der Waals forces. Due to this character, it is possible to intercalate alkali metal atoms between the layers. The initial idea was to make the alkali metal atoms donate their outer electrons to Ti-3d states in the context of driving a layered compound into a unconventional superconducting state by introducing additional electrons or holes (Tokura et al., 1989; Rotter et al., 2008), moreover the dopant should not induce structural or chemical modification (Kuntscher et al., 2010). A study of the spectral weight evolution upon alkali metal doping proved that the outer electrons of alkali metal (Na, K) were doped into the Ti3d states. Nevertheless, a soft Coulomb gap persists (Kuntscher et al., 2010). According to a series of density functional theory (DFT) calculations that have been performed on several commensurate Na doping TiOCl, Zhang et al. (2010) predicted that the Na ion enters an individual cage consisting of 1 O and 5 Cl ions. The Na doping strongly modifies the crystal field splitting of Ti d states by Na^+ ion and causes a coexistence of stabilized Ti^{3+} and Ti^{2+} ions (Zhang et al., 2010). The insulating state remains for all studied Na concentrations.

4.4 Commensurate magnetic structure of VOCl and CrOCl

V^{3+} and Cr^{3+} possess two and three 3d electrons, respectively. This brings out more complicate orbital interactions in VOCl and CrOCl, which influence the magnetic order.

VOCl was reported crystallizing in the FeOCl structure type by Haase and Brauer (1975). A phase transition has been observed at Néel temperature $T_N = 80.5$ K by the temperature-dependent magnetic susceptibility (Wiedenmann et al.,

1983). Above T_N, the magnetic susceptibility χ along the three crystallographic axes is equivalent, revealing an isotropic character. Below T_N, χ along **a** departs from those along **b** and **c**. The ordered magnetic moments in the low temperature phase are oriented along **a** axis (Wiedenmann et al., 1983). Powder neutron diffraction study demonstrates that VOCl possesses a collinear antiferromagnetic order with a wavevector $\mathbf{k}_M = (1/2, 1/2, 1/2)$ below T_N (Schönleber et al., 2009). The occurrence of antiferromagnetic order is accompanied by a monoclinic distortion with space group $P2/n$ of nuclear structure and monoclinic angle $\gamma = 90.211°$ (Komarek et al., 2009; Schönleber et al., 2009).

The magnetic susceptibilities of CrOCl in the temperature range 150 K to 300 K follow the Curie-Weiss law (Schäfer and Wartenpfuhl, 1961). Instead of the two-fold magnetic superstructure in the low temperature phase of VOCl, a four-fold magnetic superstructure of the room temperature structure was reported. The magnetic structure is collinear with the spins in the direction of the crystallographic axis **c** (Christensen et al., 1975). On cooling, CrOCl undergoes an antiferromagnetic transition at $T_N = 13.5$ K, being accompanied by a lattice distortion from orthorhombic symmetry to **a**-axis unique monoclinic symmetry. The monoclinic angle α is 90.071° determined by synchrotron x-ray diffraction experiments (Angelkort et al., 2009). A second phase transition was observed at $T_c = 27.2$ K in temperature dependent specific heat C_p experiments. However, there was no signature of this transition in x-ray diffraction experiments, suggesting a purely magnetic character of the transition (Angelkort et al., 2009). The modulated nuclear and magnetic structures have been studied, respectively (Chapter 8).

In VOCl the two valence electrons of V^{3+} occupy the $3d_{x^2-y^2}$ and $3d_{xz}$ orbitals (Fausti et al., 2007), and in CrOCl the three valence electrons of Cr^{3+} occupy the $3d_{x^2-y^2}$, $3d_{xz}$ and $3d_{yz}$ orbitals (Angelkort et al., 2009). The different symmetries of the filled $3d$ orbtials offer an explanation for the different lattice distortions of VOCl and CrOCl. On the MO bilayers, the degeneracy of exchange interactions involving the $3d_{xz}$ orbtials of V are lifted by the **c**-axis unique monoclinic lattice distortion in VOCl.

4.5 Incommensurate magnetic structure of FeOCl

Compared to the early transition metal ions, Fe^{3+} has more electrons in the $3d$ orbitals. The distribution of the five valence electrons of Fe^{3+} is still not resolved. The magnetic characters of FeOCl were first studied by Grant (1971) using Mössbauer spectroscopy, and a magnetic phase transition from the paramagnetic state to a state with antiferromagnetic order occurs at the Néel temperature T_N of 92 K. This character has been studied by several other techniques and values of T_N between 80 and 92 K have been reported. An incommensurate magnetic modulation wave vector of $\mathbf{q}_M$ = (0.5, 0.275, 0.5) at 4.4 K and a commensurate magnetic modulation wave vector of (1/2, 2/7, 1/2) at 10 K were proposed based on neutron diffraction measurements by two different research groups, respectively (Adam and Buisson, 1975; Hwang et al., 2000). Considering the amplitude of a structural modulation wave vector is twice as large as that of magnetic modulation wave vector (Section 2.4), our synchrotron x-ray experiments confirm the former value. Furthermore, we have discovered a monoclinic lattice distortion with $\gamma = 90.10^\circ$ a low temperature, sindicating strong magnetoelastic coupling (Chapter 5).

Chapter 5

Magnetoelastic coupling in the incommensurate antiferromagnetic phase of FeOCl [1]

5.1 Abstract

The antiferromagnetic phase transition of FeOCl has been studied by temperature-dependent x-ray diffraction experiments and magnetic susceptibility, heat capacity and dielectric measurements. The magnetic phase transition is found to be accompanied by a monoclinic lattice distortion, affecting the angle γ between crystallographic axes parallel to the layers comprising the quasi-two-dimensional magnetic system. The temperature-dependent magnitude of γ shows the phase transition to be of second order. Satellite reflections occur in x-ray diffraction with twice the magnetic modulation wave vector. These positions are temperature dependent, providing evidence for an incommensurate character of the magnetic order. The observed Néel temperature is $T_N = 82.0\,(2)$ K.

[1] Published as: J. Zhang, A. Wölfel, L. Li, S. van Smaalen, H. L. Williamson, and R. K. Kremer, *Phys. Rev. B* **86**, 134428 (2012).

5.2 Introduction

Layered compounds MOCl (M = Ti, Cr, V and Fe) have recently been studied because of their low-dimensional magnetic properties (Seidel et al., 2003; Saha-Dasgupta et al., 2004; Shaz et al., 2005). Different magnetic behavior of these isostructural compounds has its origin in orbital order of the various number of $3d$ electrons of the M^{3+} ions (Saha-Dasgupta et al., 2004; Fausti et al., 2007; Zhang et al., 2008; Glawion et al., 2009; Bogdanov et al., 2011). Ti^{3+} possesses a single $3d$ electron. Orbital order makes TiOCl a quasi-one-dimensional (1D) magnetic system, which develops a spin-Peierls state at low temperatures (Seidel et al., 2003; Saha-Dasgupta et al., 2004; Shaz et al., 2005). The other compounds have transition-metal ions with two or more $3d$ electrons. They form 2D magnetic systems, and exhibit antiferromagnetic order at low temperatures (Adam and Buisson, 1975; Christensen et al., 1975; Wiedenmann et al., 1983).

Magnetic order is geometrically frustrated on the arrangement of M^{3+} ions within the orthorhombic crystal structure of MOCl. Accordingly, the low-temperature phases of TiOCl have been found to be monoclinic (Shaz et al., 2005; Fausti et al., 2007; Schönleber et al., 2008). Despite earlier reports of magnetic order with orthorhombic symmetry (Christensen et al., 1975; Wiedenmann et al., 1983), VOCl has a twofold magnetic superstructure with monoclinic symmetry and strong magnetoelastic coupling as expressed by a monoclinic angle of $\gamma = 90.211$ deg and $T_{\mathrm{N}} = 80.3$ K (Komarek et al., 2009; Schönleber et al., 2009). CrOCl has a fourfold magnetic superstructure, which is again monoclinic, but with an apparent less strong magnetoelastic coupling than in VOCl, as expressed by a significantly smaller monoclinic angle of $\alpha = 90.071$ deg and $T_{\mathrm{N}} = 13.5$ K (Angelkort et al., 2009).

FeOCl was the first compound to be synthesized among the MOCl compounds (Goldstaub, 1935). The antiferromagnetic phase transition was discovered in 1971 by Mössbauer spectroscopy and since then has been characterized by several other techniques (Table 5.1). Values between 80 and 92 K have been reported for the Néel temperature. Neutron powder diffraction has shown the appearance of incommensurate superlattice reflections with an incommensurate magnetic modulation wave vector of $\mathbf{q}_M = (0.5, 0.275, 0.5)$ at $T = 4.4$ K (Adam and Buisson, 1975). More

Table 5.1: Transition temperature T_N of FeOCl

Method	T_N [K]	Reference
Mössbauer spectroscopy	92 (3)	Grant, 1971
Neutron diffraction	89 (4)	Adam and Buisson, 1975
Magnetic susceptibility	84 (1)	Bannwart et al., 1987
Neutron diffraction	$\sim$80	Hwang et al., 2000
Mössbauer spectroscopy	85 (1)	Dai et al., 2002
Magnetic susceptibility	$\sim$82	this work
Heat capacity	82.1 (2)	this work
X-ray diffraction	77.4 (1.7)	this work

recent work has suggested a commensurate modulation wave vector of (0.5, $\frac{2}{7}$, 0.5) (Hwang et al., 2000). Models for the magnetic superstructure were proposed, that are based on the assumption of orthorhombic symmetry of the crystal structure (Adam and Buisson, 1975; Hwang et al., 2000).

Here, we present the results of temperature-dependent single-crystal x-ray diffraction, which show that the magnetic phase transition of FeOCl is accompanied by the development of a monoclinic lattice distortion at low temperatures. This finding puts the magnetic order in FeOCl on equal footing with that in the other MOCl compounds. We furthermore present the temperature dependencies of the specific heat, the anisotropic magnetic susceptibility and the dielectric properties. These investigations evidence a second-order phase transition and provide a consistent value of the Néel temperature of 82.0 (2) K (Table 5.1).

5.3 Experimental

5.3.1 Crystal growth

Thin platelet single crystals of FeOCl were grown by vapor phase transport in evacuated quartz-glass ampoules according to procedures described elsewhere (Schäfer et al., 1956). Starting materials were a stoichiometric mixture of Fe_2O_3 (purity 99.999%) and $FeCl_3$ (Purity 99.99%). Small single crystals were selected for x-ray diffraction experiments and larger single crystals were used for the measurements of the magnetic, dielectric and thermal properties.

5.3.2 Magnetic and thermal measurements

The magnetic susceptibilities of two crystals of mass 0.510 mg and 1.3 mg, selected from batch 1 and 2, respectively, were measured in a Quantum Design Squid magnetometer (MPMS, Quantum Design) between 3 and 300 K in magnetic fields between 0.1 and 7 Tesla. The magnetic fields were applied along the **c** direction, which is perpendicular to the surface of the plate-like crystals, and in the **a**, **b**-plane, respectively [Fig. 5.1(a),(b)].

The same crystals were subsequently used for measurements of the heat capacity, using a Quantum Design Physical Properties Measurement System (PPMS, Quantum Design) employing the relaxation method. The crystals were attached with a minute amount of Apiezon N grease to the platform. To enable a reliable correction for the heat capacities of the empty sample platform and the Apiezon grease their heat capacities had been determined in preceding empty runs and were subsequently subtracted from the total heat capacities in order to obtain the samples¡¯ heat capacities [Fig. 5.1(c)].

The dielectric capacitances at 1kHz of the samples were measured as a function of temperature with an Andeen and Hagerling 2500A ultra precision capacitance bridge with an excitation voltage of 0.75 V [Fig. 5.1(d)]. Thin ($\sim$ 0.1 mm) optically perfect crystals with large lateral extension (several mm^2) were selected from batch 1 and electrodes were affixed by using a silver conductive paint to either side of the crystal plates.

Antiferromagnetic ordering below $\sim$82 K with the **c**-axis as easy axis is indicated by the magnetic susceptibility and the heat capacity. The latter show small λ-type anomalies at 81.6(2) K and 82.6(2) K for the crystals taken from batch 1 and 2, respectively. The entropy contained in the anomaly amounts to $\sim$0.12 J/mol K, which covers only about 1% of $R\ln(2 \times 5/2 + 1)$ expected for the ordering of a $S = 5/2$ spin system. The anomaly of the sample taken from the second batch is somewhat smaller and slightly broadened as compared to that of the crystal taken from the first batch. The magnetic susceptibility shows a broad hump with its maximum occurring at $\sim$350 K indicating pronounced short range ordering characteristic for a low-dimensional antiferromagnetic system. Antiferromagnetic ordering is not

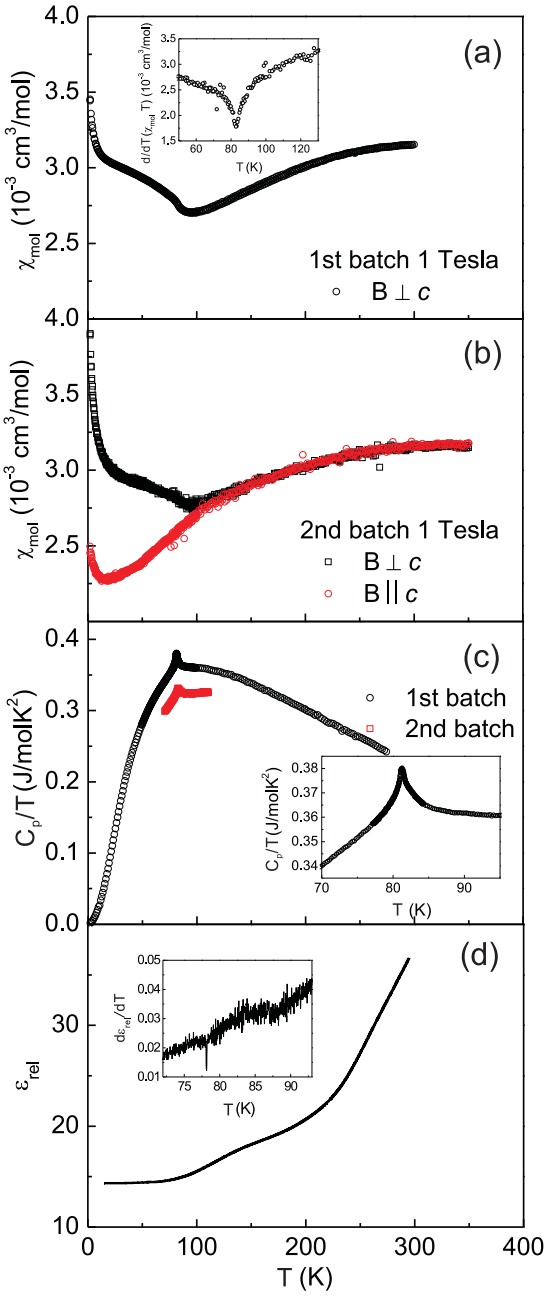

Figure 5.1: (a) Magnetic susceptibility of a crystal of FeOCl from batch 1. The inset shows the derivative with respect to temperature of the quantity $\chi_{\mathrm{mol}} \times T$. (b) Magnetic susceptibility of a crystal of FeOCl from batch 2. (c) Heat capacities of the same crystals measured in zero external magnetic field. The inset displays an enlargement of the temperature range where a λ-type anomaly is seen. (d) Relative dielectric constant of FeOCl at 1 kHz measured perpendicular to the crystal plate.

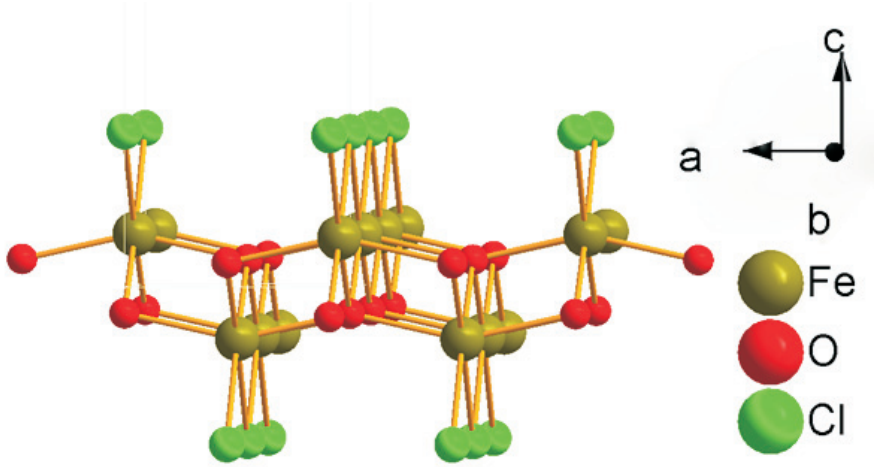

Figure 5.2: The crystal structure of FeOCl

reflected in the dielectric constant which monotonously drops starting from a room temperature value of about 35. A broad bump centered at about 150 K precedes antiferromagnetic long-range ordering. Slight wiggles are seen in the temperature derivative of ϵ_{rel}, but no distinct anomaly is detected.

5.3.3 Single-crystal x-ray diffraction

Single-crystal x-ray diffraction was measured at beamline D3 of Hasylab at DESY (Hamburg, Germany), employing synchrotron radiation of a wavelength of 0.5600 Å. Two crystals were selected for diffraction experiments. They were glued to carbon fibers and mounted on a closed-cycle helium cryostat on the Huber four-circle diffractometer at beamline D3. Crystal A was of dimensions $0.25 \times 0.13 \times 0.005$ mm^3, and Crystal B was of dimensions $0.1 \times 0.06 \times 0.005$ mm^3.

At each selected temperature the setting angles of 18 reflections were determined, from which the lattice parameters were calculated. For Crystal A at room temperature values of $a = 3.7773\,(6)$, $b = 3.3046(7)$ and $c = 7.9156\,(16)$ Å were obtained for the orthorhombic lattice parameters, in agreement with the lattice of FeOCl (Goldstaub, 1935; Lind, 1970). Similar results were obtained for crystal B. In this setting with space group $Pmmn$, layers FeOCl are stacked along **c** (Fig. 5.2).

Possible lattice distortions can be obtained from peak splittings in the direction

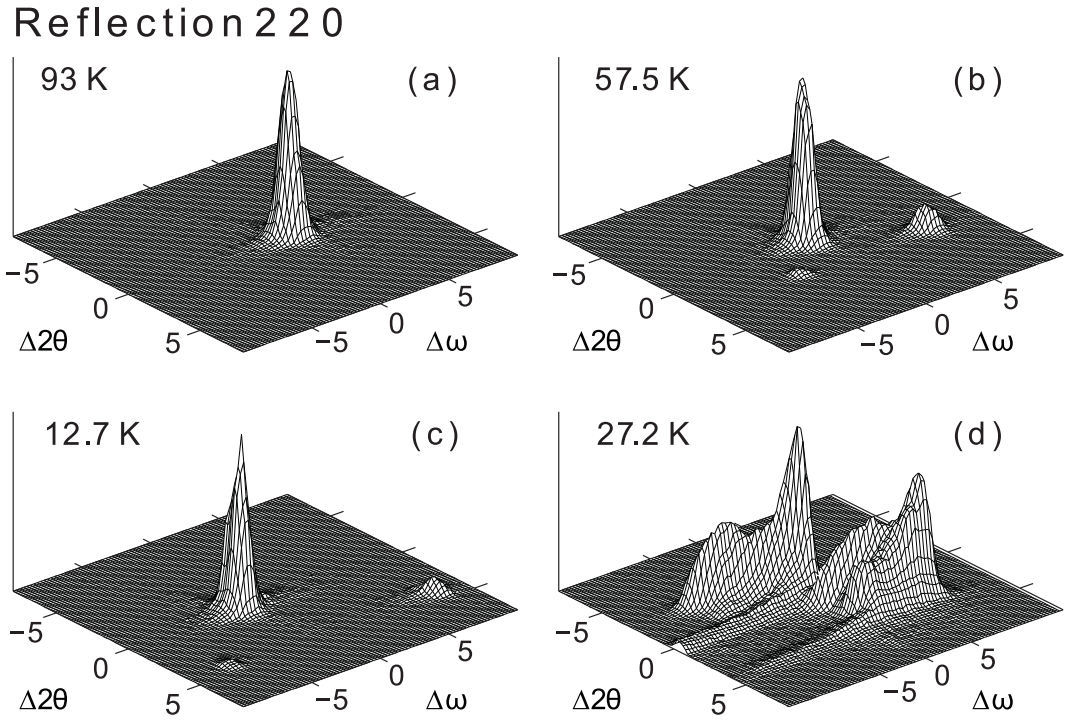

Figure 5.3: Diffracted intensity as a function of the scattering angle 2θ and the crystal orientation ω for reflection (2 2 0) of crystal A (d) and crystal B (a,b,c) at selected temperatures. $\Delta 2\theta$ and $\Delta\omega$ indicate the deviation from the center of the scan in units of 0.01 deg.

of the scattering angle 2θ. A splitting of (h k 0) would indicate a deviation from 90 deg of the angle γ. Splittings of (h 0 l) and (0 k l) allow the angles β and α, respectively, to be calculated. Accordingly, ω–2θ maps have been measured on both crystals at selected temperatures for the reflections (2 2 0), (2 0 $\bar{4}$) and (0 2 $\bar{5}$). Detector slits were set to 6×0.02 mm^2, which corresponds to an acceptance angle of 0.0031 deg in the direction of 2θ. Step sizes of 0.002 deg were chosen for both the directions ω and 2θ.

ω–2θ maps of the (2 2 0) reflection show single peaks at temperatures above T_{N}, while they show a double peak for $T < 75$ K (Fig. 5.3). The reflections (2 0 $\bar{4}$) and (0 2 $\bar{4}$) do not exhibit peak splittings at any temperature, although they do have a broadened appearance into the direction of ω at low temperatures [data not shown; compare to Fig. 5.3(d)]. Broadening into the direction of ω may be explained by internal strain due to the phase transition as well as by damage to the

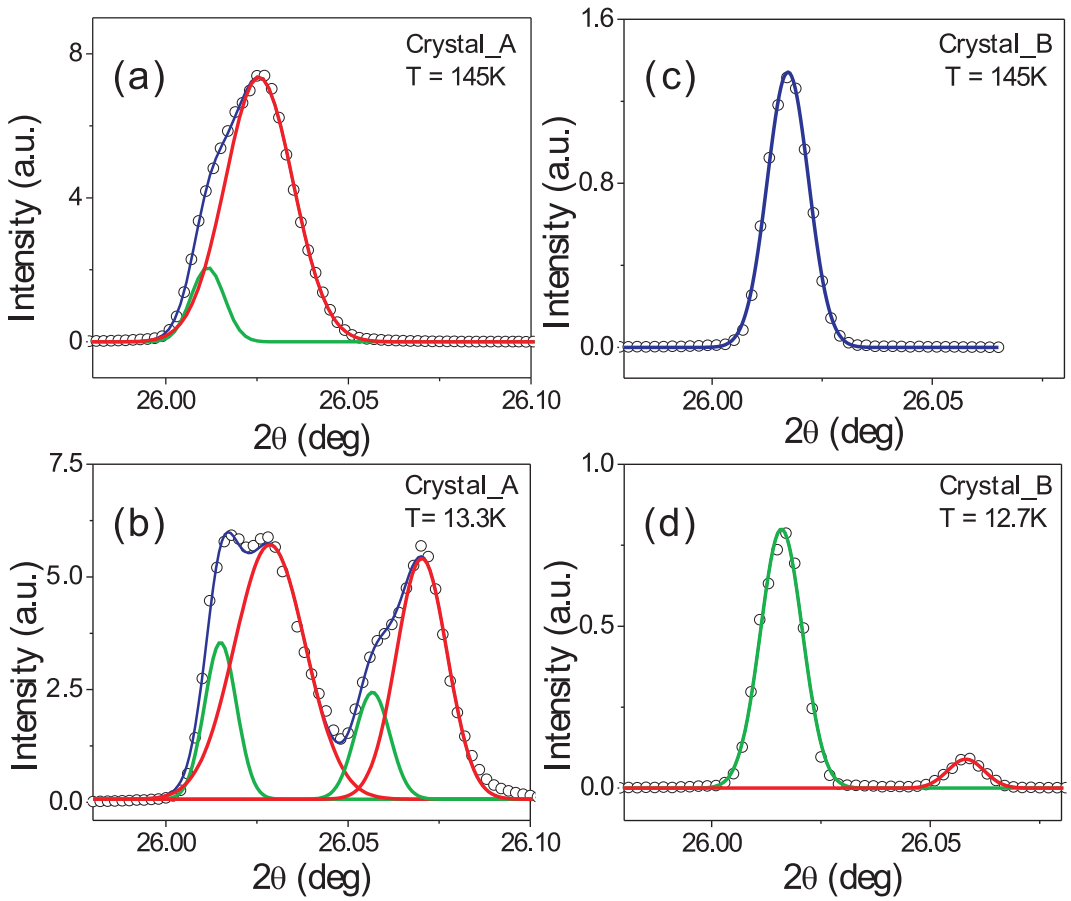

Figure 5.4: Diffracted intensity as a function of the scattering angle 2θ for the reflection (2 2 0) for both crystals at different temperatures. All peaks were fitted by Gauss functions.

crystal originating in external strain due to different thermal expansions of sample and glue. These results show that the lattice of FeOCl is **c**-unique monoclinic in the antiferromagnetic phase.

The magnitude of the splitting in 2θ can be obtained from the 2θ dependence of the diffracted intensity that is obtained by collecting all intensity measured at a single value of 2θ (integration over ω). The plot of the diffracted intensity vs 2θ at $T = 145$ K reveals that crystal A consists of two domains with orientations differing by a few hundredth of a degree, while crystal B was of much better quality [Fig. 5.4(a),(c)]. The broadened peak of crystal A is well described by two overlapping Gaussian functions, while the peak of crystal B can be fitted with a single

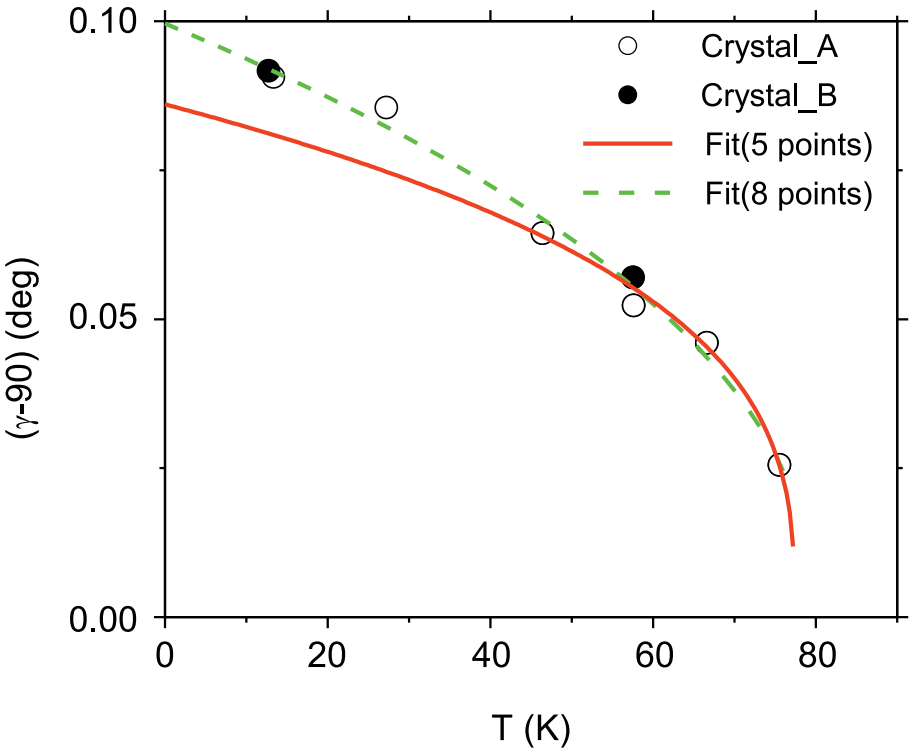

Figure 5.5: Temperature dependence of the monoclinic angle γ. The (red) solid line represents a fit of Eq. (5.1) to the five data points at $T > 40$ K. The (green) dashed line is a fit to all eight data points.

Gaussian. At low temperatures, crystal A displays two broadened peaks of similar intensities for (2 2 0), while crystal B exhibits two peaks of different intensities [Fig. 5.4(b),(d)]. These results indicate that crystal A consisted of two monoclinic domains of comparable volumes, while crystal B was almost a single domain crystal.

The peak splitting depends on temperature and it was too small to be determined close to T_N. The peak splitting in 2θ of (2 2 0) directly gives the angle γ of the monoclinic lattice. We have obtained peak-splittings at six temperatures for crystal A and at two temperatures for crystal B. Limited beam-time at the synchrotron did not allow experiments at more temperatures on crystal B. Nevertheless, the monoclinic angles for crystals A and B match very well (Fig. 5.5). The deviation from 90 deg of the monoclinic angle can be considered as order parameter, and the

temperature dependence of its value can by described by the function

$$\gamma - 90\,\mathrm{deg} = \Delta\gamma_0 \left(1 - \frac{T}{T_\mathrm{N}(\mathrm{Xray})}\right)^\beta . \tag{5.1}$$

Critical behavior according to Eq. (5.1) is only expected close to T_N. An excellent fit of Eq. (5.1) to the five data points at $T > 40$ K has been obtained (Fig. 5.5), resulting in an estimate for the transition temperature of $T_\mathrm{N}(\mathrm{Xray}) = 77.4\,(1.7)$ K and a critical exponent of $\beta = 0.32\,(9)$. The latter values is close to the critical exponent of the 3D Ising model, but the large standard uncertainty prevents a meaningful interpretation of this parameter.

The fitted function clearly underestimates the values of γ at low temperatures, thus demonstrating deviations from critical behavior below $T \approx 40$ K. A fit of reasonable quality has also been obtained for all eight data points (dashed line in Fig. 5.5). This fit resulted in somewhat different values for the two fit parameters, $T'_\mathrm{N}(\mathrm{Xray}) = 79.8\,(2.0)$ K and $\beta' = 0.46\,(5)$. The second fit function allows the determination of the extrapolated value of the monoclinic angle at $T = 0$ K as $\gamma_0 = 90.100$ deg.

In another experiment superlattice reflections were searched by **q**-scans along $\mathbf{b}^*$ for selected reflection pairs $(h\ k\ l) \rightarrow (h\ k+1\ l)$. A total of 43 **q**-scans were measured on crystal A at temperatures of 10 and 13.3 K. Superlattice reflections were found in two scans, at (1 1.45 0) (weak) and at (2 0.55 $-$2) (very weak). The values of the component q_b as obtained from the two reflections are in agreement with each other (Fig. 5.6). The strong satellite reflection could be measured at selected temperatures up to 58 K. The results of the **q**-scans show that the length of the incommensurate modulation wave vector depends on temperature.

5.4 Discussion

The crystals of FeOCl presently studied undergo an antiferromagnetic phase transition as evidenced by the temperature dependence of the magnetic susceptibility (Fig. 5.1), in agreement with the literature (Bannwart et al., 1987). The ordered

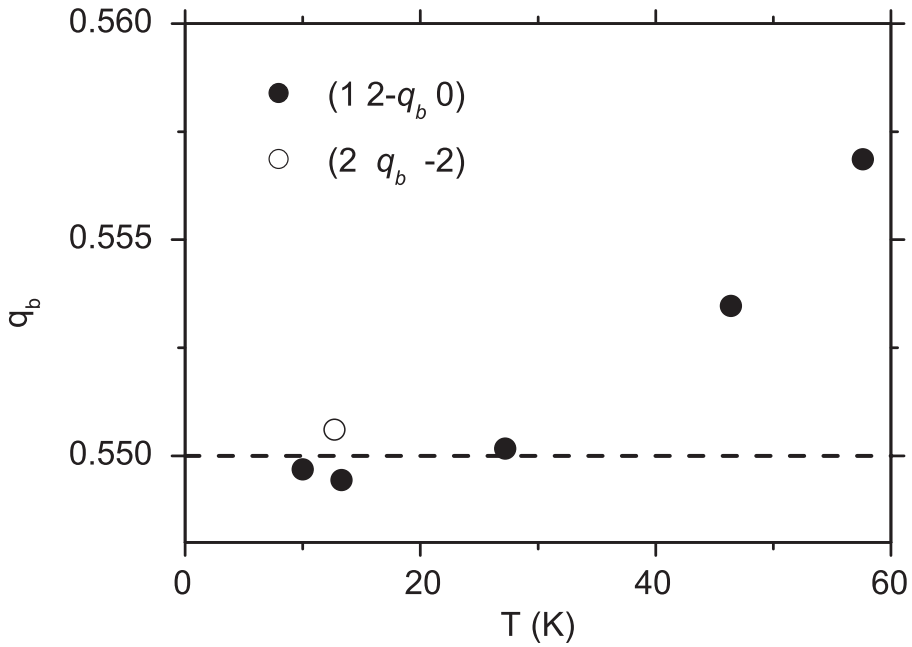

Figure 5.6: Incommensurate component q_b of the modulation wave vector $\mathbf{q}_X = (0, q_b, 0)$, as determined by **q**-scans along $\mathbf{b}^*$. The dashed line indicates value $0.550 = 2 \times 0.275$.

magnetic moments possess a component along **c**, but it cannot be excluded that there also is a component along **b** (Adam and Buisson, 1975).

Values for the Néel temperature have been reported between 80 and 92 K (Table 5.1). We have obtained a consistent value of $T_\mathrm{N} = 82.0\,(2)$ K from the temperature dependencies of x-ray diffraction, specific heat and magnetic susceptibility. This value is in accordance with the more recent values in the literature and thus will be close to the true transition temperature of pure FeOCl.

The major finding of the present experiments is the monoclinic lattice distortion, whose development accompanies the magnetic transition (Fig. 5.5). The thermal evolution of the monoclinic angle indicates the second-order character of the phase transition, and extrapolation of the measured values allows an accurate estimate of the Néel temperature (Table 5.1). The value of $\gamma = 90.10$ deg at low temperatures suggests strong magnetoelastic coupling, in agreement with the observations on VOCl and CrOCl (Komarek et al., 2009; Schönleber et al., 2009; Angelkort et al., 2009). Satellite reflections in x-ray diffraction are much weaker for FeOCl than for CrOCl or TiOCl, indicating that relative atomic coordinates deviate from their

orthorhombic values by a small amount only, and that the major structural distortion is the monoclinic lattice distortion.

Another point of debate was the precise value of the modulation wave vector of the magnetic superstructure. For a structure with antiferromagnetic order described by modulation wavevector $\mathbf{q}_M$ one can expect a structural distortion with modulation wave vector $2\mathbf{q}_M$, which may give rise to satellite reflections in x-ray diffraction (Lovesey and Collins, 1996). Since $2 \times 0.5 = 1$, we have here employed $\mathbf{q}_X = 2\mathbf{q}_M - \mathbf{a}^* - \mathbf{c}^* = (0, q_b, 0)$.

Below $T \approx 30$ K we have found that the incommensurate component of $\mathbf{q}_X$ is equal to 0.550 (Fig. 5.6). This value is exactly two times the value of 0.275 as reported for $\mathbf{q}_M$ at $T = 4.2$ K, and the present x-ray diffraction experiment confirms the observations by neutron diffraction by Adam and Buisson (Adam and Buisson, 1975). Above 40 K the modulation wave vector depends on temperature, proving that the modulation is incommensurate. Hwang et al. (2000) proposed a commensurate magnetic modulation wave vector of 2/7. The value of $2 \times 2/7 = 0.5714$ is not observed at any temperature.

The present results open the possibility of a lock-in transition with a transition temperature between 30 and 45 K, at which the magnetic modulation wave vector attains the value of $0.275 = 11/40$. However, none of the other experiments show evidence for an additional phase transition at these temperatures.

5.5 Conclusions

X-ray diffraction has shown that the antiferromagnetic phase transition of FeOCl is accompanied by a monoclinic lattice distortion, in agreement with the distortions observed for CrOCl and VOCl. The need for this distortion lies in the perfect frustration for antiferromagnetic order of the arrangement of magnetic M^{3+} ions on the orthorhombic lattice. The temperature dependence of the magnitude of the monoclinic angle has shown that the phase transition is a second-order phase transition.

The magnetic superstructure has been found to be incommensurate as evidenced by the temperature dependence of the positions of satellite reflections in x-ray

diffraction at $\mathbf{q}_X = 2\mathbf{q}_M$.

Acknowledgments

We thank Alfred Suttner for growing single crystals of FeOCl. Experiments with synchrotron radiation have been performed at beamline D3 of Hasylab (DESY, Hamburg). We are grateful to Martin Tolkiehn for technical support with these experiments. Financial support by the German Science Foundation (DFG) is gratefully acknowledged. The work of JZ has been made possible through a CSC scholarship from the China Scholarship Council.

Chapter 6

Transformation between spin-Peierls and incommensurate fluctuating phases of Sc-doped TiOCl [1]

6.1 Abstract

Single crystals of $Sc_xTi_{1-x}OCl$ ($x = 0.005$) have been grown by the vapor phase transport technique. Specific heat measurements prove the absence of phase transitions for 4-200 K. Instead, an excess entropy is observed over a range of temperatures that encompasses the incommensurate phase transition at 90 K and the spin-Peierls transition at 67 K of pure TiOCl. Temperature-dependent X-ray diffraction on $Sc_xTi_{1-x}OCl$ gives broadened diffraction maxima at incommensurate positions between $T_{c1} = 61.5\,(3)$ and ~ 90 K, and at commensurate positions below 61.5 K. These results are interpreted as due to the presence of an incommensurate phase without long-range order at intermediate temperatures, and of a highly disturbed commensurate phase without long-range order at low temperatures. The commen-

[1] Accepted as: J. Zhang, A. Wölfel, M. Bykov, A. Schönleber, S. van Smaalen, R. K. Kremer, and H. L. Williamson, *Phys. Rev. B* (2014).

surate phase is attributed to a fluctuating spin-Peierls state on an orthorhombic lattice. The monoclinic symmetry and local structure of the fluctuations are equal to the symmetry and structure of the ordered spin-Peierls state of TiOCl. A novel feature of $Sc_xTi_{1-x}OCl$ ($x = 0.005$) is a transformation from one fluctuating phase (the incommensurate phase at intermediate temperatures) to another fluctuating phase (the spin-Peierls-like phase). This transformation is not a phase transition occurring at a critical temperature, but it proceeds gradually over a temperature range of ∼10 K wide. The destruction of long-range order requires much lower levels of doping in TiOCl than in other low-dimensional electronic crystals, like the canonical spin-Peierls compound $CuGeO_3$. An explanation for the higher sensitivity to doping has not been found, but it is noticed that it may be the result of an increased two-dimensional character of the doped magnetic system. The latter would support the formation of phases with quasi-long-range order, described in the literature as Kosterlitz–Thouless phases.

6.2 Introduction

Materials supporting low-dimensional electronic systems are known for their exotic properties, including phase transitions towards charge-density wave (CDW) or spin-density wave (SDW) states (Gruner, 1994). Specific to compounds containing quasi-one-dimensional (1D) magnetic chains is the possibility of a first-order phase transition to a spin-Peierls state at low temperatures (Bray et al., 1983). The spin-Peierls state is characterized by the presence of spin-singlet pairs and a finite energy gap for magnetic excitations, resulting in vanishing magnetic response at low temperatures. The singlet pairs are a consequence of a distortion of the crystal structure leading to a dimerization along the chains that enhances the spin exchange within each dimer. Spin-Peierls distortions can be measured by x-ray diffraction, and the magnitude of the dimerization can be taken as order parameter for the spin-Peierls state.

Theoretically it has been shown that 1D systems exhibit fluctuations of the order parameter of substantial magnitude up to temperatures well above the transition temperature T_c (Gruner, 1994). Correlation lengths are anisotropic and the largest

value can be found for the direction along the 1D system. Structural fluctuations can be traced by x-ray diffraction experiments. They are typically indicated by diffuse scattering which is concentrated in one, two or three directions in reciprocal space. In case of long correlation lengths, reflections can be observed of a width that is related to the inverse correlation length. Domain size effects or imperfections (*e.g.* stacking faults, internal strain and impurities) of a real specimen may lead to additional broadening of the Bragg reflections, rendering it difficult to disentangle dynamical fluctuation regimes from the effects of imperfections in real crystals.

Ideal one-dimensional magnetic systems do not show long-range ordering. The unavoidable interchain coupling, even though much weaker than the intrachain coupling, drives the systems to long-range magnetic ordering at low temperatures. One way of suppressing long-range order is the substitution of magnetic atoms by non-magnetic impurities. For example, $CuGeO_3$ undergoes a canonical spin-Peierls transition at a temperature of $T_{SP} = 14$ K (Hase et al., 1993). Replacement of as little as 3% of the Cu^{2+} ions by non-magnetic Zn^{2+} atoms is sufficient to completely suppress the spin-Peierls transition (Hase et al., 1993). Instead, antiferromagnetic order develops below $T = 4$ K for dopings up to 8% (Hase et al., 1993; Oseroff et al., 1995; Kojima et al., 1997; Grenier et al., 1998). At larger doping levels long-range magnetic order does not develop at any finite temperature. Suppression of the spin-Peierls state by a few percent of non-magnetic doping is the magnetic counterpart of the suppression of a charge-density-wave (CDW) state in 1D electronic materials induced by doping into the metallic chains (Schneemeyer et al., 1984; Gruner, 1994).

Due to larger magnetic exchange interactions along the chains (Seidel et al., 2003; Hase et al., 1993), the spin-Peierls systems TiOCl, TiOBr and $TiPO_4$ exhibit significantly higher transition temperatures than $T_{SP} = 14$ K of $CuGeO_3$. However, the phase diagrams of these systems are more complicated than the phase diagram of $CuGeO_3$, since the spin-Peierls state is preceded by an incommensurate magnetic state at intermediate temperatures (Beynon and Wilson, 1993; Seidel et al., 2003; van Smaalen et al., 2005; Law et al., 2011). Several studies have recently been published on the effects of doping on the properties of TiOCl (Beynon and Wilson, 1993; Seidel et al., 2003; Clancy et al., 2008; 2010; Zhang et al., 2010; Aczel et al., 2011). Zhang et al. (2010) reported band-structure calculations that indicate that TiOCl remains

insulating upon doping with either non-magnetic, isovalent Sc^{3+} or monovalent Na^{+} or other ions. The most interesting finding was the complete suppression of the spin-Peierls state in $Sc_xTi_{1-x}OCl$ for doping levels of $x = 0.01$ and 0.03, while long-range magnetic order does not appear down to very low temperatures either (Clancy et al., 2008; 2010; Aczel et al., 2011). This behaviour is qualitatively different from that of other spin-Peierls compounds like $CuGeO_3$. There, the spin-Peierls state persists up to 3% doping, and is then replaced by antiferromagnetic order (Aczel et al., 2011).

Here we present the results of a study by single-crystal x-ray diffraction performed on samples of TiOCl in which 0.5% of the Ti atoms has been replaced by isovalent Sc atoms. Our temperature-dependent x-ray diffraction data reveal that $Sc_xTi_{1-x}OCl$ ($x = 0.005$) undergoes a transition to an incommensurate phase at approximately the same temperature as is observed for TiOCl. A spin-Peierls-like transition occurs at $T_{c1} = 61.5\,(3)$ K, somewhat lower than the transition temperature of 67 K found in pure TiOCl (Seidel et al., 2003; Shaz et al., 2005; Hemberger et al., 2005). Structure refinements against the integrated intensities of the broadened Bragg reflections at $T = 8$ K show that the structural distortions are similar to the distortions in the spin-Peierls state of non-substituted TiOCl. Based on measurements of the specific heat we conclude that both the incommensurate and spin-Peierls-like phases lack true long-range order. The observed apparent transition between these two states is interpreted as a novel type of phase transition between crystalline states supporting different kinds of fluctuations.

6.3 Experimental and results

6.3.1 Crystal growth

A mixture of TiO_2, Ti, $TiCl_4$ and $ScCl_3$ corresponding to $x = 0.005$ was used to grow single crystals of $Sc_xTi_{1-x}OCl$ by chemical vapor phase transport in evacuated quartz-glass ampoules according to the procedure described in detail by (Schäfer et al., 1958). Transparent crystals of red-brown color were obtained that showed less well developed facets than the yellow-brown crystals of TiOCl do. Initial x-ray diffraction experiments on several specimens confirmed the lattice parameters

to be those of TiOCl. ω Scans of selected Bragg reflections were used for testing several crystals at room temperature. Most of the specimens revealed broadened Bragg reflections, indicating a large mosaic spread and poor crystal quality. Such crystals were discarded for the temperature-dependent x-ray diffraction experiments. Finally, a crystal of dimensions $0.22 \times 0.06 \times 0.008$ mm^3 was identified and selected for the diffraction experiments reported in the following.

6.3.2 Specific heat

The heat capacities were determined on a collection ($\sim$ 2 mg) of well shaped crystals of $Sc_xTi_{1-x}OCl$ ($x = 0.005$) with a Physical Properties Measurement System (PPMS, Quantum Design), employing the relaxation method. The crystals were attached to the calorimeter platform with a minute amount of Apiezon N grease. The heat capacity of the platform and the Apiezon grease were measured in a preceding run and subtracted from the total heat capacities. A reference sample of TiOCl was measured in the same manner. Figure 6.1 displays the heat capacities of $Sc_xTi_{1-x}OCl$ ($x = 0.005$) and TiOCl in a C_p/T representation. The specific heat C_p of $Sc_xTi_{1-x}OCl$ ($x = 0.005$) does not exhibit the characteristic anomalies associated with the phase transitions as they are clearly revealed for the TiOCl sample. For $Sc_xTi_{1-x}OCl$ ($x = 0.005$) the anomalies rather appear to be smeared out, rendering an excess heat capacity over a broad temperature regime embracing the area where the anomalies occurred for TiOCl. The entropies contained in the anomalies in TiOCl and in the broad smeared excess heat capacity of $Sc_xTi_{1-x}OCl$ ($x = 0.005$) are about the same, indicating that the sharp transitions seen for TiOCl have been replaced by a broad fluctuation regime, which extends over a large temperature range of more than $\sim$50 K, *i.e.* more than twice the temperature regime where the incommensurate intermediate phase is seen.

6.3.3 Temperature-dependent x-ray diffraction

X-ray diffraction experiments were performed on the Huber four-circle diffractometer at beamline D3 of Hasylab at DESY (Hamburg, Germany), employing radiation of a wavelength of 0.5600 Å. Diffracted intensities were measured by a scintillation

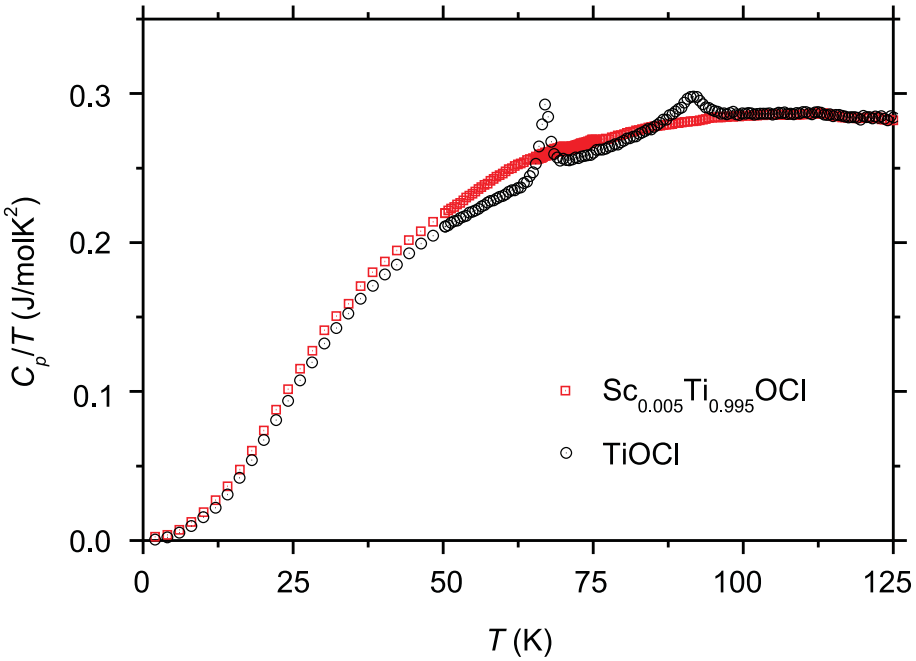

Figure 6.1: (Color online) Temperature dependence of the heat capacity C_p plotted as C_p/T of $Sc_xTi_{1-x}OCl$ ($x = 0.005$) (red squares) and of TiOCl (black circles). The latter data are in agreement with Ref. (Hemberger et al., 2005).

detector. The single crystal of $Sc_xTi_{1-x}OCl$ ($x = 0.005$) (Section 6.3.1) was glued onto a carbon fiber attached to a copper pin and mounted on a closed-cycle helium cryostat, allowing cooling of the sample down to below 8 K. At each selected temperature the orientation matrix was determined from the accurately measured setting angles of 20 Bragg reflections. Lattice parameters obtained from the orientation matrices are in agreement with those of TiOCl.

Limitation of crystal orientations as imposed by the closed-cycle cryostat allowed only about 1/8 of all possible Bragg reflections to be measured. For the present sample this implied that many $(0\ k\ l)$ and $(h\ 0\ l)$ reflections were accessible. Reflections in the $l = 0$ plane [$(h\ k\ 0)$ reflections] of reciprocal space were not available. TiOCl has monoclinic symmetries in its incommensurate and spin-Peierls phases (Shaz et al., 2005; Schönleber et al., 2008). Therefore, monoclinic lattice distortions were investigated by searching for splittings of the $(0\ 2\ -4)$, $(2\ 0\ -5)$ and $(2\ -2\ -4)$ reflections. A splitting of these reflections in the direction of the scattering angle 2θ implies a deviation from 90 deg of the angles α, β and γ, respectively. Employ-

ing procedures described elsewhere (Angelkort et al., 2009), the diffracted intensity around these three reflections was measured as a function of 2θ and the crystal orientation ω, resulting in so-called ω–2θ maps (Fig. 6.2). Such maps were collected

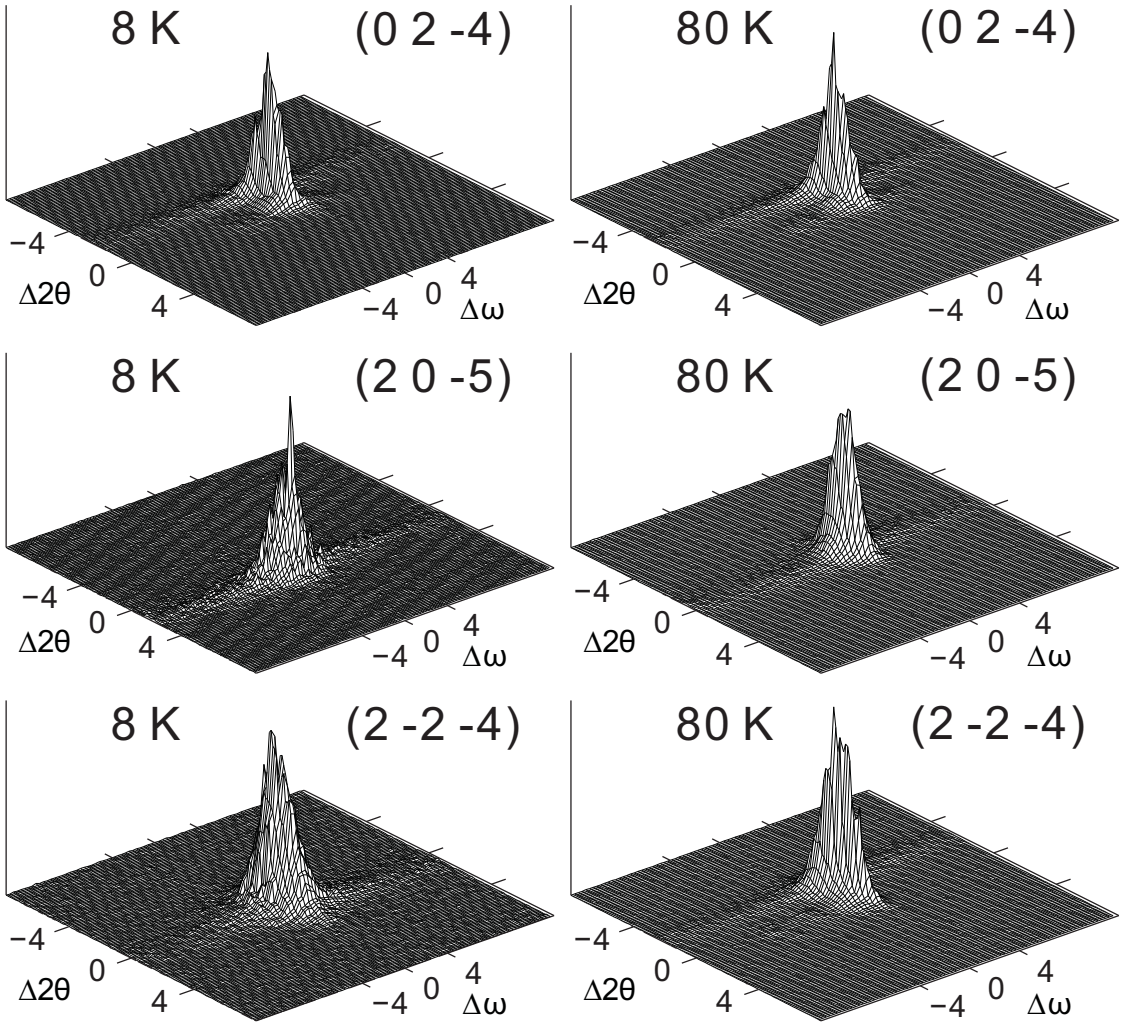

Figure 6.2: Diffracted intensity as a function of the scattering angle 2θ and the crystal orientation ω for several Bragg reflections at temperatures of 8 and 80 K. $\Delta 2\theta$ and $\Delta\omega$ indicate the deviation from the center of scan in units of 0.01 deg.

at temperatures of 8, 80, 100 and 298 K, thus covering the spin-Peierls, incommensurate and normal phases. None of the peaks appeared to be split at any of the four temperatures (see supplementary Figs. B.1–B.4). This finding indicates that the lattice remains orthorhombic down to $T = 8$ K. Integrating the diffracted in-

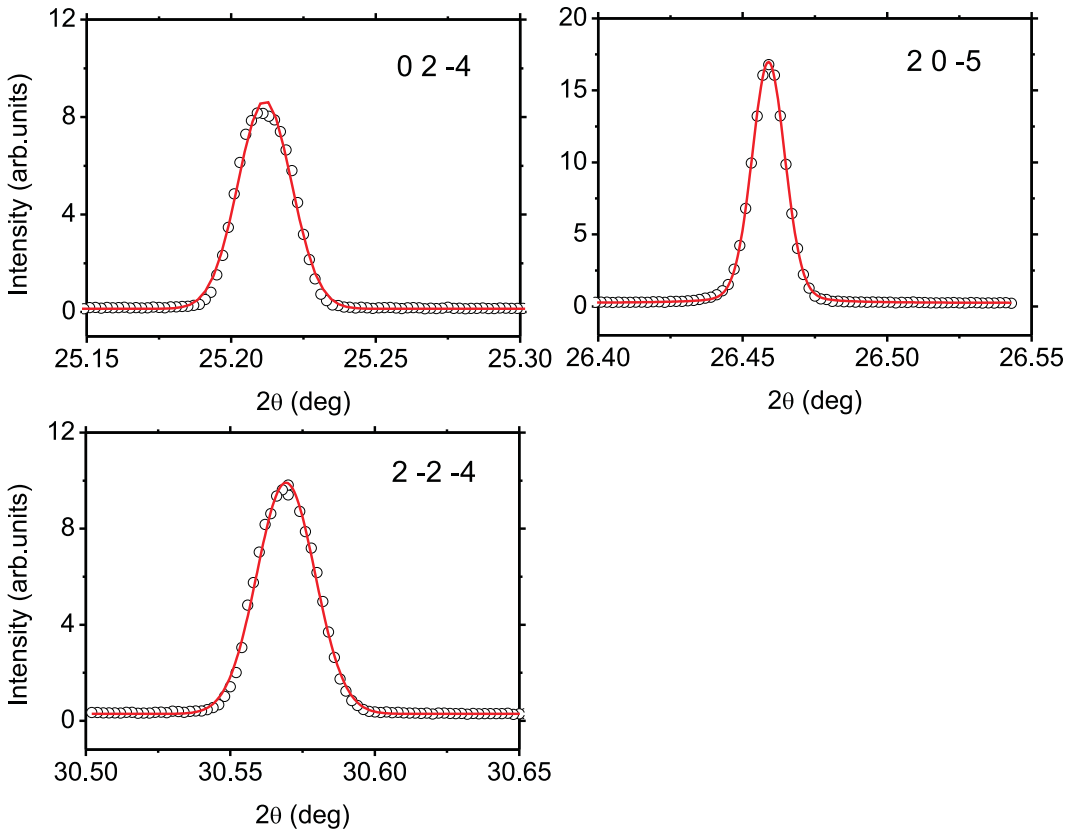

Figure 6.3: Diffracted intensity versus the scattering angle 2θ at $T = 80$ K. Data points have been obtained by integration along ω in the ω–2θ maps (see Fig. 6.2). The solid curves represent fits by pseudo-Voigt functions.

tensities over the direction ω results in the dependence of diffracted intensity on the scattering angle 2θ. These plots even more clearly prove the absence of a splitting of reflections (see Fig. 6.3 and supplementary Figs. B.5–B.8).

Superlattice reflections were investigated at selected temperatures between 52.5 and 90 K by q scans along $\mathbf{a}^*$ centered at $(1\ -0.5\ -9)$, $(0\ -2.5\ -3)$, $(0\ -1.5\ -1)$ and $(0\ -1.5\ -2)$. A single superlattice peak was observed at $(h\ k + 0.5\ l)$ in each scan between 52.5 and 60 K. These superlattice reflections indicate a commensurate modulation with a propagation vector $\mathbf{q}_{SP} = (0, 0.5, 0)$. They are found at the same positions as the superlattice reflections of pristine TiOCl in the spin-Peierls phase below T = 67 K. Between 62.5 K and 87.5 K the scans reveal two superlattice peaks at incommensurate positions described by $(h \pm q_1\ k + 0.5\ l)$ (Fig. 6.4

and supplementary Figs. B.9–B.17). The magnitudes of the incommensurate com-

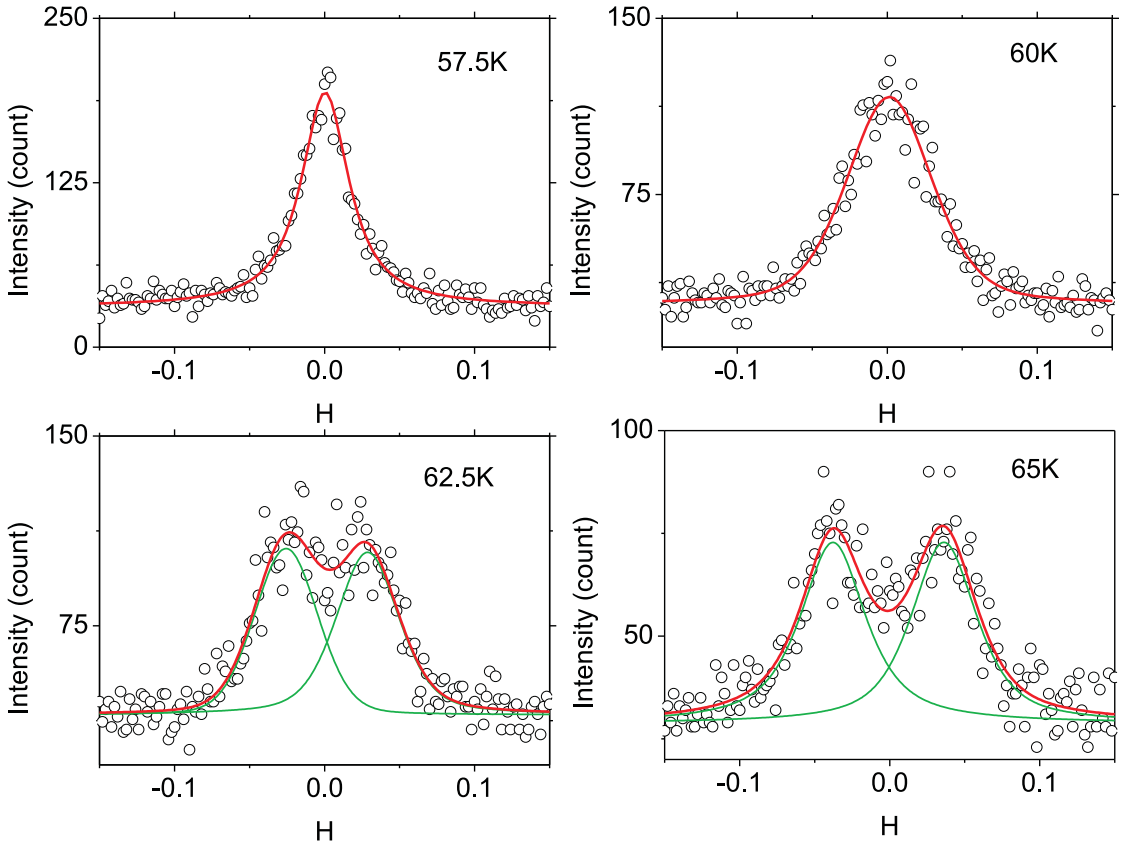

Figure 6.4: q Scans along $\mathbf{a}^*$ centered at $(0\ -2.5\ -3)$ at selected temperatures as indicated. Solid curves represent pseudo-Voigt functions fitted to the data.

ponent q_1 have been determined from the separations within pairs of superlattice reflections observed in each q scan. The positions of the superlattice reflections were determined from fits of pseudo-Voigt profile functions to the data, employing an individual function for each reflection (Fig. 6.4). The values of q_1 as obtained from the four different q scans are in excellent agreement with each other. The temperature dependence of q_1 is well described by a critical power law

$$q_1 = q_1^0 \left(T - T_{c1}\right)^{2\beta} . \tag{6.1}$$

The fit to the data resulted in an accurate estimate of the critical temperature T_{c1} marking the transition between the states with incommensurate and commensurate

superlattice reflections, respectively (Fig. 6.5). The value of $T_{c1} = 61.5\,(3)$ K is 5.5 K lower than the value of the spin-Peierls transition temperature in TiOCl. The resolution of our experiment was insufficient to resolve a possibly very small

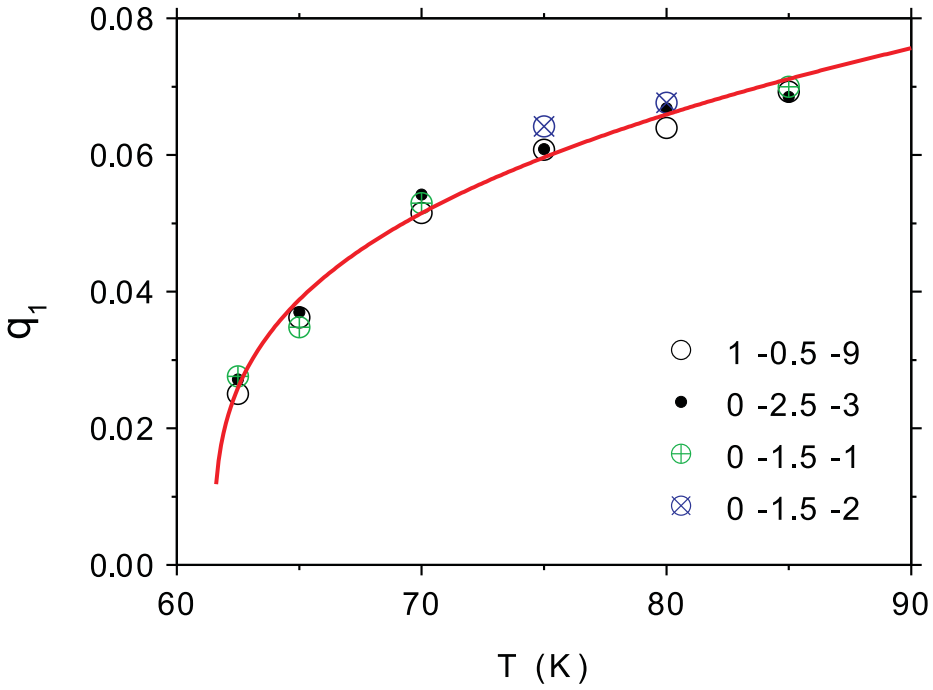

Figure 6.5: Temperature dependence of the incommensurate component q_1 of the modulation wave vector $\mathbf{q} = (q_1, 1/2, 0)$, as determined from q scans. The solid line represents a fit of Eq. 6.1 to the data, resulting in $q_1^0 = 0.026\,(2)$, $T_{c1} = 61.5\,(3)$ K and $2\beta = 0.32\,(3)$.

incommensurate component of the modulation wave vector along $\mathbf{b}^*$, as it has been established for TiOCl (Schönleber et al., 2006; Krimmel et al., 2006).

ω Scans were performed at the commensurate positions $(1\ -0.5\ -9)$, $(0\ -2.5\ -3)$ and $(0\ -1.5\ -1)$ and at the positions of 27 main reflections for selected temperatures between 8 and 87.5 K (see supplementary Figs. B.18– B.29). Integrated intensities of the main reflections are nearly independent of temperature. Generally, the main reflections are much narrower than the commensurate satellite reflections. However, the width of some reflections varied with temperature. For example, between 8 and 87.5 K the FWHM of the reflection $(1\ -1\ -8)$ varies between 0.0278 and 0.0132 deg (Fig. 6.6). Contributions to the observed variation may come from the fluctuations discussed below. However, other contributions cannot be excluded, like

a temperature-dependent uniaxial stress induced by the glue used to fix the crystal.

At low temperatures the commensurate superlattice reflections are considerably broader than the main reflections (Fig. 6.6). The FWHMs pass through a minimum

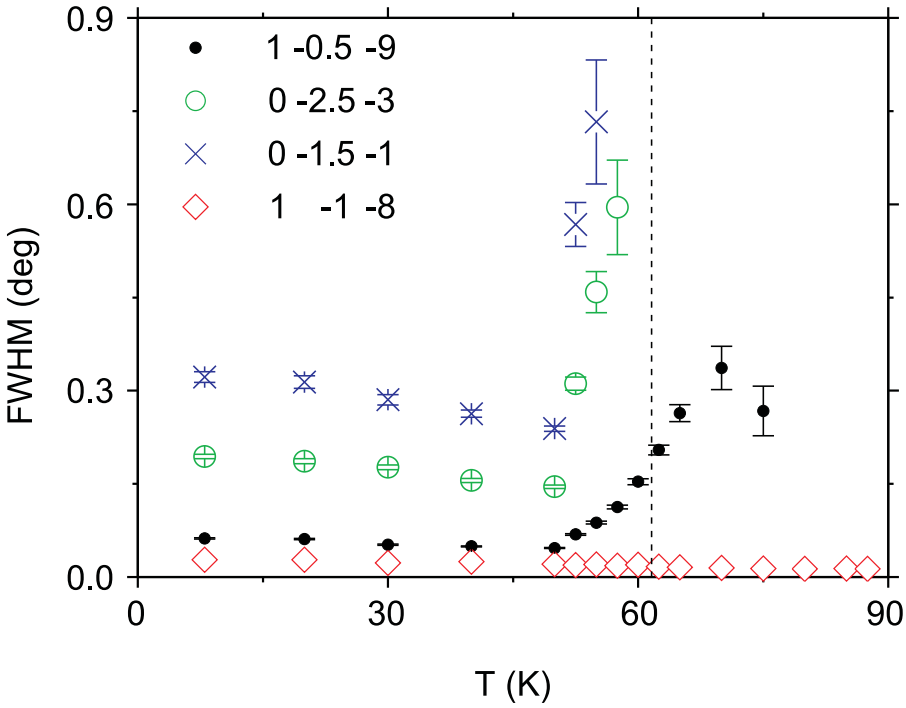

Figure 6.6: Temperature dependence of the full width at half maximum (FWHM) of the commensurate superlattice reflections and the main reflection (1 −1 −8), as they have been derived from fits of Lorentzians to the ω scans centered at the indicated positions. Error bars are given. ω Scans of ±0.5 deg wide correspond to directions in reciprocal space of ±(0.0020 −0.0335 0.0120) ∼ (0 −3 1) for reflection (1 −0.5 −9); ±(−0.0275 −0.0006 0.0034) ∼ (−8 0 1) for (0 −1.5 −1); and ±(−0.0154 −0.0002 0.0018) ∼ (−8 0 1) for (0 −2.5 −3). The vertical dashed line indicates the critical temperature $T_{c1} = 61.5$ K (see Fig. 6.5).

at 50 K and steeply increase for temperatures above 50 K. This rapid growth of the FWHM above 50 K does not allow the (0 −1.5 −1) and (0 −2.5 −3) reflections to be observed at temperatures above 57.5 K. For the (1 −0.5 −9) position, a broad diffraction ridge remains visible up to 80 K.

The different FWHM of the three measured superlattice reflections can be related to the directions of the ω scans in reciprocal space (see caption of Fig. 6.6). They indicate that both at low temperatures and in the transition region between 50 and

61.5 K, the largest correlation length is along a direction with a large component along **b**, *i.e.* along the magnetic chains, while the correlation length along **a** rapidly decreases above 50 K. Unfortunately, the restrictions imposed by the closed-cycle cryostat did not allow scattering experiments significantly outside bisecting position ($\omega \approx \theta$), so that ω scans along $\mathbf{c}^*$ or other special directions could not be performed. Therefore, conclusive information concerning the loss of correlations along **c** could not be obtained.

The directions of the ω scans on the reflections (0 −1.5 −1) and (0 −2.5 −3) are close to $\mathbf{a}^*$, but their widths are clearly insufficient to reach ω values of the incommensurate positions as found at temperatures above 61.5 K (Figs. 6.5 and 6.6). Accordingly, diffracted intensity is not found in these scans for temperatures above T_{c1}. The ω scans on (1 −0.5 −9) have component zero into the incommensurate direction (Fig. 6.6). Instead, the incommensurate positions will have been in diffraction position outside the principal diffraction plane, but still into a direction within the opening angle of the detector, because the difference (q_1 0 0) between commensurate and incommensurate scattering vectors is small as compared to the length of the scattering vector (1 −0.5 −9) itself. This explains the observed intensity above T_{c1} of this reflection.

At a temperature of 8 K the intensities of a set of main and commensurate satellite reflections have been measured up to $[\sin(\theta)/\lambda]_{max} = 0.75$ Å^{-1}, using a wider scan window for the broader superlattice reflections. Integrated intensities were obtained from the ω scans by the software REDUCE (Eichhorn, 1991), resulting in a total of 490 reliable satellite reflections. A total of 567 main reflections were obtained. However, inspection of the ω scans revealed that 141 reflections had moved out of the scan window, possibly due to a slight misalignment of the crystal. These 141 reflections were removed from the data set.

Subsequently, an absorption correction was applied using the software JANA2006 (Petricek et al., 2006), based on a crystal shape determined by inspection through an optical microscope. JANA2006 was also used for structure refinements against the integrated intensities of the reflections, following procedures applied previously for TiOCl at 10 K (Shaz et al., 2005).

The twofold superstructure has been described as a commensurately modulated

structure with $\mathbf{q} = (0,\ 1/2,\ 0)$ and superspace group $Pmmn(0\ \sigma_2\ 0)000$ [No. 59.1.9.4 with standard setting $Pmnm(0\ 0\ \sigma_3)000$] (Stokes et al., 2011). Distortions out of the basic structure of $Pmmn$ symmetry have been modeled by a single harmonic for the displacement modulation functions. Initial structure refinements lead to small negative values for the component U_{11} of the anisotropic displacement parameters (ADPs) of the Ti and O atoms. Therefore, values of these parameters were constrained to $U_{11}[\mathrm{Ti}] = U_{11}[\mathrm{O}] = 0.0009$ Å^2. The final refinement resulted in an excellent fit, with reliability parameter $R_F = 0.026$ and partial agreement factors of $R_F^{main} = 0.025$ and $R_F^{sat} = 0.032$. Different sections t_0 of superspace imply different symmetries of the twofold, $\mathbf{a} \times 2\mathbf{b} \times \mathbf{c}$ superstructure. The section $t_0 = \frac{1}{8}$ gave the best fit to the data. The corresponding structure model with the **a**-unique monoclinic space group $P2_1/m$ is similar to the twofold superstructure of TiOCl in all aspects (see Fig. 6.7) (Shaz et al., 2005). In this monoclinic structure model all Ti–Ti chains along **b** are dimerized, evidencing a spin-Peierls-type distortion.

6.4 Discussion

$Sc_xTi_{1-x}OCl$ does not develop long-range magnetic order for doping levels of $x = 0.01$ and 0.03 (Clancy et al., 2008; 2010; Aczel et al., 2011). Clancy et al. (2008; 2010) have reported x-ray diffraction experiments with a pair of non-resolved superlattice peaks at $(2 \pm q_1,\ 1/2,\ 1)$ in q scans along $\mathbf{a}^*$. The increased width of the scattering maxima in those experiments indicated short correlation lengths of $\sim$12 Å. This incommensurate scattering has been reported to be present at all temperatures below $\sim$93 K, thus indicating absence of long-range order and absence of the lock-in transition to a possible spin-Peierls state.

Here, the temperature dependence of the specific heat provides evidence for the absence of phase transitions of a sample of doping level $x = 0.005$ (Fig. 6.1). Contrary to compounds with higher doping levels reported elsewhere, a resolved pair of incommensurate superlattice peaks is observed below $T = 90$ K with a temperature-dependent incommensurability (Fig. 6.4), which is similar to that of TiOCl (Schönleber et al., 2006; Krimmel et al., 2006). However, the incommensurate propagation vector vanishes at a temperature of $T_{c1} = 61.5\,(3)$ K (Fig. 6.5),

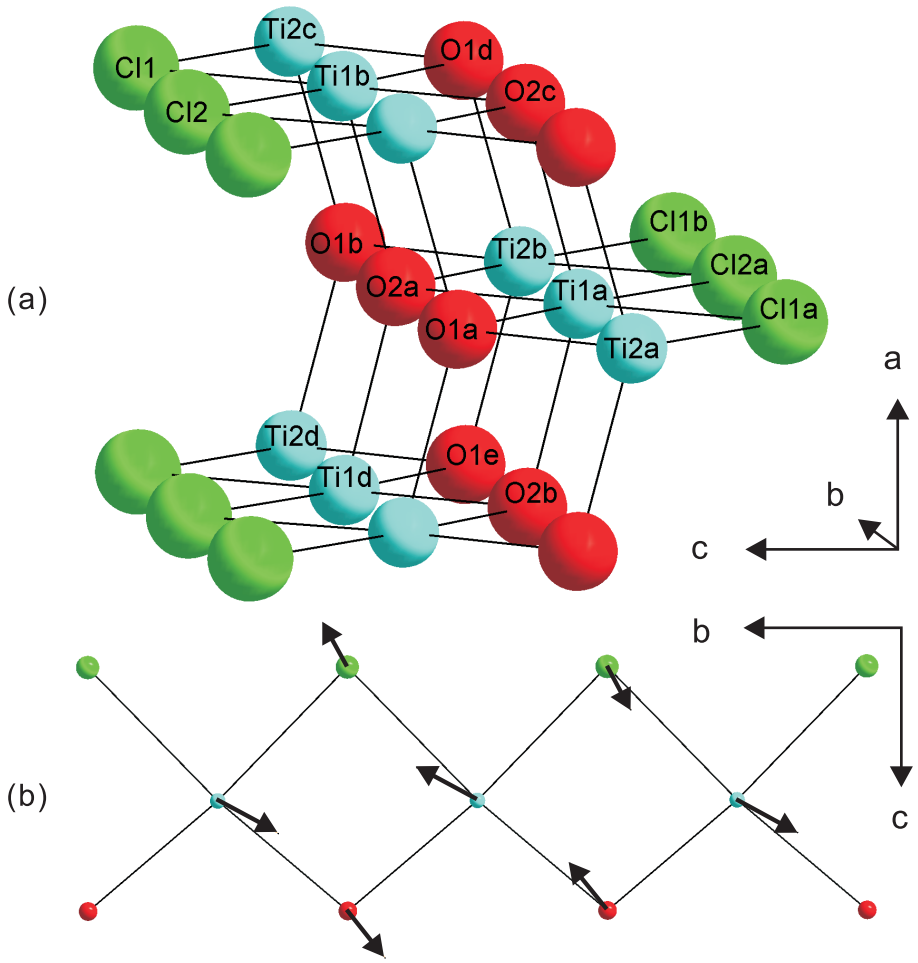

Figure 6.7: (a) Crystal structure of $Sc_xTi_{1-x}OCl$, and (b) modulation of one ribbon along **b**. Arrows indicate displacements out of the basic structure with magnitudes 20 × their true values.

about 10% lower than the transition temperature of TiOCl (67 K). This observation confirms the successful substitution of Ti by Sc. Replacement of Ti by non-magnetic Sc atoms suppresses the transition, a finding which is in general agreement with observations on other low-dimensional electronic crystals. At the same time it shows that an incommensurate–to–commensurate transition persists for the $x = 0.005$ compound, even though the thermal properties display only a broad, smeared out excess heat capacity in this temperature regime.

The widths of the superlattice reflections in the q scans is found to be considerably larger than that observed for similar scans on TiOCl (compare Fig. 6.4 to

Fig. 2 of Ref. Schönleber et al. (2006) and Fig. 2 of Ref. Krimmel et al. (2006)). ω Scans centered at the positions of selected commensurate superlattice reflections show them to be substantially broader than the main reflections (Fig. 6.6). These results strongly suggest the absence of long-range order in both the incommensurate and spin-Peierls-like phases, although correlation lengths are considerably longer than of the samples reported in Refs. Clancy et al. (2008; 2010).

The major difference to previous experiments on the system $Sc_xTi_{1-x}OCl$ is that we do detect the spin-Peierls dimerized state at low temperatures. The present x-ray diffraction experiments can only be reconciled with the absence of anomalies in the heat capacity, if we assume that thermodynamic phase transitions are suppressed by structural fluctuations, most likely of static nature. However, the correlation lengths of the fluctuations are found to be much larger than previously concluded from investigations on higher-doped samples. The refinement against the integrated intensities of the reflection maxima collected at $T = 8$ K resulted in a structure model largely equal to the dimerized structure of the spin-Peierls state of TiOCl. Within the present interpretation, the structure refinements imply that the fluctuating phase indeed is the spin-Peierls state known from TiOCl, albeit without long-range order. The interpretation as a phase without long-range order is supported by the orthorhombic lattice of $Sc_xTi_{1-x}OCl$ ($x = 0.005$) at all temperatures, despite the monoclinic symmetry of the fluctuating spin-Peierls distortions.

q Scans along $\mathbf{a}^*$ have indicated an incommensurate–to–commensurate transformation on cooling through $T_{c1} = 61.5$ K (Figs. 6.4 and 6.5). ω Scans on selected commensurate superlattice positions then have shown that correlation lengths of the fluctuations are relatively short just below T_{c1}, and increase until they reach their maximum value at $T = 50$ K and remain approximately constant below this temperature (Fig. 6.6). Instead of a sharp critical transition temperature between two thermodynamic phases, a novel aspect of the observed behavior is the gradual diminishment of the correlation length of the spin-Peierls-like fluctuations over a range of temperatures of ~ 10 K, until they are replaced by a state with incommensurate fluctuations above T_{c1}.

The absence of long-range order in both low-temperature regimes can be attributed to the presence of a small amount of non-magnetic Sc^{3+} ions replacing the

Ti^{3+} ions. Each non-magnetic site locally disrupts the magnetic order or spin-Peierls order. Since they represent point defects, long-range order should not necessarily be destroyed, if the level of doping is sufficiently small. Instead, doping would lead to a lowering of the transition temperatures. This behavior has been observed in the spin-Peierls compound $CuGeO_3$ and in 1D electronic materials exhibiting a CDW transtions, whereby the state of long-range order persists up to a few percent of doping (Gruner, 1994; Hase et al., 1993). The loss of long-range order in $Sc_xTi_{1-x}OCl$ at a doping level of $x = 0.5\%$ appears to be atypical. We have not been able to find an entirely satisfactory explanation for the singular behavior of $Sc_xTi_{1-x}OCl$. Although at present we were not able to determine the character of the spatial correlation functions, we notice that a state without true long-range order but with long correlation lengths is reminiscent of a Kosterlitz–Thouless phase with quasi-long-range order (Nishimori and Ortiz, 2011).

6.5 Conclusions

$Sc_xTi_{1-x}OCl$ with $x = 0.005$ on cooling transforms into an incommensurate phase below ~ 90 K and then into a commensurate phase below $T_{c1} = 61.5\,(3)$ K. The shift of the spin-Peierls-like transition toward temperatures lower than observed for TiOCl is in line with the effects of doping on other low-dimensional electronic crystals. However, both phases lack true long-range order. Instead, they should be considered as crystalline phases of orthorhombic TiOCl-type structures supporting incommensurate and commensurate fluctuations of particularly large correlation lengths. Temperature-dependent x-ray diffraction has shown that the commensurate fluctuations are those of a local spin-Peierls structure with monoclinic symmetry, despite the overall orthorhombic lattice symmetry.

The loss of long-range order upon Sc doping of TiOCl occurs at much lower doping levels than the destruction of long-range magnetic or CDW order in other 1D electronic crystals. Although we do not have a completely satisfactory explanation for this difference, we do like to mention the possibility that doping might be responsible for an increased 2D character of the magnetic system. The observed fluctuating states with long correlation lengths then are reminiscent of Kosterlitz–

Thouless phases in 2D systems (Nishimori and Ortiz, 2011), *i.e* existing on the TiOCl layers building the structure.

A novel feature is the transformation of one fluctuating regime to another. In agreement with the absence of long-range order, the transformation is not a phase transition occurring at a definite temperature, but it proceeds gradually over a temperature range of at least 10 K wide.

Acknowledgments

Single crystals of $Sc_xTi_{1-x}OCl$ ($x = 0.005$) have been grown by Alfred Suttner at the Laboratory of Crystallography in Bayreuth. We gratefully acknowledge Martin Tolkiehn for technical support with the experiments with synchrotron radiation at beamline D3 of Hasylab (DESY, Hamburg). We thank G. Siegle for assistance with the specific-heat measurements. Financial support has been obtained from the German Science Foundation (DFG). The work of JZ has been made possible through a CSC scholarship from the China Scholarship Council.

Chapter 7

Enlargement of incommensurate phase in TiOCl by intercalating Na

7.1 Introduction

The physical properties of materials are closely related to their structures. In contrast to conventional superconductors, the unconventional superconductors provide much higher transition temperatures (high-T_c), resulting in great interest in this field. Most of the unconventional superconductors possess layered two-dimensional structures (Korshunov and Eremin, 2008; Mizuguchi et al., 2012). The electronic properties of crystals with a layered structure can be modified by intercalation, resulting in the donation of electrons or holes to the valence bands, possibly inducing insulator-metal transitions or superconducting transitions (Lévy, 1979; Dresselhaus and Dresselhaus, 1994). α-TiNCl crystallizes in the layered FeOCl-structure type (Yamanaka et al., 2009). Pyridine and alkali metals can be intercalated in α-TiNCl. These compounds have been described as superconductors (Yamanaka et al., 1996; 2009). The transition-metal oxychloride TiOCl, a Mott insulator at room temperature, has a structure as similar as α-TiNCl (Fig. 7.1). Upon cooling, TiOCl undergoes two phase transitions. A second-order phase transition into an incommen-

surate phase proceeds at $T_{c2} = 90$ K (Shaz et al., 2005). Furthermore, a first order phase transition towards a commensurate spin-Peierls phase occurs at $T_{c1} = 67$ K (Seidel et al., 2003; Shaz et al., 2005; Schönleber et al., 2006). Both low-temperature phases are characterized by monoclinic distortions of the lattice.

TiOCl crystallizes in the FeOCl structure type with space group $Pmmn$. Ti–O double layers and two layers of Cl atoms stack along the crystallographic direction **c** alternately (Fig. 7.1). The adjacent layers of Cl atoms are connected to each

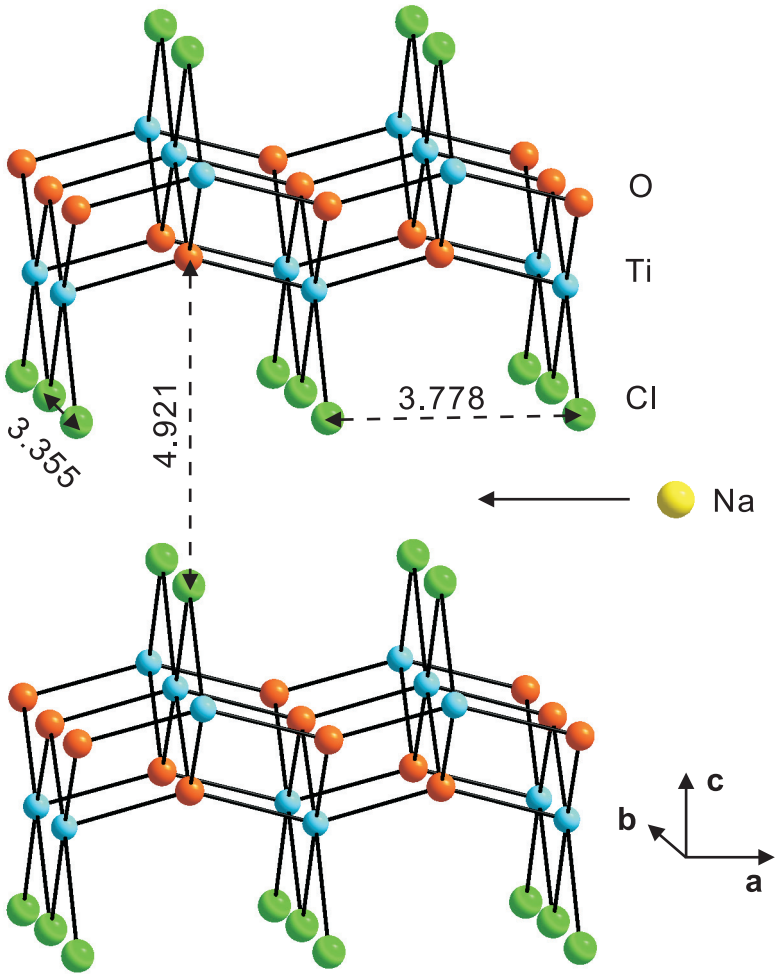

Figure 7.1: Crystal structure of TiOCl at room temperature and the schematic diagram shows where Na atoms go. The distances between atoms are calculated in terms of the structure model of TiOCl at room temperature (Shaz et al., 2005). The unit of the distances marked is Å.

other via van der Waals interactions. Therefore it appears feasible to intercalate atoms between these layers. Theoretical studies based on density functional theory (DFT) have been performed to explore intercalation in TiOCl and TiOBr. A study with *ab initio* local-density approximation combined with multi-orbital dynamical mean field theory (LDA+DMFT) for TiOCl reveals a possible first-order Mott-Hubbard transition to a correlated metallic state (Craco et al., 2006). Within the Parrinello-Rahman scheme, *ab initio* molecular dynamics studies with the Car-Parrinello projector-augmented wave (CP-PAW) method were performed in order to study the Na intercalated TiOCl (Zhang et al., 2010). The intercalation of Na in TiOCl strongly modifies the crystal field splitting of Ti $3d$ states and causes a coexistence of stabilized Ti^{3+} and Ti^{2+} ions (Zhang et al., 2010). Since the spin-Peierls state in TiOCl is caused by dimerization of Ti^{3+} ions, the influence of electron doping on spin-Peierls phase should be large, but the compound remains insulating. Experimentally, the samples of Na and K intercalated TiOCl and TiOBr were prepared by Kuntscher et al. (2010), following the procedure of electron doping in $YBa_2Cu_3O_{7-\delta}$ (Hossain et al., 2008). The intercalation leads to drastic changes in the electronic properties of TiOCl and TiOBr, but the Coulomb gap remains (Kuntscher et al., 2010).

Studies of doping Sc atoms into TiOCl have demonstrated different behaviors in dependence on the concentration of dopant. Long-range magnetic order in $Sc_xTi_{1-x}OCl$ ($x = 0.01$ and 0.03) were not observed (Clancy et al., 2008; 2010; Aczel et al., 2011). The spin-Peierls phase was suppressed and incommensurate phase was present at all temperature below about 93 K. At the doping level of $x = 0.005$, $Sc_xTi_{1-x}OCl$ transformed from an incommensurate phase into a commensurate phase below $T_{c1} = 61.5(3)$ K. The phase transition was defined as a spin-Peierls-like transition, the temperature of which is about 10% lower than that of undoped TiOCl (67 K) (Chapter 6).

Here we present the experimental studies of Na intercalated TiOCl. Synchrotron radiation was employed to investigate Na_xTiOCl ($x = 0.01$) single crystals. It is found that the introduction of Na into TiOCl enlarges the temperature range of the incommensurate phase. The temperature T_{c1} of phase transition from incommensurate to commensurate phase is 64.86(2) K, about 2 K lower than that of undoped

TiOCl. The role of Na intercalation is discussed.

7.2 Experimental and results

Single crystals have been grown by chemical-vapor transport (Schäfer et al., 1958; Shaz et al., 2005). A stoichiometric mixture of NaN_3, $TiCl_3$, and TiO_2 was put in evacuated quartz-glass ampoules as the starting materials. Crystals of dimensions of approximately $0.2 \times 0.1 \times 0.005$ mm^3 were selected for pre-testing the quality. Crystals with a FWHM of the peaks in the ω scans that was smaller than 0.1° were kept for the temperature-dependent experiments.

A single crystal of dimensions of $0.18 \times 0.05 \times 0.005$ mm^3 was glued to a carbon fiber which was attached to a closed-cycle helium cryostat mounted on a Huber four-circle diffractometer at beamline D3 of Hasylab at the Deutsches Elektronen-Synchrotron (Hamburg, Germany). Single-crystal x-ray diffraction experiments were performed from room temperature down to 8 K, employing monochromatic x-rays of a wavelength of 0.5600 Å. A point detector were used in the expeirments.

The orthorhombic lattice parameters were determined at each selected temperature from the setting angles of 17 reflections. At $T = 8$ K they are $a = 3.820(12)$, $b = 3.383(8)$, $c = 8.089(18)$ Å. Possible lattice distortions can be determined from the splitting of reflections in the direction of the scattering angle 2θ, if the crystal is twinned. A splitting of (h k 0), (h 0 l), and (0 k l) would imply a deviation from 90° of the angle γ, β and α, respectively. In a first experiment, so-called ω-2θ maps have been measured for three reflections, (2 2 0), (2 0 -4), and (0 2 -5) at both 298 K and 8 K. As for the previous experiments on MOCl compounds, the detector slits were set to 6×0.02 mm^2, corresponding to an acceptance angle of 0.0031° in the direction of 2θ. ω Scans of 121 steps with step sizes of 0.002° were performed for a series of 81 2θ values. The interval of adjacent 2θ values was 0.002° (Angelkort et al., 2009).

Only single maximum was observed in each ω-2θ map of all three reflections at both 298 K and 8 K (Fig. 7.2). The 2θ dependence of the diffracted intensity is obtained by collecting all intensity measured at a single value of 2θ. The profiles of the diffracted intensity as a function of the scattering angle 2θ for all three reflections at both 298 K and 8 K reveal only single maxima (Fig. 7.3). These results suggest

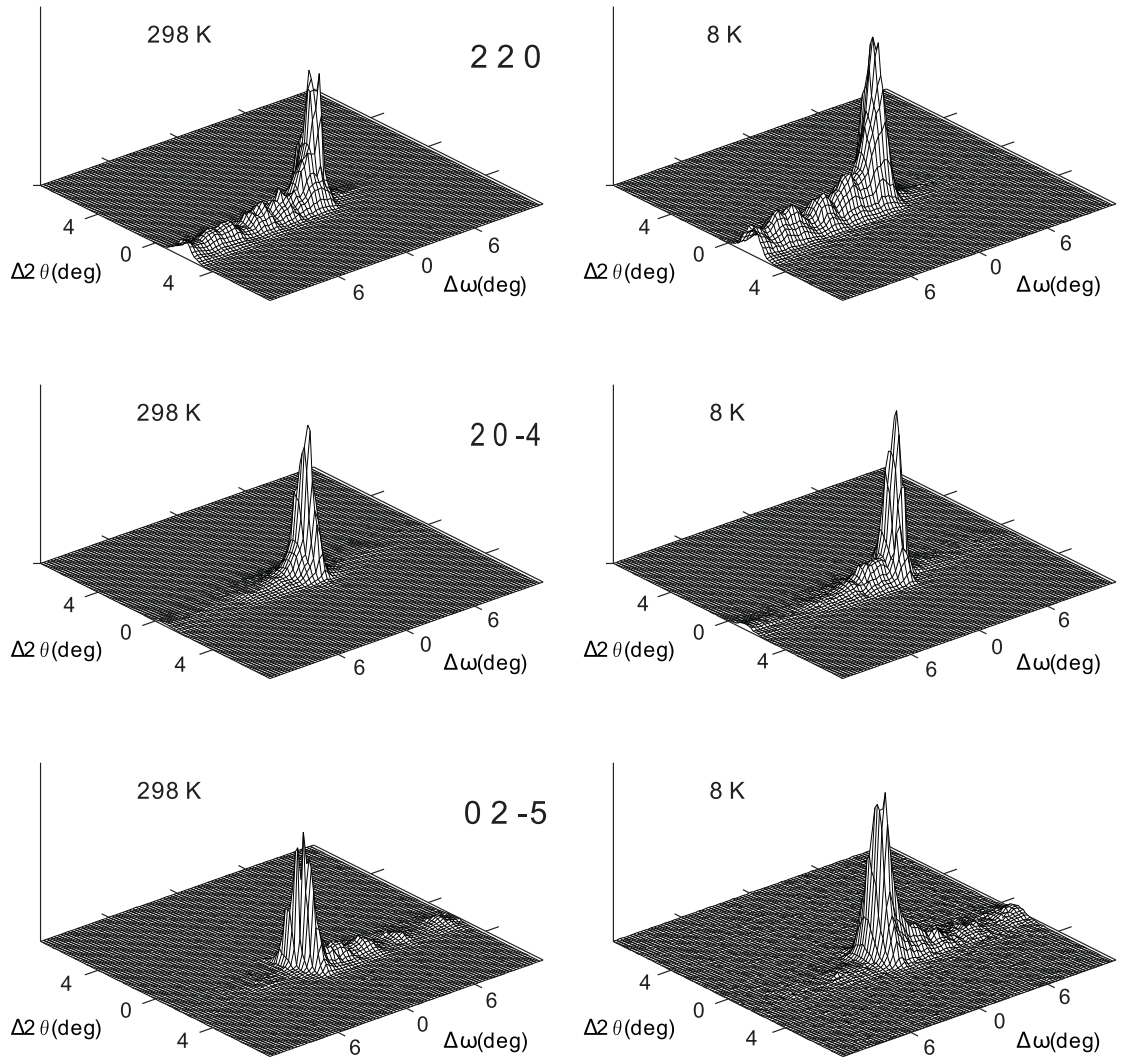

Figure 7.2: Diffracted intensity as a function of the scattering angle 2θ and the crystal orientation ω for reflections (2 2 0), (2 0 -4) and (0 2 -5) at selected temperatures. $\Delta 2\theta$ and $\Delta\omega$ indicate the deviation from the center of the scan in units of 0.01°.

that the angles of α, β and γ are 90°, indicating that the lattice is orthorhombic at both low and high temperatures.

A series of ω scans on superlattice reflections with **q** vector (0, 1/2, 0) were performed at 8 K to search for commensurate superlattice reflections as they exist in the low-temperature phase of TiOCl. A number of 41 peaks were found after scanning 53 positions of commensurate superlattice reflections. q Scans performed on reflections (2 3.5 -1), (0 2.5 -3), (0 1.5 -2), and (1 0.5 -9) show single and sharp

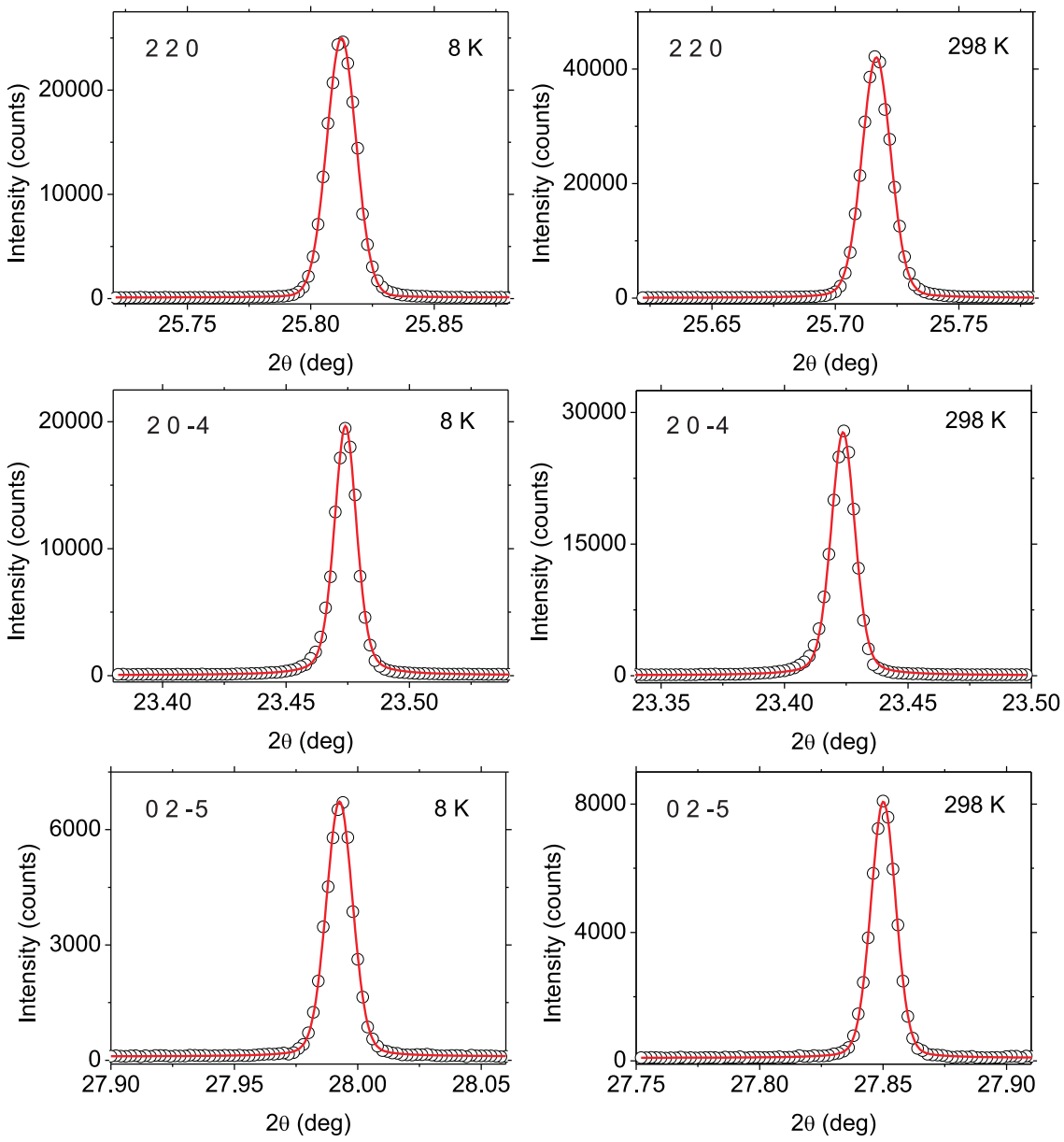

Figure 7.3: Diffracted intensity as a function of scattering angle 2θ for the reflection (2 2 0), (2 0 -4) and (0 2 -5) at 8 and 298 K. All peaks were fitted by pseudo-Voigt functions. The FWHM of these three reflections are 0.014°, 0.011° and 0.013° at 8K; 0.014°, 0.011° and 0.012° at 298K;

peaks which indicate the commensurate phase remains after intercalating 1% Na in TiOCl, similar to 0.5% Sc doped TiOCl in our previous study (Chapter 6).

In a next experiment q scans along $\mathbf{a}^*$ were performed on (2 3.5 $\pm$1) at selected

temperatures between 8 K and 95 K to search whether the incommensurate phase remains or would be suppressed by the intercalation of Na. Up to 65 K only one maximum can be observed. At higher temperatures split peaks are observed until 91 K. Above 92 K, no obvious maxima appear. For the reflection (2 3.5 1), the FWHM at 64.5 K is almost double of that at 64 K (Fig. 7.4). Three maxima

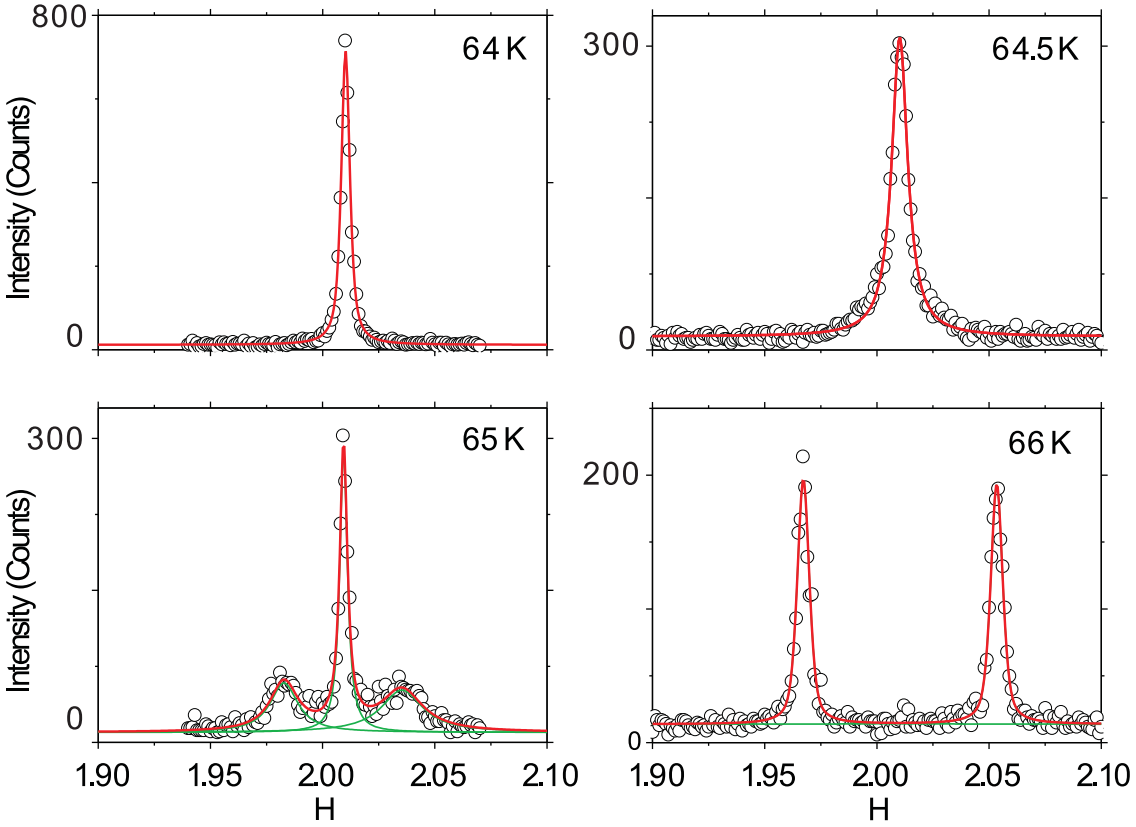

Figure 7.4: q Scans along $\mathbf{a}^*$ centered at (2 3.5 1) at selected temperatures as indicated. solid curves represent pseudo-Voigt functions fitted to the data.

can be observed at 65 K, indicating the beginning of the phase transition. For the reflections (2 3.5 -1), a single maxima persists until 65 K and peak splitting occurs at 66 K. These behaviors indicate that the phase transition from incommensurate phase to commensurate phase occurs at $T_{c1} = 65(1)$ K, which is slightly lower than the transition at 67 K of undoped TiOCl (Shaz et al., 2005; Schönleber et al., 2006). Above T_{c1}, the scans reveal two superlattice peaks at incommensurate positions described by $(h \pm q_1\ k + 0.5\ l)$. The magnitudes of the incommensurate component

q_1 is half of the separations within pairs of superlattice reflections that observed in each q scan. To determine the positions of superlattice reflections, pesudo-Voigt profile functions were fitted to the data by individual functions for each reflection. The temperature-dependent magnitude of the incommensurate component q_1 is well described by a critical power law

$$q_1 = q_1^0 \, (T - T_{c1})^{2\beta} \, . \tag{7.1}$$

An accurate estimate of the critical temperature $T_{c1} = 64.86(2)$ K is derived from the fit to the data up to 80 K (Fig. 7.5). The fit to all data up to 91 K results in a

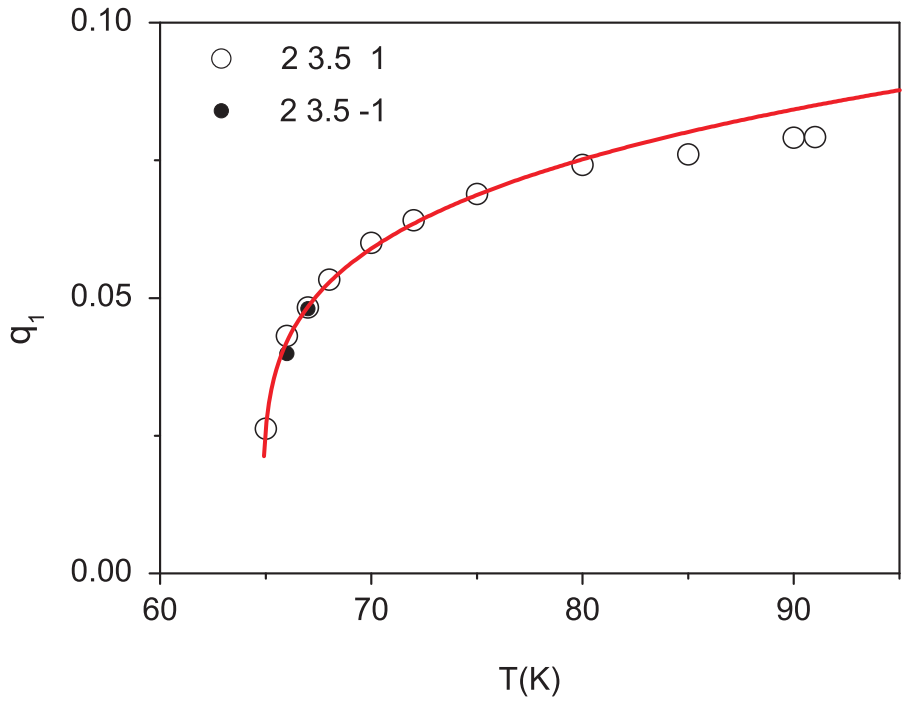

Figure 7.5: Temperature dependence of the incommensurate component q_1 of the modulation wave vector $\mathbf{q} = (q_1, 1/2, 0)$, as determined from q scans. The solid line represents a fit of Eq. 7.1 to the data, resulting in $q_1^0 = 0.0409\,(7)$, $T_{c1} = 64.86\,(2)$ K and $2\beta = 0.22\,(1)$.

T_{c1} of 64.91(3) K, which is less accurate.

ω Scans were performed both at the commensurate position (2 3.5 1) between 63 and 65 K and at the incommensurate position (2-q_1 3.5 1) above 66 K for selected temperatures. Intensities of these commensurate and incommensurate superlattice

reflections were derived from Lorentz fits. The integrated intensities above T_{c1} are well described by a function

$$I(T) = I_0\sqrt{1 - T/T_{c2}}. \tag{7.2}$$

The fit to this function results in an estimate of $T_{c2} = 92.8(7)$ K for the temperature of transition to the normal phase (Fig. 7.6), higher than 90 K of undoped TiOCl (Schönleber et al., 2006).

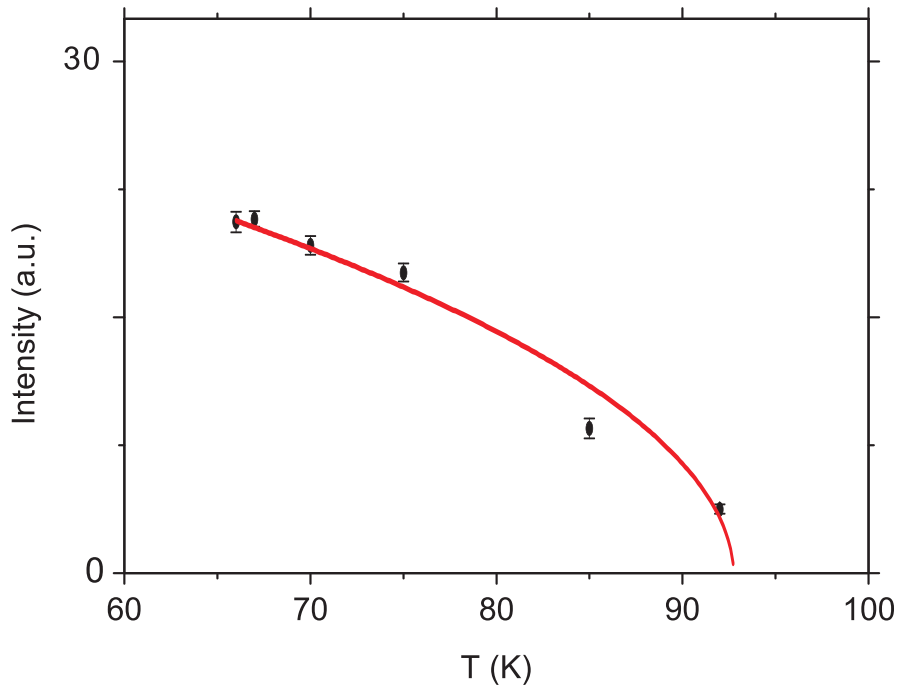

Figure 7.6: Temperature dependence of the intensities of the incommensurate superlattice reflections $(2 - q_1\ 3.5\ 1)$. Error bars are indicated. The line represents a fit with Eq. 7.2 with $T_{c2} = 92.8(7)$ K.

Between 63 K and 65 K the FWHM of commensurate superlattice reflections is constant at 0.068(2)°, while that of incommensurate superlattice reflections above 66 K gradually decreases from 0.084(3)° down to 0.033(3)° upon increasing temperature (Fig. 7.7).

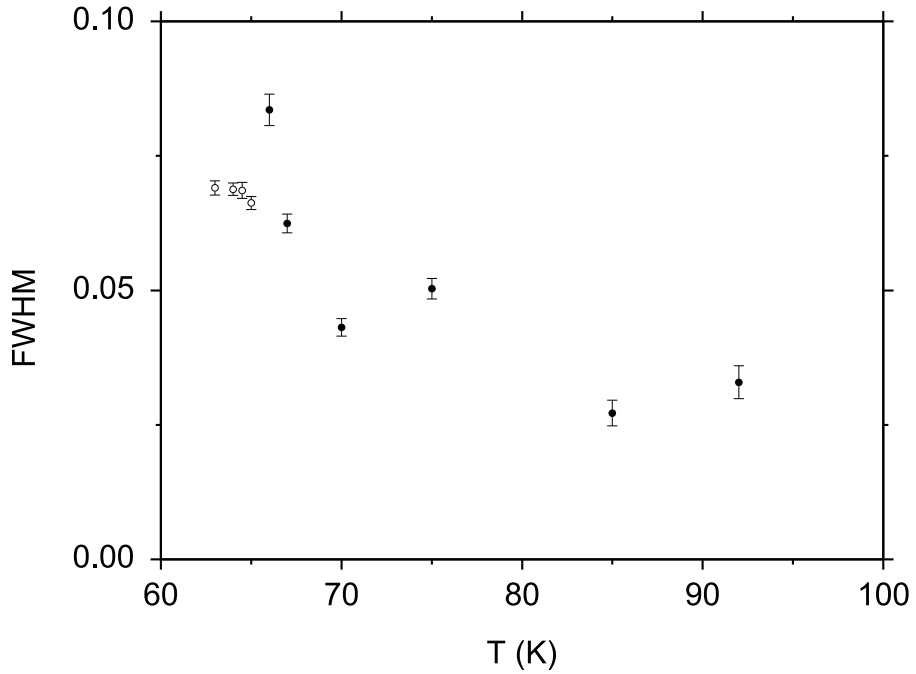

Figure 7.7: Temperature dependence of the full width at half maximum (FWHM) derived from fits of Lorentzians to the ω scans centered at the commensurate superlattice reflections (2 3.5 1) (open circles) and incommensurate superlattice reflections ($2 \pm q_1$ 3.5 l) (points). Error bars are indicated.

7.3 Discussion

In the room temperature structure of TiOCl, the distance between a Cl atom and the nearest O atom of the next TiOCl layer is 4.921 Å. The distance between two neighboring Cl atoms along lattice direction **a** is 3.778 Å, and along **b** is 3.355 Å (Fig. 7.1). The effective ionic radii of Na^+ and Ti^{3+} are 1.02 and 0.67 Å, respectively (Shannon, 1976). Thus comparing to substitute Na for Ti, it is easier to intercalate Na into the gap of neighboring layers. This intercalation model has also been employed to investigate the effect of Na intercalation within the framework of density functional theory (Zhang et al., 2010). Same to the $Sc_xTi_{1-x}OCl$ ($x = 0.005$), Na_xTiOCl ($x = 0.01$) possesses an orthorhombic lattice at 8 K, which was confirmed by the measurement of ω-2θ maps. This result is different from the monoclinic lattice in undoped TiOCl at 8 K. The incommensurate propagation vector is present below a temperature of $T_{c2} = 92.8(7)$ K until a temperature of $T_{c1} = 64.86(2)$ K. This

behavior is similar to spin-Peierls transition in undoped TiOCl but different from the spin-Peierls-like transformation in $Sc_xTi_{1-x}OCl$ ($x = 0.005$) (Chapter 6). This phenomenon may provide evidence of intercalation but not doping. The temperature of spin-Peierls phase transition is about 2 K lower than that of undoped TiOCl, while the temperature of phase transition into incommensurate is about 3 K higher than that of 90 K of undoped TiOCl (Shaz et al., 2005; Schönleber et al., 2006; Schönleber et al., 2008). The temperature range of incommensurate phase is enlarged under the intercalation of Na, which indicates the successful intercalation.

The formation of spin-Peierls phase results from the dimerization of Ti^{3+} ions along the crystallographic direction **b**, in which procedure the $3d$ electron of Ti^{3+} plays an important role. The lack of $3d$ electron of a dopant of Sc^{3+} modifies the spin-Peierls state (Clancy et al., 2008; 2010; Aczel et al., 2011 and Chapter 6). The Na atoms offers their outer s electron to the Ti–O double layers, inducing a coexistence of Ti^{3+} and Ti^{2+} (Zhang et al., 2010). This may influence the formation of dimerization of Ti–Ti pairs. With the increasing concentration of Na, the Ti–Ti pairs may vanish completely due to the increasing amount of Ti^{2+} . The similar spin-Peierls behavior of Na_xTiOCl ($x = 0.01$) and undoped TiOCl suggests that Na_xTiOCl ($x = 0.01$) remains an insulator, in line with theoretical studies (Craco et al., 2006; Zhang et al., 2010).

Due to the limitation of beamtime, ω scans were not performed on the main reflections. Here a similar method as that used in Fig. 7.3 was employed to obtain the profiles of ω scans by reprocessing the data of ω-2θ maps: the ω dependence of the diffracted intensity is obtained by collecting all intensity measured at a single value of ω. The resulting reflection profiles show very sharp peaks but with shoulders. (supplementary Fig. C.1). As the intensities of the shoulders are much lower than those of the single peaks, one may calculate the FWHM without counting the contribution of the shoulders. Therefore, the FWHM of the three main reflections is between $0.009(1)^\circ$ and $0.014(1)^\circ$ at both 298 and 8 K (supplementary Table C.2). The FWHM is even smaller than that of main reflections in $Sc_xTi_{1-x}OCl$ ($x = 0.005$) (Chapter 6) and TiOCl (Schönleber et al., 2008). The higher value at 8 K than at 298 K can be explained by anisotropic stress due to different thermal expansion of the crystal and the glue that was used to fix the crystal (Chapter 6).

Below T_{c1}, the FWHM of the commensurate superlattice reflection (2 3.5 1) in the ω scans is a constant value of 0.068(2)° (Fig. 7.7). The FWHM is at least 5 times lager than that of the main reflections, indicating the large width relate not with the mosaic spread of the crystal but with the atomic modulations. In addition, it is about 3 times larger than 0.02° of (-2 -3.5 -1) in undoped TiOCl (Schönleber et al., 2006). These results may imply the absence of long-range order in the commensurate phase. Above T_{c1}, the FWHM of incommensurate superlattice reflections (Fig. 7.7) and that of undoped TiOCl (Schönleber et al., 2006, Fig. 2b) is comparable, which suggests the existence of the long-range order in the incommensurate phase.

The FWHM of the commensurate superlattice reflections (2 3.5 1) and (2 3.5 -1) in q scans at 64K (below T_{c1}) are determined to be 0.0045(1)° and 0.0066(2)°, respectively. These values are even smaller than 0.025(3)° of (-2 -1.5 -1) at 66 K (Schönleber et al., 2006), as well as smaller than 0.022(4)° of (0 1.5 0) at 66.84 K (Krimmel et al., 2006) in undoped TiOCl. Same behavior is also observed for their incommensurate superlattice reflections. These results would indicate that the long-range order exist in both the commensurate and incommensurate phases.

Depending on the present results, a definite conclusion of the existence of long-range order in the low-temperature phases of Na_xTiOCl ($x = 0.01$) cannot be made. Other techniques need to be employed to uncover the whole behavior of Na_xTiOCl ($x = 0.01$), and more x-ray experiments of different concentrations of Na intercalated TiOCl are required to explore the mechanism of interaction between Na and TiOCl.

7.4 Conlusion

Na_xTiOCl with $x = 0.01$ has been studied by temperature-dependent x-ray diffraction. Upon cooling, Na_xTiOCl transforms into an incommensurate phase at T_{c2} = 92.8(7) K and subsequently into a spin-Peierls phase at T_{c1} = 64.86(2) K. The intercalation of Na atoms enlarges the temperature range of the incommensurate phase of TiOCl. The limited experimental information prevents a definition about the existence or not of long-range order in the low-temperature phases.

Acknowledgments

Single crystals of Na_xTiOCl ($x = 0.01$) have been grown by Alfred Suttner at the Laboratory of Crystallography in Bayreuth. We gratefully acknowledge Martin Tolkiehn for technical support with the experiments with synchrotron radiation at beamline D3 of Hasylab (DESY, Hamburg). Financial support has been obtained from the German Science Foundation (DFG). The work of JZ has been made possible through a CSC scholarship from the China Scholarship Council.

Chapter 8

Nuclear and magnetic superstructure of CrOCl at 8 K

8.1 Introduction

Transition-metal oxyhalides MOX (M = Ti, V, Cr, and Fe; X = Cl, Br, I) have earned considerable attention over the past few decades, due to their complex magnetic properties. The major difference of these isostructural compounds is the numbers of d electrons of the transition-metal atoms, which is considered as the origin of their diverse behavior. A precise structure refinement will be of benefit to the understanding of interactions between atoms in a crystal. The modulated crystal structures of TiOCl and VOCl of the low-temperature phases have been reported (Shaz et al., 2005; Schönleber et al., 2009), but the modulated structure of CrOCl in the low-temperature phase is still unknown. Upon cooling, TiOCl undergoes two phase transitions at 90 K and 67 K (Shaz et al., 2005), while VOCl and FeOCl undergo only one phase transition at 80.3 K and 81 K, respectively (Wiedenmann et al., 1983; Zhang et al., 2012). For CrOCl, a clear phase transition was established at 13.5 K, and a second transition was discovered at about 27.2 K by the temperature dependence experiment of the specific heat (Angelkort et al., 2009).

CrOCl is isostructural to FeOCl, with space group $Pmmn$ at room temperature (Schäfer and Wartenpfuhl, 1961). The crystal structure consists of slabs CrOCl

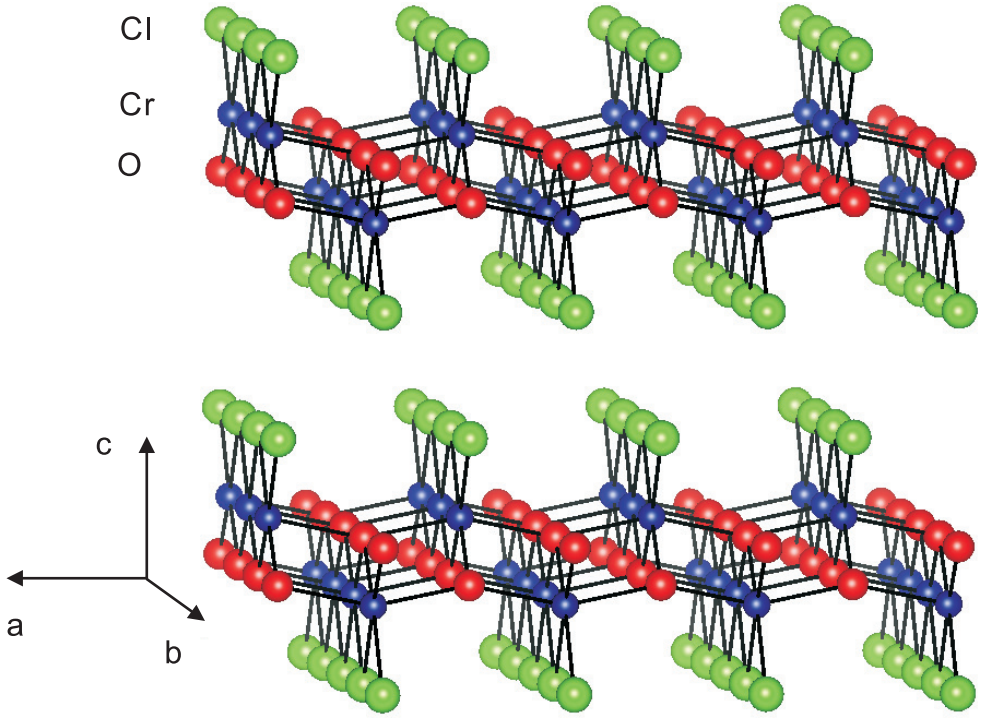

Figure 8.1: Crystal structure of CrOCl.

as displayed in Fig. 8.1. Cr–O double layers are bounded by layers of Cl atoms. Successive slabs are interconnected by weak van der Waals interactions. Along **b**, Cr atoms align in a chain. In VOCl, two d electrons of V^{3+} occupy $3d_{x^2-y^2}$, $3d_{xz}$ orbitals, resulting in a **c**-axis unique monoclinic lattice distortion of the state with antiferromagnetic order (Komarek et al., 2009; Schönleber et al., 2009). The three d electrons of Cr^{3+} in CrOCl are supposed to occupy the $3d_{x^2-y^2}$, $3d_{xz}$ and $3d_{yz}$ orbitals, corresponding to an **a**-axis unique monoclinic lattice distortion of the AFM state at low temperatures (Angelkort et al., 2009). The mechanism of orbital occupation in FeOCl is still not very clear, but a **c**-axis unique monoclinic lattice distortion was observed (Chapter 5).

In the present study, we report the modulated structure of CrOCl at 8 K based on x-ray diffraction data obtained with synchrotron radiation. The symmetry of CrOCl is confirmed as **a**-axis unique monoclinic at 8 K (Angelkort et al., 2009), with spacegroup $P2_1/m$ and lattice parameter $a = 3.8539(9)$, $b = 3.1693(9)$, $c = 7.6569(22)$ Å and $\alpha = 90.06(2)°$.

8.2 Experimental

8.2.1 Preparation of CrOCl

Single crystals of CrOCl were grown by chemical vapour transport in evacuated quartz-glass ampoules, starting with stoichimometric amounts of $CrCl_3$ and Cr_2O_3 and employing $HgCl_2$ as transport agent (Schäfer and Wartenpfuhl, 1961; Nocker and Gruehn, 1993; Angelkort et al., 2009). The crystal shape is plate-like with very small thickness along the **c** axis. The typical size of an individual crystal is up to 3 mm along the **a** and **b** axes. Crystals were mounted on carbon fibers with aid of two-component glue. Dozens of crystal was tested on a laboratory diffractometer Mach3, with Mo K_α radiation. A crystal with narrow widths of the Bragg reflections in ω scans was selected for the low-temperature experiment.

8.2.2 X-ray diffraction experiments

A crystal of dimensions $0.32 \times 0.06 \times 0.004$ mm^3 was selected for x-ray diffraction experiments at Hasylab, employing radiation of a wavelength of 0.5600 Å. Diffraction at room temperature confirmed the FeOCl structure type with space group $Pmmn$. In order to meet the low temperature requirements, a closed-cycle helium cryostat was employed. Two beryllium caps were used to isolate air at low temperature.

With the aid of the four-circle diffractometer at beamline D3, integrated intensities of Bragg reflections up to a resolution of $\sin(\theta)/\lambda = 0.89$ Å^{-1} were measured with a point detector at 8 K. A modulation wave vector $\mathbf{q} = (0,\ 1/2,\ 0)$ was employed to determine the position of satellite reflections. In the data collection, ω scans were performed with 101 steps and a step size of 0.005 °. The exposure time for each step was 1 second for main reflections, while it was 4 seconds for the weaker satellite reflections. However, due to the limitation of beryllium caps and the body of cryostat, not all octants can be reached. Finally, a number of 806 main reflections and 929 satellite reflections were collected. Most of the reflections at 8 K were split into two peaks in the ω scans, consistent with the previous results (Angelkort et al., 2009). ω Scans were performed subsequently on several selected reflections at 298 K, 8 K, and 17 K (Fig 8.2). Peak splitting only occurs at 8 K, indicating that the

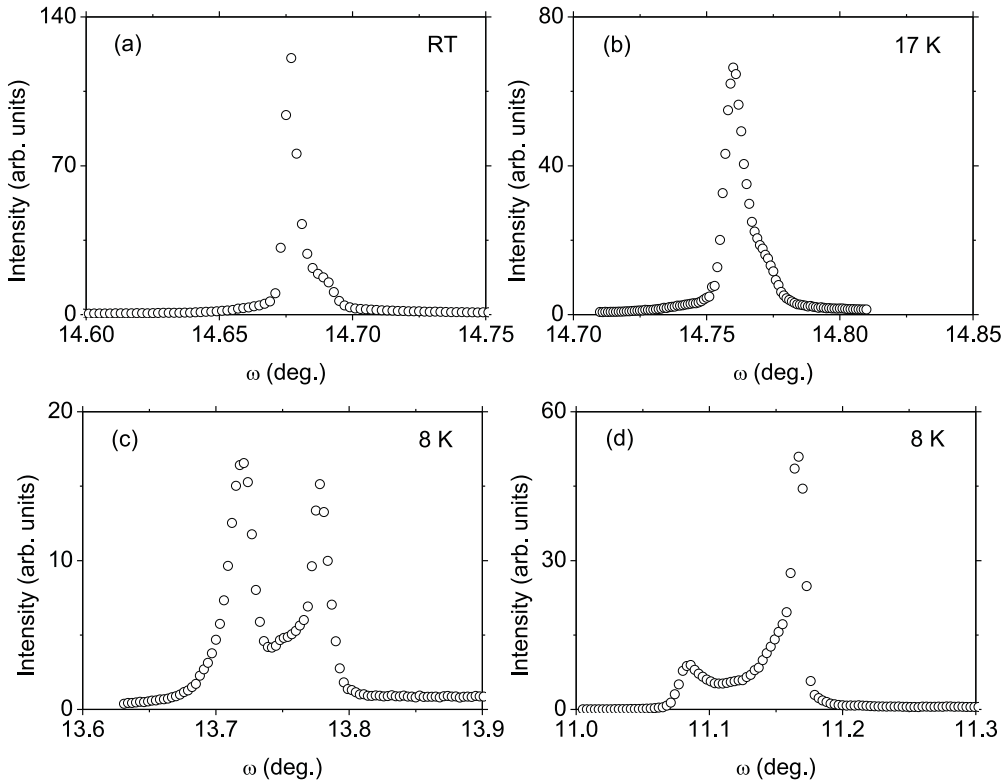

Figure 8.2: Diffracted intensity as a function of the crystal orientation ω for reflections (0 -2 5) (a-c) and (2 0 4) (d), at temperatures as indicated.

lattice distortion should accompany the magnetic phase transition at 13.5 K.

Diffraction data were processed by the computer program REDUCE. Combined intensities were determined for the two peaks in each ω scan. The integrated intensities were corrected to eliminate the effects of varying intensity of the incident beam. By checking the profiles of ω scans, 19 reflections were removed due to a high shoulder of the peak, which do not provide the real intensities (Supplementary Table D.1). An absorption correction was applied using the computer program JANA2006, based on a crystal shape determined by inspection under an optical microscope. After absorption correction, R_{int} was improved from 0.0574 to 0.0563.

8.3 Structure refinement and discussion

JANA2006 was used for structure refinements against the integrated intensities, following the procedures described by Shaz et al. (2005). Integrated intensities of both main Bragg reflections and satellite Bragg reflections were imported into JANA2006. Four integers $hklm$ were employed to index reflections, where $m = 0$ indicates main reflections and $m = 1$ means satellite reflections. The orientation matrix used in the experiments gave a value of 89.94° for the angle α. In order to use a monoclinic setting with $\alpha = 90.06°$, a coordinate transformation was applied as defined by the change of indices to (-h k -l m). Both main and satellite reflections were indexed with respect to the orthorhombic unit cell at room temperature and the modulation wave vector $\mathbf{q}$ = (0, 1/2, 0).

First of all, the basic structure was refined against the main reflections. The basic structure model was taken from Christensen et al. (1975). Considering the monoclinic distortion of CrOCl at 8 K, the orthorhombic superspace group $Pmmn(0\sigma_2 0)000$ ($\sigma_2 = 0.5$), as well as a supercell $a \times 2b \times c$ with monoclinic symmetry and space group $P2_1/m$ (**a**-axis unique) were employed for the structure refinement. In all superspace refinements, $t_0 = 1/8$ was applied. The intensities of reflections (1 0 0), (3 0 0) and (5 0 0) were not observed, in line with the systematic extinctions. Finally, 1127 reflections were recognized as observed reflections with $I > 3\sigma(I)$.

The modulated structure was refined against all data. At 4.2K, CrOCl was reported to possess a four-fold antiferromagnetic structure with magnetic supercell $a \times 4b \times c$ (Christensen et al., 1975). Thus the magnetic modulation wave vector $\mathbf{q}_m$ is (0, 1/4, 0), half of the lattice modulation wave vector $\mathbf{q}$, in accordance with the theory expressed in section 2.4. In order to combine the nuclear structure refinement and magnetic structure refinement, a uniform modulation wave vector should be employed. Here, a lattice modulation vector of (0, 1/4, 0) was used. Thus the satellite reflections will be treated as the second-order satellite reflections, and the commensurate modulated structure was described by a single harmonic modulation function of second-order for each Cr, O and Cl,

$$\mathbf{u}(\bar{x}_4) = [u_x^2 \sin(4\pi\bar{x}_4), u_y^2 \sin(4\pi\bar{x}_4), u_z^2 \sin(4\pi\bar{x}_4)], \tag{8.1}$$

Where $\bar{x}_4 = t + \mathbf{q} \cdot \bar{\mathbf{x}}$ and t is the phase of the modulation.

Table 8.1: Experimental and crystallographic data of modulated nuclear structure of CrOCl at 8 K.

Chemical formula	CrOCl
M_r	99.3
Crystal system	Orthorhombic
Superspace group	$Pmmn(0\sigma_2 0)$s0s
Wavevectors	$\mathbf{q} = 0.25\mathbf{b}^*$
t_0	1/8
a (Å)	3.8539(9)
b (Å)	3.1693(9)
c (Å)	7.6569(22)
α	90.06(2)
V (Å^3)	93.5
Z	2
Supercell	a 4b c
Supercell space group	$P2_1/c11$
Crystal shape (mm^3)	0.32 × 0.06 × 0.004 mm^3
Diffractometer	Huber four-circle diffractometer
$[\sin(\theta)/\lambda]_{max}$ (Å^{-1})	0.89
Absorption correction	Gaussian (JANA2006)
T_{min} / T_{max}	0.7293 / 0.9848
Criterion of observability	$I > 3\sigma(I)$
R_{int}(obs./all)	0.0491/0.0491
No. of measured reflections	1465
No. of unique reflections (obs./all)	821/1043
No. of main reflections (obs./all)	487/515
No. of 2^{nd} order satellite reflections (obs./all)	334/528
Average redundancy	1.402
Refined parameters	21
Extinction parameters	0.61(15)
R_F (obs.) all/main/satellite reflections	0.0339/0.0300/0.0680
$wR_F{}^2$ (obs.) all/main/satellite reflections	0.0517/0.0507/0.0696
GoF (obs.)	3.63
Twinning axis, angle (°)	(0 0 1), 180
Relative twin volumes	0.5396(92)/0.4604(92)

The refinement was successful within superspace group $Pmmn(0\sigma_2 0)s0s$. The components of the first-order harmonic modulation parameters were set to 0. The

refinement converged at a low observed $R_F = 0.039$, and a detailed refinement report is present in Tables 8.1 and 8.2

Table 8.2: Relative atomic coordinates, ADPs (Å^2) and Fourier amplitudes (Å) of the modulation function [Eq. (8.1)] for each of the three crystallographically independent atoms of the basic structure.

Superspace group	$Pmmn(0\sigma_2 0)000$ basic structure	$Pmmn(0\sigma_2 0)s0s$ $\mathbf{q}$ = (0, 1/4, 0)
y[Cr]	0.5	0.5
z[Cr]	0.1082(0)	0.1082(0)
U_{11}[Cr]	0.0002(2)	0.0002(2)
U_{22}[Cr]	0.0007(2)	0.0007(1)
U_{33}[Cr]	0.0022(2)	0.0021(2)
U_{iso}[Cr]	0.0010(1)	0.0010(1)
u_y^2[Cr]·b	–	0.0055(2)
u_z^2[Cr]·c	–	-0.0085(1)
y[O]	0	0
z[O]	0.9442(2)	0.9443(1)
U_{11}[O]	0.0009(5)	0.0008(3)
U_{22}[O]	0.0031(5)	0.0031(3)
U_{33}[O]	0.0031(5)	0.0037(4)
U_{iso}[O]	0.0026(3)	0.0026(2)
u_y^2[O]·b	–	0.0080(8)
u_z^2[O]·c	–	0.0081(7)
y[Cl]	0	0
z[Cl]	0.3278(1)	0.3278(0)
U_{11}[Cl]	0.0034(2)	0.0034(2)
U_{22}[Cl]	0.0020(2)	0.0020(2)
U_{33}[Cl]	0.0025(2)	0.0025(2)
U_{iso}[Cl]	0.0027(1)	0.0026(1)
u_y^2[Cl]·b	–	-0.0055(3)
u_z^2[Cl]·c	–	-0.0028(2)

x[Cr], x[O], x[Cl] = 0

The amplitudes of the modulation wave are about one tenth of those of TiOCl (Shaz et al., 2005), implying that the modulation of atoms in CrOCl is much weaker than that in TiOCl. The modulated distances between Cr–Cr atoms in the Cr–Cr chains are shown in Table 8.3.

Magnetic structure refinement was performed against neutron powder diffrac-

Table 8.3: Selected geometric parameters of distances in the superstructure of CrOCl at 8 K (this work) and TiOCl at 10 K (Shaz et al., 2005). The atoms are labeled by the same method which was used to describe TiOCl by Shaz et al. (2005): Crystallographically independent atoms are indicated by numbers 1 and 2; Different but symmetry–equivalent atoms are indicated by an additional letter. Standard uncertainties are included.

Atoms (CrOCl)	Distance (Å)	Atoms (TiOCl)	Distance (Å)
Cr1a – Cr2a[a]	3.1771(2)	Ti1a – Ti2a[a]	3.429(1)
Cr1a – Cr2b[a]	3.1616(2)	Ti1a – Ti2b[a]	3.254(1)

[a]Distances within a single ribbon parallel to **b**.

tion data collected at 8 K by A. Schönleber. Several superspace groups were employed to fit the refinement of magnetic structure to check the best structure model. The best magnetic structure was refined with the magnetic superspace group $Pmmn.1'(0\sigma_2 0)s0ss$ (Petricek et al., 2010; Perez-Mato et al., 2012) and modulation wave vector (0, 1/4, 0). However, due to a technical limitation of JANA2006, it is not possible to refine the magnetic structure with orthorhombic superspace group and α angle slightly deviating from 90° at the same time. Here, the magnetic superspace group $P2_1/m.1'(0\sigma_2\sigma_3)0s$ was used, while additional symmetry restrictions on coordinates, displacive parameters of atoms and modulation parameters of magnetic moments were applied according to the symmetry of the orthorhombic magnetic superspace group $Pmmn.1'(0\sigma_2 0)s0ss$. Under the setting of this model, the magnetic modulation parameters $M_z^1[\mathrm{Cr}] = 3.84(19)$ and $M_y^1[\mathrm{Cr}] = 1.2(8)$ were obtained. A further refinement was performed with the value of $M_y^1[\mathrm{Cr}]$ fixed to 0. Within this setting, $M_z^1[\mathrm{Cr}] = 3.90(18)$ was obtained.

In a last refinement, the parameters of displacive modulation functions that were obtained via the refinement of modulated nuclear structure of CrOCl were applied to the magnetic structure (Table 8.4), resulting in 79 observed second-order satellite reflections. The changes of R_F are listed in Table 8.5. The influence of the displacive modulation on the magnetic structure is very small (Table 8.6). The ordered magnetic moment is parallel to **c** (Fig. 8.3), consistent with previous studies (Christensen et al., 1975; Angelkort et al., 2009). But the magnitude of magnetic moment is modulated, in contrast to a previous study (Christensen et al., 1975). In the **bc** plane, an individual Cr atom is surrounded by 2 O atoms and 2 Cl atoms.

Table 8.4: Experimental and crystallographic data of magnetic structure of CrOCl refined with atoms displacive modulation functions.

Chemical formula	CrOCl
M_r	99.3
Crystal system	Orthorhombic
Superspace group	$Pmmn1'(0\sigma_2 0)$s0ss
Temperature (K)	8
Wavevectors	$\mathbf{q} = 0.25\mathbf{b}^*$
a (Å)	3.8632(1)
b (Å)	3.1777(1)
c (Å)	7.6757(1)
α	90.07(0)
V (Å^3)	94.23
Z	2
Supercell	a 4b c
Supercell space group	$P2_1/c11$
Radiation type	Neutron
Wavelength (Å)	1.46271
No. of unique reflections (obs./all)	618/1049
No. of main reflections (obs./all)	237/262
No. of 1^{st} order satellites (obs./all)	302/525
No. of 2^{nd} order satellites (obs./all)	79/262
Refined parameters	14
R_F (obs.)	0.0482
R_F (obs.)(main)	0.0441
R_F (obs.)(1^{st} order satellite)	0.0771
R_F (obs.)(2^{nd} order satellite)	0.0743
$wR_F{}^2$ (obs.)	0.0655
$wR_F{}^2$ (obs.)(main)	0.0578
$wR_F{}^2$ (obs.)(1^{st} order satellite)	0.0720
$wR_F{}^2$ (obs.)(2^{nd} order satellite)	0.0669
$\mathrm{R}_{profile}$	0.0490
$\mathrm{wR}_{profile}$	0.0688

When the 2 O atoms move close to each other and the 2 Cl atoms move apart from each other, the magnitude of magnetic moment is larger (Cr3a in Fig. 8.3).

Table 8.5: The values of R_F and $wR_F{}^2$ for the observed reflections, without modulated nuclear structure and with modulated nuclear structure with fixed modulation parameters from Table 8.2.

	without modulation	with modulation
R_F (obs.)	0.0480	0.0482
R_F (obs.)(main reflections)	0.0441	0.0441
R_F (obs.)(1^{st} order satellite reflections)	0.0772	0.0771
R_F (obs.)(2^{nd} order satellite reflections)	–	0.0743
$wR_F{}^2$ (obs.)	0.0654	0.0655
$wR_F{}^2$ (obs.)(main reflections)	0.0579	0.0578
$wR_F{}^2$ (obs.)(1^{st} order satellite reflections)	0.0723	0.0720
$wR_F{}^2$ (obs.)(2^{nd} order satellite reflections)	–	0.0669
$\mathrm{R}_{profile}$	0.0490	0.0490
$\mathrm{wR}_{profile}$	0.0688	0.0688

Table 8.6: Relative atomic coordinates and ADPs (Å^2) for each of the three crystallographically independent atoms of the basic structure, before and after applying the Fourier amplitudes in Table 8.2.

	without modulation	with modulation
y[Cr]	0.5	0.5
z[Cr]	0.1077(11)	0.1077(11)
U_{11}[Cr]	0.0188(27)	0.0188(27)
U_{22}[Cr]	0.0113(24)	0.0112(24)
U_{33}[Cr]	0.0068(54)	0.0068(54)
U_{iso}[Cr]	0.0123(21)	0.0123(22)
M_z^1[Cr]	3.9020(1756)	3.9043(1756)
y[O]	0	0
z[O]	0.9438(9)	0.9438(9)
U_{11}[O]	0.0225(22)	0.0225(22)
U_{22}[O]	0.0178(17)	0.0178(17)
U_{33}[O]	0.0107(33)	0.0107(33)
U_{iso}[O]	0.0170(14)	0.0170(14)
y[Cl]	0	0
z[Cl]	0.3286(6)	0.3286(6)
U_{11}[Cl]	0.0220(12)	0.0220(12)
U_{22}[Cl]	0.0166(10)	0.0166(10)
U_{33}[Cl]	0.0133(25)	0.0132(25)
U_{iso}[Cl]	0.0173(10)	0.0173(10)

x[Cr], x[O], x[Cl] = 0

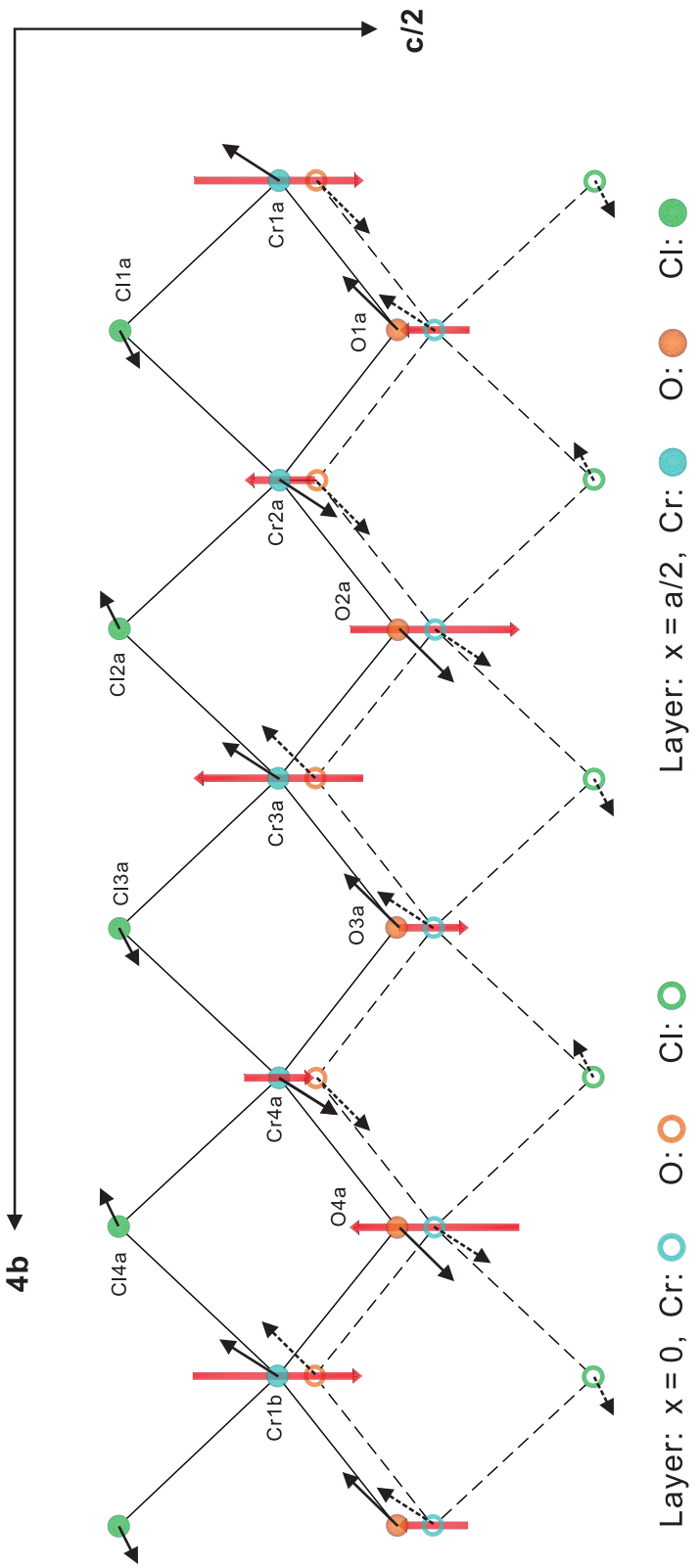

Figure 8.3: Magnetic modulated structure of CrOCl at 8 K. The direction and amplitude of magnetic moment are indicated by the big red arrows. The direction of small black arrows indicate atomic displacements (100× their true values). CrOCl possesses a two-fold magnetic supercell at 8 K.

Table 8.7: Selected interatomic distances and bond angles in the superstructure of CrOCl at 8 K. Crystallographically independent atoms are indicated by numbers. Different but symmetry equivalent atoms are indicated by and additional letter. Standard uncertainties are given in parentheses.

Atoms	Distance (Å)	Atoms	Distance (Å)
Cr1a – O1a	2.0244(1)	Cr1a – Cl1a	2.3242(1)
Cr2a – O1a	2.0284(1)	Cr2a – Cl1a	2.3248(1)
Cr2a – O2a	2.0269(1)	Cr2a – Cl2a	2.3253(1)
Cr3a – O2a	2.0279(1)	Cr3a – Cl2a	2.3190(1)
Cr3a – O3a	2.0244(1)	Cr3a – Cl3a	2.3242(1)
Cr4a – O3a	2.0284(1)	Cr4a – Cl3a	2.3248(1)
Cr4a – O4a	2.0269(1)	Cr4a – Cl4a	2.3253(1)
Cr1b – O4a	2.0279(1)	Cr1b – Cl4a	2.3190(1)
Atoms	Angle (deg.)	Atoms	Angle (deg.)
Cr1a – O1a – Cr2a	103.625(1)	Cr1a – Cl1a – Cr2a	86.500(1)
Cr2a – O2a – Cr3a	102.847(1)	Cr2a – Cl2a – Cr3a	86.086(1)
Cr3a – O3a – Cr4a	103.625(1)	Cr3a – Cl3a – Cr4a	86.500(1)
Cr4a – O4a – Cr1b	102.847(1)	Cr4a – Cl4a – Cr1b	86.086(1)

8.4 Conclusion

The nuclear and magnetic superstructures of CrOCl at 8 K have been determined. The positions of the nuclear and magnetic superlattice reflections in the low-temperature phase indicate a two-fold, 2**b** nuclear superstructure and a four-fold, a 4**b** magnetic superstructure of CrOCl, respectively. The modulation of the atoms in CrOCl is very weak, about one tenth of that in TiOCl. Both the nuclear and the magnetic structures possess an **a**-unique monoclinic symmetry. The ordered magnetic moment is parallel to **c**, and the magnitude of which is modulated.

Acknowledgments

Single crystals of CrOCl have been grown by Alfred Suttner at the Laboratory of Crystallography in Bayreuth. We gratefully acknowledge Martin Tolkiehn for technical support with the experiments with synchrotron radiation at beamline D3 of

Hasylab (DESY, Hamburg). Financial support has been obtained from the German Science Foundation (DFG). The work of JZ has been made possible through a CSC scholarship from the China Scholarship Council.

Chapter 9

Summary

The present work reports on the behaviors of temperature-dependent magnetic order of the transition-metal oxychlorides MOCl (M = Ti, Cr, Fe); further studies were performed on scandium-doped TiOCl and sodium-intercalated TiOCl. Single crystals of MOCl were grown by the chemical vapor phase transport method. At ambient condition, all compounds MOCl are isostructural with the orthorhombic space group $Pmmn$. They have a layered structure with each of the MOCl slabs containing a double MO layer sandwiched between Cl layers on each side. The slabs of MOCl are stacked along the lattice direction **c** and separated by van der Waals gaps. Within the MO layers, electrons on neighboring M atoms in a chain along **b** interact via direct exchange; moreover, interactions of the electrons may also exist between M atoms on neighboring chains by direct exchange, as well as by M–O–M superexchange. The different magnetic behaviors of MOCl are related to the different numbers of $3d$ electrons of M^{3+}.

The main experimental technique employed is x-ray diffraction at synchrotron stations. Profiles of so-called ω-2θ maps on selected reflections were measured to search for monoclinic lattice distortions of FeOCl, $Sc_xTi_{1-x}OCl$ (x = 0.005) and Na_xTiOCl (x = 0.01). The Néel temperature of FeOCl was derived from the temperature-dependent value of the monoclinic angle. **q** Scans were performed with the aim of determining the wave vectors of the modulated nuclear structure. The temperature-dependent components of **q** vectors were used to determine the temperature of transformation between incommensurate and commensurate fluctu-

ating regimes in $Sc_xTi_{1-x}OCl$ (x = 0.005) and the temperature of spin-Peierls phase transition in Na_xTiOCl (x = 0.01). Data collections were performed of integrated intensities of Bragg reflections. These data were used to refine structure models of CrOCl and $Sc_xTi_{1-x}OCl$ ($x = 0.005$) at 8 K. By combining the atomic modulation parameters with the magnetic structure of CrOCl, the modulated magnetic order of CrOCl at 8 K have been studied.

For FeOCl, the antiferromagnetic phase transition has been studied by temperature-dependent anisotropic magnetic susceptibility, heat capacity, dielectric measurements and x-ray diffraction experiments. These investigations reveal a second-order phase transition and provide a consistent Néel temperature of 82.0(2) K, in line with the previous values claimed by other research groups. The main discovery is that the magnetic phase transition of FeOCl is accompanied by a monoclinic lattice distortion, in agreement with the distortions observed for CrOCl, VOCl and TiOCl. The value of monoclinic distortion angle γ is 90.1° at 8 K. The ordered magnetic moments possess a component along **c**, but a component along **b** may exist as well. Very few superlattice reflections, which are quite weak, were observed by **q** scans at selected temperatures up to 58 K. The results of **q** scans show a temperature-dependent length of incommensurate modulation wave vector.

Upon cooling, TiOCl undergoes a phase transition to an incommensurately modulated state at $T_{c2} = 90$ K, and then a first-order phase transition to the spin-Peierls state at $T_{c1} = 67$ K. For $Sc_xTi_{1-x}OCl$ ($x = 0.005$), the specific heat does not show any anomalies. Instead of the anomalies, an excess heat capacity is found over a broad temperature range where the anomalies occurred for TiOCl. The equivalent entropies contained in the anomalies in TiOCl and in the broad excess heat capacity in $Sc_xTi_{1-x}OCl$ ($x = 0.005$), demonstrate that sharp phase transitions have been replaced by fluctuation regimes. **q** Scans were performed along a^* centered on selected reflections (h k+1/2 l) at temperatures between 52.5 and 90 K. The appearance of a single superlattice peak between 52.5 and 60 K indicates a commensurate regime. Above 62.5 K, two superlattice peaks at incommensurate positions described by ($h \pm q_1$ k+1/2 l) were observed, indicating an incommensurate regime. The transformation from incommensurate regime to commensurate regime occurs below $T_{c1} = 61.5(3)$. However, both regimes lack long-range order.

Instead, they should be recognized as crystalline phases of orthorhombic TiOCl-type structures supporting incommensurate and commensurate fluctuations of particularly large correlation lengths. Instead of a phase transition occurring at a definite temperature, a transformation of one fluctuating regime to another describes this feature.

Unlike substituting Ti for Sc, Na_xTiOCl (x = 0.01) was obtained by intercalating Na into the gaps between TiOCl layers. The temperature of T_{c1} = 64.86(2) K was determined by the temperature-dependent **q** scans along a^*, about 2 K lower than that of pure TiOCl. The temperature of T_{c2} = 92.8(7) K was determined by the temperature-dependence of the intensities of the incommensurate superlattice reflections, about 3 K higher than that of pure TiOCl. These behaviors reveal an enlarged temperature interval of the incommensurate state.

The modulated structure of CrOCl at 8 K was determined from x-ray diffraction data of synchrotron x-ray radiation. The appearance of two-fold nuclear superlattice reflections is in agreement with a four-fold magnetic superstructure. The magnitude of the modulation of Cr atoms in CrOCl is about one tenth that of Ti atoms in $Sc_xTi_{1-x}OCl$ (x = 0.005) and TiOCl. The refinement of magnetic structure was almost not affected by introducing atomic modulation parameters derived from the refinement of modulated nuclear structure.

Chapter 10

Zusammenfassung

Die vorliegende Arbeit behandelt das temperaturabhängige Verhalten der magnetischen Ordnung der Übergangsmetalloxychloride MOCl (M = Ti, Cr, Fe); weitere Untersuchungen wurden an Scandium-dotiertem TiOCl und an Natrium-interkaliertem TiOCl durchgeführt.

MOCl-Einkristalle wurden mittels chemischen Transports in der Gasphase gezüchtet. Alle Verbindungen MOCl sind bei Normalbedingungen isostrukturell in der orthorhombischen Raumgruppe $Pmmn$. Sie zeigen Schichtstrukturen, die aus "MOCl-Scheiben" aufgebaut sind. Jede dieser Scheiben besteht aus einer MO-Doppelschicht, die auf beiden Seiten von Cl-Schichten umgeben ist. Diese "MOCl-Scheiben" sind dann entlang der Gitterrichtung **c** gestapelt und durch van der Waals-Lücken voneinander getrennt. In den MO-Schichten wechselwirken Elektronen benachbarter M-Atome in den Ketten entlang **b** über direkten Austausch; darüberhinaus kann es auch zu einer Wechselwirkung der Elektronen zwischen den M-Atomen benachbarter Ketten kommen, sowohl als direkter Austausch, als auch als M–O–M Superaustausch. Das unterschiedliche magnetische Verhalten dieser Verbindungen hängt mit der unterschiedlichen Zahl der $3d$ Elektronen in MOCl zusammen.

Die hier verwendete experimentelle Hauptmethode ist Synchrotron-Röntgenbeugung. Profile sogenannter ω-2θ-Karten von ausgewählten Reflexen wurden gemessen und ausgewertet, um für FeOCl, $Sc_xTi_{1-x}OCl$ (x = 0.005) und Na_xTiOCl (x = 0.01) nach monoklinen Gitterverzerrungen zu suchen. Die Néel-Temperatur von FeOCl

wurde über die Temperaturabhängigkeit des monoklinen Winkels bestimmt. Mit Hilfe von **q**-Scans wurden die Wellenvektoren der modulierten nuklearen Strukturen bestimmt und aus den temperaturabhängigen Komponenten dieser **q**-Vektoren dann die Umwandlungstemperatur zwischen den inkommensurablen und kommensurablen fluktuierenden Regimen in $Sc_xTi_{1-x}OCl$ (x = 0.005) und die Temperatur der spin-Peierls Phasenumwandlung in Na_xTiOCl (x = 0.01). Es wurden Datensammlungen integrierter Intensitäten von Bragg Reflexen durchgeführt. An diesen Daten wurden die Strukturmodelle von CrOCl und von $Sc_xTi_{1-x}OCl$ ($x = 0.005$) bei 8 K verfeinert. Durch Kombination der atomaren Modulationsparameter mit der magnetischen Struktur von CrOCl wurde die modulierte magnetische Ordnung von CrOCl bei 8 K untersucht.

Für FeOCl wurde die antiferromagnetische Phasenumwandlung mittels temperaturabhängiger anisotroper magnetischer Suszeptibilität, Wärmekapazität, dielektrischen Messungen und Röntgenbeugungsexperimenten untersucht. Es wurde eine Phasenumwandlung zweiter Ordnung gefunden, für die die unterschiedlichen Methoden eine konsistente Néel-Temperatur von 82.0(2) K ergaben. Dies stimmt mit Werten anderer Forschergruppen überein. Die "Hauptentdeckung" ist, dass die magnetische Phasenumwandlung von FeOCl von einer monoklinen Gitterverzerrung begleitet wird, in Übereinstimmung mit den Verzerrungen, wie sie bei CrOCl, VOCl and TiOCl beobachtet werden. Der Wert des monoklinen Verzerrungswinkels γ beträgt bei 8 K 90.1°. Die geordneten magnetischen Momente besitzen eine Komponente entlang **c**, wobei auch eine zusätzliche Komponente entlang **b** möglich ist. Einige wenige Überstrukturreflexe, die sehr schwach sind, konnten mittels **q**-Scans bei ausgewählten Temperaturen bis 58 K vermessen werden. Als Ergebnis zeigen diese **q**-Scans, dass der Betrag des inkommensurablen Modulationswellenvektors temperaturabhängig ist.

Wird TiOCl gekühlt, durchläuft es bei $T_{c2} = 90$ K eine Phasenumwandlung in einen inkommensurabel modulierten Zustand und dann bei $T_{c1} = 67$ K eine Phasenumwandlung erster Ordnung in einen spin-Peierls Zustand. Für $Sc_xTi_{1-x}OCl$ ($x = 0.005$) zeigt die spezifische Wärme keine Anomalien. Stattdessen findet sich eine Überschusswärmekapazität über einen breiten Temperaturbereich, in dem die Anomalien für TiOCl auftreten. Die sich entsprechenden Entropien, die in den

Anomalien in TiOCl und der breiten Überschusswärmekapazität in $Sc_xTi_{1-x}OCl$ ($x = 0.005$) enthalten sind, zeigen auf, dass die scharfen Phasenumwandlungen durch fluktuierende Regime ersetzt wurden. **q**-Scans entlang a^* wurden im Temperaturbereich zwischen 52.5 and 90 K durchgeführt, zentriert auf ausgewählten Reflexen (h k+1/2 l). Das Auftreten eines einzelnen Überstrukturpeaks in den einzelnen Scans zwischen 52.5 and 60 K deutet auf ein kommensurables Regime. Oberhalb 62.5 K wurden in den Scans je zwei Überstrukturpeaks auf den inkommensurablen Lagen ($h \pm q_1$ k+1/2 l) beobachtet, die ein inkommensurables Regime anzeigen. Der Übergang vom inkommensurablen zum kommensurablen Regime findet unterhalb $T_{c1} = 61.5(3)$ statt. Da jedoch beide Regime ein Fehlen der langreichweitigen Ordnung zeigen, sollten sie stattdessen als kristalline Phasen der orthorhombischen TiOCl-Typ Strukturen verstanden werden, die inkommensurable und kommensurable Fluktuationen mit besonders langen Korrelationslängen zeigen. Anstelle einer Phasenumwandlung bei einer festen Temperatur beschreibt ein Übergang von einem in ein anderes fluktuierendes Regime dieses Merkmal.

Anders als beim Substituieren von Ti durch Sc wurde Na_xTiOCl (x = 0.01) durch Interkalation von Na in die Lücken zwischen den TiOCl-Scheiben gewonnen. Die Umwandlungstemperatur von $T_{c1} = 64.86(2)$ K wurde durch temperaturabhängige **q**-Scans entlang a^* ermittelt und liegt etwa 2 K niedriger als bei reinem TiOCl. Die Umwandlungstemperatur von $T_{c2} = 92.8(7)$ K wurde aus der Temperaturabhängigkeit der Intensitäten der inkommensurablen Überstrukturreflexe bestimmt und liegt etwa 3 K höher als bei reinem TiOCl. Es liegt also ein größeres Temperaturintervall des inkommensurablen Zustands vor.

Die modulierte Struktur von CrOCl bei 8 K wurde aus Synchrotron-Röntgenbeugungsdaten bestimmt. Das Auftreten von Überstrukturreflexen einer zweifachen nuklearen Überstruktur steht im Einklang mit der vierfachen magnetischen Überstruktur. Die Größe der Modulation des Cr-Atoms in CrOCl ist etwa ein Zehntel derjenigen des Ti in $Sc_xTi_{1-x}OCl$ ($x = 0.005$) und in TiOCl. Die Verfeinerung der magnetischen Struktur wird kaum durch die Einführung atomarer Modulationsparameter beeinflusst, die aus der Verfeinerung der modulierten nuklearen Struktur abgeleitet sind.

Appendix A

Supplementary materials: FeOCl

A.1 Profiles of 2θ-dependent ω-scans

Data of Crystal A

Profiles measured on reflection (2 2 0)

The step sizes in 2θ direction is 0.002 deg. The step sizes in ω direction is 0.004 deg at 46.4 K and 66.6 K, 0.002 deg at the other temperatures. The measuring time for the ω-scans was chosen to be 0.5 s per step.

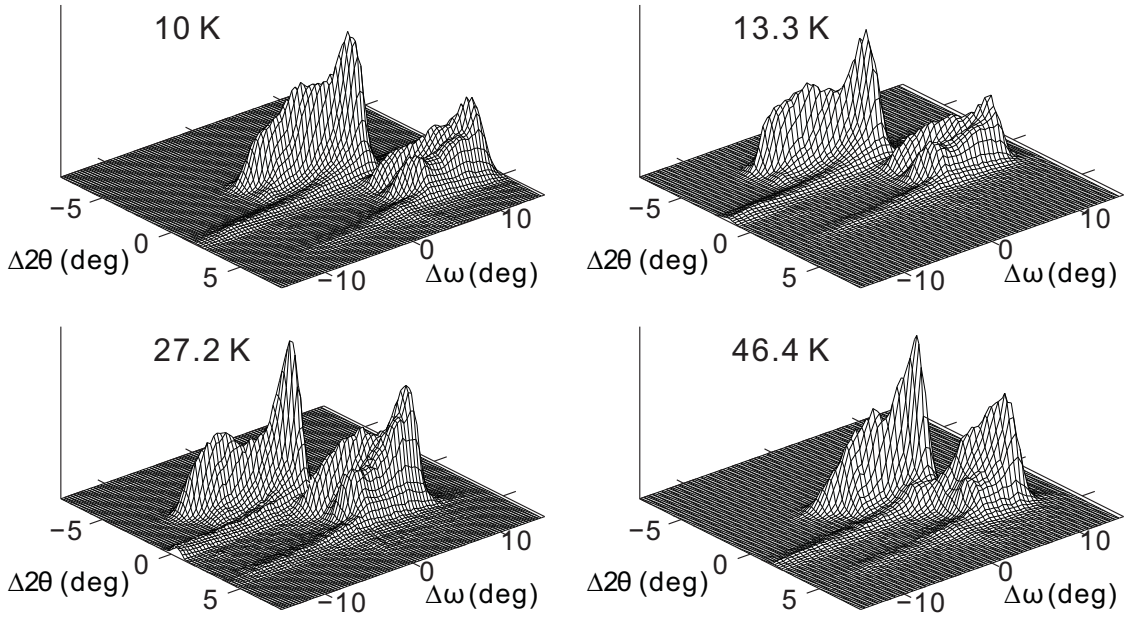

Figure A.1: Diffracted intensity as a function of the scattering angle 2θ and the crystal orientation ω for reflection (2 2 0) of crystal A. $\Delta 2\theta$ and $\Delta\omega$ indicate the deviation from the center of the scan in units of 0.01 deg. The center of map is at $2\theta_c$, ω_c (deg): 26.025, 12.996 10 K; 26.060, 13.012 13.3 K; 26.039, 13.034 27.2 K; 26.030 12.998 46.4 K. Crystal temperatures are indicated.

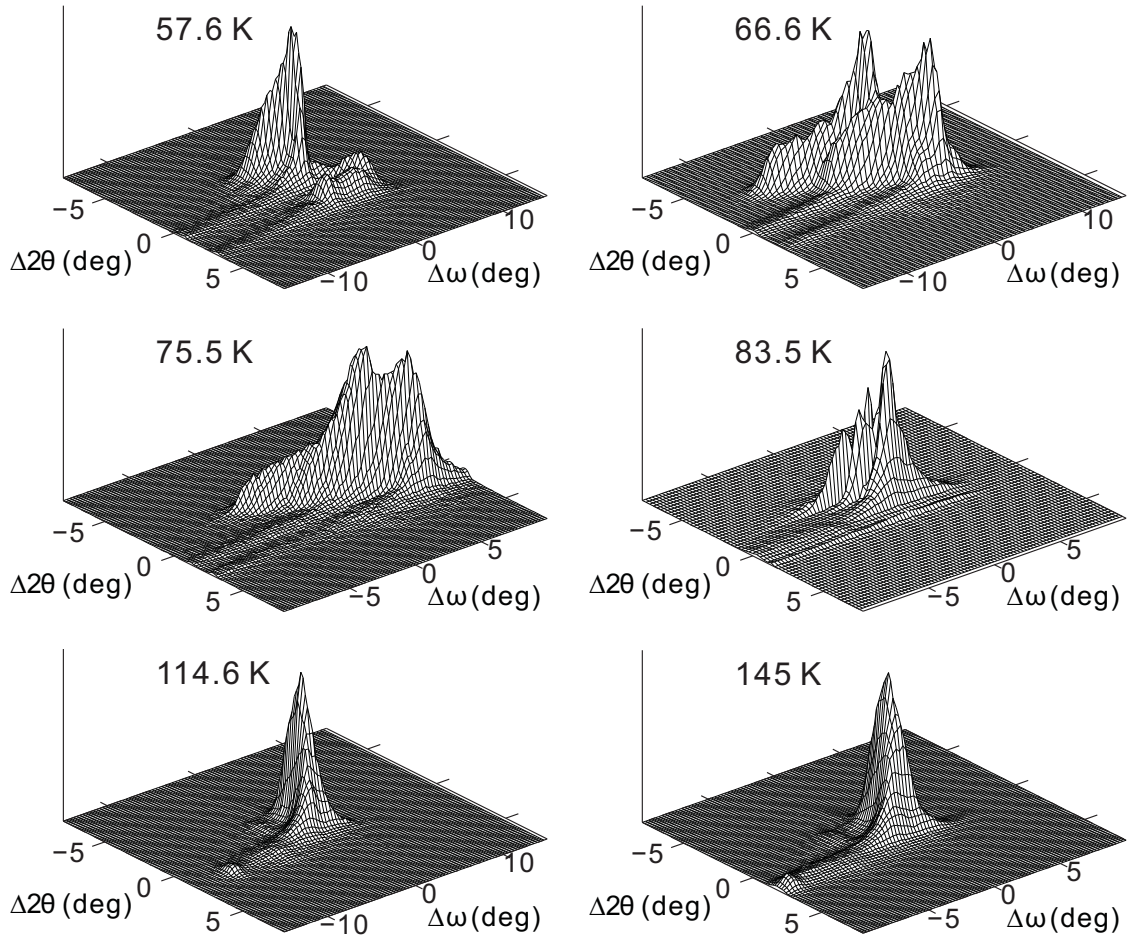

Figure A.2: Diffracted intensity as a function of the scattering angle 2θ and the crystal orientation ω for reflection (2 2 0) of crystal A. $\Delta 2\theta$ and $\Delta\omega$ indicate the deviation from the center of the scan in units of 0.01 deg. The center of map is at $2\theta_c$, ω_c (deg): 26.041, 13.044 57.6 K; 26.048, 13.036 66.6 K; 26.037, 13.002 75.5 K; 26.046, 13.031 83.5 K; 26.034, 13.007 114.6 K; 26.021, 13.041 145 K. Crystal temperatures are indicated.

Profiles measured on reflection (2 0 -4)

The step sizes in 2θ and ω direction are both 0.008 deg at 13.3 K and 66.6 K, 0.002 deg at 114.6 K and 145 K. The measuring time for the ω-scans was chosen to be 0.5 s per step.

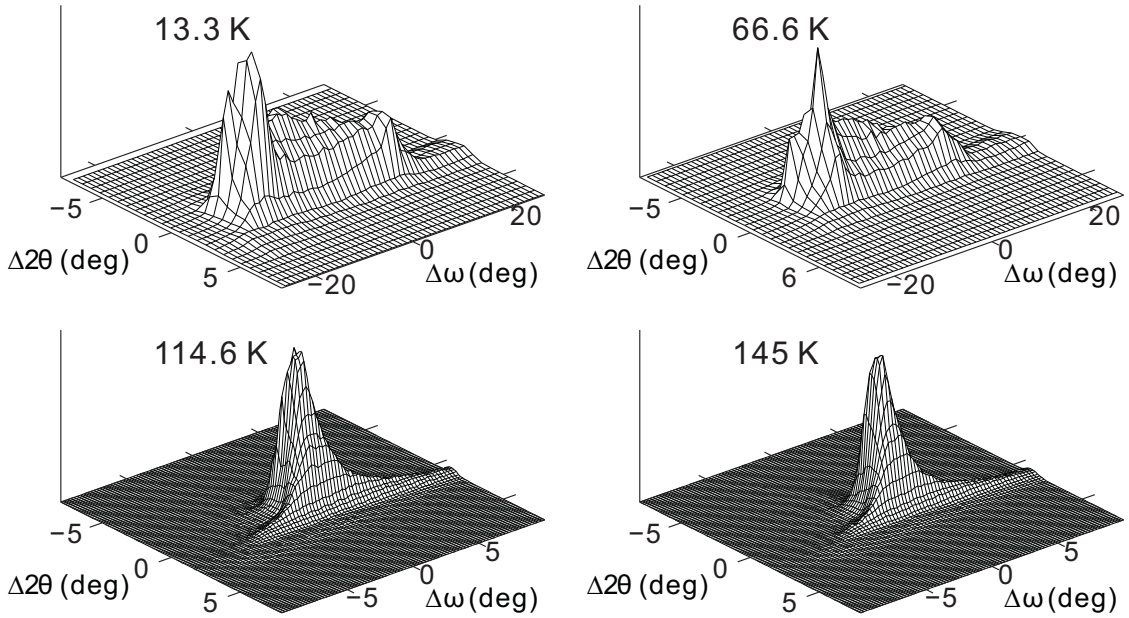

Figure A.3: Diffracted intensity as a function of the scattering angle 2θ and the crystal orientation ω for reflection $(2\ 0\ -4)$ of crystal A. $\Delta 2\theta$ and $\Delta\omega$ indicate the deviation from the center of the scan in units of 0.01 deg. The center of map is at $2\theta_c$, ω_c (deg): 23.071, 12.001 13.3 K; 23.706, 11.978 66.6 K; 23.680, 11.866 114.6 K; 23.666, 11.862 145 K. Crystal temperatures are indicated.

Profiles measured on reflection (0 2 -5)

The step sizes in 2θ and ω direction are both 0.008 deg at 13.3 K and 66.6 K, 0.002 deg at 114.6 K and 145 K. The measuring time for the ω-scans was chosen to be 0.5 s per step.

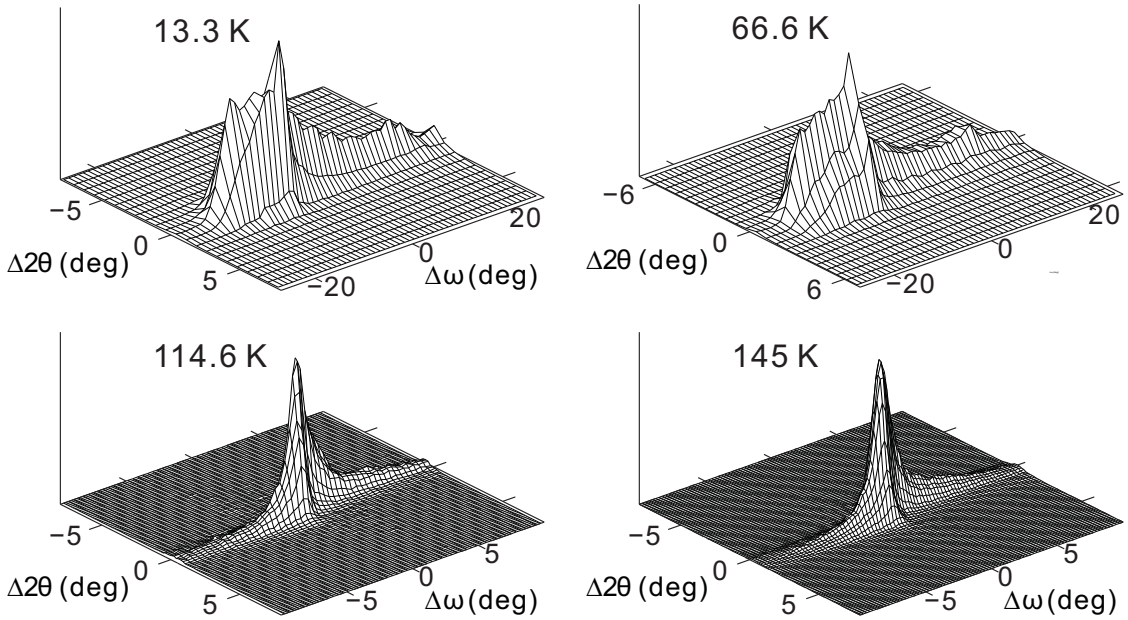

Figure A.4: Diffracted intensity as a function of the scattering angle 2θ and the crystal orientation ω for reflection $(0\ 2\ -5)$ of crystal A. $\Delta 2\theta$ and $\Delta\omega$ indicate the deviation from the center of the scan in units of 0.01 deg. The center of map is at $2\theta_c$, ω_c (deg): 28.420, 14.300 13.3 K; 28.410, 14.300 66.6 K; 28.394, 14.232 114.6 K; 28.374, 14.205 145 K. Crystal temperatures are indicated.

Profiles of 2θ-dependent ω-scans of Crystal B

Profiles measured on reflection (2 2 0)

The step sizes in 2θ and ω direction are both 0.002 deg at all temperatures. The measuring time for the ω-scans was chosen to be 0.5 s per step.

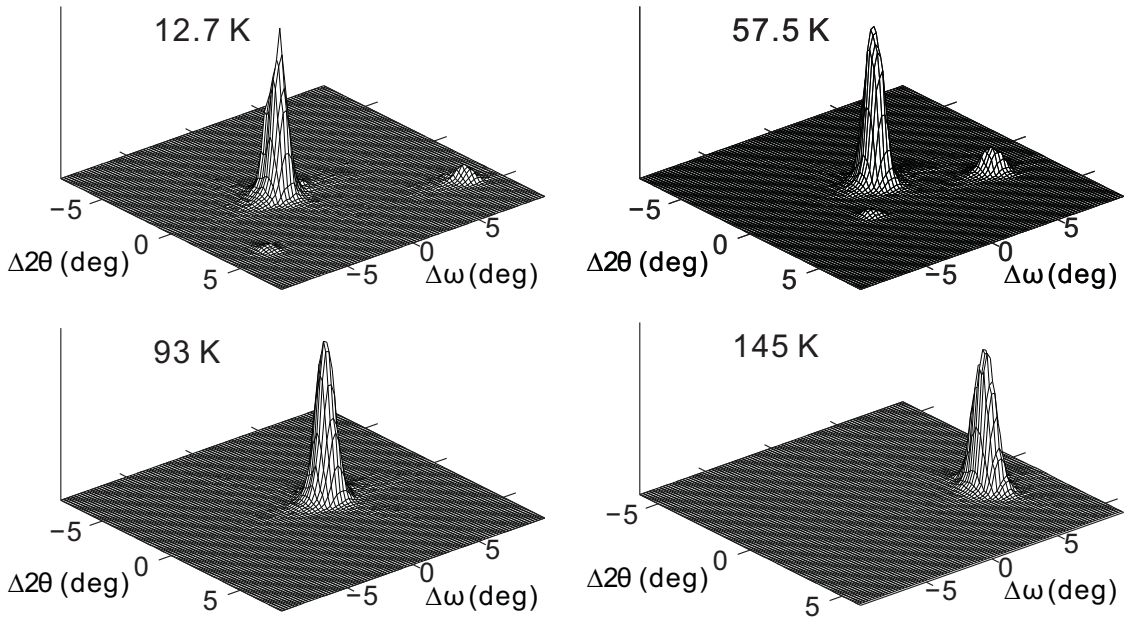

Figure A.5: Diffracted intensity as a function of the scattering angle 2θ and the crystal orientation ω for reflection (2 2 0) of crystal A. $\Delta 2\theta$ and $\Delta\omega$ indicate the deviation from the center of the scan in units of 0.01 deg. The center of map is at $2\theta_c$, ω_c (deg): 26.017, 13.085 12.7 K; 26.025, 13.065 57.5 K; 26.029, 13.043 93 K; 26.005, 13.041 145 K. Crystal temperatures are indicated.

Profiles measured on reflection (2 0 -4)

The step sizes in 2θ and ω direction are both 0.002 deg at all temperatures. The measuring time for the ω-scans was chosen to be 0.5 s per step.

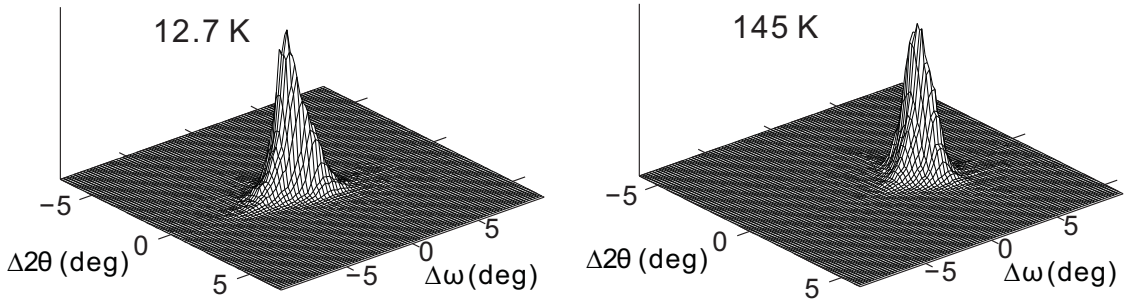

Figure A.6: Diffracted intensity as a function of the scattering angle 2θ and the crystal orientation ω for reflection $(2\ 0\ -4)$ of crystal A. $\Delta 2\theta$ and $\Delta\omega$ indicate the deviation from the center of the scan in units of 0.01 deg. The center of map is at $2\theta_c$, ω_c (deg): 23.691, 11.882 12.7 K; 23.651, 11.872 145 K. Crystal temperatures are indicated.

Profiles measured on reflection (0 2 -5)

The step sizes in 2θ and ω direction are both 0.002 deg at all temperatures. The measuring time for the ω-scans was chosen to be 0.5 s per step.

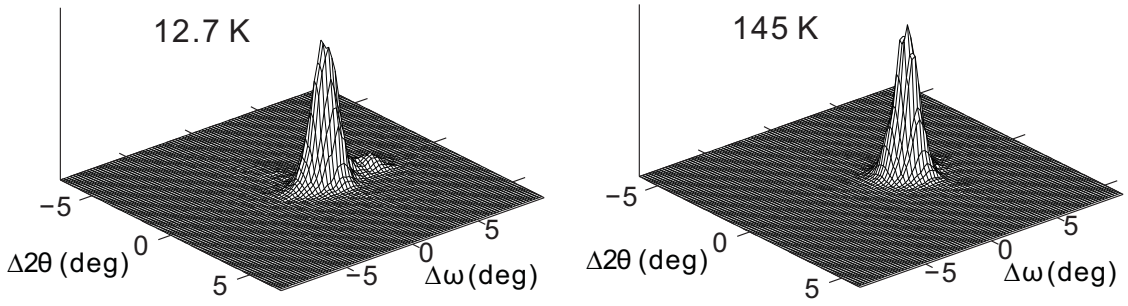

Figure A.7: Diffracted intensity as a function of the scattering angle 2θ and the crystal orientation ω for reflection $(0\ 2\ -5)$ of crystal A. $\Delta 2\theta$ and $\Delta\omega$ indicate the deviation from the center of the scan in units of 0.01 deg. The center of map is at $2\theta_c$, ω_c (deg): 28.431, 14.243 12.7 K; 28.384, 14.273 145 K. Crystal temperatures are indicated.

A.2 Profiles fitting for determination of the peak position of FeOCl

To determine the reflection splitting the measured reflection intensities of the 2θ-dependent ω-scans were summed for equal 2θ-values. The resulting intensities plotted against the 2θ values yields a pseudo powder diagram whose profile was fitted using Gauss functions.

Data of Crystal A

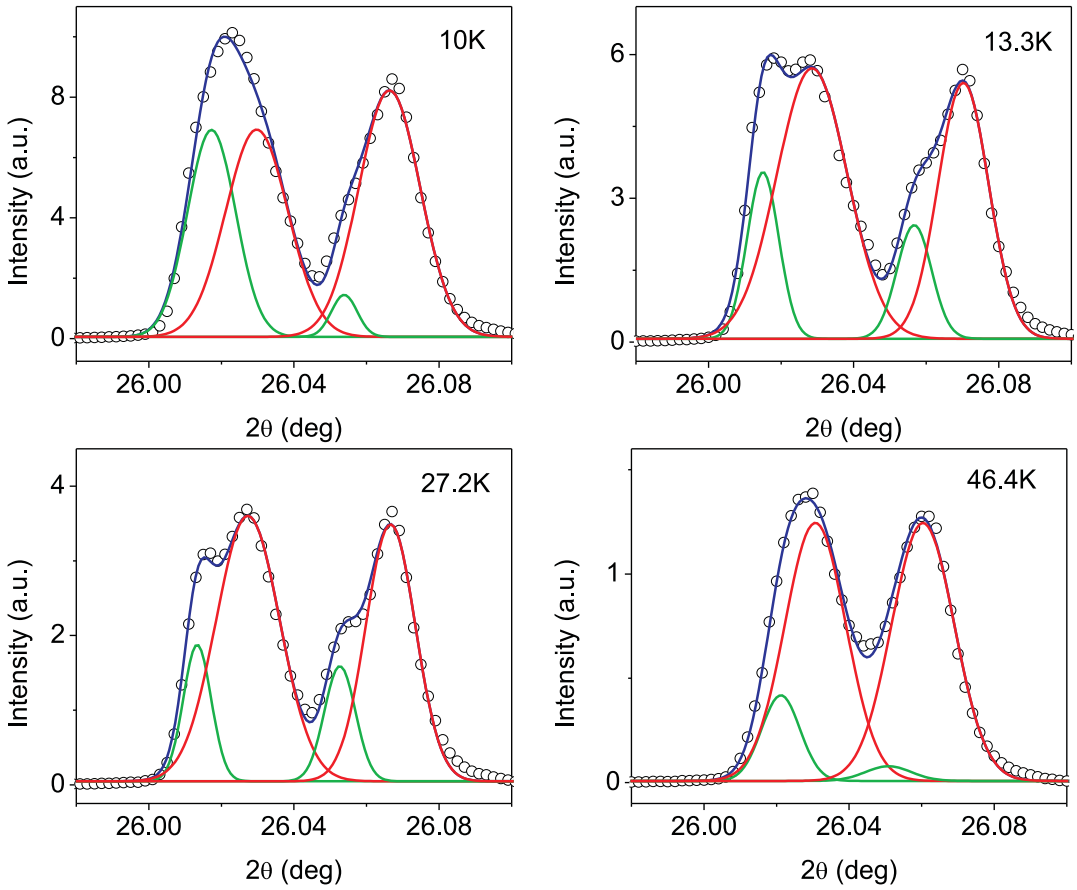

Figure A.8: Reflection profiles of reflection (2 2 0) were derived from 2θ dependent ω-scans by summing of the reflection intensities for same 2θ values. The solid curve represent the superposed curves of Gauss-type functions.

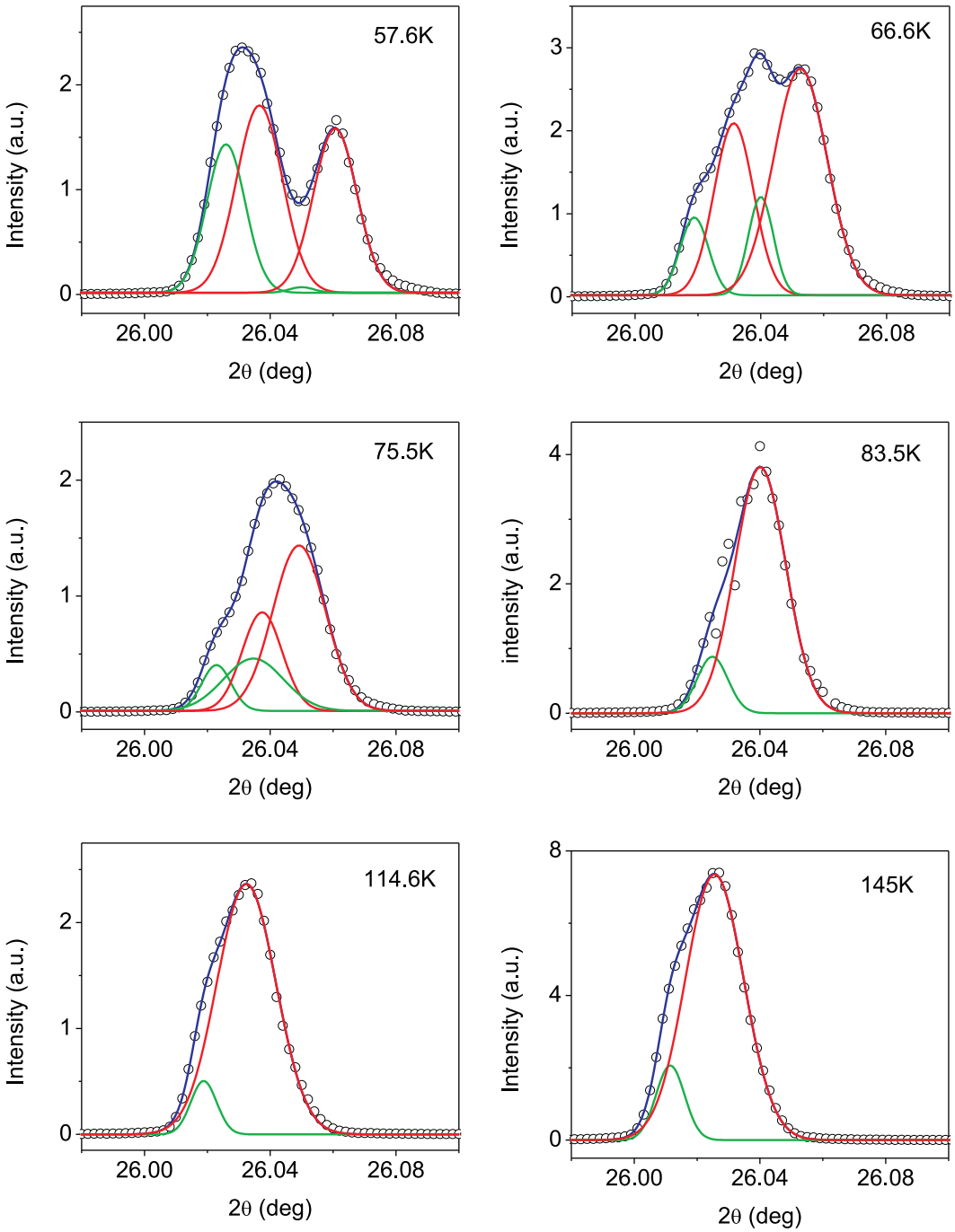

Figure A.9: Reflection profiles of reflection (2 2 0) were derived from 2θ dependent ω-scans by summing of the reflection intensities for same 2θ values. The solid curve represent the superposed curves of Gauss-type functions.

Data of Crystal B

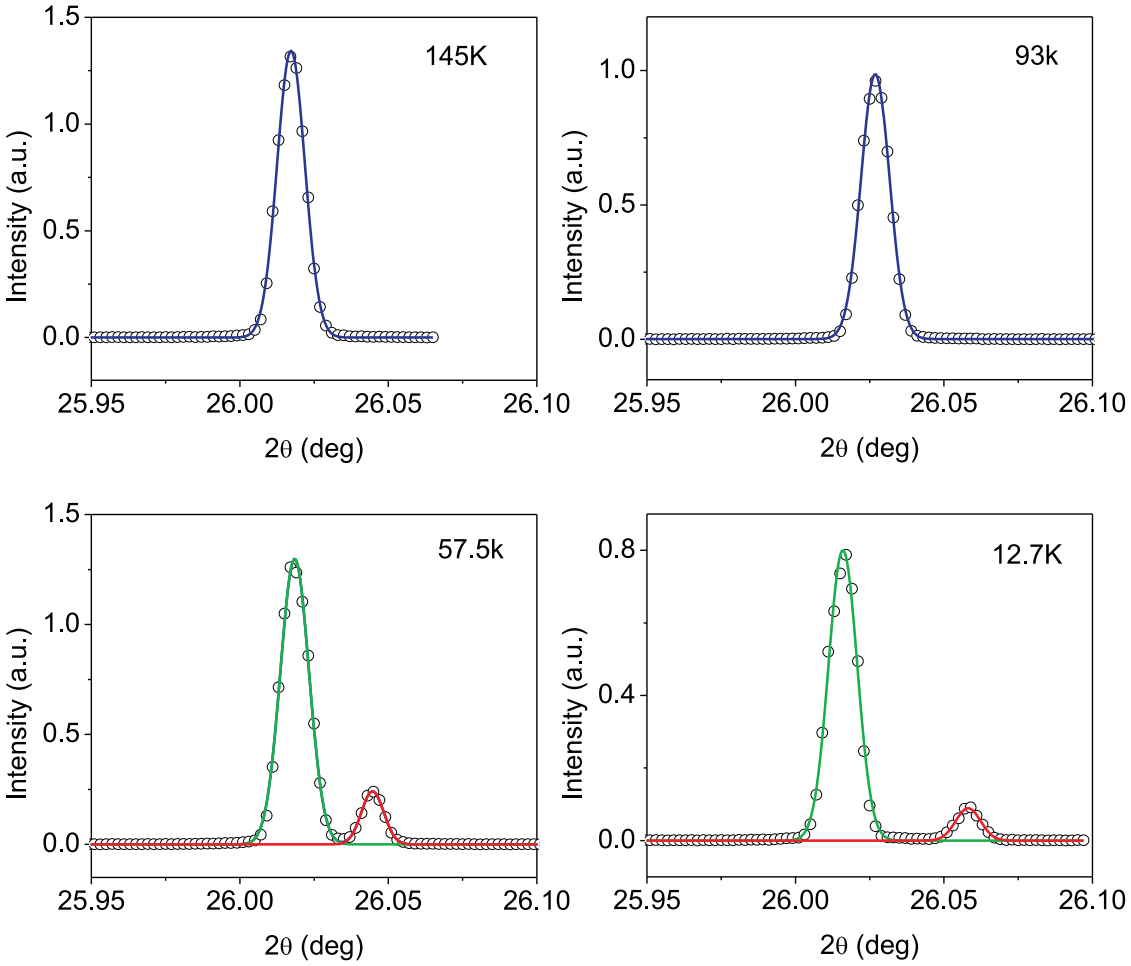

Figure A.10: Reflection profiles of reflection (2 2 0) were derived from 2θ dependent ω-scans by summing of the reflection intensities for same 2θ values. The solid curve represent the superposed curves of Gauss-type functions.

Values of splitting in 2θ and monoclinic angle γ

Table A.1: Values of splittings in 2θ and monoclinic angle γ.

	Crystal A			Crystal B	
T (K)	$\Delta 2\theta$ Å	$\gamma \mathring{A}$		$\Delta 2\theta$ Å	γ Å
12.7	–	–	–	0.04217	90.09169
13.3	0.04169	90.09064	–	–	–
27.2	0.03933	90.08553	–	–	–
46.4	0.02966	90.06446	–	–	–
57.5	–	–	–	0.02622	90.05700
57.6	0.02408	90.05232	–	–	–
66.6	0.02117	90.04605	–	–	–
75.5	0.01175	90.02557	–	–	–

A.3 Structural distortion with modulation wave vector

In order to study the structural distortion with modulation wave vector, q scans were performed to find satellite reflections. The data in Table A.2 and A.3 have been plotted in Chapter 5 Fig. 5.6.

q Scans of satellite reflections

Table A.2: q Scans of crystal A

T (K)	(1 1 0)	(1 2-q_b 0)	(1 2 0)	q_b
10.0	1.00053	1.45886	2.01835	0.54969
13.3	1.00070	1.45918	2.01827	0.54944
27.2	0.99989	1.4569	2.01585	0.55017
46.4	1.00199	1.45447	2.01532	0.55347
57.6	0.99902	1.44846	2.01323	0.55686

Table A.3: q Scans at crystal B

T (K)	(2 0 -2)	(2 q_b -2)	(2 1 -2)	q_b
12.7	-0.00094	0.54925	0.99879	0.55061

Appendix B

Supplementary materials: $Sc_xTi_{1-x}OCl$

B.1 Profiles of main reflections at selected temperatures

For selected main reflections so-called ω–2θ maps were obtained by repeated ω scans at a series of values for 2θ. Detector slits were set to 6×0.02 mm^2, which corresponds to an acceptance angle in the direction of 2θ of 0.0031 deg. The step size in the 2θ direction was 0.002 deg. The step size in the ω direction was 0.001 deg at $T = 298$ K and 0.002 deg at the other temperatures. The measuring time was chosen to be 0.5 s per step.

Profiles measured on reflection (0 2 -4)

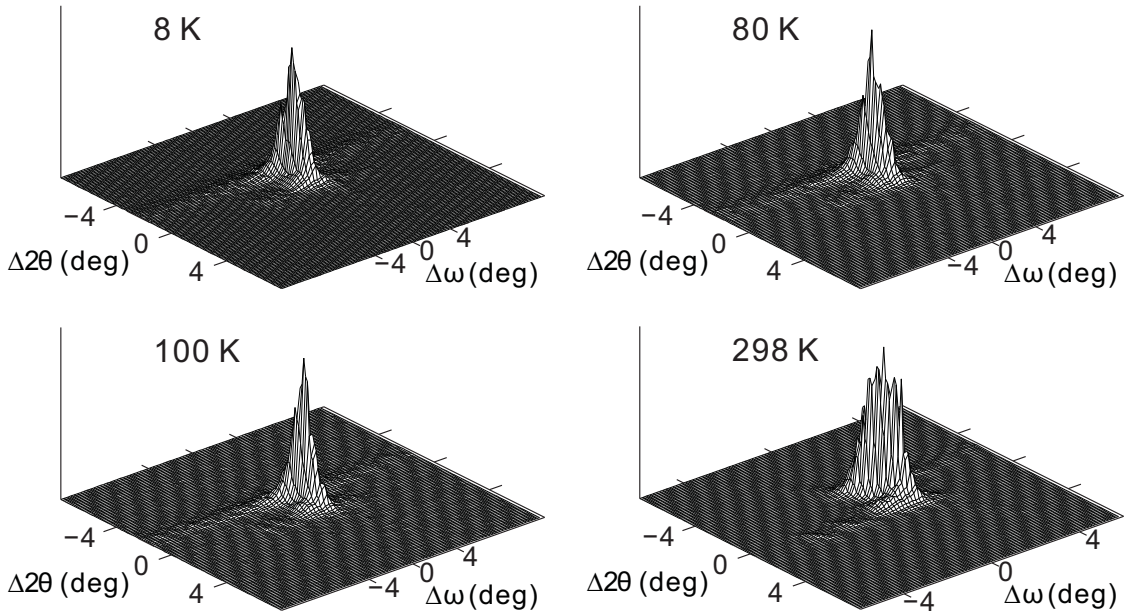

Figure B.1: Diffracted intensity as a function of the scattering angle 2θ and the crystal orientation ω centered at reflection (0 2 -4). ω–2θ maps are given for four temperatures, as indicated. $\Delta 2\theta$ and $\Delta\omega$ indicate the deviation from the center of the scan in units of 0.01 deg. The centers of maps are at $2\theta_c$, ω_c: 25.239, 12.611 deg at 8 K; 25.224, 12.614 deg at 80 K; 25.203, 12.603 deg at 100 K; 25.096 12.547 deg at 298 K.

Profiles measured on reflection (2 0 -5)

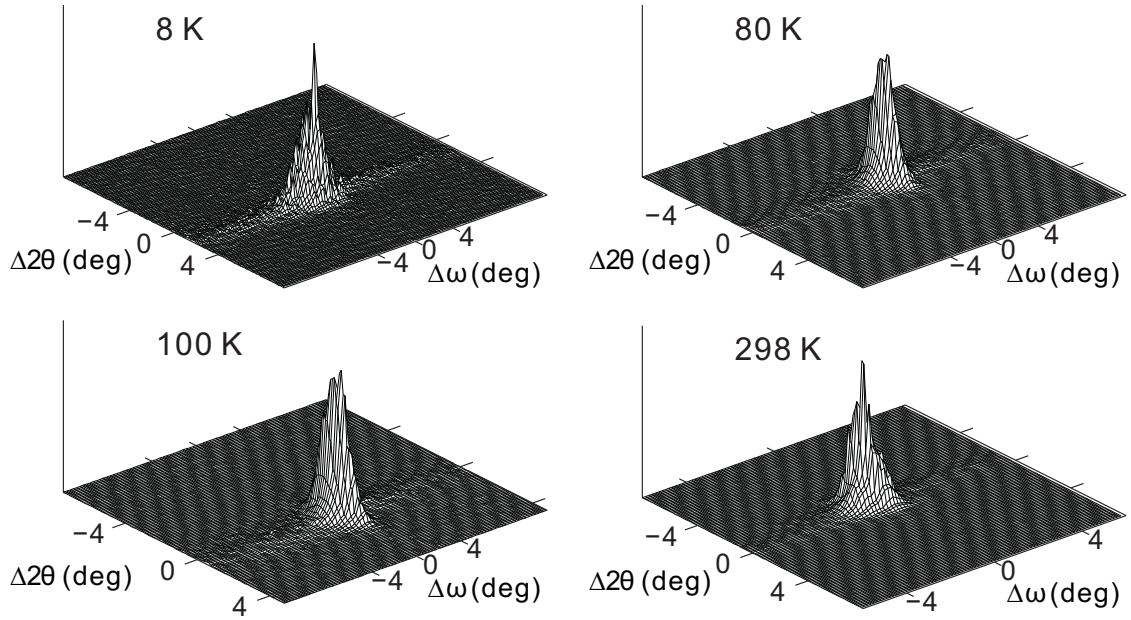

Figure B.2: Diffracted intensity as a function of the scattering angle 2θ and the crystal orientation ω centered at reflection (2 0 -5). ω–2θ maps are given for four temperatures, as indicated. $\Delta 2\theta$ and $\Delta\omega$ indicate the deviation from the center of the scan in units of 0.01 deg. The centers of maps are at $2\theta_c$, ω_c: 26.452, 13.241 deg at 8 K; 26.463, 13.262 deg at 80 K; 26.45, 13.247 deg at 100 K; 26.427, 13.211 deg at 298 K.

Profiles measured on reflection (2 -2 -4)

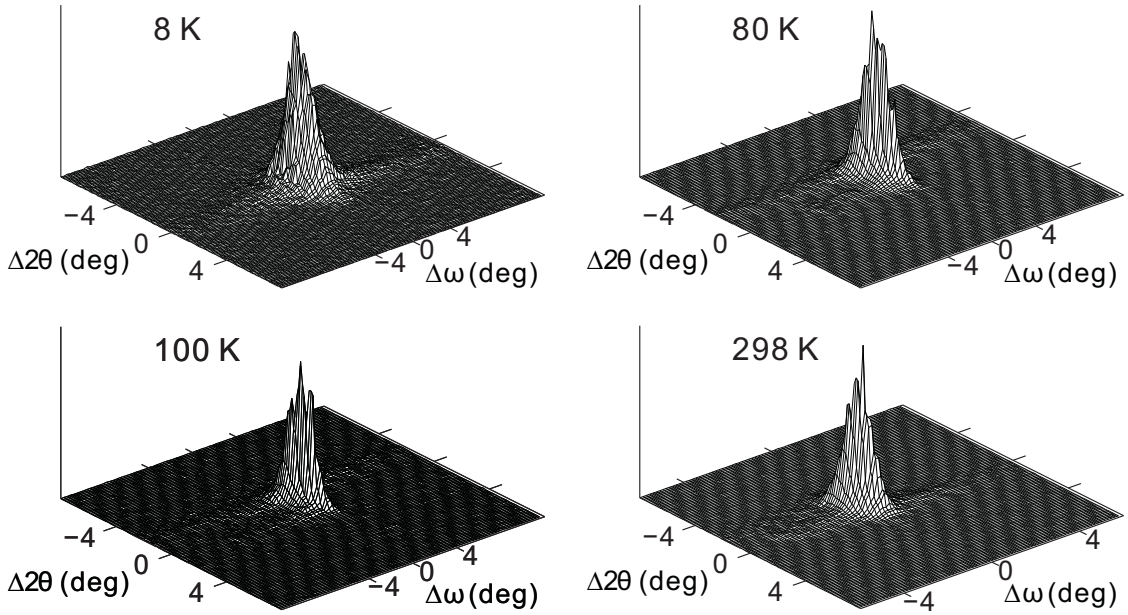

Figure B.3: Diffracted intensity as a function of the scattering angle 2θ and the crystal orientation ω for reflection (2 -2 -4). ω–2θ maps are given for four temperatures, as indicated. $\Delta 2\theta$ and $\Delta\omega$ indicate the deviation from the center of the scan in units of 0.01 deg. The centers of maps are at $2\theta_c$, ω_c: 30.572, 15.234 deg at 8 K; 30.582, 15.303 deg at 80 K; 30.567, 15.282 deg at 100 K; 30.488, 15.238 deg at 298 K.

Profiles measured on reflection (-1 -1 -1)

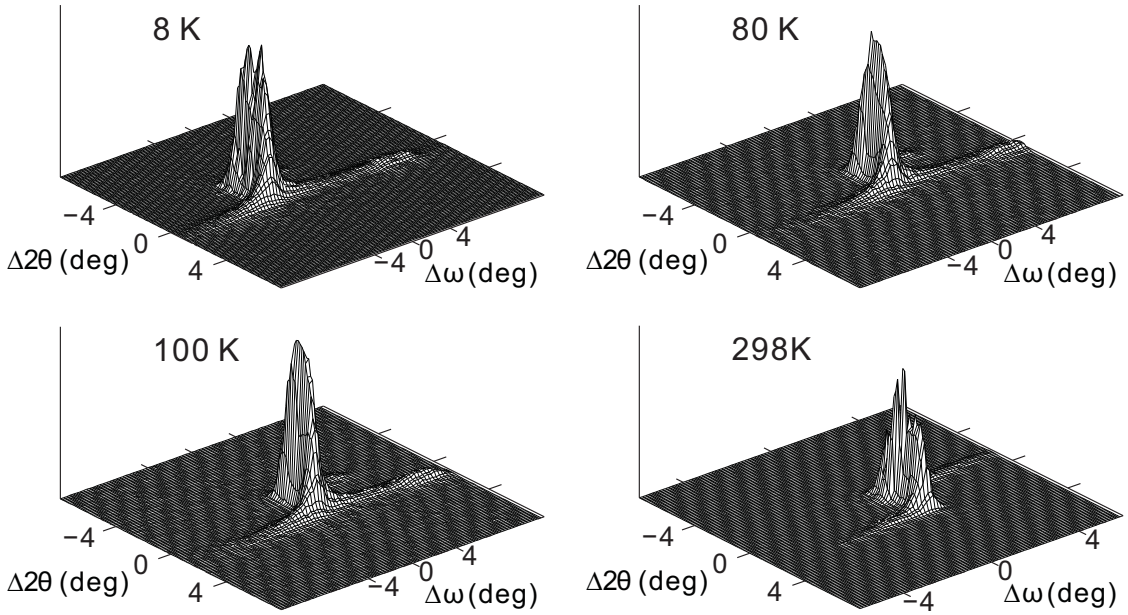

Figure B.4: Diffracted intensity as a function of the scattering angle 2θ and the crystal orientation ω for reflection (-1 -1 -1). ω–2θ maps are given for four temperatures, as indicated. $\Delta 2\theta$ and $\Delta\omega$ indicate the deviation from the center of the scan in units of 0.01 deg. The centers of maps are at $2\theta_c$, ω_c: 13.483, 6.755 deg at 8 K; 13.475, 6.705 deg at 80 K; 13.461, 6.701 deg at 100 K; 13.417, 6.708 deg at 298 K.

B.2 Dependence of the scattered intensity on diffraction angle 2θ

For each Bragg reflection the scattered intensity as a function of the scattering angle 2θ has been obtained by integrating the ω–2θ maps over ω. The resulting reflection profiles contain a single peak, which has been fitted by a pseudo-Voigt function in each case. These data indicate the absence of any splitting of the diffraction maxima. They are thus in agreement with orthorhombic symmetry of the crystal lattice at all temperatures.

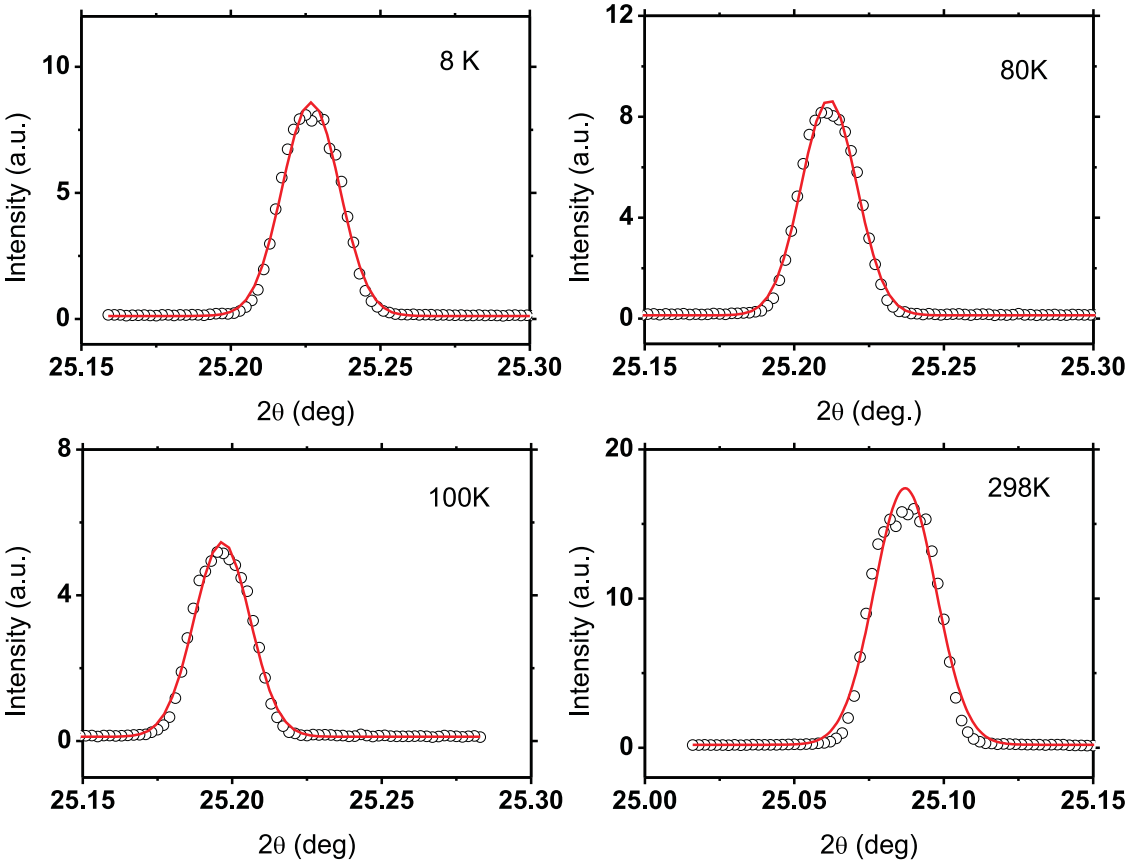

Figure B.5: Reflection profiles of the reflection (0 2 -4) for four different temperatures, as indicated. They have been obtained by integration along ω of the data in Fig. B.1. Solid curves represent fits by pseudo-Voigt functions.

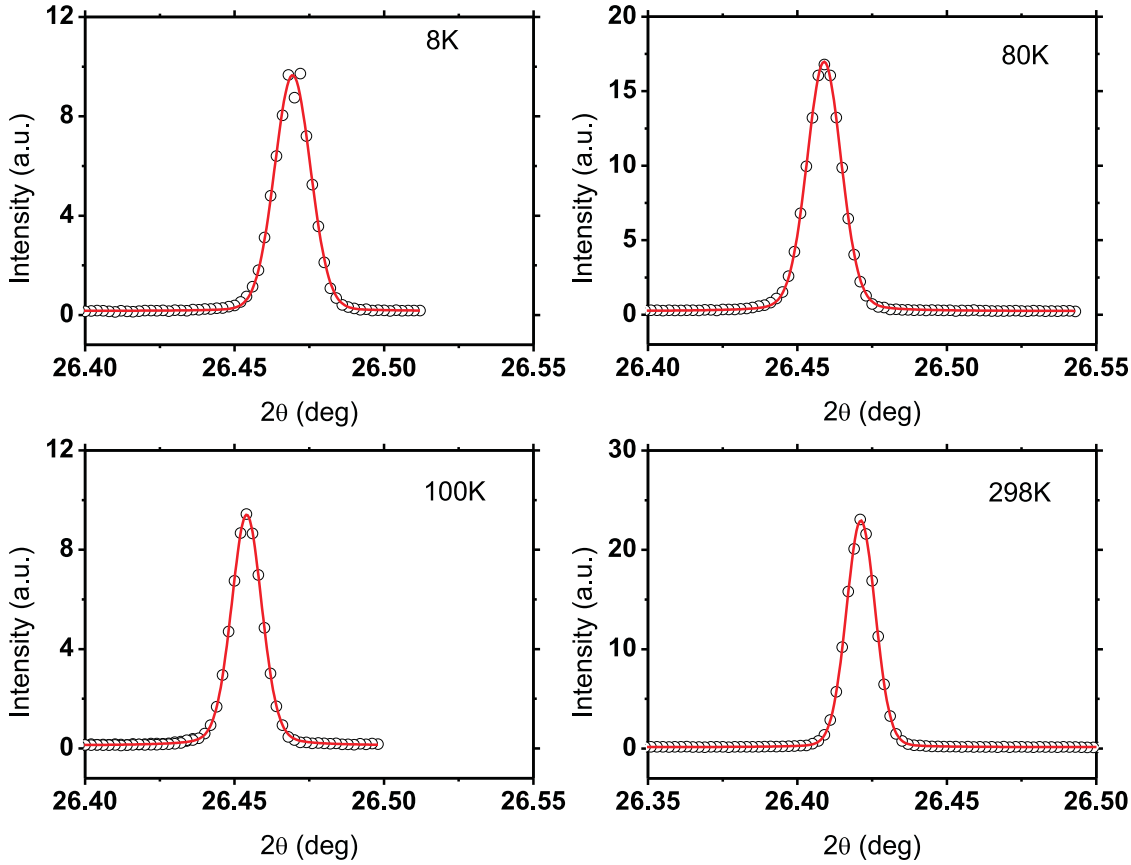

Figure B.6: Reflection profiles of the reflection (2 0 -5) for four different temperatures, as indicated. They have been obtained by integration along ω of the data in Fig. B.2. Solid curves represent fits by pseudo-Voigt functions.

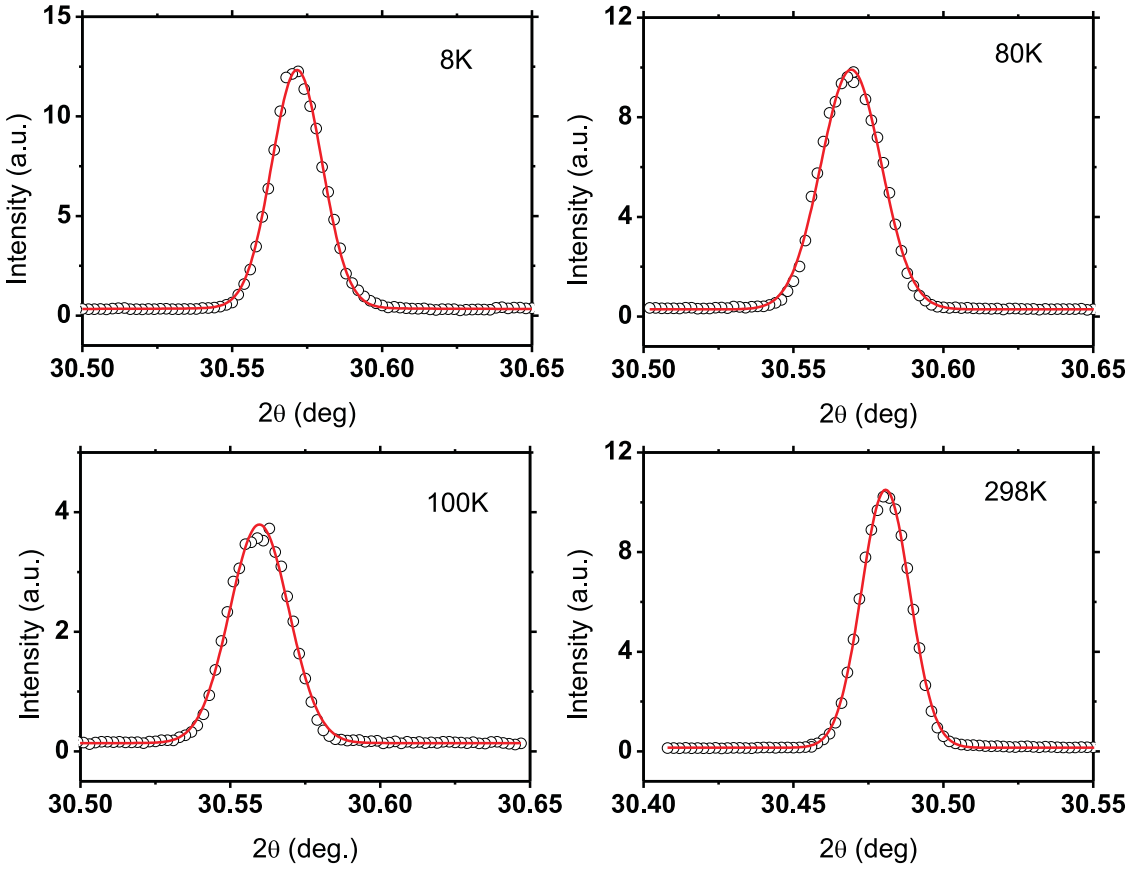

Figure B.7: Reflection profiles of the reflection (2 -2 -4) for four different temperatures, as indicated. They have been obtained by integration along ω of the data in Fig. B.3. Solid curves represent fits by pseudo-Voigt functions.

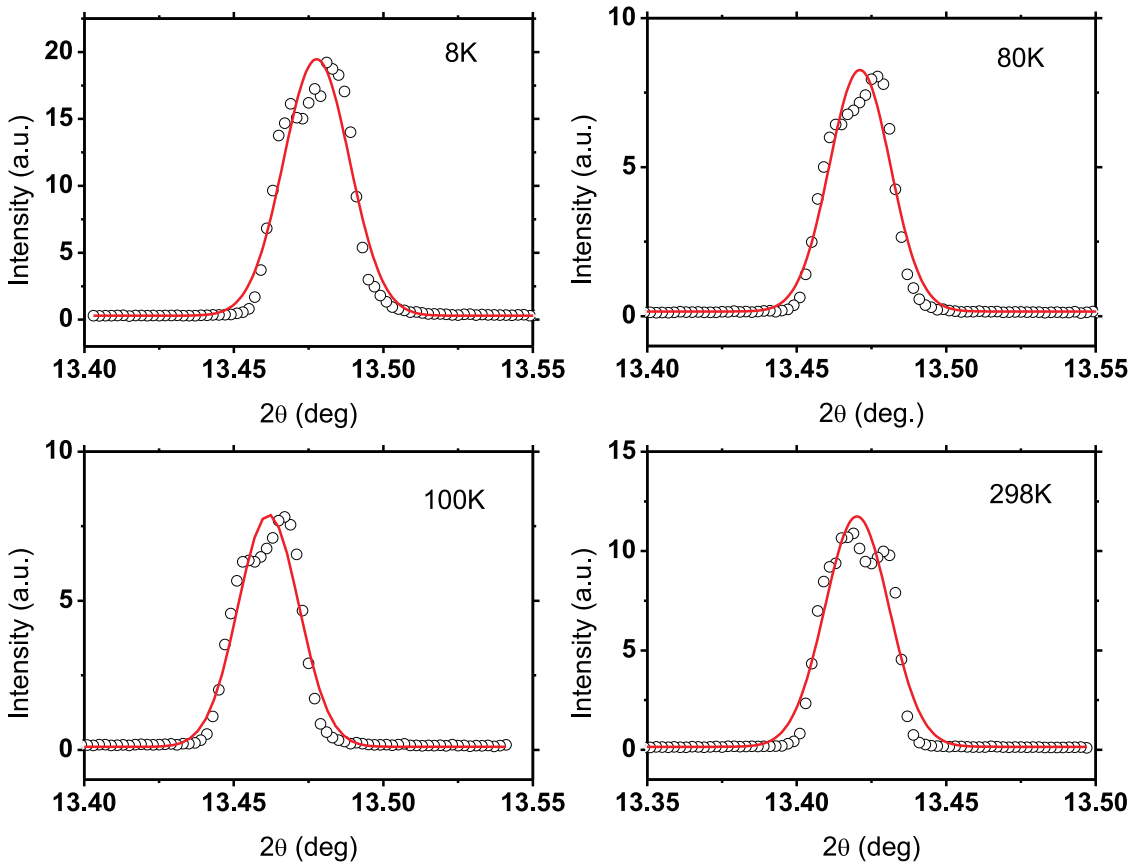

Figure B.8: Reflection profiles of the reflection (-1 -1 -1) for four different temperatures, as indicated. They have been obtained by integration along ω of the data in Fig. B.4. Solid curves represent fits by pseudo-Voigt functions.

Table B.1: Position (x_c) and FWHM of the reflection profiles in Figs. B.5–B.8, as fitted by pseudo-Voigt functions.

	0 2 -4		2 0 -5		-1 -1 -1		2 -2 -4	
T (K)	x_c	FWHM	x_c	FWHM	x_c	FWHM	x_c	FWHM
8	25.22677	0.02248	26.46939	0.01418	13.47766	0.02618	30.57163	0.01992
80	25.21163	0.0218	26.45894	0.01351	13.47112	0.02417	30.56926	0.02375
100	25.19663	0.02205	26.45406	0.01204	13.46162	0.02403	30.55968	0.02331
298	25.08693	0.02456	26.42123	0.01139	13.42016	0.02519	30.48074	0.01902

B.3 Reflection positions by q scans

q Scans at selected superlattice positions have been measured in dependence of temperature. They allow the determination of the components of the commensurate and incommensurate modulation wave vectors at each temperature.

q Scans have been performed along $\mathbf{a}^*$ centered at commensurate positions $(h\ k{+}\frac{1}{2}\ l)$. The scans encompass the range $(h - 0.15) \rightarrow (h + 0.15)$ by 151 steps of step size 0.002. The exposure time was 8 s per step.

q Scans along a* centered at (1 -0.5 -9)

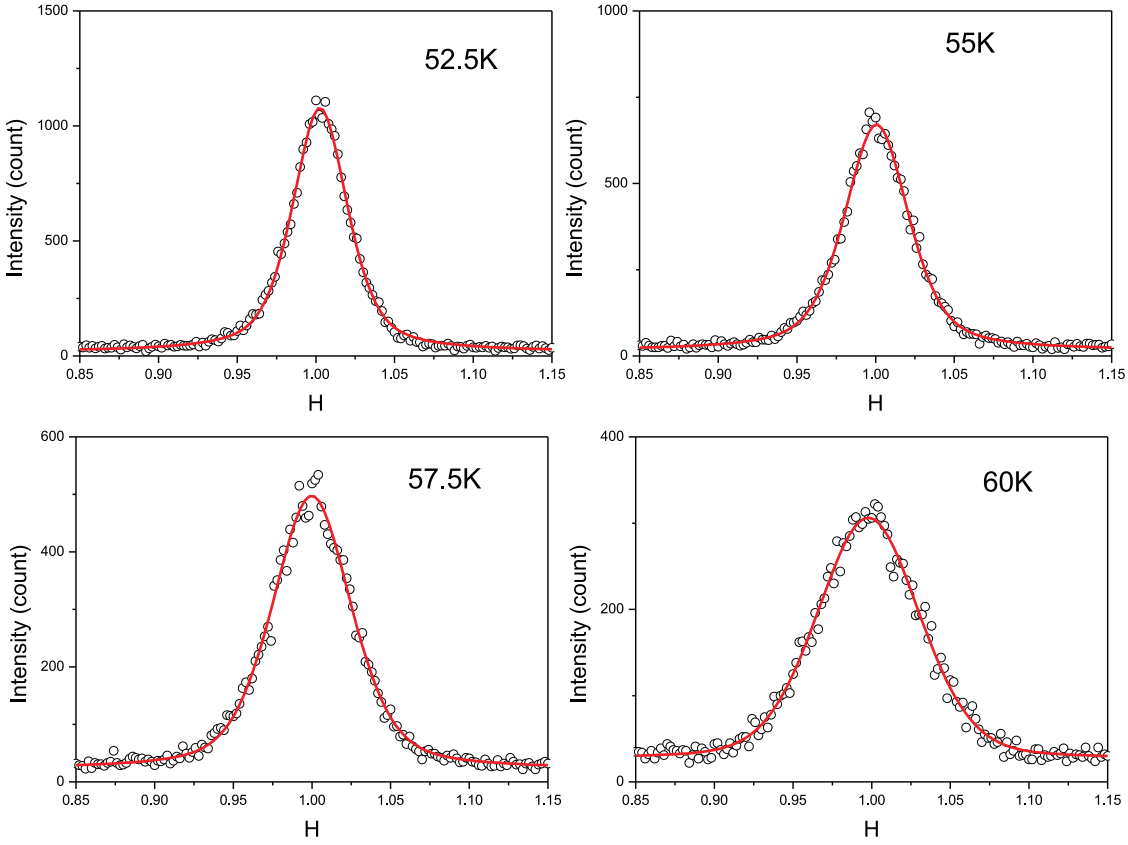

Figure B.9: q Scans centered on (1 -0.5 -9) for temperatures of 52.5, 55, 57.5 and 60 K. All scans show a single peak as demonstrated by the successful fit of a pseudo-Voigt function to the data (solid lines).

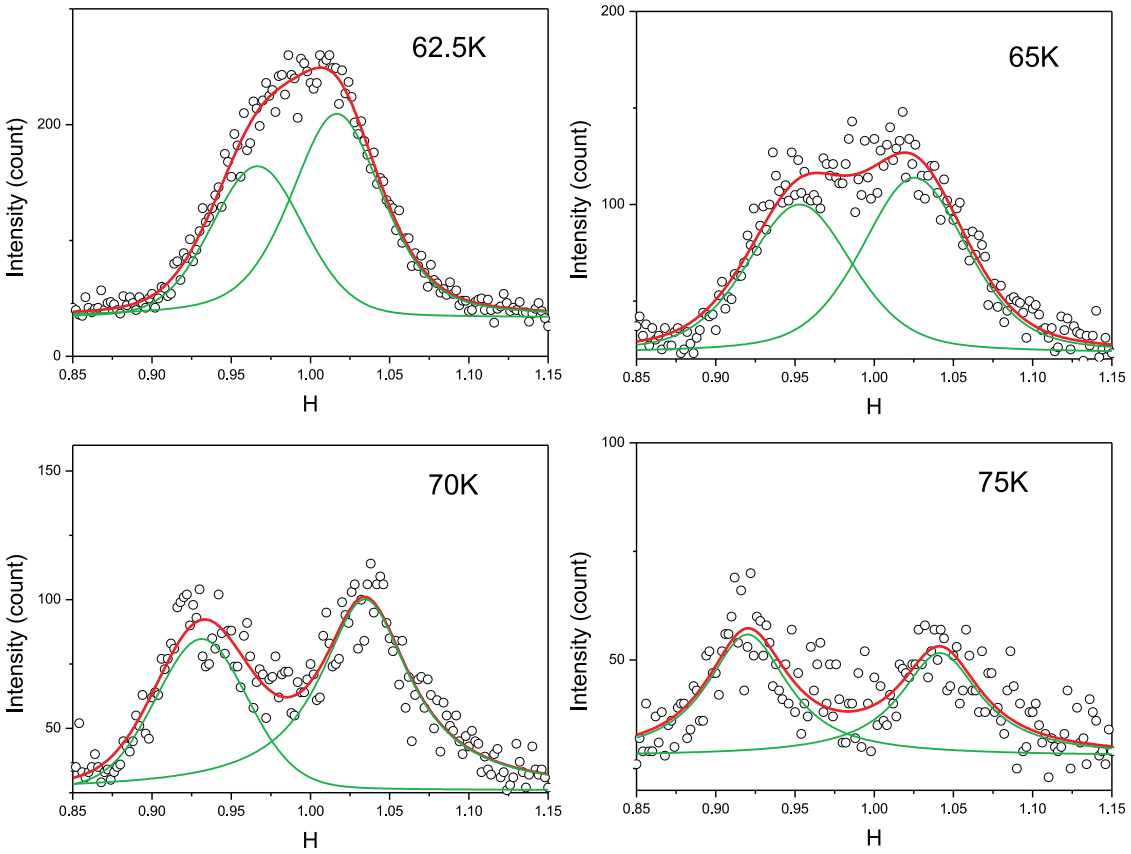

Figure B.10: q Scans centered on (1 -0.5 -9) for temperatures of 62.5, 65, 70 and 75 K. All scans show a double peak as demonstrated by the successful fit of two pseudo-Voigt functions to the data (solid lines).

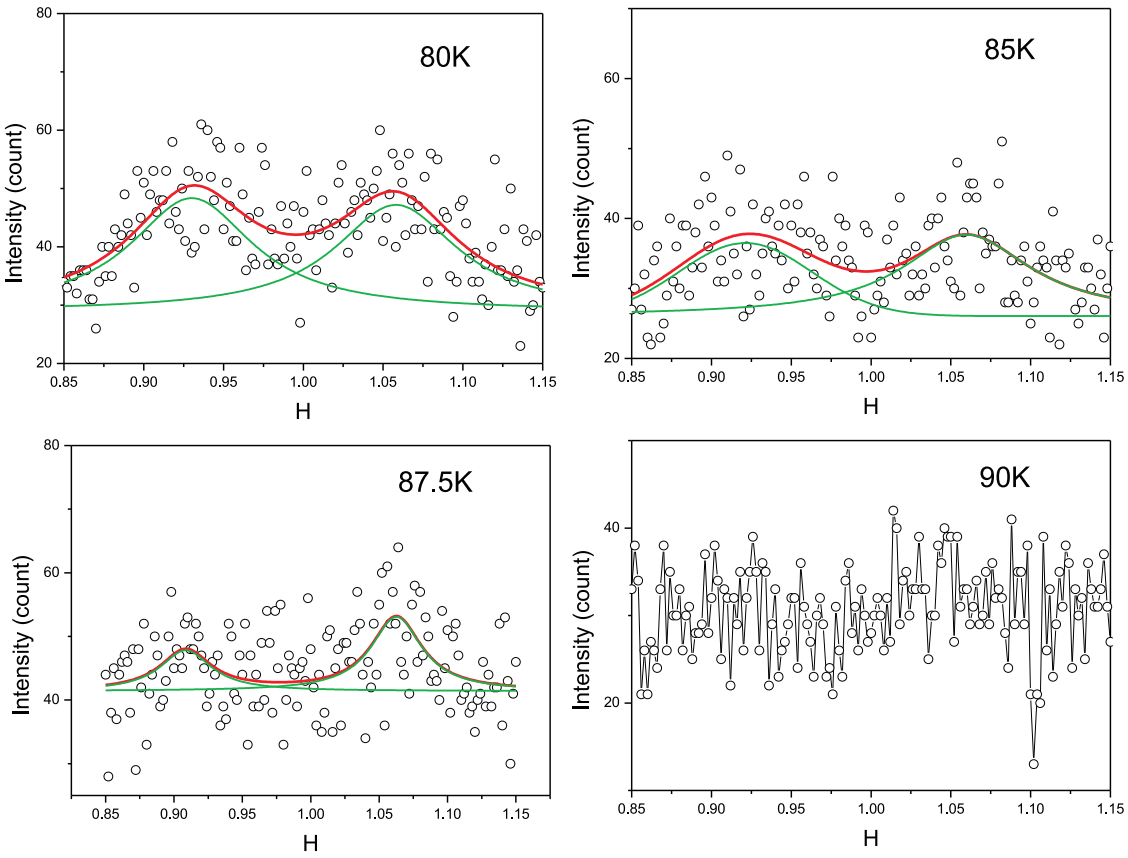

Figure B.11: q Scans centered on (1 -0.5 -9). Scans at 80, 85 and 87.5 K show a double peak as demonstrated by the successful fit of two pseudo-Voigt functions to the data (solid lines). A peak is not found in the scan at $T = 90$ K.

q Scans along a* centered at (0 -2.5 -3)

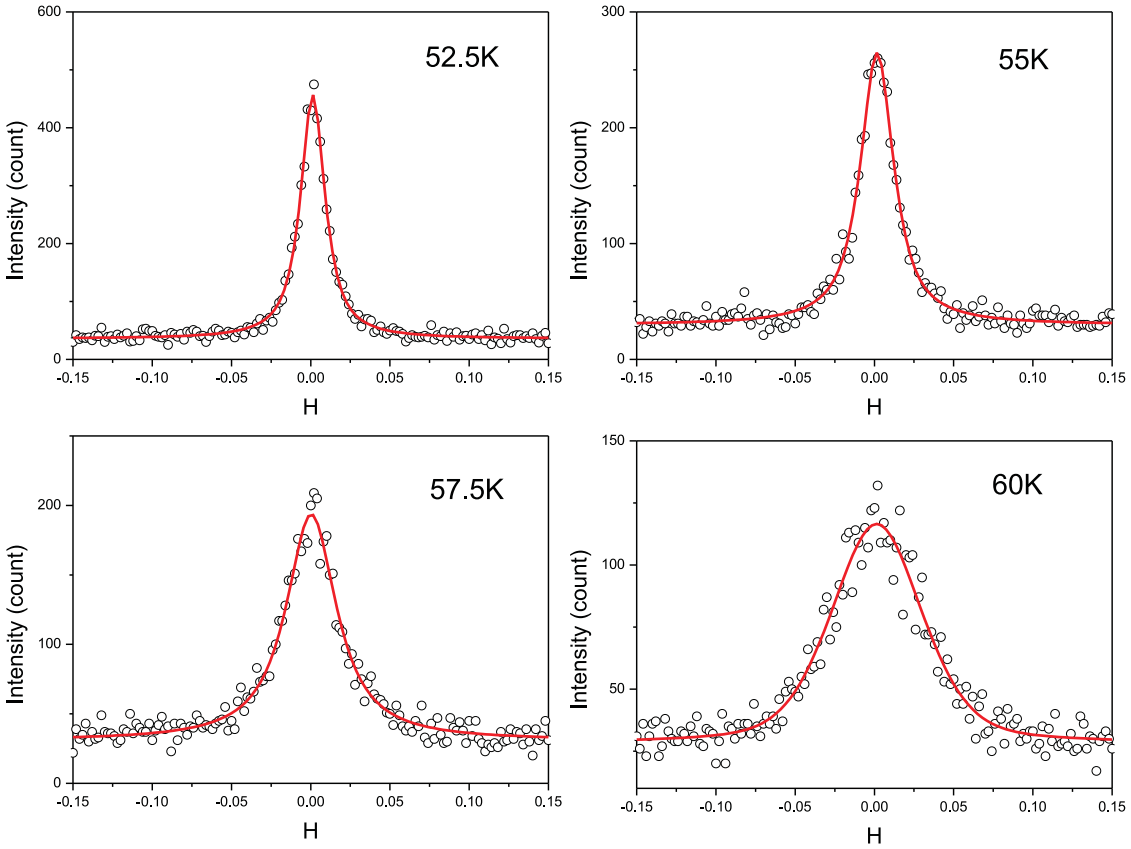

Figure B.12: q Scans centered on (0 -2.5 -3) for temperatures of 52.5, 55, 57.5 and 60 K. All scans show a single peak as demonstrated by the successful fit of a pseudo-Voigt function to the data (solid lines).

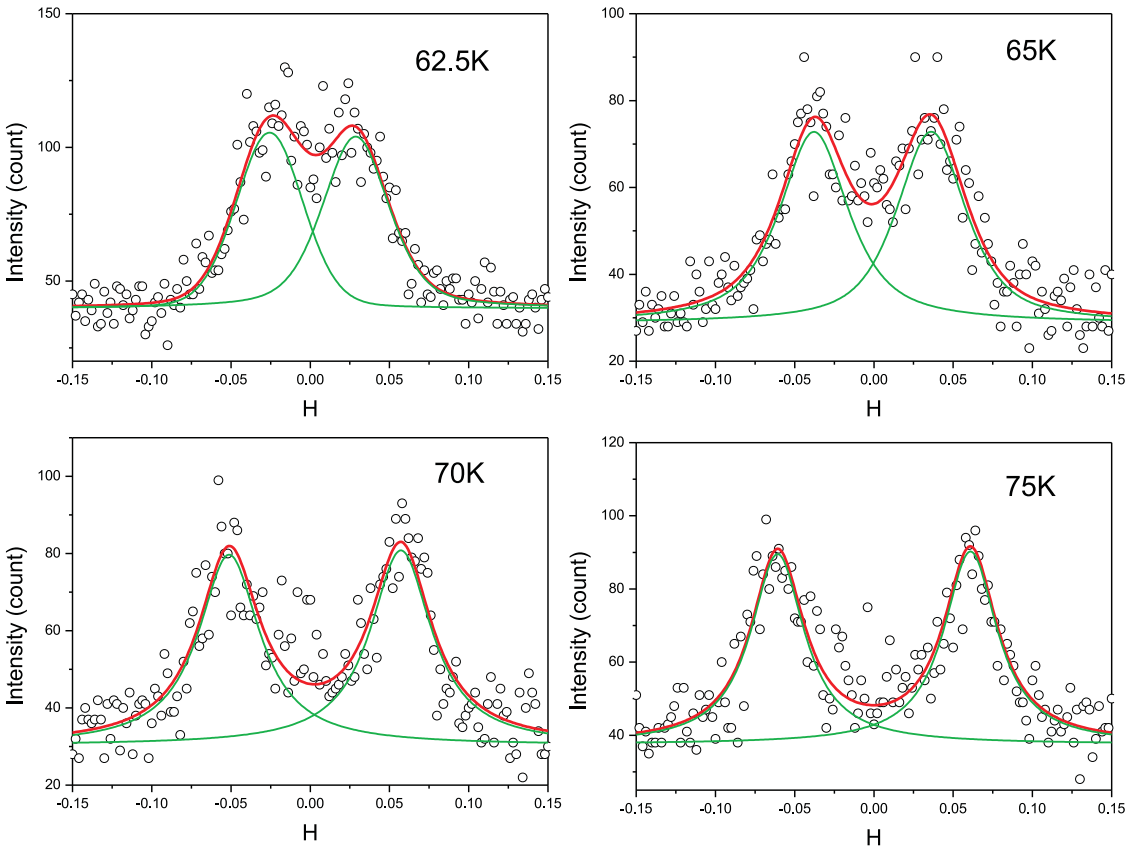

Figure B.13: q Scans centered on (0 -2.5 -3) for temperatures of 62.5, 65, 70 and 75 K. All scans show a double peak as demonstrated by the successful fit of two pseudo-Voigt functions to the data (solid lines).

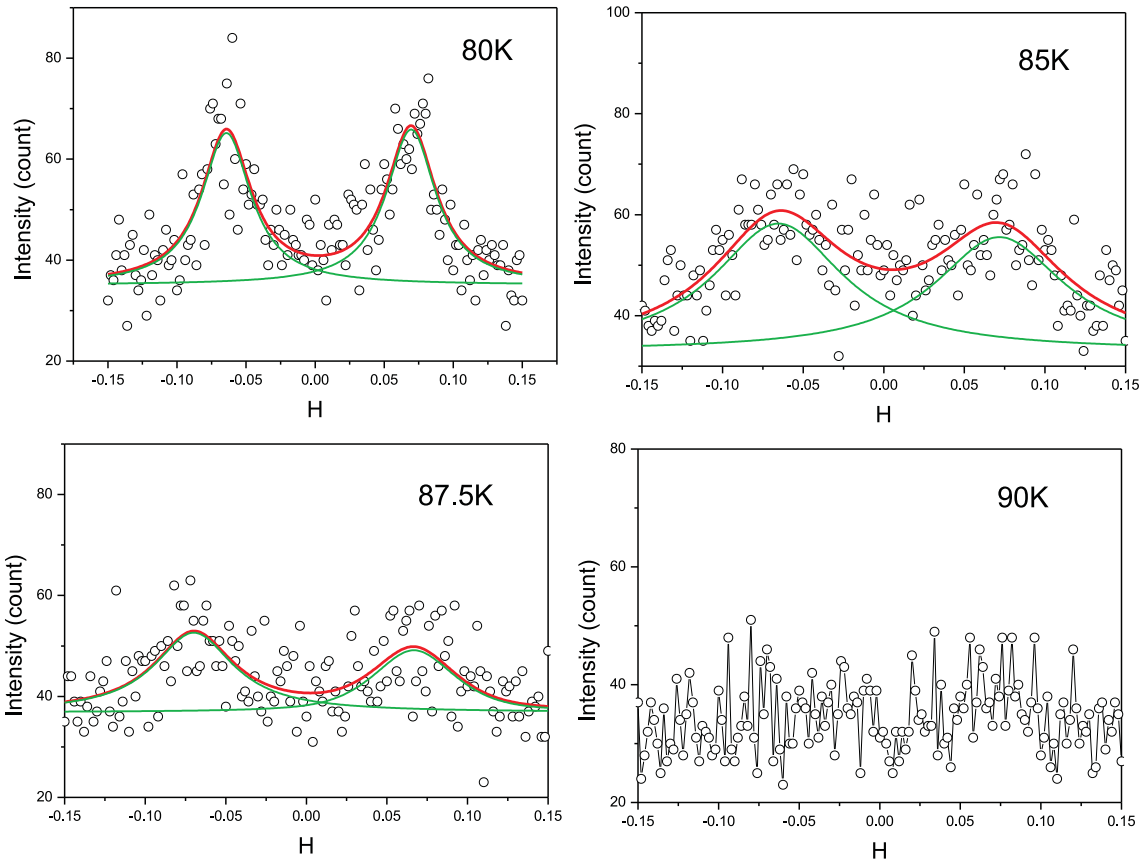

Figure B.14: q Scans centered on (0 -2.5 -3). Scans at 80, 85 and 87.5 K show a double peak as demonstrated by the successful fit of two pseudo-Voigt functions to the data (solid lines). A peak is not found in the scan at $T = 90$ K.

q Scans along a* centered at (0 -1.5 -1)

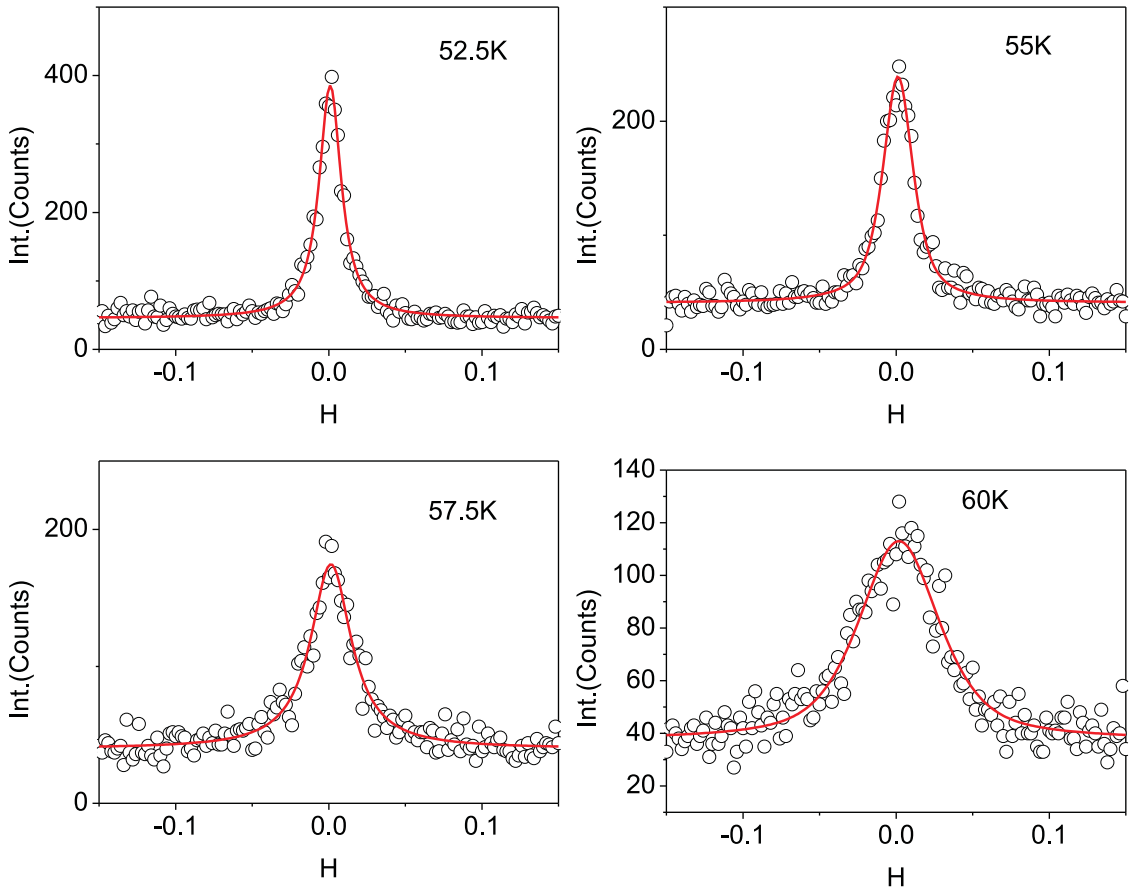

Figure B.15: q Scans centered on (0 -1.5 -1) for temperatures of 52.5, 55, 57.5 and 60 K. All scans show a single peak as demonstrated by the successful fit of a pseudo-Voigt function to the data (solid lines).

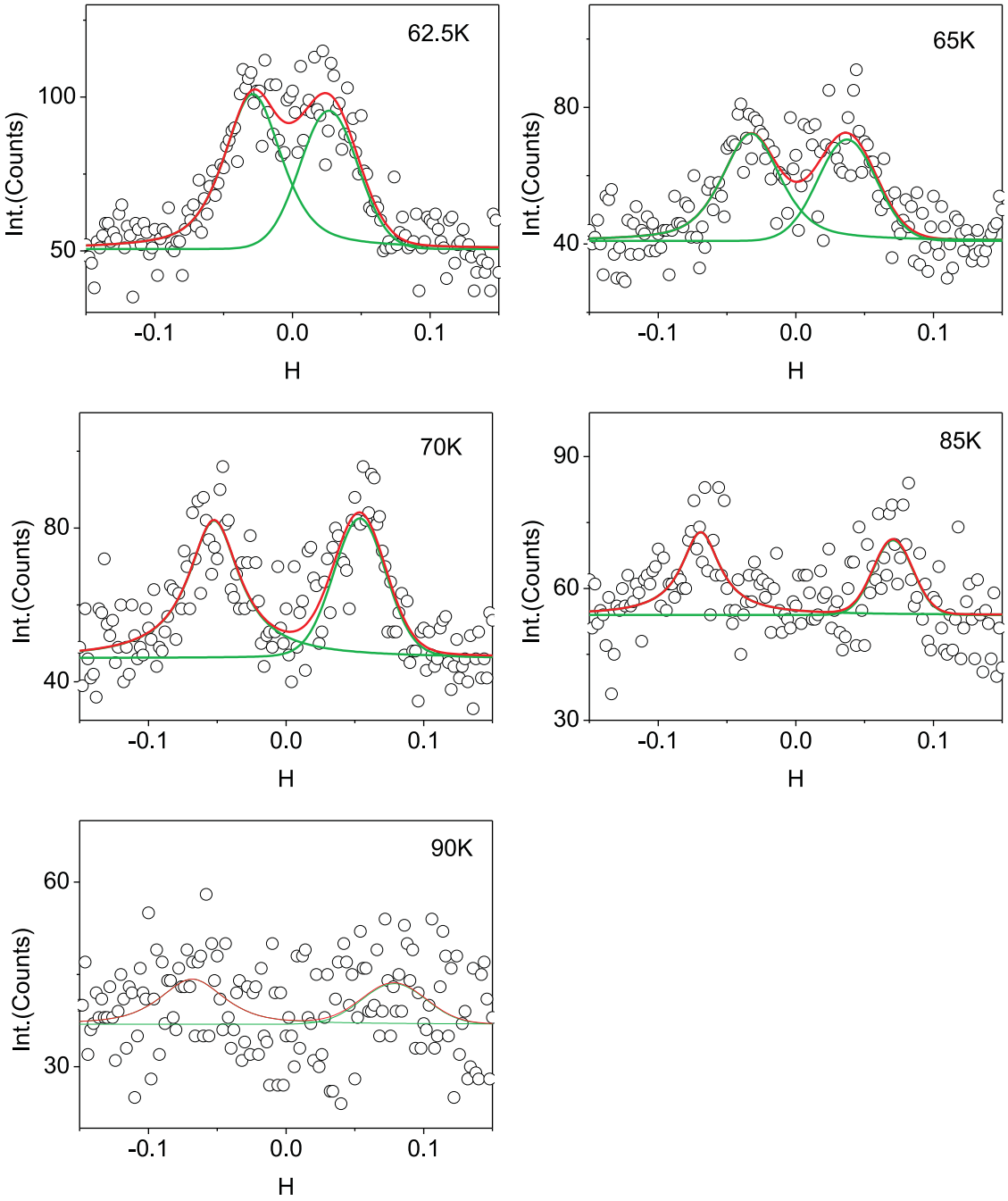

Figure B.16: q Scans centered on (0 -1.5 -1). Scans at 62.5, 65, 70 and 85 K show a double peak as demonstrated by the successful fit of two pseudo-Voigt functions to the data (solid lines). A peak is not found in the scan at $T = 90$ K.

q Scans along a* centered at (0 -1.5 -2)

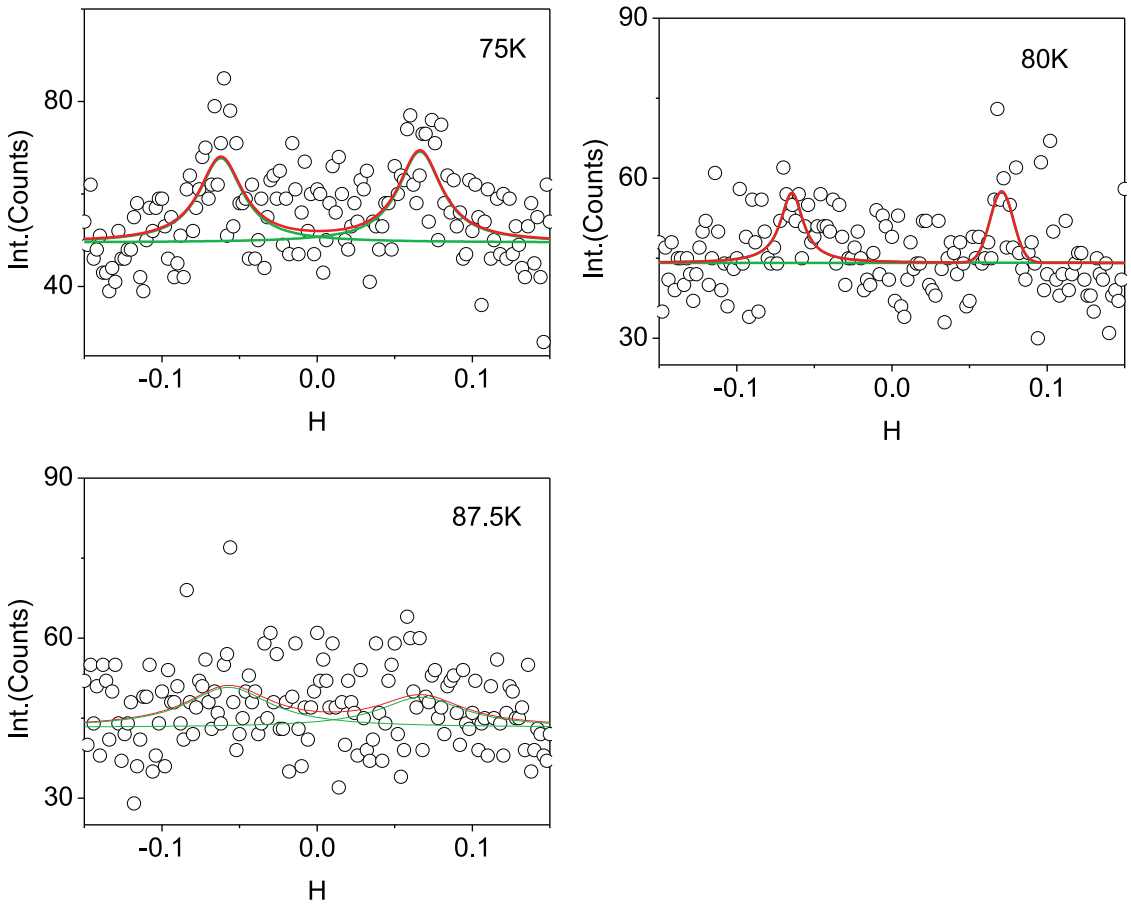

Figure B.17: q Scans centered on (1 -1.5 -2). Scans at 75 and 80 K show a double peak as demonstrated by the successful fit of two pseudo-Voigt functions to the data (solid lines). A peak is not found in the scan at $T = 87.5$ K.

B.4 ω Scans at the positions of main reflections and commensurate and incommensurate satellite reflections

ω Scans at commensurate satellite reflections

ω Scans of 1 deg wide were performed at commensurate satellite reflections in 101 steps of step size 0.01 deg. The time of exposure was 4 s per step.

ω Scans centered at (1 -0.5 -9)

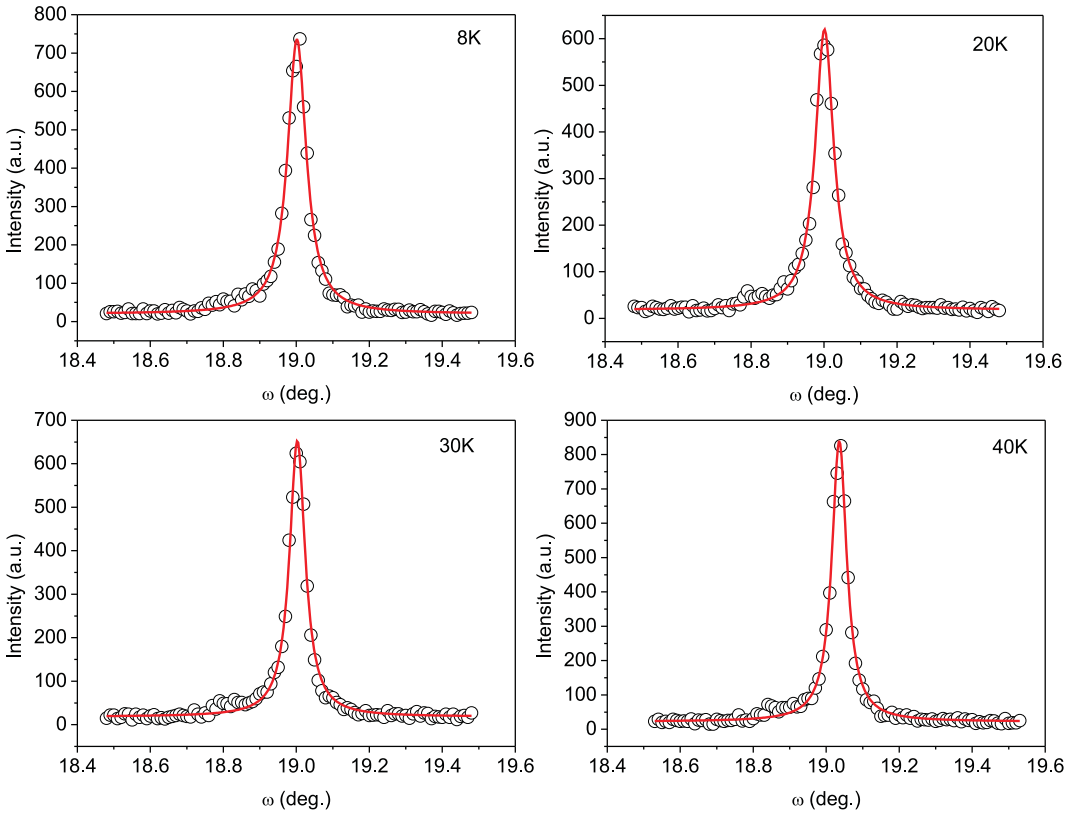

Figure B.18: ω Scans centered at (1 -0.5 -9) at different temperatures as indicated. The solid lines represent the fit by Lorentz functions. The position x_c and the FWHM of the peaks are: 19.0016(4), 0.0621(2) deg at 8 K; 19.0011(4), 0.0611(11) deg at 20 K; 19.0028(3), 0.0522(10) deg at 30 K; 19.0357(3), 0.0493(9) deg at 40 K.

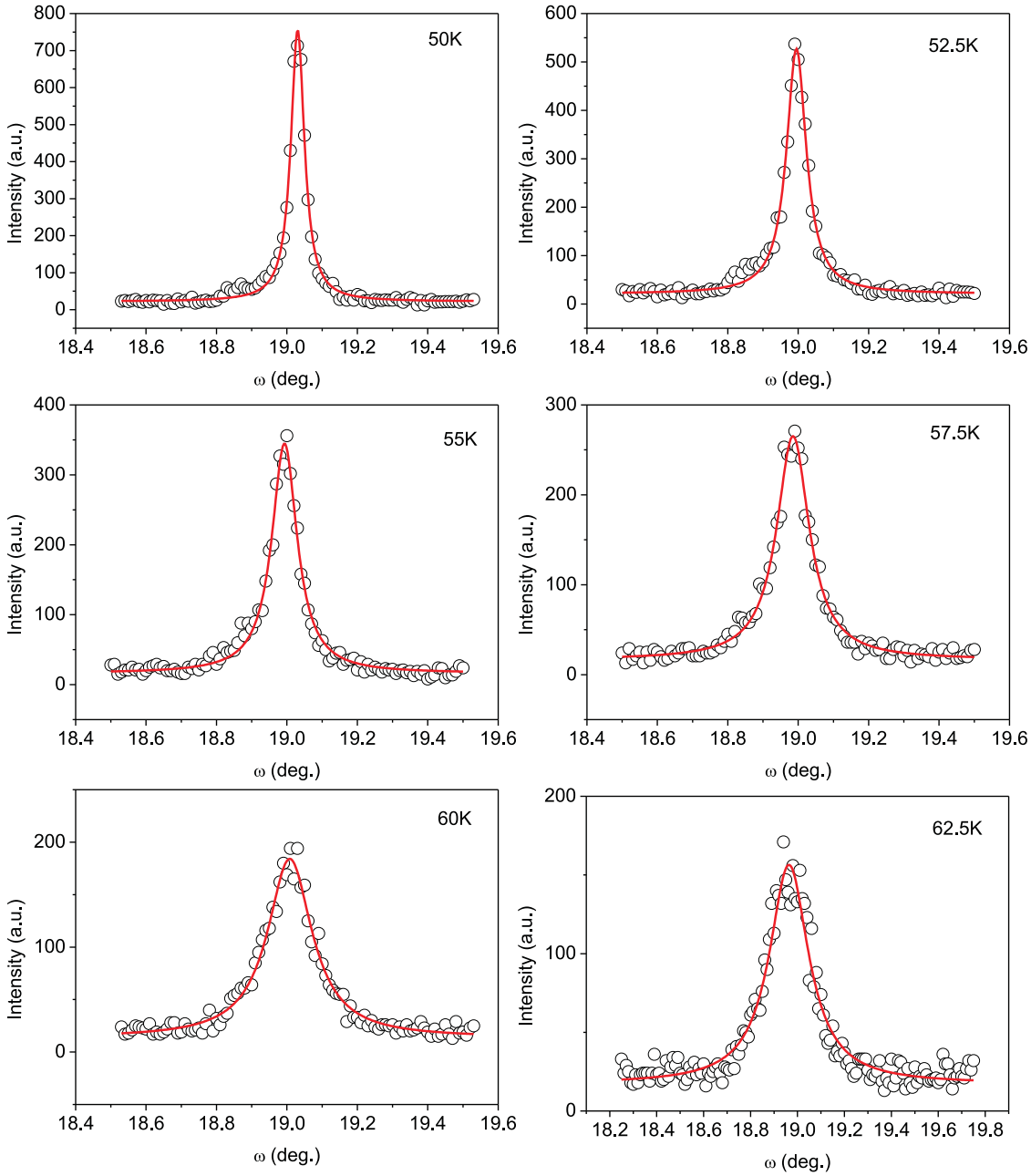

Figure B.19: ω Scans centered at (1 -0.5 -9) at different temperatures as indicated. The solid lines represent the fit by Lorentz functions. The position x_c and the FWHM of the peaks are: 19.0305(3), 0.0467(9) deg at 50 K; 18.9949(4), 0.0686(14) deg at 52.5 K; 18.9931(7), 0.0876(22) deg at 55 K; 18.9851(8), 0.1127(29) deg at 57.5 K; 19.0081(13), 0.1536(48) deg at 60 K; 18.9636(22), 0.2045(78) deg at 62.5 K.

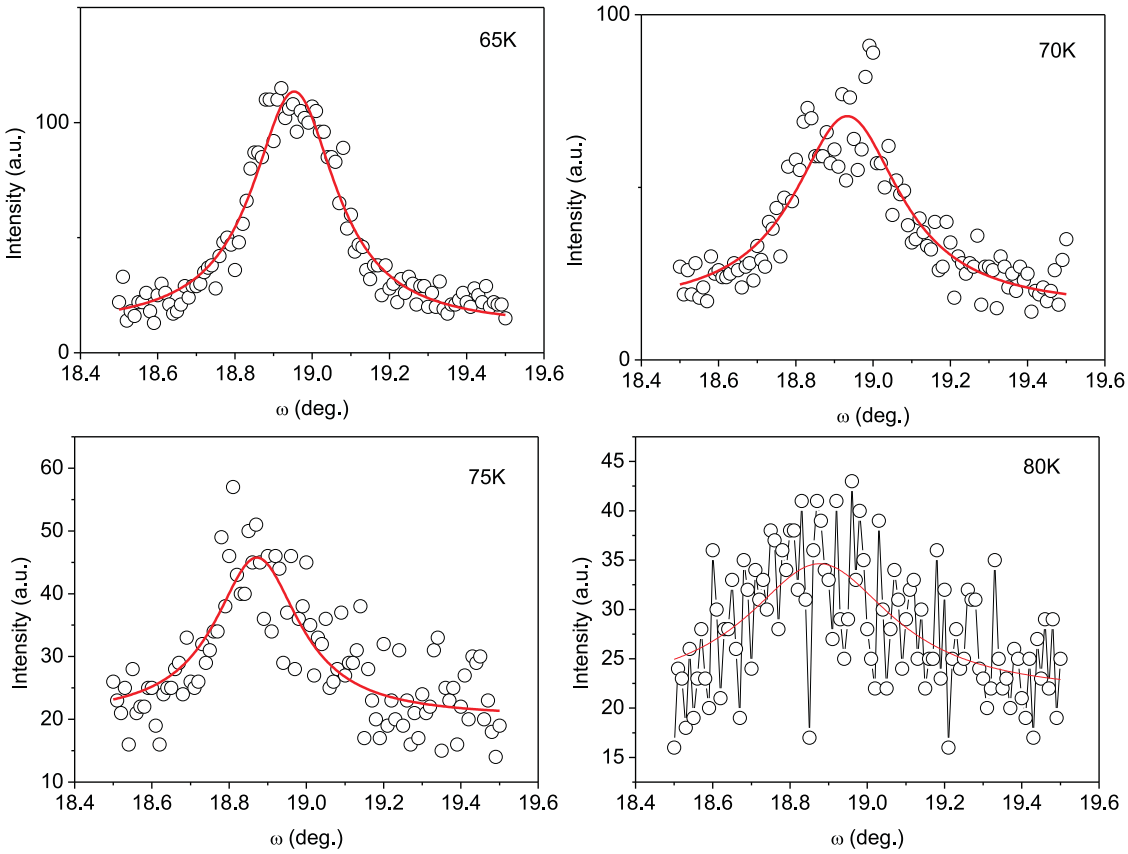

Figure B.20: ω Scans centered at (1 -0.5 -9) at different temperatures as indicated. The solid lines represent the fit by Lorentz functions. The position x_c and the FWHM of the peaks are: 18.9532(30), 0.2639(138) deg at 65 K; 18.9331(65), 0.3366(348) deg at 70 K; 18.8718(90), 0.2672(399) deg at 75 K; 18.8763(221), 0.4631(1404) deg at 80 K.

ω Scans centered at (0 -2.5 -3)

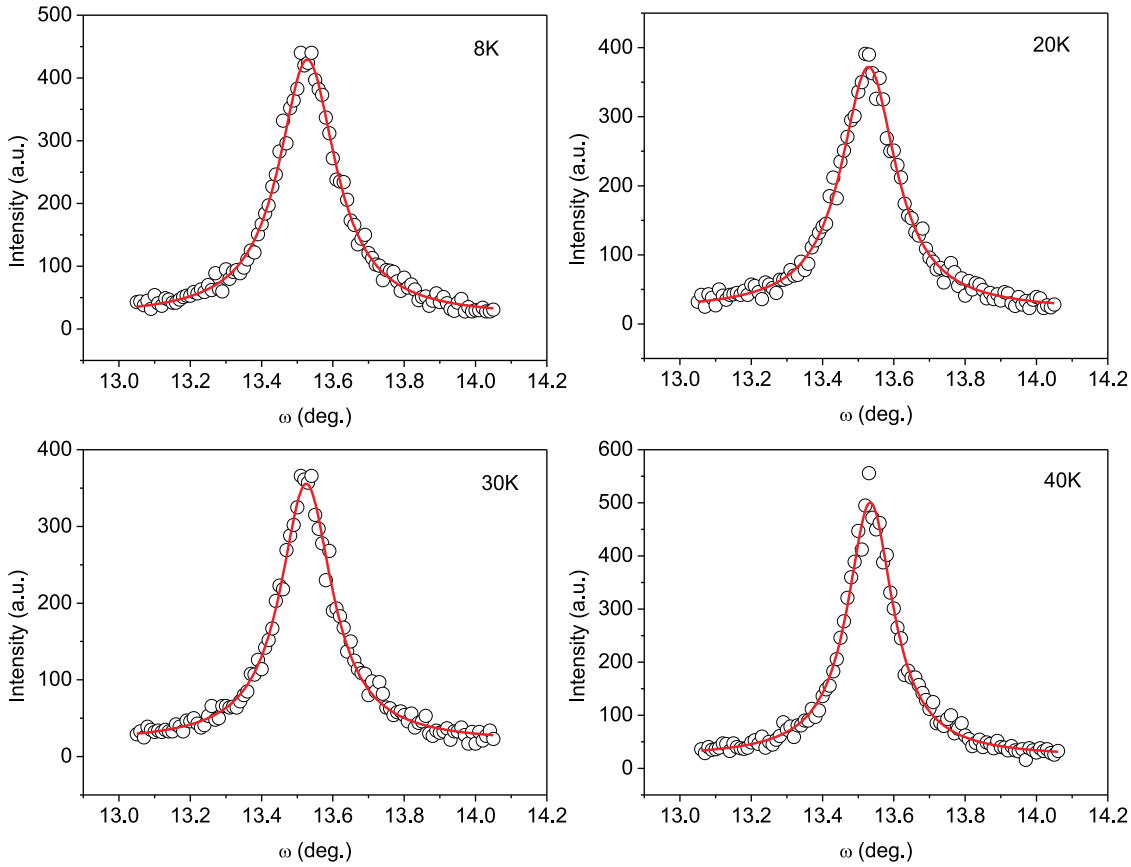

Figure B.21: ω Scans centered at (0 -2.5 -3) at different temperatures as indicated. The solid lines represent the fit by Lorentz functions. The position x_c and the FWHM of the peaks are: 13.5282(9), 0.1939(36) deg at 8 K; 13.5289(10), 0.1863(40) deg at 20 K; 13.5253(10), 0.1768(39) deg at 30 K; 13.5339(9), 0.1555(34) deg at 40 K.

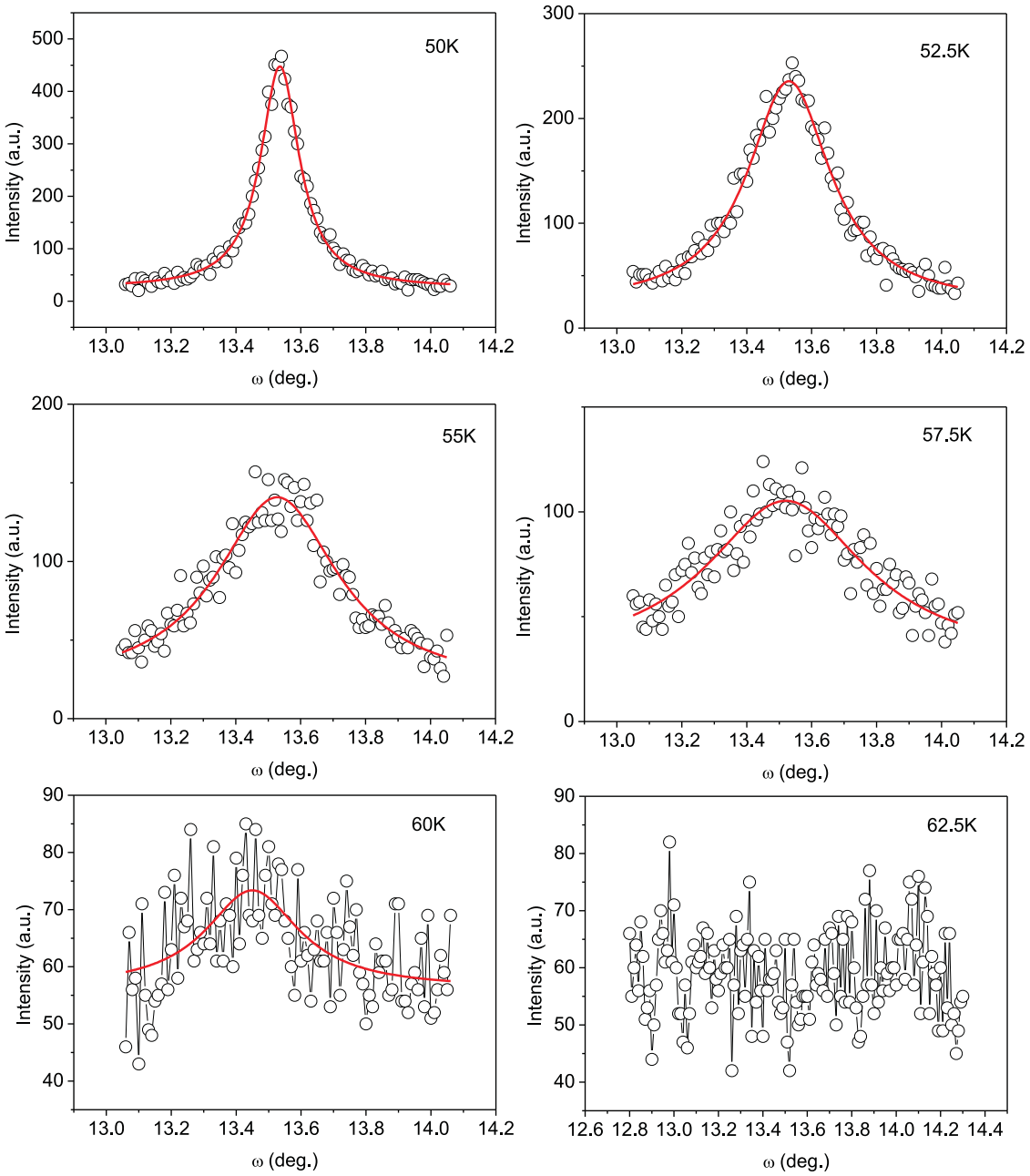

Figure B.22: ω Scans centered at (0 -2.5 -3) at different temperatures as indicated. The solid lines represent the fit by Lorentz functions. The position x_c and the FWHM of the peaks are: 13.5355(8), 0.1454(27) deg at 50 K; 13.5300(21), 0.3114(107) deg at 52.5 K; 13.5281(49), 0.4587(332) deg at 55 K; 13.5201(77), 0.5952(761) deg at 57.5 K; 13.4497(205), 0.3517(1086) deg at 60 K.

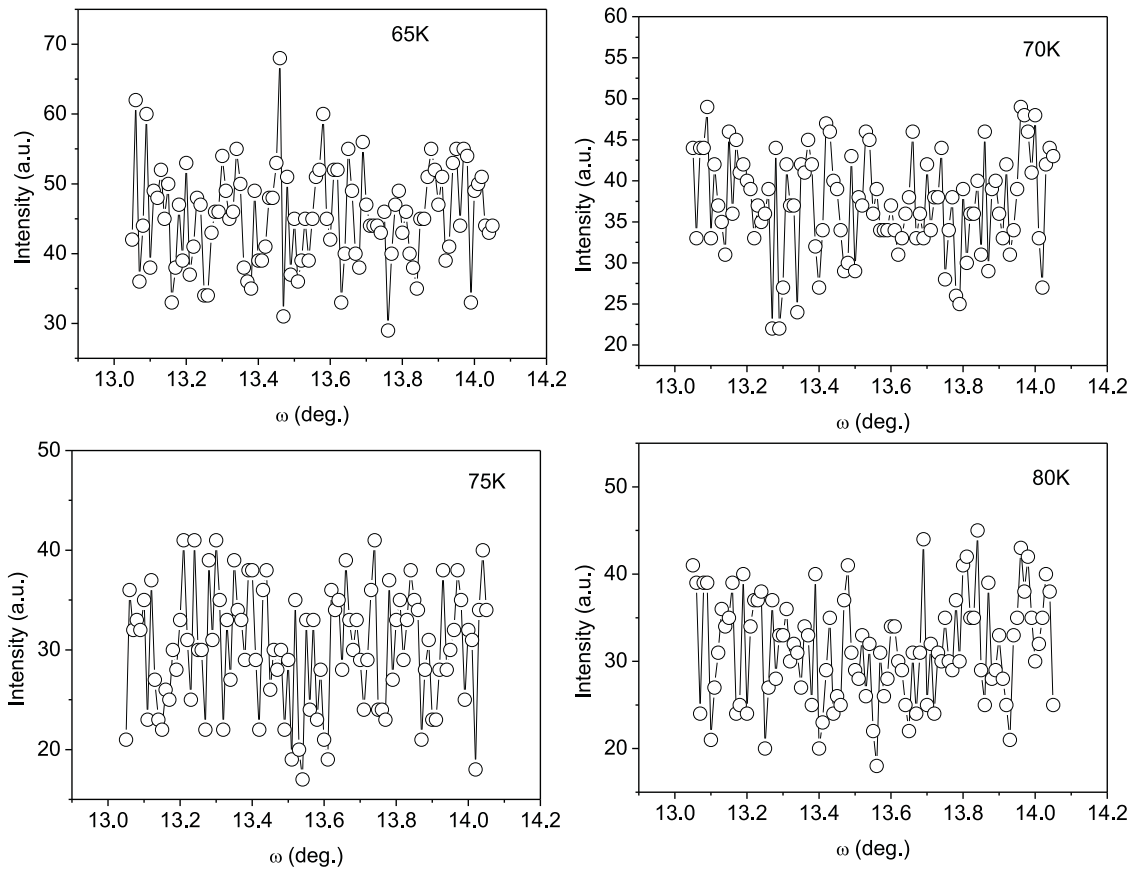

Figure B.23: ω Scans centered at (0 -2.5 -3) at different temperatures as indicated. Reflection maxima have not been observed.

ω Scans centered at (0 -1.5 -1)

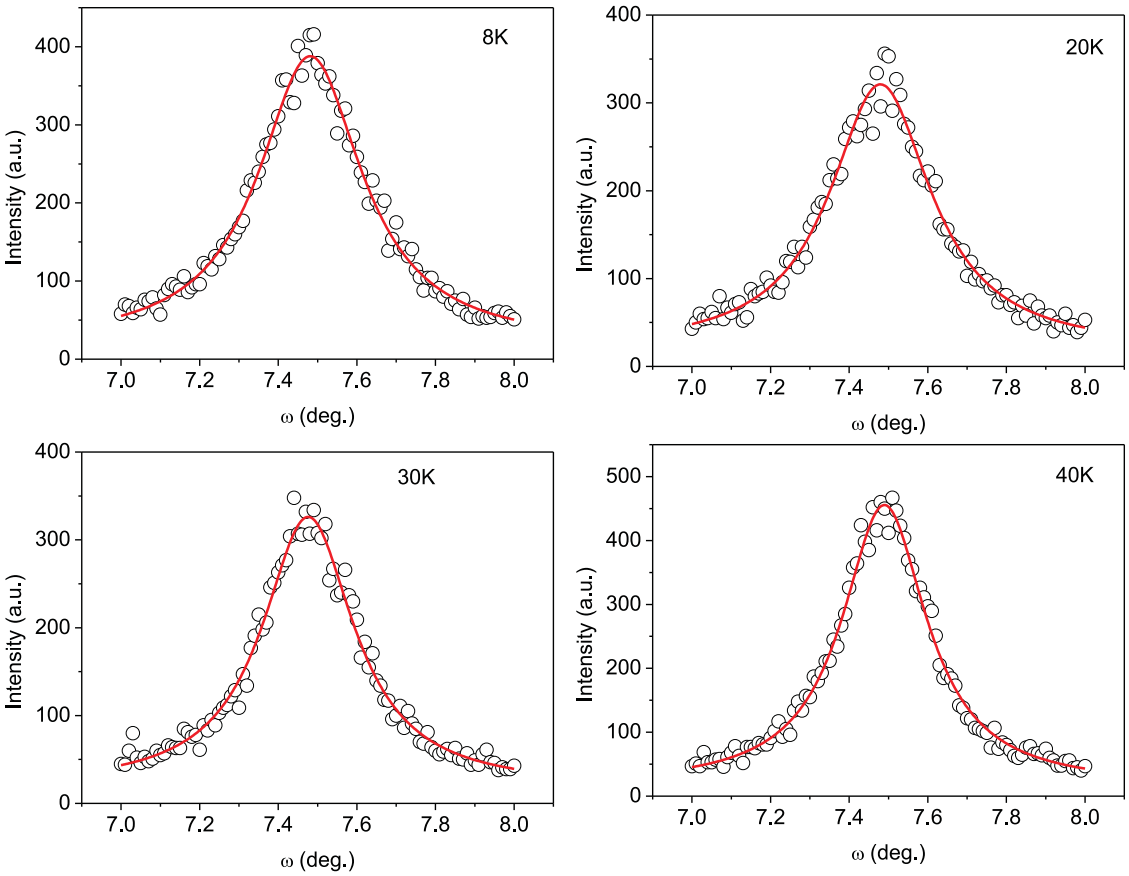

Figure B.24: ω Scans centered at (0 -1.5 -1) at different temperatures as indicated. The solid lines represent the fit by Lorentz functions. The position x_c and the FWHM of the peaks are: 7.4814(16), 0.3219(87) deg at 8 K; 7.4795(19), 0.3138(100) deg at 20 K; 7.4759(17), 0.2853(84) deg at 30 K; 7.4894(13), 0.2629(59) deg at 40 K.

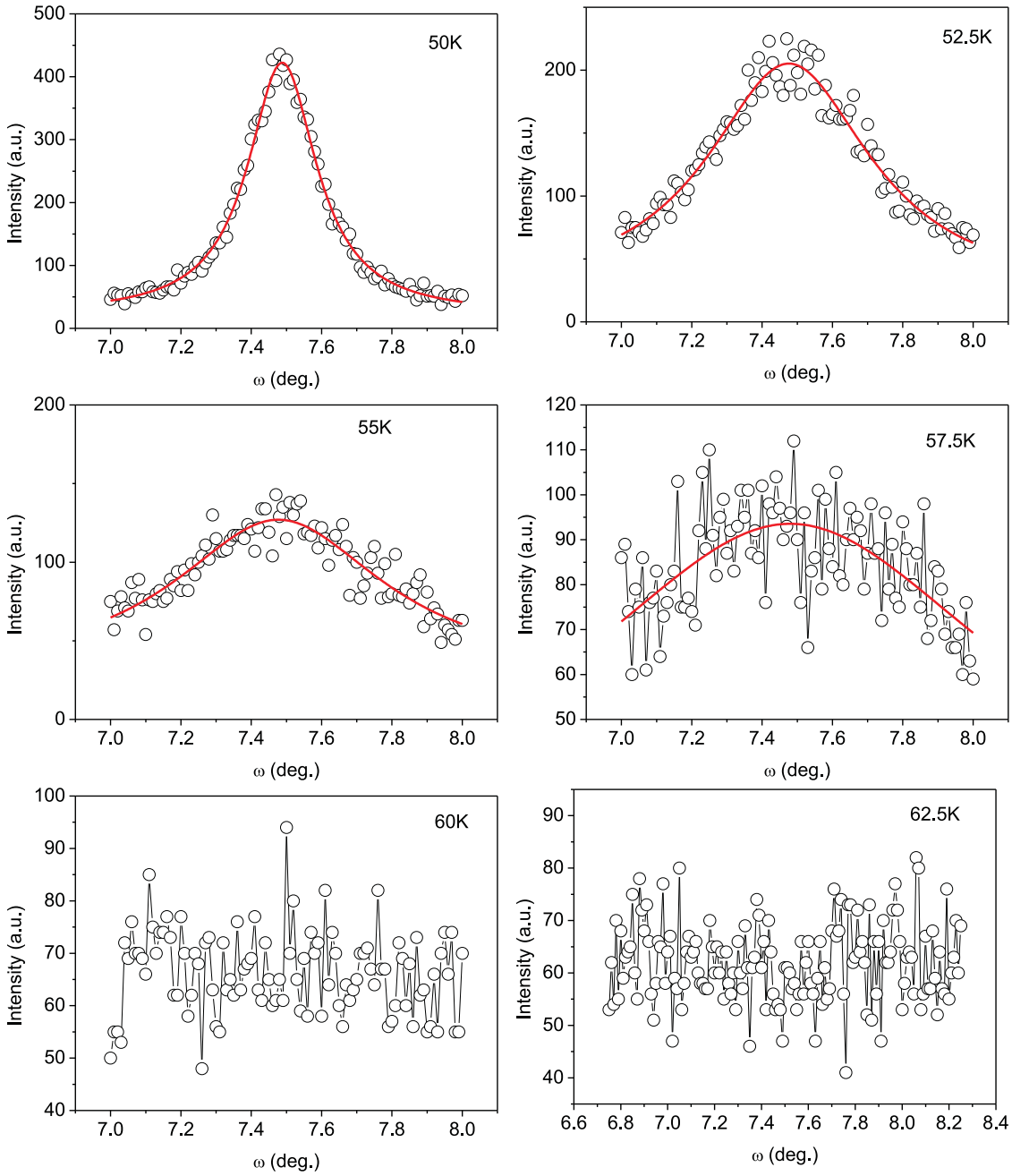

Figure B.25: ω Scans centered at (0 -1.5 -1) at different temperatures as indicated. The solid lines represent the fit by Lorentz functions. The position x_c and the FWHM of the peaks are: 7.4880(10), 0.2389(44) deg at 50 K; 7.4761(38), 0.5675(355) deg at 52.5 K; 7.4772(73), 0.7325(998) deg at 55 K; 7.4800, 1.4818(1140) deg at 57.5 K. Scans at 60 and 62.5 K do not exhibit reflection maxima.

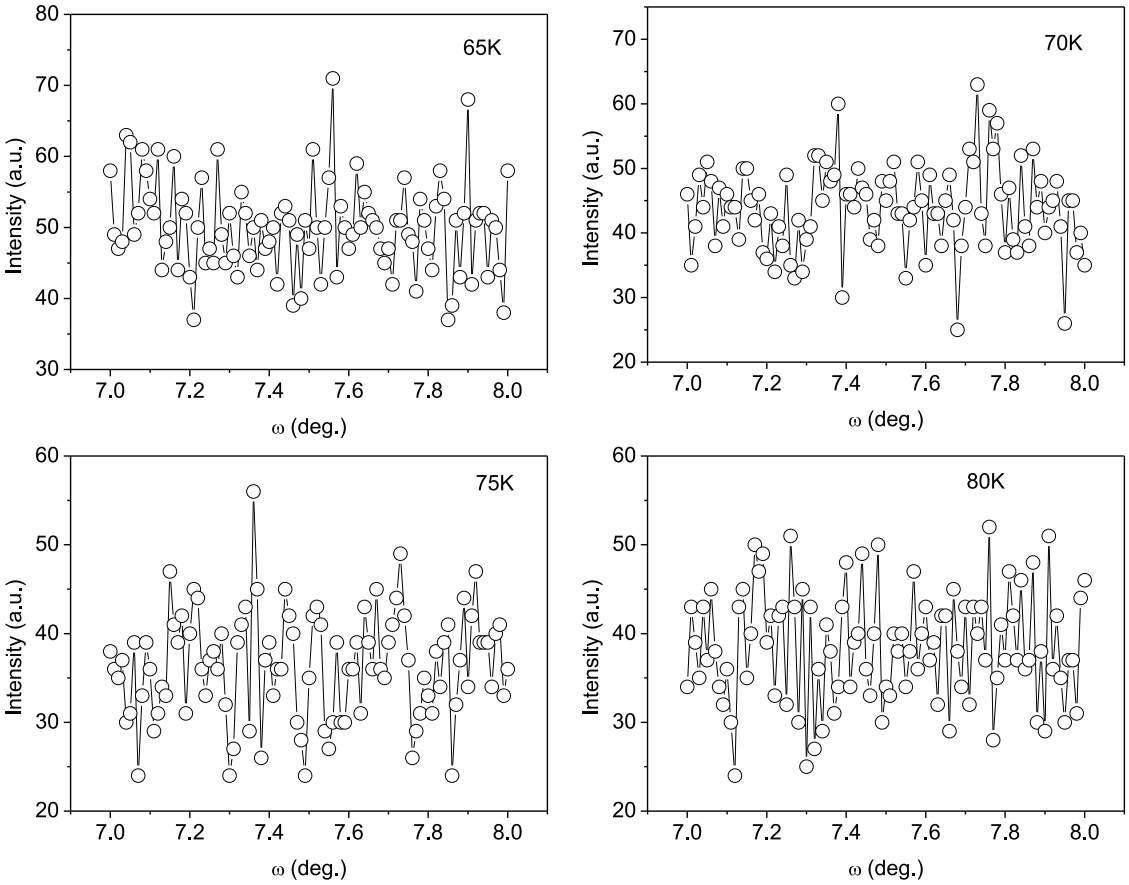

Figure B.26: ω Scans centered at (0 -1.5 -1) at different temperatures as indicated. The scans do not show any reflection maxima.

ω Scans at main reflections

ω Scans of 0.2 deg wide were performed at positions of main reflections in 101 steps of step size 0.002 deg. The time of exposure was 0.5 s per step. Here, only the scans of the reflection (1 -1 -8) are shown.

ω Scans centered at (1 -1 -8)

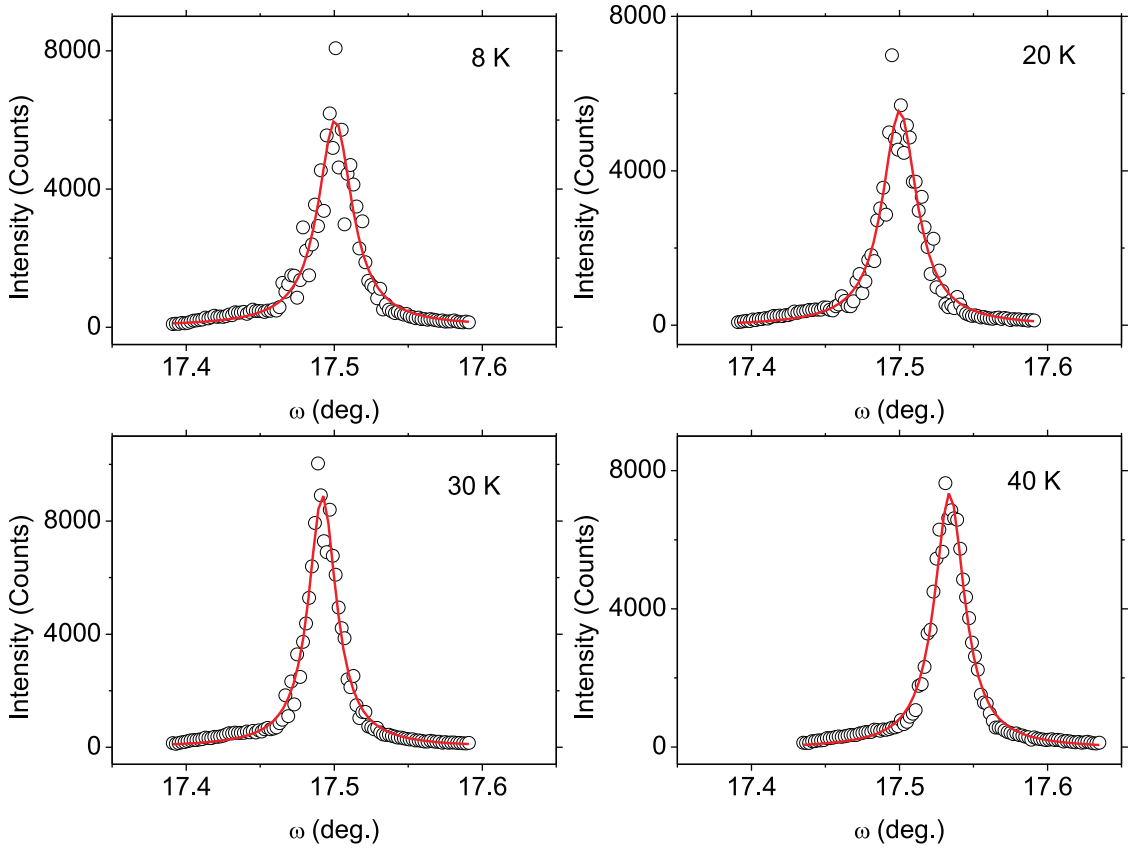

Figure B.27: ω Scans centered at (1 -1 -8) at different temperatures as indicated. The solid lines represent the fit by Lorentz functions. The position x_c and the FWHM of the peaks are: 17.5006(5), 0.0278(16) deg at 8 K; 17.5001(4), 0.0280(13) deg at 20 K; 17.4921(2), 0.0227(8) deg at 30 K; 17.5339(2), 0.0246(6) deg at 40 K.

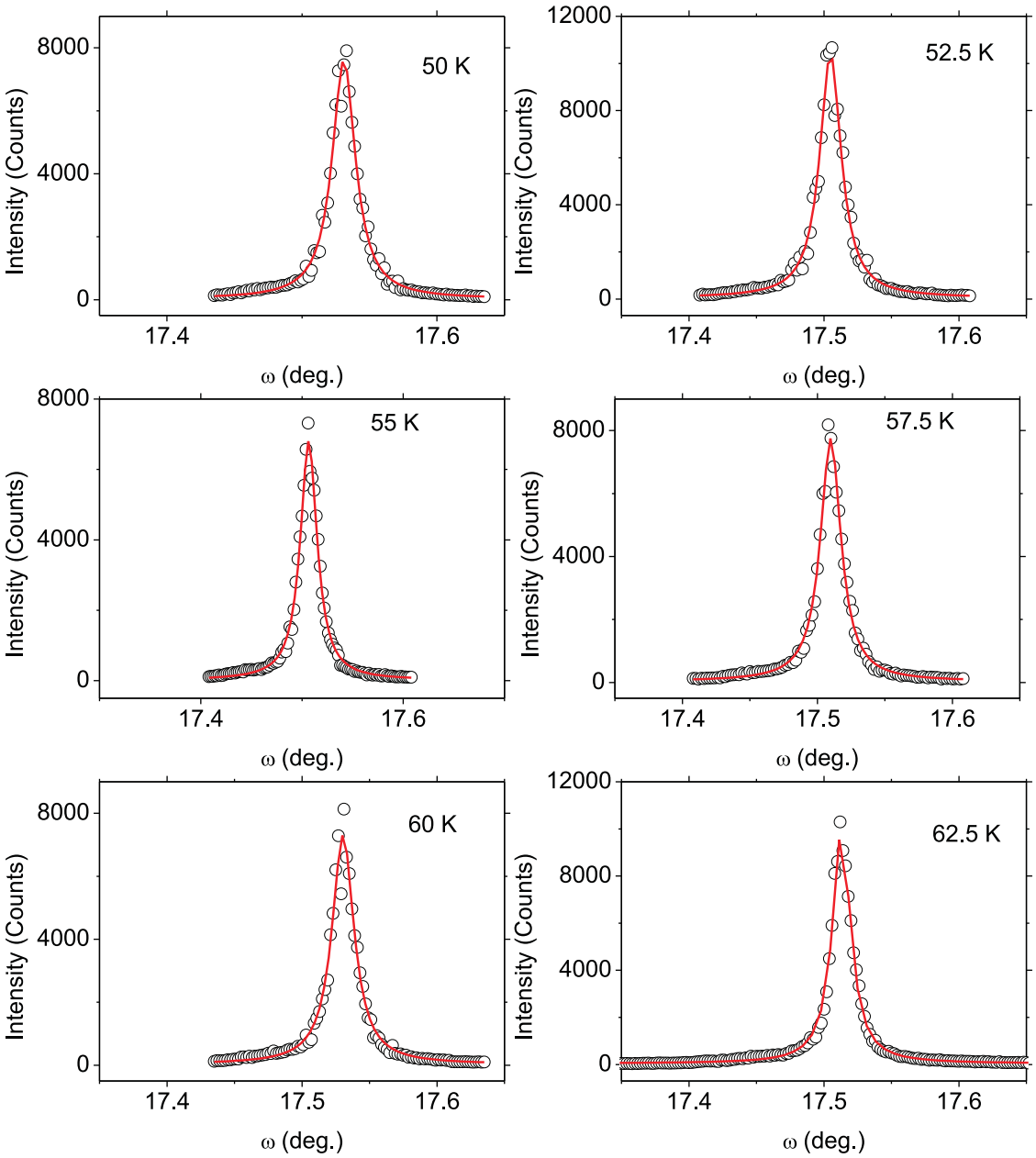

Figure B.28: ω Scans centered at (1 -1 -8) at different temperatures as indicated. The solid lines represent the fit by Lorentz functions. The position x_c and the FWHM of the peaks are: 17.5309(1), 0.0209(5) deg at 50 K; 17.5049(1), 0.0192(4) deg at 52.5 K; 17.5066(1), 0.0201(4) deg at 55 K; 17.5099(1), 0.0184(3) deg at 57.5 K; 17.5304(2), 0.0198(6) deg at 60 K; 17.5130(1), 0.0165(2) deg at 62.5 K.

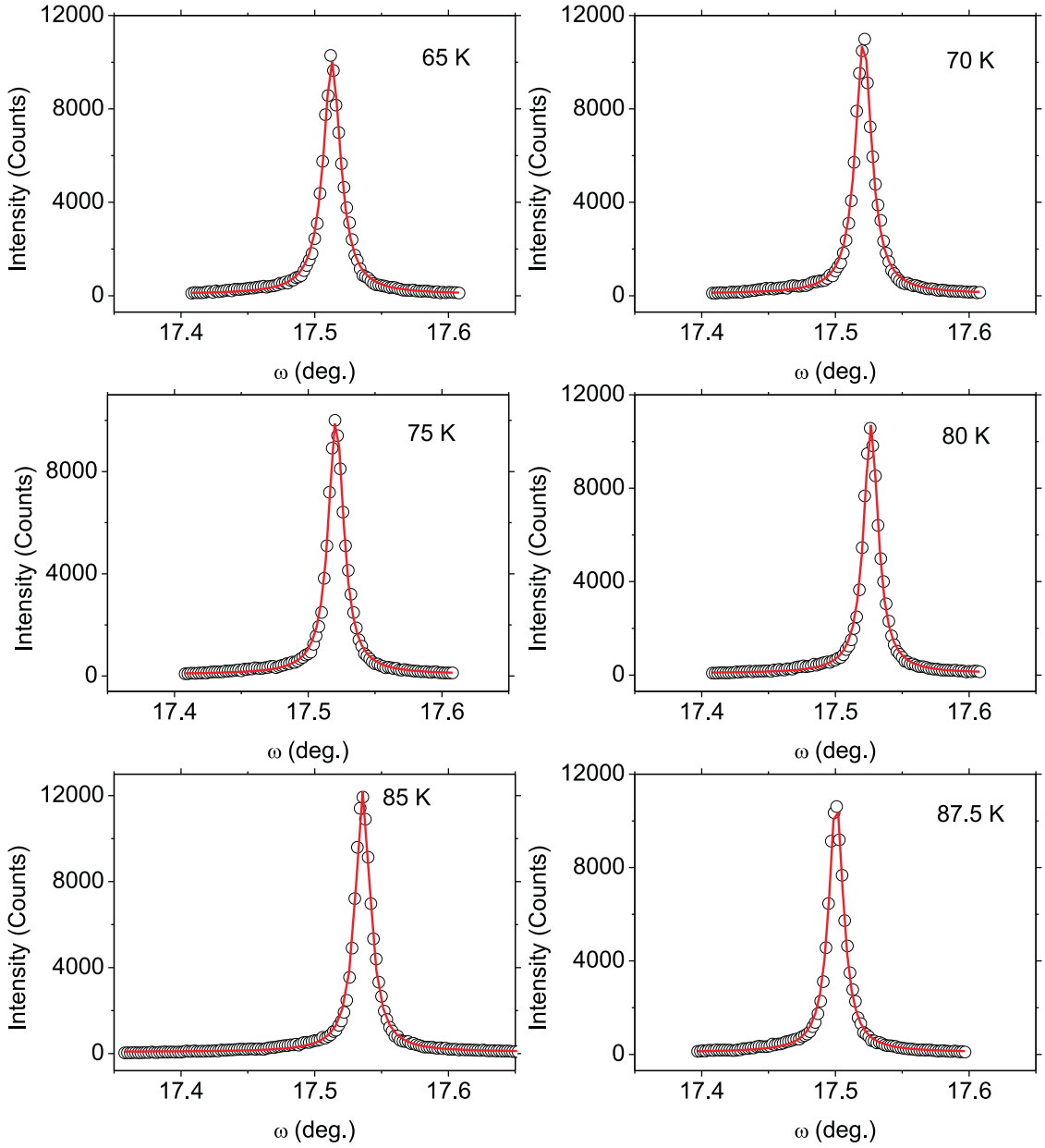

Figure B.29: ω Scans centered at (1 -1 -8) at different temperatures as indicated. The solid lines represent the fit by Lorentz functions. The position x_c and the FWHM of the peaks are: 17.5129(1), 0.0156(2) deg at 65 K; 17.5211(1), 0.0145(2) deg at 70 K; 17.5208(1), 0.0138(2) deg at 75 K; 17.5266(1), 0.0131(2) deg at 80 K; 17.53602(4), 0.0136(1) deg at 85 K; 17.5006(1), 0.0132(2) deg at 87.5 K.

Table B.2: Full-width-at-half-maximum (FWHM) of the Lorentz functions fitted to the peaks in the ω scans on satellite reflections (Figs. B.18–B.26) and on the main reflection (1 -1 -8) (Figs. B.27–B.29). These values have been plotted in Fig. 6.6 of the main article.

	1 -0.5 -9		0 -2.5 -3		0 -1.5 -1		1 -1 -8	
T (K)	FWHM	s.u.	FWHM	s.u.	FWHM	s.u.	FWHM	s.u.
8	0.06213	0.00121	0.19392	0.00362	0.32191	0.0087	0.0278	0.00162
20	0.06114	0.0011	0.18633	0.00396	0.31376	0.01004	0.02804	0.00133
30	0.05216	0.00103	0.17678	0.00386	0.28532	0.00842	0.02271	0.00078
40	0.04934	0.00088	0.15547	0.00341	0.26292	0.00591	0.02457	0.00063
50	0.04665	0.00086	0.14544	0.00272	0.23887	0.00441	0.02088	0.00047
52.5	0.06857	0.00141	0.31138	0.01067	0.56751	0.03546	0.0181	0.00018
55	0.08761	0.00218	0.45869	0.03323	0.73252	0.09979	0.0201	0.00036
57.5	0.11266	0.00285	0.59523	0.07607	–	–	0.01839	0.00034
60	0.15356	0.00475	–	–	–	–	0.01977	0.00057
62.5	0.2045	0.00772	–	–	–	–	0.01748	0.00015
65	0.26386	0.01377	–	–	–	–	0.01558	0.00022
70	0.33661	0.03477	–	–	–	–	0.01454	0.00019
75	0.26721	0.03994	–	–	–	–	0.01381	0.00018
80	0.46308	0.1404	–	–	–	–	0.01311	0.00017
85	–	–	–	–	–	–	0.01362	0.00014
87.5	–	–	–	–	–	–	0.0132	0.00019

Appendix C

Supplementary materials: Na_xTiOCl

C.1 Dependence of the scattered intensity on diffraction angle 2θ

For each Bragg reflection the scattered intensity as a function of the scattering angle 2θ has been obtained by integrating the ω–2θ maps over ω (Fig. 7.2). The resulting reflection profiles contain a single peak, which has been fitted by a pseudo-Voigt function in each case (Fig. 7.3). These data indicate the absence of any splitting of the diffraction maxima. They are thus in agreement with orthorhombic symmetry of the crystal lattice at all temperatures.

Table C.1: Position (x_c) and FWHM of the reflection profiles in Fig. 7.3, as fitted by pseudo-Voigt functions.

	2 2 0		2 0 -4		0 2 -5	
T (K)	x_c	FWHM	x_c	FWHM	x_c	FWHM
8	25.81(52)	0.01399(7)	23.47(17)	0.01067(11)	27.99(55)	0.01267(11)
298	25.72(34)	0.01372(9)	23.42(15)	0.01144(12)	27.85(33)	0.01193(5)

C.2 Dependence of the scattered intensity on angle ω

For each Bragg reflection the scattered intensity as a function of the angle ω has been obtained by integrating the ω–2θ maps over 2θ (Fig. 7.2). The resulting reflection profiles of (2 2 0) and (0 2 -5) contain peaks with long shoulders in different sides at both 298 K and 8 K. The profile of (2 0 -4) at 298 K shows a single peak, while that at 8 K displays a single peak with a nasty shoulder (Fig. C.1).

The steps size of these profiles is 0.002°. Without considering the shoulders, the FWHM of (2 2 0), (2 0 -4), (0 2 -5) are listed in Table C.2.

Table C.2: FWHM of the reflection profiles in Fig. C.1, as obtained by counting the data points.

	FWHM		
T (K)	2 2 0	2 0 -4	0 2 -5
8	0.011(1)	0.009(1)	0.013(1)
298	0.014(1)	0.011(1)	0.014(1)

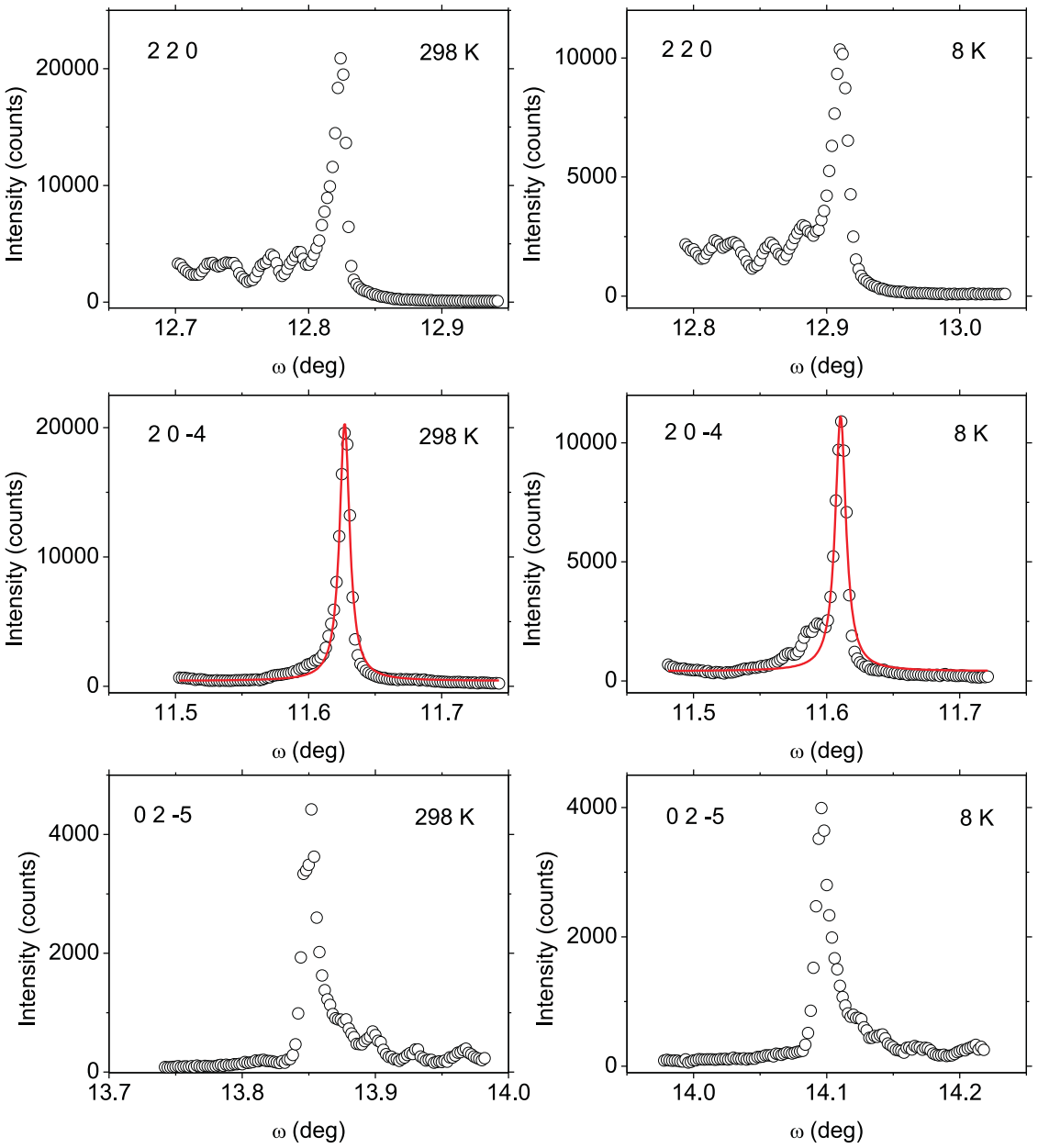

Figure C.1: Reflection profiles of reflections for two different temperatures, as indicated. They have been obtained by integration along 2θ of the data in Fig. 7.2. The profiles of (2 0 -4) at both 298 K and 8 K are fitted by Lorentz functions, resulting in the FWHM of 0.0092(2)° and 0.0098(4)°, respectively.

C.3 Reflection positions by q scans

q Scans at selected superlattice positions have been measured in dependence of temperature. They allow the determination of the components of the commensurate and incommensurate modulation wave vectors at each temperature.

q Scans have been performed along $\mathbf{a}^*$ centered at commensurate positions (h k+$\frac{1}{2}$ l). The step size of scans is 0.002 and the exposure time was 4 s per step.

q Scans along a* centered at (2 3.5 1)

For the q scans at temperatures of 64, 64.5, 65 and 66 K, please refer to main text (Chapter 7, Fig. 7.4)

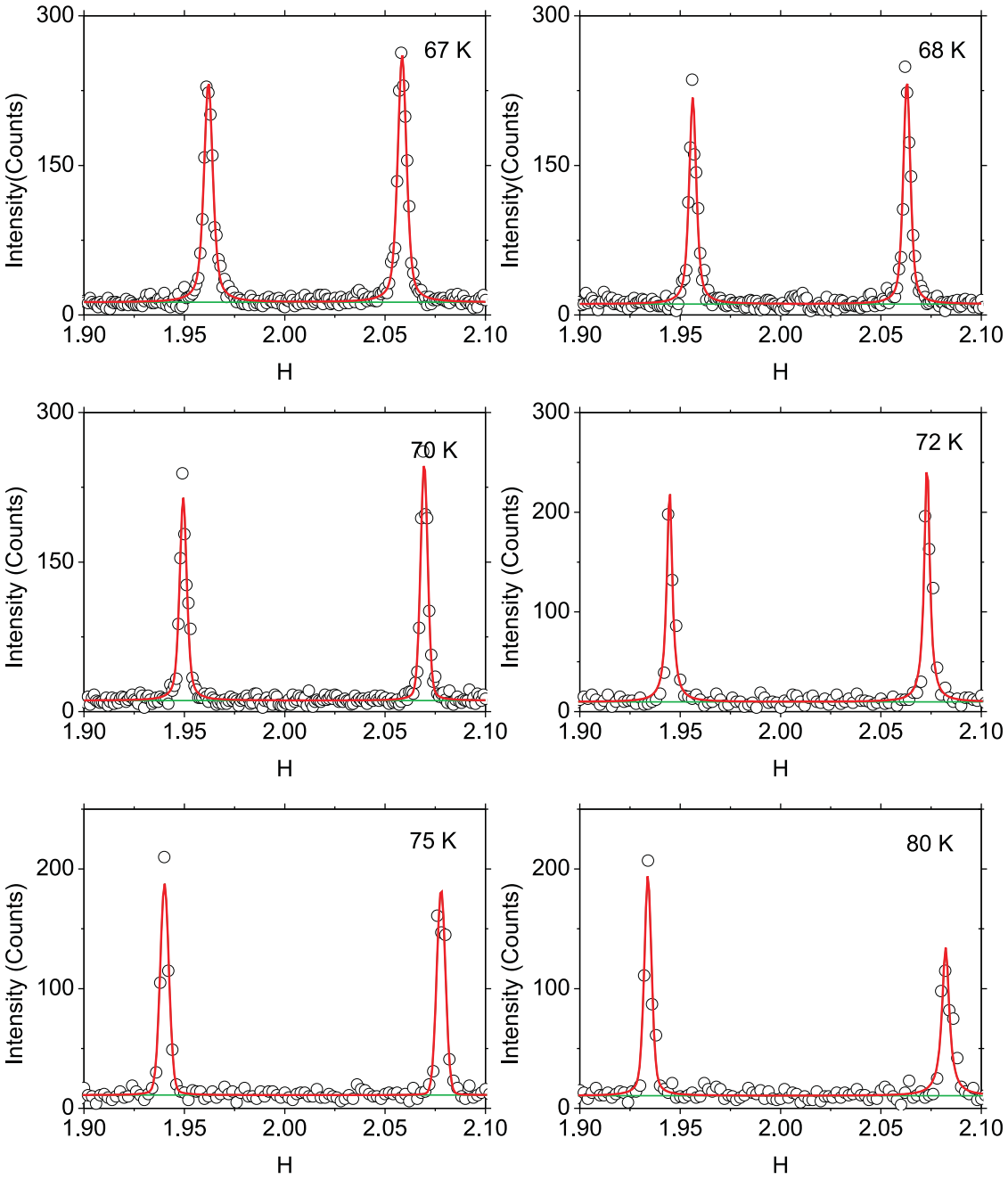

Figure C.2: q Scans centered on (2 3.5 1) for temperatures of 67, 68, 70, 72, 75 and 80 K. All scans show a double peak as demonstrated by the successful fit of two pseudo-Voigt functions to the data (solid lines).

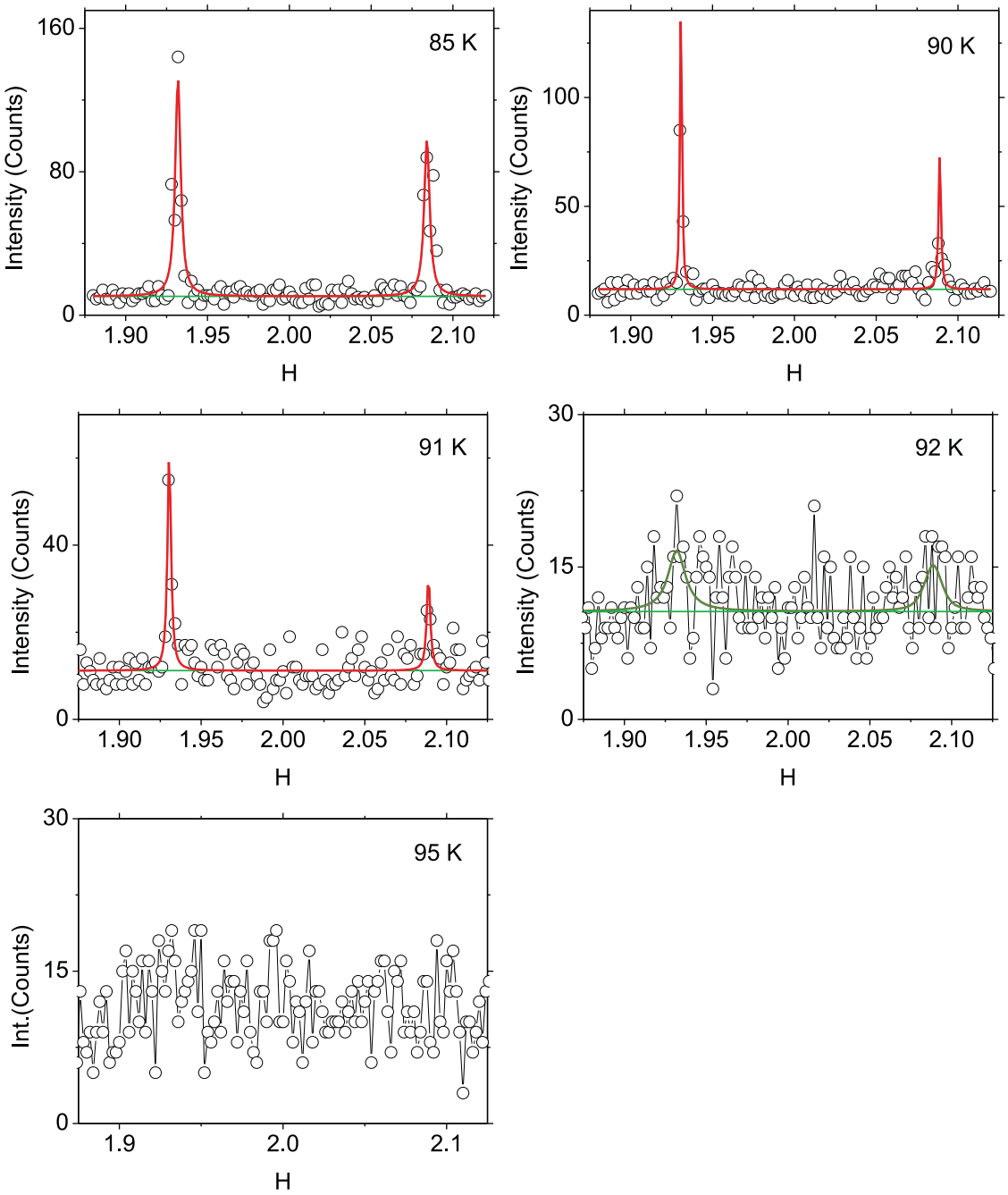

Figure C.3: q Scans centered on (2 3.5 1). Scans at 85, 90 and 91 K show a double peak as demonstrated by the successful fit of two pseudo-Voigt functions to the data (solid lines). A clear peak is not found in the scans at 92 and 95 K.

q Scans along a* centered at (2 3.5 -1)

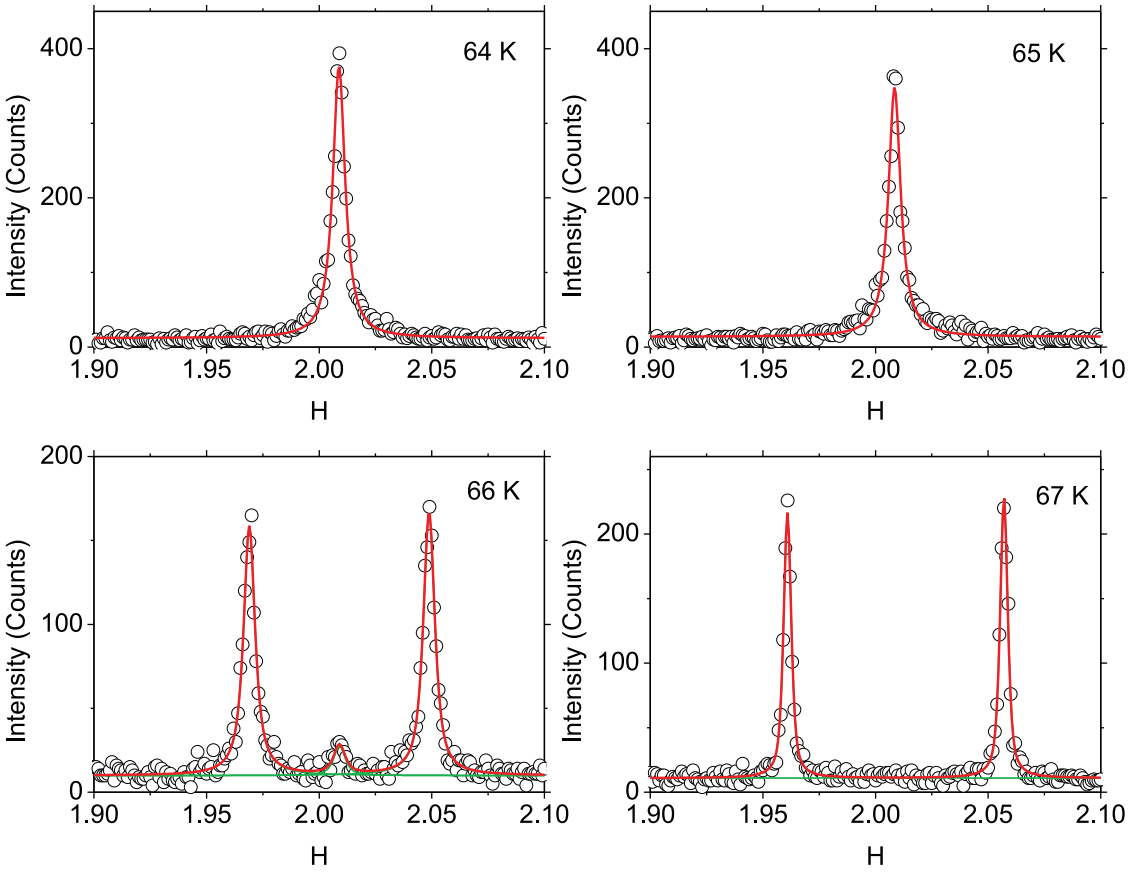

Figure C.4: q Scans centered on (2 3.5 -1) for temperatures of 64, 65, 66 and 67 K. First two scans show a single peak as demonstrated by the successful fit of a pseudo-Voigt function to the data (solid lines). The scan at 66 K is fitted by three pseudo-Voigt function. The scan at 67 K is fitted by two pseudo-Voigt function.

Calculations of component $\mathbf{q}_1$ of the modulation wave vector

Table C.3: Position (x_{c1} and x_{c2}) and FWHM of the reflection profiles in Figs. 7.4 and C.2–C.3, as fitted by pseudo-Voigt functions.

T (K)	x_{c1}	x_{c2}	x_{c2}-x_{c1}	q_1	FWHM
65	1.9827(8)	2.0353(12)	0.0526(14)	0.0263(7)	–
66	1.9672(2)	2.0534(2)	0.0862(3)	0.0431(2)	0.0064(2)
67	1.9620(2)	2.0585(1)	0.0965(2)	0.0483(1)	0.0052(1)
68	1.9562(2)	2.0629(2)	0.1067(3)	0.0534(2)	0.0042(1)
70	1.9494(2)	2.0695(2)	0.1201(3)	0.0601(2)	0.0042(1)
72	1.9447(4)	2.0730(4)	0.1283(6)	0.0642(3)	0.0032(6)
75	1.9401(3)	2.0779(3)	0.1378(4)	0.0689(2)	0.0051(2)
80	1.9339(3)	2.0823(5)	0.1484(6)	0.0742(3)	0.0043(2)
85	1.9320(5)	2.0841(8)	0.1521(9)	0.0761(5)	0.0040(4)
90	1.9307(3)	2.0889(8)	0.1582(9)	0.0791(5)	0.0017(5)
91	1.9305(7)	2.0889(20)	0.1584(21)	0.0792(11)	0.0025(8)

Table C.4: Position (x_{c1} and x_{c2}) and FWHM of the reflection profiles in Figs. C.4, as fitted by pseudo-Voigt functions.

T (K)	x_{c1}	x_{c2}	x_{c2}-x_{c1}	q_1	FWHM
66	1.9690(2)	2.0488(387)	0.0798(387)	0.0399(194)	0.0061(2)
67	1.9609(1)	2.0571(1)	0.0962(1)	0.0481(1)	0.0040(1)

C.4 ω Scans at the positions of commensurate and incommensurate satellite reflections

ω Scans of 1 deg wide were performed at commensurate and incommensurate satellite reflections in 101 steps of step size 0.01 deg. The time of exposure was 4 s per step.

ω Scans at commensurate satellite reflections

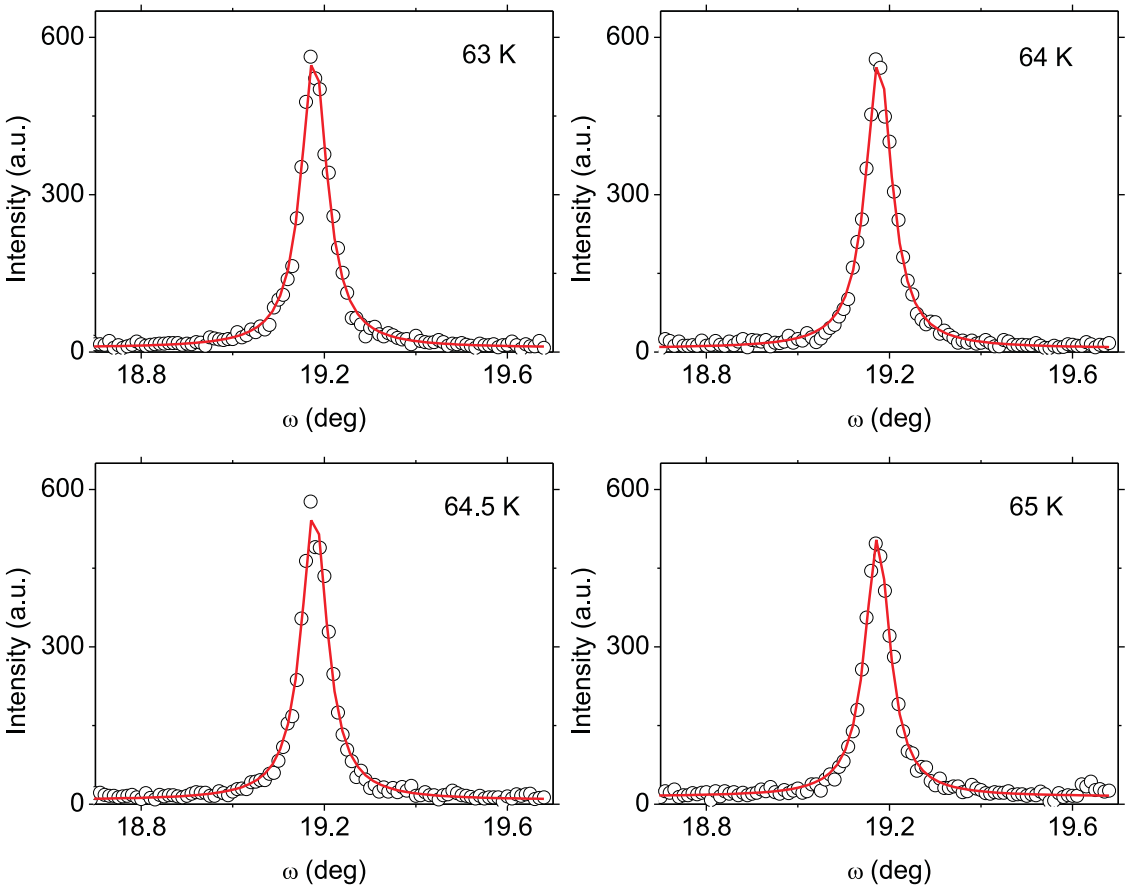

Figure C.5: ω Scans centered at (2 3.5 1) at different temperatures as indicated. The solid lines represent the fit by Lorentz functions. The position x_c and the FWHM of the peaks are: 19.1778(4), 0.0690(13) 63 K; 19.1770(4), 0.0688(11) 64 K; 19.1781(4), 0.0686(15) 64.5 K; 19.1741(4), 0.0662(12) 65 K.

ω Scans at incommensurate satellite reflections

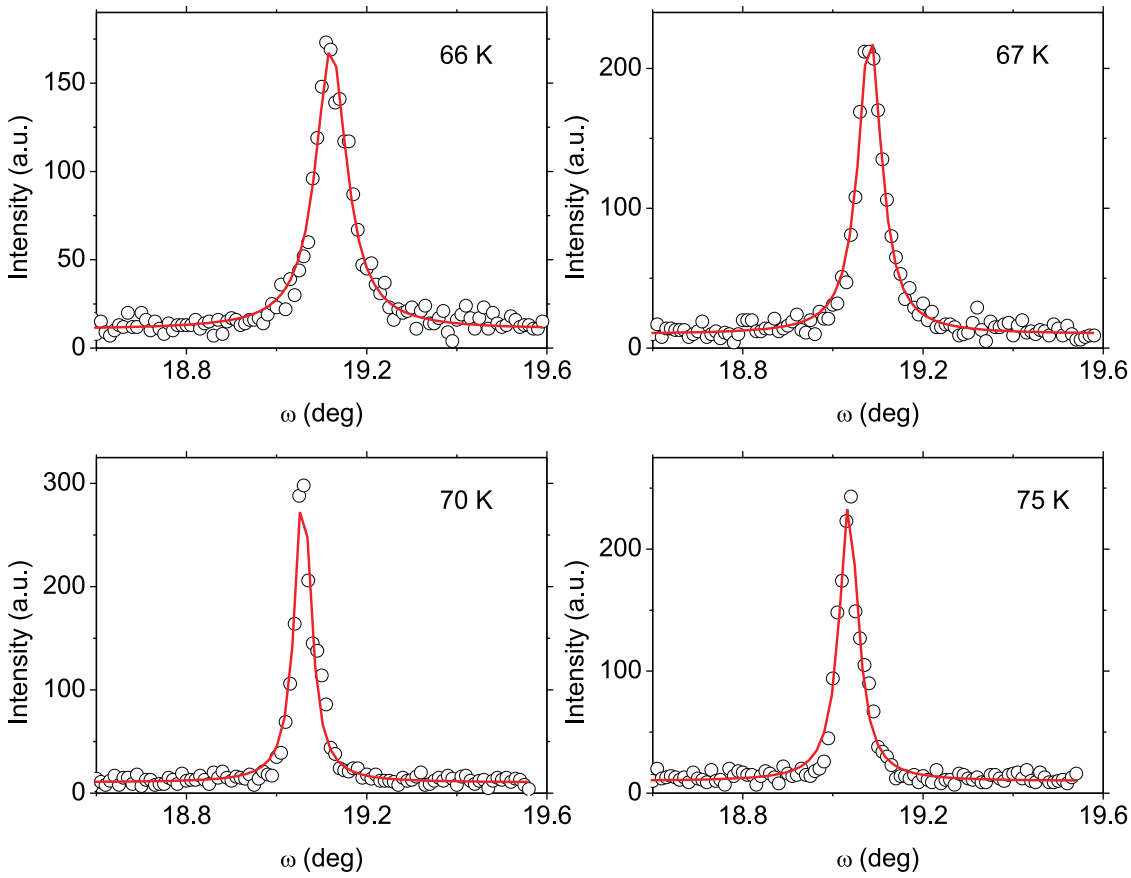

Figure C.6: ω Scans centered at (2-q_1 3.5 1) at different temperatures as indicated. The solid lines represent the fit by Lorentz functions. The position x_c and the FWHM of the peaks are: 19.1211(9), 0.0836(29) 66 K; 19.0823(6), 0.0624(17) 67 K; 19.0585(5), 0.0431(16) 70 K; 19.0351(6), 0.0503(19) 75 K.

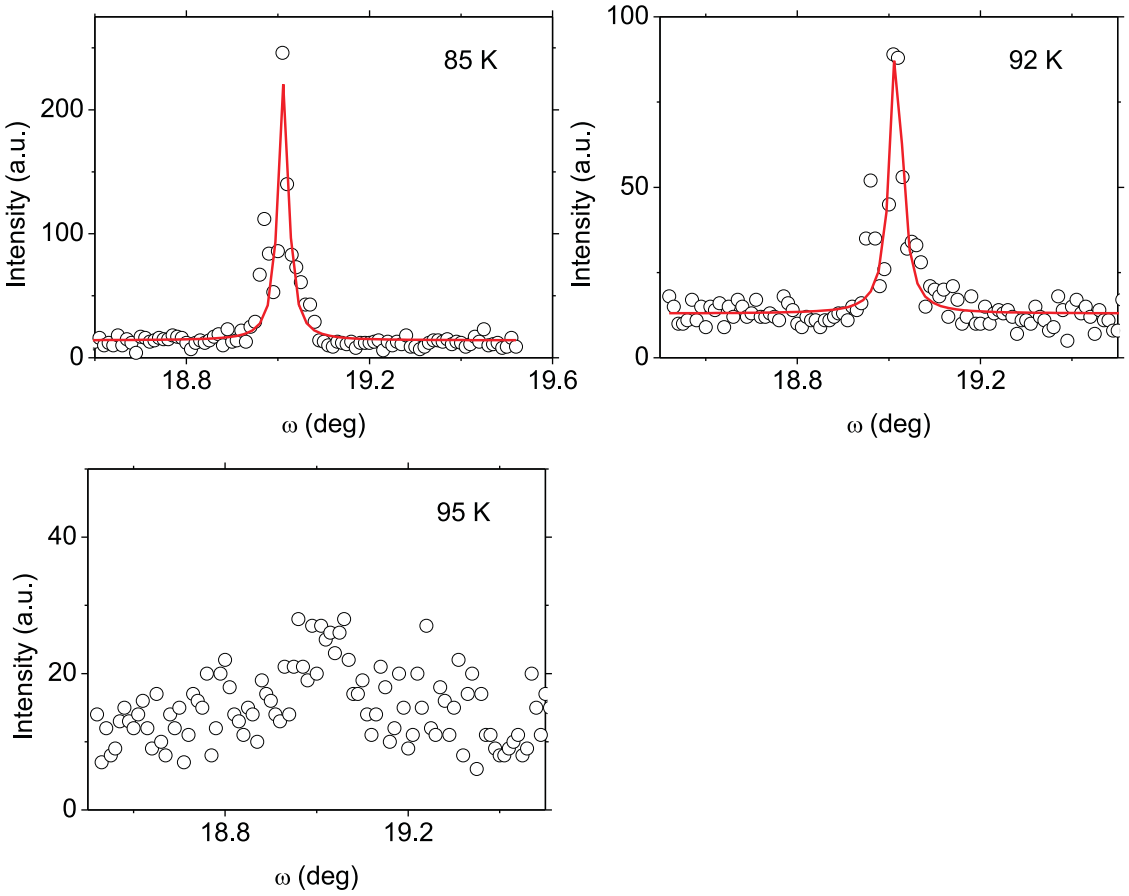

Figure C.7: ω Scans centered at (2-q_1 3.5 1) at different temperatures as indicated. The solid lines represent the fit by Lorentz functions. The position x_c and the FWHM of the peaks are: 19.0118(8), 0.0272(24) 85 K; 19.0158(10), 0.0329(31) 92 K; A peak is not observed at 95 K.

Appendix D

Supplementary materials: CrOCl

Table D.1: 19 reflections were removed due to the high shoulder in the profile of the diffraction peaks, which do not provide the real intensities.

h	k	l	h	k	l	h	k	l	h	k	l
-1	-2	0	0	-2	-7	0	0	-1	1	-3	-6
0	-2	-4	-1	-3	-6	1	-2	0	0	-5	-6
0	-2	-3	0	-3	-8	2	-1	4	0	-4	-9
0	-1	-1	0	-3	-7	1	-3	-5	0	-4	-7
0	-1	1	0	-3	-6	2	-3	1			

Bibliography

Aczel, A., MacDougall, G., Ning, F., Rodriguez, J., Saha, S., Chou, F., Imai, T. and Luke, G. (2011). Absence of static magnetic order in lightly-doped $Ti_{1-x}Sc_xOCl$ down to 1.7 K, *Phys. Rev. B* **83**(13): 134411.

Adam, A. and Buisson, G. (1975). Structure magnétique cycloïdale de FeOCl, *phys. stat. sol. (a)* **30**(1): 323–329.

Anderson, P. E., Liu, J. Z. and Shelton, R. N. (1997). Effect of cobalt doping on the magnetic properties of the spin-Peierls cuprate $CuGeO_3$, *Phys. Rev. B* **56**: 11014–11021.

Angelkort, J. (2009). *Characterization of phase transitions by the analysis of crystal structures*, doctoral thesis, University of Bayreuth.

Angelkort, J., Wölfel, A., Schönleber, A., van Smaalen, S. and Kremer, R. K. (2009). Observation of strong magnetoelastic coupling in a first-order phase transition of CrOCl, *Phys. Rev. B* **80**(14): 144416.

Bannwart, R. S., Phillips, J. E. and Herber, R. H. (1987). Magnetic susceptibility of FeOCl, *J. Solid State Chem.* **71**(2): 540–542.

Beynon, R. J. and Wilson, J. A. (1993). TiOCl, TiOBr - are these RVB d1, S=1/2 materials? the results of scandium substitution set in the context of other S=1/2 systems of current interest for high-temperature superconductivity and the metal-insulator transition, *J. Phys.: Condens. Matter* **5**(13): 1983.

Binnewies, M., Glaum, R., Schmidt, M. and Schmidt, P. (2012). *Chemical vapor transport reactions*, Walter de Gruyter GmbH and Co. KG, Berlin.

Bogdanov, N., van den Brink, J. and Hozoi, L. (2011). Ab initio computation of d-d excitation energies in low-dimensional Ti and V oxychlorides, *Phys. Rev. B* **84**: 235146.

Borovik-Romanov, A. S. and Grimmer, H. (2006). Mangetic Properties, *International Tables for Crystallography* **vol. D**: 102–149.

Bray, J. W., Hart, H. R., Interrante, J. L. V., Jacobs, I. S., Kasper, J. S., Watkins, G. D. and Wee, S. H. (1975). Observation of a spin-Peierls transition in a Heisenberg antiferromagnetic linear-chain system, *Phys Rev. Lett.* **35**: 744.

Bray, J. W., Interrante, L. V., Jacobs, I. S. and Bonner, J. C. (1983). The spin-Peierls transition, *in* J. S. Miller (ed.), *Extended linear chain compounds, Vol. 3*, Plenum Press, New York.

Buzdin, A. I. and Bulaevskiĭ, L. N. (1980). Spin-Peierls transition in quasi-one-dimensional crystals, *Soviet Physics Uspekhi* **23**(7): 409.

Bykov, M., Zhang, J., Schönleber, A., Wölfel, A., Ali, S. I., van Smaalen, S., Glaum, R., Koo, H.-J., Whangbo, M.-H., Reuvekamp, P. G., Law, J. M., Hoch, C. and Kremer, R. K. (2013). Spin-Peierls distortions in $TiPO_4$, *Phys. Rev. B* **88**: 184420.

Chatterji, T. (2006). *Neutron Scattering from Magnetic Materials*, Elsevier Science, Amsterdam.

Chesnut, D. B. (1966). Instability of a linear spin arry: Application to Würster's blue perchlorate, *J. Chem. Phys.* **17**: 4677.

Christensen, A. N., T, J. and S, Q. (1975). Preparation and Magnetic Properties of CrOCl, *Acta Chemica Scandinavica A* **28**: 1171.

Clancy, J., Gaulin, B., Castellan, J., Rule, K. and Chou, F. (2008). Suppression of the commensurate spin-Peierls state in Sc-doped $Ti_{1-x}Sc_xOCl$ (x=0.0, 0.01, and 0.03), *Phys. Rev. B* **78**(1): 014433.

Clancy, J. P., Gaulin, B. D. and Chou, F. C. (2010). Critical properties of the unconventional spin-Peierls system TiOBr, *Phys. Rev. B* **81**(2): 024411.

Craco, L., Laad, M. S. and Müller-Hartmann, E. (2006). Metallizing the Mott insulator TiOCl by electron doping, *J. Phys.: Condens. Matter* **18**(48): 10943–10953.

Dai, Y.-D., Yu, Z., He, Y., Huang, H.-B., Shao, T., Lin, J., Ali, A. M., Jiang, Z.-Y. and Hsia, Y.-F. (2002). Mössbauer studies on the spiral antiferromagnetic coupling in iron oxychloride, *Chem. Phys. Lett.* **358**(5): 473 – 478.

Dresselhaus, M. S. and Dresselhaus, G. (1994). New Directions in Intercalation Research, *Mol. Cryst. Liq. Cryst.* **244**(1): 1–12.

Eichhorn, K. D. (1991). *= R E D U C E = - Calculation of Intergrated Intensities from Step-Scan-Measured Bragg-Reflections for Both Neutrons and X-rays*, version (5.0) edn.

Fausti, D., Lummen, T., Angelescu, C., Macovez, R., Luzon, J., Broer, R., Rudolf, P., van Loosdrecht, P., Tristan, N., Büchner, B., van Smaalen, S., Möller, A., Meyer, G. and Taetz, T. (2007). Symmetry disquisition on the TiOX phase diagram (X=Br,Cl), *Phys. Rev. B* **75**(24): 245114.

Fujii, Y., Nakao, H., Yosihama, T., Nishi, M., Nakajima, K., Kakurai, K., Isobe, M., Ueda, Y. and Sawa, H. (1997). New Inorganic Spin-Peierls Compound NaV_2O_5 Evidenced by X-Ray and Neutron Scattering, *J. Phys. Soc. Jpn.* **66**(2): 326–329.

Glawion, S., Scholz, M. R., Zhang, Y. Z., Valenti, R., Saha-Dasgupta, T., Klemm, M., Hemberger, J., Horn, S., Sing, M. and Claessen, R. (2009). Electronic structure of the two-dimensional Heisenberg antiferromagnet VOCl: a multiorbital Mott insulator, *Phys. Rev. B* **80**: 155119.

Goldstaub, S. (1935). FeOCl, *Bull. Soc. Fr. Mineral.* **58**: 49–69.

Grant, R. W. (1971). Magnetic Structure of FeOCl, *J. Appl. Phys.* **42**(4): 1619–1620.

Gregson, A. K. (1974). Magnetic susceptibility measurements, *in* P. Day (ed.), *Electronic Structure and Magnetism of Inorganic Compounds: Volume 3*, Vol. 3, The Royal Society of Chemistry, pp. 153–217.

Grenier, B., Renard, J.-P., Veillet, P., Paulsen, C., Dhalenne, G. and Revcolevschi, A. (1998). Scaling in dimer breaking by impurities in $CuGeO_3$:A comparative experimental study of Zn-, Mg-, Ni-, and Si-doped single crystals, *Phys. Rev. B* **58**: 8202–8205.

Grenier, B., Renard, J.-P., Veillet, P., Regnault, L.-P., Lorenzo, J., Paulsen, C., Dhalenne, G. and Revcolevschi, A. (1999). Universal phase diagram of Si-, Zn-, Mg- and Ni-doped $CuGeO_3$: spin-Peierls order and antiferromagnetism, *Physica B: Condensed Matter* **259**(0): 954–955.

Gruner, G. (1994). *Density waves in solids*, Addison–Wesley, Reading, Massachusetts.

Haase, A. and Brauer, G. (1975). Vanadium Oxychlorid, *Acta. Crystallogr. B* **31**: 2521–2522.

Haravifard, S., Rule, K. C., Dabkowska, H. A., Gaulin, B. D., Yamani, Z. and Buyers, W. J. L. (2007). Neutron and x-ray scattering studies of the lightly doped spin-Peierls system $Cu_{1-x}Cd_xGeO_3$, *J. Phys.: Condens. Matter* **19**(43): 436222.

Hase, M., Terasaki, I., Sasago, Y., Uchinokura, K. and Obara, H. (1993). Effects of substitution of Zn for Cu in the spin-Peierls cuprate, $CuGeO_3$: The suppression of the spin-Peierls transition and the occurrence of a new spin-glass state, *Phys. Rev. Lett.* **71**: 4059–4062.

Hemberger, J., Hoinkis, M., Klemm, M., Sing, M., Claessen, R., Horn, S. and Loidl, A. (2005). Heat capacity of the quantum magnet TiOCl, *Phys. Rev. B* **72**: 012420.

Hoinkis, M. (2006). *Phase Transitions in Low-Dimensional Transition Metal Compounds*, doctoral thesis, University of Augsburg.

Hoinkis, M., Sing, M., Schäfer, J., Klemm, M., Horn, S., Benthien, H., Jeckelmann, E., Saha-Dasgupta, T., Pisani, L., Valentí, R. and Claessen, R. (2005). Electronic structure of the spin-1/2 quantum magnet TiOCl, *Phys. Rev. B* **72**(12): 125127.

Holz, A., Penson, K. A. and Bennemann, K. H. (1977). Qualitative theory for first- and second-order lattice phase transitions in quasi-one-dimensional systems, *Phys. Rev. B* **16**: 3999–4011.

Hone, D. W. and Richards, P. M. (1974). One- and Two-Dimensional Magnetic Systems, *Annual Review of Materials Science* **4**(1): 337–363.

Hong, X. Q. and Hirsch, J. E. (1992). Superconductivity in the transition-metal series, *Phys. Rev. B* **46**: 14702–14712.

Hossain, M. A., Mottershead, J. D. F., Fournier, D., Bostwick, A., McChesney, J. L., Rotenberg, E., Liang, R., Hardy, W. N., Sawatzky, G. A., Elfimov, I. S., Bonn, D. A. and Damascelli, A. (2008). In situ doping control of the surface of high-temperature superconductors, *Nature Phys.* **4**: 527–531.

Huizinga, S., Kommandeur, J., Sawatzky, G. A., Thole, B. T., Kopinga, K., de Jonge, W. J. M. and Roos, J. (1979). Spin-Peierls transition in N-methyl-N-ethyl-morpholinium-ditetracyanoquinodimethanide [MEM-$(TCNQ)_2$], *Phys. Rev. B* **19**: 4723–4732.

Hwang, S. R., Li, W.-H., Lee, K. C., Lynn, J. W. and Wu, C.-G. (2000). Spiral magnetic structure of Fe in Van der Waals gapped FeOCl and polyaniline-intercalated FeOCl, *Phys. Rev. B* **62**(21): 14157–14163.

Imai, T. and Chou, F. C. (2003). Novel Spin-Gap Behavior in Layered S=1/2 Quantum Spin System TiOCl.

Jacobs, I. S., Bray, J. W., Hart, H. R., Interrante, J. L. V., Kasper, J. S. and Watkins, G. D. (1976). Spin-Peierls transition in magnetic donor-acceptor compounds of tetrathiafulvalene (TTF) with bisdithiolene metal complexes, *Phys Rev. B* **14**: 3036.

Jens Als-Nielsen, D. M. (2011). *Elements of Modern X-ray Physics, 2nd Edition*, John Wiley and Sons, New York.

Kataev, V., Baier, J., Möller, A., Jongen, L., Meyer, G. and Freimuth, A. (2003). Orbital order in the low-dimensional quantum spin system TiOCl probed by ESR, *Phys. Rev. B* **68**: 140405.

Kimura, T. and Tokura, Y. (2000). Layered magnetic manganites, *Annual Review of Materials Science* **30**(1): 451–474.

Klein, C. (2010). *The mar345dtb User's Guide - online manual*, Marresearch GmbH.

Kojima, K. M., Fudamoto, Y., Larkin, M., Luke, G. M., Merrin, J., Nachumi, B., Uemura, Y. J., Hase, M., Sasago, Y., Uchinokura, K., Ajiro, Y., Revcolevschi, A. and Renard, J.-P. (1997). Antiferromagnetic Order with Spatially Inhomogeneous Ordered Moment Size of Zn- and Si-Doped $CuGeO_3$, *Phys. Rev. Lett.* **79**: 503–506.

Komarek, A. C., Taetz, T., Fernandez-Diaz, M. T., Trots, D. M., Möller, A. and Braden, M. (2009). Strong magneto-elastic coupling in VOCl: neutron and synchrotron powder x-ray diffraction study, *Phys. Rev. B* **79**: 104425.

Korshunov, M. M. and Eremin, I. (2008). Theory of magnetic excitations in iron-based layered superconductors, *Phys. Rev. B* **78**: 140509.

Krimmel, a., Strempfer, J., Bohnenbuck, B., Keimer, B., Hoinkis, M., Klemm, M., Horn, S., Loidl, a., Sing, M., Claessen, R. and Zimmermann, M. (2006). Incommensurate structure of the spin-Peierls compound TiOCl in zero and finite magnetic fields, *Phys. Rev. B* **73**(17): 172413.

Kuntscher, C., Klemm, M., Horn, S., Sing, M. and Claessen, R. (2010). Possible metallization of the Mott insulators TiOCl and TiOBr: Effects of doping and external pressure, *Eur. Phys. J. Spl. Top.* **180**(1): 29–42.

Landee, C. P. and Turnbull, M. M. (2013). Recent Developments in Low-Dimensional Copper(II) Molecular Magnets, *Eur. J. Inorg. Chem.* **2013**(13): 2266–2285.

Law, J. M., Hoch, C., Glaum, R., Heinmaa, I., Stern, R., Kang, J., Lee, C., Whangbo, M.-H. and Kremer, R. K. (2011). Spin-Peierls transition in the S=1/2 compound $TiPO_4$ featuring large intrachain coupling, *Phys. Rev. B* **83**: 180414.

Lépine, Y., Caillé, A. and Larochelle, V. (1978). Potassium-tetracyanoquinodimethane (K-TCNQ): A spin-Peierls system, *Phys. Rev. B* **18**: 3585–3592.

Lévy, F. A. (1979). *Intercalated layered Materials*, D. Reidel Publishing Company, Dordrecht.

Lind, M. D. (1970). Refinement of the crystal structure of iron oxychloride, *Acta Crystallogr. B* **26**(4): 1058–1062.

Lovesey, S. and Collins, S. (1996). *X-Ray Scattering and Absorption by Magnetic Materials*, Oxford Series on Synchrotron Radiation, Clarendon Press.

Lumsden, M. D., Gaulin, B. D. and Dabkowska, H. (1998). Critical phenomena at the spin-Peierls transition in doped $CuGeO_3$, *Phys. Rev. B* **58**: 12252–12259.

Macovez, R., Luzon, J., Schiessling, J., Sadoc, A., Kjeldgaard, L., van Smaalen, S., Fausti, D., van Loosdrecht, P., Broer, R. and Rudolf, P. (2007). Hybridization, superexchange, and competing magnetoelastic interactions in TiOBr, *Phys. Rev. B* **76**(20): 205111.

Maddock, A. G. (1997). *Mössbauer Spectroscopy, 1st Edition*, Elsevier Science, Amsterdam.

Manabe, K., Ishimoto, H., Koide, N., Sasago, Y. and Uchinokura, K. (1998). Antiferromagnetic long-range order in $Cu_{1-x}Zn_xGeO_3$ with extremely low Zn concentration, *Phys. Rev. B* **58**: R575–R578.

Miller, J. S. (1983). *Extended linear chain compounds*, Plenum Press.

Mizuguchi, Y., Fujihisa, H., Gotoh, Y., Suzuki, K., Usui, H., Kuroki, K., Demura, S., Takano, Y., Izawa, H. and Miura, O. (2012). BiS2-based layered superconductor Bi4O4S3, *Phys. Rev. B* **86**: 220510.

Nishimori, H. and Ortiz, G. (2011). *Elements of phase transitions and critical phenomena*, Oxford University Press, Oxford.

Nocker, K. and Gruehn, R. (1993). Zum chemischen Transport von CrOCl und Cr_2O_3 – Experimente und Modellrechnungen zur Beteiligung von $CrOCl_{2,g}$, *Z. Anorg. Allg. Chem.* **619**: 699–710.

Oseroff, S. B., Cheong, S.-W., Aktas, B., Hundley, M. F., Fisk, Z. and Rupp, Jr., L. W. (1995). Spin-Peierls State versus Néel State in Doped $CuGeO_3$, *Phys. Rev. Lett.* **74**: 1450–1453.

Perez-Mato, J. M., Ribeiro, J. L., Petricek, V. and Aroyo, M. I. (2012). Magnetic superspace groups and symmetry constraints in incommensurate magnetic phases, *J. Phys.: Condens. Matter* **24**(16): 163201.

Petricek, V., Dusek, M. and Palatinus, L. (2006). JANA2006, *Institute of Physics, Prague, Czech Republic* .

Petricek, V., Fuksa, J. and Dusek, M. (2010). Magnetic space and superspace groups, representation analysis: competing or friendly concepts?, *Acta Crystallogr. A* **66**(6): 649–655.

Rotter, M., Tegel, M. and Johrendt, D. (2008). Superconductivity at 38 K in the Iron Arsenide $(Ba_{1-x}K_x)Fe_2As_2$, *Phys. Rev. Lett.* **101**: 107006.

Saha-Dasgupta, T., Valentí, R., Rosner, H. and Gros, C. (2004). TiOCl, an orbital-ordered system?, *Europhysics Letters (EPL)* **67**(1): 63–69.

Sasaki, T., Mizumaki, M., Kato, K., Watabe, Y., Nishihata, Y., Takata, M. and Akimitsu, J. (2005). Observation of Phase Transition with Lattice Distortion in the Low-dimensional Quantum Spin System TiOBr by Synchrotron X-ray Diffraction, Evidence of Spin-Peierls Transition?, *J. Phys. Soc. Jpn.* **74**(8): 2185–2188.

Schäfer, H., Wartenpfuhl, F. and Weise, E. (1958). Über Titanchloride. V. Titan(III)-oxychlorid, *Zeitschrift für anorganische und allgemeine Chemie* **295**(3-4): 268–280.

Schäfer, H. and Wartenpfuhl, F. Z. (1961). Das Chrom(III)oxydchlorid CrOCl, *Z. Anorg. Allgem. Chem.* **308**: 282.

Schäfer, H., Wittig, F. E. and Jori, M. (1956). Untersuchungen am System Fe_2O_3-$FeCl_3$–H_2O-HCl. IX. Die thermochemische Beständigkeit des Eisenoxychlorids FeOCl, *Z. Anorg. Allg. Chem.* **287**(1): 61–70.

Schneemeyer, L. F., DiSalvo, F. J., Spengler, S. E. and Waszczak, J. V. (1984). Dramatic impurity effects on the charge-density wave in potassium molybdenum bronze, *Phys. Rev. B* **30**: 4297–4301.

Schönleber, A., Angelkort, J., van Smaalen, S., Palatinus, L., Senyshyn, A. and Morgenroth, W. (2009). Phase transition, crystal structure, and magnetic order in VOCl, *Phys. Rev. B* **80**(6): 064426.

Schönleber, A., Shcheka, G. and van Smaalen, S. (2008). Normal-to-incommensurate phase transition in the spin-Peierls compound TiOCl: An x-ray diffraction study, *Phys. Rev. B* **77**(9): 094117.

Schönleber, A., van Smaalen, S. and Palatinus, L. (2006). Structure of the incommensurate phase of the quantum magnet TiOCl, *Phys. Rev. B* **73**(21): 214410.

Seidel, A., Marianetti, C. A., Chou, F. C., Ceder, G. and Lee, P. A. (2003). $S = 1/2$ chains and spin-Peierls transition in TiOCl, *Phys. Rev. B* **67**: 020405(R).

Shannon, R. D. (1976). Revised effective ionic radii and systematic studies of interatomic distances in halides and chalcogenides, *Acta Crystallogr. A* **32**(5): 751–767.

Shaz, M., van Smaalen, S., Palatinus, L., Hoinkis, M., Klemm, M., Horn, S. and Claessen, R. (2005). Spin-Peierls transition in TiOCl, *Phys. Rev. B* **71**(10): 100405.

Spaldin, N. A. (2010). *Magnetic Materials: Fundamentals and Applications*, 2 edn, Cambridge University Press.

Stokes, H. T., Campbell, B. J. and van Smaalen, S. (2011). Generation of $(3 + d)$-dimensional superspace groups for describing the symmetry of modulated crystalline structures, *Acta Crystallogr. A* **67**: 45–55.

Takaoka, Y. and Motizuki, K. (1979). Spin-Peierls Transition in Alkali-TCNQ Salts, *J. Phys. Soc. Jpn.* **47**(6): 1752–1759.

Tokura, Y., Takagi, H. and Uchida, S. (1989). A superconducting copper oxide compound with electrons as the charge carriers, *Nature* **337**: 345–347.

Uchinokura, K. (2002). Spin-Peierls transition in $CuGeO_3$ and impurity-induced ordered phases in low-dimensional spin-gap systems, *J. Phys.: Condens. Matter* **14**(10): R195.

van Smaalen, S., Palatinus, L. and Schönleber, A. (2005). Incommensurate interactions and nonconventional spin-Peierls transition in TiOBr, *Phys. Rev. B* **72**(2): 020105.

Wiedenmann, A., Venien, J. P., Palvadeau, P. and Rossat-Mignod, J. (1983). Magnetic ordering of the quasi-two-dimensional system VOCl, *J. Phys. C: Solid State Phys.* **16**(27): 5339.

Yamanaka, S., Kawaji, H., Hotehama, K.-i. and Ohashi, M. (1996). A new layer-structured nitride superconductor. Lithium-intercalated β-zirconium nitride chloride, Li_xZrNCl, *Adv. Mater.* **8**(9): 771–774.

Yamanaka, S., Yasunaga, T., Yamaguchi, K. and Tagawa, M. (2009). Structure and superconductivity of the intercalation compounds of TiNCl with pyridine and alkali metals as intercalants, *J. Mater. Chem.* **19**: 2573–2582.

Zhang, J., Wölfel, A., Li, L., van Smaalen, S., Williamson, H. L. and Kremer, R. K. (2012). Magnetoelastic coupling in the incommensurate antiferromagnetic phase of FeOCl, *Phys. Rev. B* **86**: 134428.

Zhang, Y.-Z., Foyevtsova, K., Jeschke, H. O., Schmidt, M. U. and Valentí, R. (2010). Can the Mott Insulator TiOCl be Metallized by Doping? A First-Principles Study, *Phys. Rev. Lett.* **104**(14): 146402.

Zhang, Y.-Z., Jeschke, H. and Valentí, R. (2008). Two Pressure-Induced Transitions in TiOCl: Mott Insulator to Anisotropic Metal, *Phys. Rev. Lett.* **101**(13): 136406.

Publications

J. Zhang, A. Wölfel, L. Li, S. van Smaalen, H. L. Williamson, and R. K. Kremer
Magnetoelastic coupling in the incommensurate antiferromagnetic phase of FeOCl.
Physical Review B, **86**, 134428 (2012).

M. Bykov, J. Zhang, A. Schönleber, A. Wölfel, Sk I. Ali, A. van Smaalen, R. Glaum, H.-J. Koo, M.-H. Whangbo, P.G. Reivekamp, J.M. Law, C. Hoch, and R.K. Kremer
Spin-Peierls distortions in TiPO4.
Physical Review B, **88**, 184420 (2013).

J. Zhang, A. Wölfel, M. Bykov, A. Schönleber, S. van Smaalen, R. K. Kremer, and H. L. Williamson
Transformation between spin-Peierls and incommensurate fluctuating phases of Sc-doped TiOCl.
Physical Review B (Accepted).

Acknowledgements

First and foremost, I would like to express my heartily thankful to my supervisor, Prof. Dr. Sander van Smaalen, a respectable and responsible scholar, who has provided me with guidance and support during the development of this dissertation. Without his expert instruction, impressive patient and kindness, this dissertation would not have reached its present form. His vigorous academic observation enlightens me not only in this dissertation but also in my future study.

Special thank goes out to PD Dr. Andreas Schönleber for his guidance in my work and life in Bayreuth. He helped me with the Zusammenfassung of this thesis. I would also like to thank Denise Kelk-Huth for her support over my time at University of Bayreuth. I would like to thanks all my current and ex-colleagues Joachim Angelkort, SK Imran Ali, Maxim Bykov, Somnath Dey, Franz Fischer, Dr. Jeanette Held, Dr. Christian Hübschle, Guoming Hao, Dr. Liang Li, Dr. Swastik Mondal, Leila Noohinejad, Dr. Siriyara Jagannatha Prathapa, Alfred Suttner and Dr. Alexander Wölfel for providing a nice working environment.

Furthermore, I would like to thank my family for their generous and consistent support. I also want to thank all of my friends for their friendships and helps to me.

Erklärung

Ich versichere hiermit eidesstattlich, dass ich diese Dissertation selbstständig und nur unter Verwendung angebener Quellen und zulässiger Hilfsmittel erstellt habe. Ich habe bisher keine Promotionsversuche unternommen. Ich habe bisher weder die Hilfe von gewerblichen Promotionsberatern bzw. -vermittlern in Anspruch genommen, noch werde ich sie künftig in Anspruch nehmen.

Jian Zhang

Bayreuth, den 09.07.2014